An extensive analysis for externally driven flow in microchannels

Thesis Submitted by

Sujit Saha

Doctor of Philosophy (Engineering)

Department of Mechanical Engineering

Faculty Council of Engineering & Technology

Jadavpur University

Kolkata, India

2025

INDEX NO. 238/18/E

1. Title of the Thesis:

An extensive analysis for externally driven flow in microchannels

2. Name, Designation & Institution of the Supervisor:

Dr. Balaram Kundu
Professor
Department of Mechanical Engineering,
Jadavpur University,
Kolkata – 700 032, India

3. List of Publications:

International journal

(i) **Saha, S.,** & Kundu, B. Dual-objective optimization of time-periodic electroviscous flow of Oldroyd-B nanofluids in microchannels. ***Chemical Engineering Journal*** 2025;521;166849 ***(Q1) (Impact factor- 13.2)***
DOI: https://doi.org/10.1016/j.cej.2025.166849

(ii) **Saha, S.,** & Kundu, B. Highest electro-viscous energy and lowest irreversibility analysis for Maxwell fluid in transient microchannel flow. ***Applied Thermal Engineering*** 2025; 267:125764. ***(Q1) (Impact factor- 6.9)***
DOI: https://doi.org/10.1016/j.applthermaleng.2025.125764

(iii) **Saha, S.,** & Kundu, B. Multi-objective optimization of electrokinetic energy conversion efficiency and entropy generation for streaming potential driven electromagnetohydrodynamic flow of couple stress Casson fluid in microchannels with slip-dependent zeta potentials, ***Energy*** 2023;284: 129288. **(Q1) (Impact factor- 9.4)**
DOI: https://doi.org/10.1016/j.energy.2023.129288

(iv) **Saha, S.,** & Kundu, B. Electroosmotic pressure-driven oscillatory flow and mass transport of Oldroyd-B fluid un-der high zeta potential and slippage conditions in microchannels. ***Colloids and Surfaces A: Physicochemical and Engineering Aspects*** 2022; 647:129070. ***(Q1) (Impact Factor- 5.4)***
DOI: https://doi.org/10.1016/j.colsurfa.2022.129070

(v) Kundu, B., & **Saha, S.** Review and analysis of electro-magnetohydrodynamic flow and heat transport in microchannels. ***Energies*** 2022; 15: 7017. ***(Q1) (Impact factor- 3.2)***
DOI: https://doi.org/10.3390/en15197017

(vi) **Saha, S.,** & Kundu, B. Techno-economic assessment of ion transport and concentration polarization in nanochannel-based electrokinetic desalination systems. ***Water Research*** 2025; ***(Q1) (Impact Factor-12.4)*** *(Communicated)*

4. List of Patents: Nil

5. List of Presentations in National / International /Conferences/Workshops/ Symposiums

(i) **Saha, S.,** & Kundu, B. Electroosmotic slip fluid flow of power law fluids in parallel plate microchannel. Presented at the International Conference on Energy and Sustainable Development, Jadavpur University, Kolkata, India, 2020.

(ii) **Saha, S.,** & Kundu, B. A semi-analytical approach to determine the EDL potential distribution in rectangular microchannel. Presented at 5th International Conference on Advances in Mechanical Engineering, Yildiz Technical University, Istanbul, Turkey, 2019.

(iii) **Saha, S.,** & Kundu, B. Exact Analytical Determination of Nusselt Number for Flow Through a Microchannel Under Electric and Magnetic Field. In Advances in Mechanical Engineering (pp. 893-905), Springer, Singapore, 2018.

"Statement of Originality"

I Shri **Sujit Saha** registered on 23th April, 2018 do hereby declare that this thesis entitled "*An extensive analysis for externally driven flow in microchannels*" contains literature survey and original research work done by the undersigned candidate as part of Doctoral studies. All information in this thesis has been obtained and presented in accordance with existing academic rules and ethical conduct. I declare that, as required by these rules and conduct, I have fully cited and referred all materials and results that are not original to this work. I also declare that I have checked this thesis as per the "Policy on Anti Plagiarism, Jadavpur University, 2019", and the level of similarity as checked by iThenticate software is 2 %.

Signature of Candidate: Sujit Saha

Date:31.12.2025

Place: Kolkata

Certified by Supervisor:

31-12-2025

Dr. Balaram Kundu
Professor
Department of Mechanical Engineering
Jadavpur University
Kolkata 700032, India

Date:31.12.2025

Place: Kolkata

Signature of Supervisor and date with office Seal

Dr. Balaram Kundu
Professor
Dept. of Mechanical Engineering
Jadavpur University
Kolkata-700032

Certificate from the Supervisor

This is to certify that the thesis entitled *"An extensive analysis for externally driven flow in microchannels"* submitted by Shri. *Sujit Saha*, who got his name registered on 23th April, 2018 for the award of Ph.D. (Engineering.) degree of Jadavpur University is absolutely based upon his own work under the supervision of Dr. Balaram Kundu and that neither his thesis nor any part of the thesis has been submitted for any degree or any other academic award anywhere before.

31-12-2025

(Dr. Balaram Kundu)
Professor
Department of Mechanical Engineering
Jadavpur University
Kolkata 700032, India

Date:31.12.2025

Place: Kolkata

Signature of Supervisor and date with office Seal

Dr. Balaram Kundu
Professor
Dept. of Mechanical Engineering
Jadavpur University
Kolkata-700032

Dedication

This dissertation is devoted with my deepest love and gratitude to *My Beloved Parents*, my greatest source of strength and inspiration. Their constant encouragement, sacrifices, and faith in me made this journey possible.

I also dedicate this work to *The Buddha*, whose teachings filled my life with wisdom, compassion, clarity, and peace. His guidance gave me strength in moments of doubt, light in times of uncertainty, and serenity throughout this journey. For the gift of good health, inner courage, and the power to think and grow, I bow in humble gratitude.

With reverence and love, I offer this work.

Acknowledgements

Research is defined as the systematic effort to gain new knowledge. This journey toward discovery becomes possible with guidance, encouragement, and unwavering support. Throughout my PhD journey, I encountered many challenges, and I owe immense gratitude to those who helped me overcome them.

I would like to acknowledge my PhD supervisor, Prof. Balaram Kundu, for his supervision during my doctoral research.

I extend my sincere gratitude to my Research Advisory Committee members, Prof. Sudip Simlandi and Prof. Prokash Chandra Roy, for their invaluable feedback. I also thank Prof. Himadri Chattopadhyay and Prof. Nilkanta Barman for their guidance and support.

I would also like to express my gratitude to my parents (Shri. Monoranjan Saha and Smt. Kajal Saha), my elder brother (Shri. Samir Saha), and my little nephew (Shri. Ishan Saha) for standing by me always and keeping faith in me. It cannot be expressed in words what my family has done for me and continues to do. I thank them for supporting me at every step of my life and for their constant affection.

I would also like to thank Dr. Sutapa Mondal for being there for me in my vulnerable moments and being a source of constant motivation.

To my friends, seniors, juniors, and lab-mates at Jadavpur University, especially Dr. Soumitra Pati, Dr. Sayan Das, Dr. Pramod Wankhede, Dr. Ritwik Bagchi, Mr. Sabyasachi Mondal, Mr. Satyajit Das Karmakar, Mr. Risav Dutta, Mr. Jayanarayan Mahakud, Mr. Kumar Abanindra Jana, and Mr. Indrajit Bag, thank you for your camaraderie and collaboration.

I gratefully acknowledge the Department of Mechanical Engineering, the Head of the Department, and the staff of the Heat Power Laboratory for their valuable technical assistance.

My gratitude also extends to the New PG Cum Research Scholars' Hostel at Jadavpur University for providing accommodation during my research.

Finally, I thank the AICTE-NDF/ADF, Government of India, for their financial support throughout my PhD tenure.

Signature: Sujit Saha
31/12/2025

(Sujit Saha)

Abstract

This thesis provides a detailed investigation of electrohydrodynamic transport phenomena in microchannels, thoroughly examining the interaction between electroosmotic (EOF) and streaming-potential-driven (SPF) flows in response to the simultaneous effects of electric, magnetic, and thermal field variations. The study advances theoretical, computational, and practical frameworks to address momentum, energy, and heat transport governed by nonlinear equations, incorporating Newtonian, and non-Newtonian rheology (Oldroyd-B, Couple stress Casson, Maxwell models), magnetic nanofluids (Fe_3O_4-H_2O), slip/jump boundary conditions, and multi-physical interactions such as Lorentz forces, Hall currents, ion slip, Joule heating, viscous dissipation, and thermal radiation.

Building on this framework, the thesis develops a semi mathematical model is developed to examine microscale transport of Oldroyd-B fluids in electroosmotic pressure driven flows under time periodic oscillations and wall slip conditions. A finite difference method (MATLAB bvp4c) is employed to solve the strongly non-linear electrical potential and concentration equations. A time-periodic oscillation effect on the velocity profile, concentration distribution, and mass transport is analyzed under low or high zeta potentials at the wall. The results show that fluid elasticity significantly enhances flow oscillations and mass transport, with a peak velocity increase of 142.75% at $\bar{\xi}$=4 compared to $\bar{\xi}$=1, and a 21.01% rise in velocity amplitude as the elasticity parameter increases from $\bar{\lambda}_1$=0.1 to $\bar{\lambda}_1$=0.2. A resonant mass transfer behavior driven by the coupled effects of angular Reynolds number and fluid elasticity is also identified, highlighting the potential of oscillatory viscoelastic flows for enhanced microfluidic transport applications.

Building upon this, the study examines electrokinetically driven flow, thermal transport, and energy conversion in microchannels containing hybrid viscoplastic fluids under slip-sensitive boundaries. A model for pressure-driven viscoelastic Casson fluids with couple-stress effects incorporates slip-modulated surface potential and external electric and magnetic fields, and is optimized using the non-dominated sorting genetic algorithm-II (NSGA-II) algorithm to enhance energy harvesting and reduce thermodynamic inefficiencies. The findings show that microstructural couple-stress and Casson viscoplasticity strongly influence streaming potential, energy harvesting, thermal gradients, and heat transfer, while frictional losses, ohmic heating, and radiation significantly affect convective thermal performance. According to the results, the electrokinetic energy conversion (EKEC) efficiency increases with slip-modulated surface charge potentials in couple-stress Casson fluid, couple-stress fluid, Casson fluid, and Newtonian fluid by 45.92%, 47.10%, 42.81%, and 37.68%, respectively, compared to scenarios with fixed surface charge potentials. At the center of the microchannel, under thermal jump boundary conditions, the temperature rises by 2.95% relative to systems governed by no-jump boundary constraints.

The unsteady pressure driven streaming potential flow of viscoelastic Fe_3O_4-H_2O nanofluids through porous media is analysed under transient forces, Hall current,

Lorentz force, and ion slip effects. The Maxwell fluid model is solved using separation of variables and the finite difference method, with emphasis on electroviscous heat transfer rate and entropy generation. A multi objective optimization framework based on the Non-Dominated Sorting Grey Wolf Optimizer Algorithm (NSGWOA) and NSGA-II is employed to enhance electroviscous heat transfer while reducing entropy production through Pareto optimal solutions. Five decision variables namely relaxation time, Hall current, ion slip parameter, nanofluid volume fraction, and Hartmann number are considered. The results reveal a 1.92% reduction in streaming current with 2% nanoparticle loading and an 809.91% increase in electrokinetic energy conversion efficiency for slip dependent zeta potential compared to the slip free case. Further optimization using the Technique for Order of Preference by Similarity to Ideal Solution (TOPSIS) yields a 128% enhancement in heat transfer rate and an 82.5% reduction in entropy production.

The analysis is extended to electromagnetohydrodynamic time periodic wavy streaming potential flows of Oldroyd-B fluids relevant to drug delivery and biomolecular separation. Finite difference methods are employed to evaluate velocity field, volume flow rate, concentration distribution, mass transfer rate, temperature, Nusselt number, and entropy generation in a largely unexplored regime. A multi parameter multi objective optimization strategy using the NSGWOA and NSGA-II is developed to simultaneously improve heat transfer and minimize entropy generation. Four key parameters namely Hartmann number, electrokinetic width, zeta potential, and Dukhin number are optimized, and Pareto optimal solutions are identified using the TOPSIS. The optimized results demonstrate a 6.286% improvement in the Nusselt number and a 6.872% reduction in thermal irreversibility, along with a comparative assessment of NSGWOA and NSGA-II.

Extending toward practical implementation, this thesis introduces rectangular and hyperbolic nanochannel architectures for gravity-assisted desalination using ion concentration polarization (ICP) in nanochannel array systems. A computational framework is used to assess flow characteristics, desalination effectiveness, energy demand, and economic viability, with particular attention to scalability in freshwater generation. At an applied potential of 30 V_0 (thermal voltage is V_0), the rectangular nanochannel achieves an approximately 48% greater reduction in outlet Cl^- concentration than the hyperbolic configuration, indicating that geometric sharpness suppresses anion transport and enhances desalination efficiency. The parallelization of nanochannels under gravitational effects demonstrates high-throughput desalination while mitigating fouling issues inherent in conventional membranes.

Data-driven frameworks, including neural networks and adaptive neuro-fuzzy systems, are used to predict optimal Pareto solutions for electroviscous heat transfer and entropy generation from NSGWOA, with the neuro-fuzzy system achieving the lowest mean absolute percentage error. Combining hybrid finite difference methods, optimization algorithms, and machine learning, this work unifies electroosmotic and streaming potential phenomena to guide the design of advanced microdevices for biomolecule separation, energy harvesting, and sustainable water purification, setting a benchmark for predictive optimization in microscale thermos-fluidics.

Title of the thesis

An extensive analysis for externally driven flow in microchannels

Contents

List of Figures

List of Tables

Nomenclature

Abbreviations

ANN	artificial neural network
ANFIS	adaptive neuro-fuzzy inference systems
CSF	couple stress fluid
EDL	electrical double layer
EOF	electroosmotic fluid
EKEC	electrokinetic energy conversion
EMHD	electro-magneto-hydrodynamic
ICP	ion concentration polarisation
LOC	Lab-on-a-Chip
PNP	Poisson-Nernst-Planck
MHD	magneto-hydrodynamic
ML	machine learning
NSGA-II	non-dominated sorting genetic algorithm
NSGWOA	non-dominated gray wolf optimizer algorithm
MAPE	mean absolute percentage error
RMSE	root mean squared error
PNP	Poisson-Nernst-Planck
SRR	salt removal ratio

Symbols

a	velocity slip length (m)
a_1	first order/upper wall velocity slip length (m)
a_1'	upper wall velocity slip length (m)
$\bar{a}$	normalised slip parameter, (a/h)
$\bar{a}_1$	normalised first order/upper wall velocity slip parameter, (a_1/h)
$\bar{a}_1'$	normalised lower wall velocity slip parameter, (a_1'/h)
$\bar{a}_2$	normalised second order velocity slip, (a_2/h)
b	concentration slip length (m)
$\bar{b}$	normalised concentration slip parameter, (b/h)
B	magnetic field vector (T)
Be	Bejan number
Br	Brinkmann number
c	concentration field of the solute (mol m^{-3})
c_1	higher concentration of solute (mol m^{-3})
c_2	lower concentration of solute (mol m^{-3})
c_m	Concentration of membrane (mol m^{-3})
c_0	bulk concentration (mol m^{-3})
c_{out}	outlet concentration (mol m^{-3})
c_p	specific heat at constant pressure (J kg^{-1} K^{-1})

$(c_p)_f$	specific heat capacity of base fluid (J kg^{-1} K^{-1})
$(c_p)_s$	specific heat capacity of magnetic nanoparticles (J kg^{-1} K^{-1})
c_u	flow oscillation effect on concentration field (mol m^{-3})
c_u^0	complex amplitude on concentration field (mol m^{-3})
C_u	normalised oscillation effect on concentration field, $c_u/(c_1$-$c_2)$
C_u^0	normalised complex amplitude of oscillation effect on concentration field, $c_u^0/(c_1$-$c_2)$
$\tilde{C}_u^0$	normalised complex conjugate of oscillation effect on concentration field
d	temperature jump length (m)
$\bar{d}$	normalised jump parameter, (d/h)
d_1	first order/upper wall temperature jump length (m)
$\bar{d}_1$	first order/upper wall temperature jump
d_1'	lower wall temperature jump length (m)
$\bar{d}_1'$	normalised lower wall temperature jump, (d_1'/h)
d_2	second order temperature jump length (m)
$\bar{d}_2$	normalised second order temperature jump length, (d_2/h)
D^+	diffusivity of cation (m^{2}s^{-1})
D^-	diffusivity of anion (m^{2}s^{-1})
Du	Dukhin number, $\sigma_{stern}/(h\sigma_B)$
d_h	hydraulic diameter of the channel (m)
e	electron charge (C)
$e_{i,j}$	(i,j)th component of the rate of deformation
E	electric field vector (Vm^{-1})
E_s^0	complex amplitude of streaming potential (Vm^{-1})
$\bar{E}_s^0$	complex amplitude of normalised induced electric field by streaming potential, E_s^0/ E_{ref}
E_0	complex amplitude of electric field by electroosmotic flow (Vm^{-1})
$\bar{E}_s$	dimensionless streaming potential
E_{ref}	reference streaming potential (V m^{-1})
E_s	electric field induced by streaming potential (V m^{-1})
E_x	electric field in x direction (V m^{-1})
E_y	electric field in y direction (V m^{-1})
E_z	electric field in z direction (V m^{-1})
E_z^0	complex amplitude of external electric field in z direction (Vm^{-1})
F	body force vector per unit volume (N m^{-3})
F	Faraday constant (Cmol^{-1})
f	ionic friction factor (N s m^{-1})
f_d	drag coefficient (kgs^{-1})

g	gravitational constant (ms^{-2})
h	half-height of the microchannel (m)
h_c	convective heat transfer coefficient ($W\ m^{-2}\ K^{-1}$)
ha	horizontal array length (m)
hs	gap length between two arrays (m)
h_h	horizontal length of the hyperbolic nanochannel (m)
h_r	horizontal length of the rectangular nanochannel (m)
$\bar{I}_s$	non-dimensional streaming potential
I_{stern}	stern layer current (A)
J	local current density vector (Am^{-2})
j	Joule heating (Wm^{-3})
$\mathbf{J}_{\pm}$	flux density of ion species ($mol\ m^{-2}\ s^{-1}$)
J_h	dimensionless Joule heating parameter
$\tilde{k}$	Rosseland absorption coefficient (m^{-1})
k_B	Boltzmann constant ($J\ K^{-1}$)
k_T	thermal conductivity ($W\ m^{-1}\ K^{-1}$)
κ_p	permeability within the porous matrix (m^2)
K	dimensionless electrokinetic thickness, (kh)
Kn	Knudsen number
L	length of the microchannel (m)
l	length of the array (m)
m_x	time-space averaged mass transfer rate ($mol\ m^{-2}\ s^{-1}$)
$\bar{m}_x$	normalised time-space averaged mass transfer rate, $(m_xL)/D(c_1-c_2)$
n	outward normal vector
Nr	thermal radiation parameter, $(16T_a^3\sigma)/(3\tilde{k}k_T)$
Nu	Nusselt number,$(h_cd_h)/k_T$, $(h_ch)/k_T$, and $(h_ch)/(k_T)_f$
p_y	yield stress (Pa)
p	pressure (Pa)
p_0	gauge pressure (Pa)
(-dp/dx)	pressure gradient ($Pa\text{-}m^{-1}$)
dp_0/dx	complex amplitude of hydrostatic pressure gradient ($Pa\ m^{-1}$)
Pe_D	diffusive Pèclet number, $u_{HS}h/D$, and $u_{ref}h/D$
Pe_ω	Redefined Pèclet number, $(Re_\omega Sc\Delta z)/Im\ (2i\langle U_0\rangle)$
q(t)	volume flow rate per unit width as a function of time
$q_0(t)$	complex amplitude of volume flow rate per unit width as a function of time
Q	dimensionless volumetric flow rate
Q_{in}	input volumetric flow rate without considering streaming potential ($m^3\ s^{-1}$)
$\mathbb{R}$	real part of the complex number
R	universal gas constant ($J\ mol^{-1}K^{-1}$)
Re_ω	angular Reynolds number, $(\rho h^2\omega)/\mu$, and $(\rho_f h^2\omega)/\mu_f$
Sc	Schmidt number, υ/D

S_C	dimensionless entropy generation due to combined interaction of electromagnetic diffusion
S_G	dimensionless form of entropy generation rate
$(s_g)_{total}$	total volumetric entropy generation rate per unit half-height of the channel ($Wm^{-4}K^{-1}$)
	dimensionless total entropy generation rate, $(s_g)_{total}h^2/(k_T)_f$
$S_{G,C}$	entropy generation due to combined interaction of electromagnetic diffusion ($W\,m^{-4}K^{-1}$)
$S_{G,H}$	entropy generation due to thermal diffusion ($W\,m^{-4}K^{-1}$)
$S_{G,J}$	entropy generation due to Joule heating ($W\,m^{-4}K^{-1}$)
$S_{G,M}$	entropy generation due to Joule heating ($W\,m^{-4}K^{-1}$)
$S_{G,V}$	entropy generation due to viscous friction of the fluid ($W\,m^{-4}K^{-1}$)
S_H	dimensionless entropy generation due to thermal diffusion
S_J	dimensionless entropy generation due to Joule heating
S_M	dimensionless entropy generation due to magnetic field
S_V	dimensionless entropy generation due to viscous friction of the fluid
u	flow velocity along the y direction (ms^{-1})
U	dimensionless flow of velocity, u/u_{HS}, and u/u_{ref}
U	flow velocity vector ($m\,s^{-1}$)
u_{av}	average velocity ($m\,s^{-1}$)
u_c	creeping flow velocity ($m\,s^{-1}$)
u_{ref}, u_{HS}	reference flow velocity ($m\,s^{-1}$)
U_{av}	non-dimensional average velocity, u_{av}/u_{HS}, and u_{av}/u_{ref}
v	particle velocity vector.
V_0	thermal voltage (V)
V_E	applied voltage (V)
x	coordinate along the flow direction (m)
y	transverse coordinate (m)
Y	dimensionless transverse coordinate, y/h
z	lateral coordinate (m)
Δz	tidal displacement (m)
ΔZ	dimensionless tidal displacement, Δz/h
z_v	valency of ions

Greek Symbols

α	ionic Péclet number
α_e	Hall parameter
α_s	ion slip parameter
β	dimensionless Casson parameter
γ	dimensionless couple stress parameter
γ_r	specific heat capacity ratio

λ_r	ratio of the retardation timescale to the relaxation timescale, λ_2/λ_1
θ	normalised temperature of fluid, k_T $(T-T_w)/(q_w h)$, $(k_T)_f$ $(T_w-T)/(q_w h)$, $(k_T)_f$ $(T-T_w)/(q_w h)$, and $(T-T_w)/(T_i-T_w)$
θ_0	non-dimensional complex amplitude of temperature, $(T_0-T_w)/(T_i-T_w)$
θ_m	dimensionless bulk mean fluid temperature
$\bar{\xi}_{a1}$	upper wall dimensionless zeta potential, $(ez_v\xi_1)/(k_B T_a)$
$\bar{\xi}_{a2}$	lower wall dimensionless zeta potential, $(ez_v\xi_2)/(k_B T_a)$
λ_1	relaxation time (s)
$\bar{\lambda}_1$	normalised relaxation time, $(\lambda_1\mu/\rho h^2)$, and $(\lambda_1\mu_f/\rho_f h^2)$
λ_2	retardation time (s)
λ_D	Debye length (m^{-1})
λ_m	mean free path (m)
λ_r	ratio of the retardation time to relaxation time, (λ_2/λ_1)
μ	dynamic viscosity of viscoplastic fluid (kg m^{-1} s^{-1})
μ_m	electrophoretic mobility
μ_f	base fluid viscosity (kg m^{-1} s^{-1})
μ_s	magnetic nanoparticle viscosity (kg m^{-1} s^{-1})
$\boldsymbol{\Omega}$	normalised external electric field, $E_z/(u_{ref}B_y)$, and $E_{ref}/(u_{ref}B_y)$
ρ	density of liquid (kg m^{-3})
ρ_f	base fluid density (kg m^{-3})
ρ_s	magnetic nanoparticle density (kg m^{-3})
ρ_{eff}	nanofluid effective fluid density
ρ_r	ratio of the nanofluid effective permittivity to the base fluid permittivity, ρ_{eff}/ρ_f
ρ_e	net charge density per unit volume in the diffuse layer (C m^{-3})
$\boldsymbol{\sigma}$	shear stress tensor (N m^{-2})
σ_{yx}	shear stress (N m^{-2})
σ_{yx}^0	complex amplitude of shear stress (N m^{-2})
σ_B	bulk ionic conductivity (nS cm^{-1})
σ_e	electrical conductivity of the electrolyte solution (S m^{-1})
σ_{eff}	nanofluid effective electrical conductivity (sm^{-1})
σ_f	base fluid electrical conductivity (sm^{-1})
σ_r	ratio of the nanofluid effective electrical conductivity to the base fluid electrical conductivity, σ_{eff}/σ_f
σ_s	magnetic nanoparticle electrical conductivity (sm^{-1})
σ_{surf}	surface charge density (mC m^{-2})
σ_T	thermal accommodation coefficient
σ_v	tangential momentum accommodation coefficient
$\boldsymbol{\sigma_1}$	elastic stress tensor (Nm^{-2})
η_c	electrokinetic energy conversion efficiency

η_h	electroviscous heat transfer rate
ϕ	volume fraction of nanoparticles
Θ	ratio of constant wall temperature to heat flux, $(k_T T_w)/(q_w h)$, and $(k_T)_f T_w/(q_w h)$
$\psi_{nanowall}$	surface charge density nanochannel array (Cm^{-2})
Λ	aspect ratio, h/L

Subscripts

a	absolute
av	average
eff	effective
m	mean
ref	reference
x	longitudinal coordinate
xy	plane
y	transverse coordinate
yx	plane
z	lateral coordinate

Organization of the thesis

The structure of this thesis has been organized as follows to ensure a coherent and systematic presentation of the research work.

Chapter 1: Introduction

Introduces electrokinetic forces (e.g., electric double layer interactions, Lorentz forces) and their role in microscale transport phenomena. Discusses the physics of Lab-on-a-Chip (LOC) systems, focusing on energy conversion, heat dissipation, and fluid-structure interactions in micro-confined geometries. Challenges in balancing viscous dissipation, thermal radiation, Joule heating, and entropy generation are framed through thermodynamic and hydrodynamic principles.

Chapter 2: Literature review

A meticulous review of existing literature is presented to elucidate the current advancements and unresolved challenges in the domain of electrohydrodynamic and electroosmotic and streaming potential flows. Special focus is given to hybrid fluid models involving Newtonian and non-Newtonian behaviors. Through critical comparison of methodologies, this chapter identifies key research gaps, especially in enhancing thermal transport and minimizing entropy generation, thereby laying the groundwork for the subsequent chapters.

Chapter 3: Thermal transport in EMHD-driven Newtonian electroosmotic flow: second-order slip/jump effects

This chapter formulates an analytical model of Newtonian fluid flow under the influence of coupled electric and magnetic fields, with special consideration of second-order velocity slip and temperature jump conditions. The intricate interplay of Lorentz forces and wall effects on heat transfer enhancement is explored, offering valuable insights into the role of higher-order boundary phenomena in microfluidic thermal transport.

Chapter 4: Time-periodic electroosmotic flow and mass transfer analysis for Oldroyd-B fluids

The viscoelastic behavior of biofluids such as blood and saliva is examined in this chapter through the lens of time-periodic electroosmotic flow. The influence of slip boundary conditions on mass transport and bio-molecule separation is highlighted. This analysis contributes to a better understanding of microfluidic separation techniques in biomedical applications

Chapter 5: Entropy generation in EMHD driven streaming potential flow: couple stress Casson fluid dynamic analysis

A hybrid rheological model combining Couple-Stress (micropolar) and Casson (yield-stress) fluids is developed to analyse entropy generation in streaming potential

flows. The work dissects competing irreversibility sources, viscous dissipation, Joule heating, and thermal conduction under EMHD forcing. Results demonstrate that fluid microstructure (e.g., particle rotation in Couple-Stress fluids) and yield-stress behavior dramatically alter entropy hotspots, guiding the design of energy-efficient viscoplastic microsystems

Chapter 6: Dynamic Maxwell streaming potential irreversibility flow

A transient viscoelastic model is developed in this chapter to study the evolution of electrokinetic parameters such as velocity, streaming potential, and temperature distribution over time. The influence of relaxation time on energy conversion efficiency and thermal entropy generation is investigated in depth, providing a dynamic perspective on Maxwell fluid behavior under varying field conditions.

Chapter 7: Heat, mass, and entropy analyses in periodic electroviscous Oldroyd-B fluids

Employing the Oldroyd-B fluid model, this chapter solves the governing equations for momentum, energy, and mass transport in a time-periodic electroviscous environment. Parameters such as electrokinetic energy conversion efficiency, concentration distribution, Nusselt number, and entropy generation are evaluated, highlighting the coupled effects of flow physics and molecular diffusion in confined geometries.

Chapter 8: Ion transport phenomena in electrokinetic desalination systems with ion concentration polarization in nanochannel arrays

This chapter investigates electrokinetic desalination through nanochannel arrays embedded with ion-selective membranes. The impact of electric fields applied with gravitational forces is studied to understand salt removal efficiency. The findings contribute to the advancement of energy-efficient, miniaturized desalination systems.

Chapter 9: Integrated multi-objective optimization, MCDM, and ML analysis of couple-Stress Casson, Maxwell, and Oldroyd-B Fluids

Based on the mathematical analyses from preceding chapters, this chapter integrates multi-objective optimization, multi-criteria decision making (MCDM), and machine learning (ML) approaches to evaluate the performance of couple stress Casson, Maxwell, and Oldroyd-B fluids. The Machine learning predict emergent behaviors in untrained parameter regimes, bridging microscale physics with artificial intelligence-driven design.

Chapter 10: Conclusions and direction for future studies

The study concludes by synthesizing key insights: electrokinetic-thermal coupling dictates microscale energy efficiency, viscoelastic memory enables tunable transport, and hybrid fluid models unlock multifunctional microdevices. Future directions propose exploring quantum-electrokinetic phenomena and AI-optimized fluid-structure interactions for next-generation LOC systems.

Chapter 1. Introduction

Significant progress in fluid and ion transport through miniature systems has made microfluidics an appealing field for researchers. Investigating the physics of confined liquid flow at small scales unveils the complexities of both natural and artificial processes, leading to diverse technological applications that operate on distinct scales from conventional systems. The unique properties and behaviors of microfluidic systems continue to drive extensive study and innovation. Among these advancements, microchannels play a pivotal role, offering advantages such as rapid analysis [1], compact designs [2], and cost-effective manufacturing [3]. Microfluidic systems epitomize the consolidation of chemical analysis and processing onto a miniaturized platform, drastically minimizing the temporal and spatial demands of diagnostic procedures [4]. Additionally, microchannels facilitate efficient heat transport and fluid motion. Their dimensions vary based on the fluid type: hydraulic diameters for liquids typically range from 200 µm to 1000 µm, while for gases, they are much smaller, between 10 µm and 200 µm. The concept, first introduced by Tuckerman and Pease in 1981, marked a shift from conventional gas flow channels, often exceeding 3 mm in size.

Microchannels have diverse applications across multiple fields, including biological cell analysis [5], energy harvesting [6], micro-electromechanical systems (MEMS) [7], liquids containing long-chain molecules as polymeric suspensions [8], mass flow controller [9], reduction of mixing time for sampling [10], lowering of bleeding during surgeries [11], cell separation with development of magnetic devices [12] and feeding vessels for cancer tumors [13], and many more. These wide-ranging uses highlight their versatility and impact on scientific and medical advancements, shaping the future of technology and healthcare.

Electrokinetic phenomena play a crucial role in facilitating liquid flow through microchannels, particularly in biofluid applications. Hence, the attention of the researchers turns towards non-Newtonian fluids to describe the non-linear relationship between shear stress and shear rate. A diverse array of biological and chemical systems – including blood plasma, including blood plasma [14], colloid suspensions [15], macromolecular solutions (e.g., protein [16], and DNA solutions [17], bodily secretions like saliva [18], and synovial fluid [19], exhibit non-Newtonian flow characteristics. These systems require sophisticated rheological models to accurately describe their flow dynamics. Most display non-Newtonian behavior, meaning their flow characteristics change under viscoelastic and viscoplastic stresses. To describe these dynamics, viscoelastic and viscoplastic models are employed, aiding in the study of biofluids in microscale environments. These insights drive progress in medical diagnostics, drug delivery, and biological analysis.

Amidst global challenges of energy scarcity and environmental deterioration linked to fossil fuel dependence, efforts to develop environmentally friendly, sustainable, and renewable energy solutions have gained significant momentum. By developing various portable devices for the harvested energy from different resources

in domestic contexts, the dependency of contemporary society on centralized power sources reduces. Sustainable energy systems like wind turbines, photovoltaic arrays, and geothermal installations can drastically lower carbon footprints, yet their effectiveness is frequently hindered by regional and climatic factors. A significant share of hydropower generation relies on turbine systems employing electromechanical conversion processes, where rotational energy drives electrical output. In contrast, a prominent renewable method harnesses hydrokinetic energy harvesting, which leverages water's inherent motion. However, the spatial and infrastructural demands of large-scale dam infrastructure limit their viability for decentralized energy solutions. An innovative alternative exploits electrohydrodynamic principles, such as streaming potential effects, to directly transform fluid motion into electrical energy without mechanical intermediaries [20]. Streaming current facilitates the direct conversion of pressure-driven hydraulic energy into electrical energy within fluidic systems. Determining streaming potential hinges on maintaining charge balance principles (electroneutrality). Advances in electrokinetic methods have spurred significant interest in harnessing energy through these mechanisms. Such systems leverage solid-liquid interfacial streaming potential to advance microfluidic Lab-on-a-chip technologies, incorporating miniature energy harvesters whose performance is quantified by the electrokinetic energy conversion (EKEC) efficiency metric. It may open the exploration of new renewable energy [21] and can significantly impact studies of harvesting electrical power, the desalination process, and self-power sensors. Microfluidic energy harvesting involves integrating electrokinetic energy systems into microfluidic devices, enabling the electricity generation by moving small liquid volumes. This electricity can then be utilized to power micro-electromechanical systems (MEMS) or micro-sensors [22]. Electrokinetic energy systems can aid in desalination processes by implementing the ion selective membrane [23]. Electrokinetic energy systems can power sensors and monitoring devices in remote locations or areas with limited access to traditional power sources [24]. These self-powered sensors, such as water quality or groundwater level measurements, can be used for environmental monitoring.

Fluid maldistribution in microchannels reduces the efficiency of heat exchangers and leads to uneven thermal performance [25], highlighting the need for innovative solutions to enhance thermal transfer. In microscale magnetohydrodynamic (MHD) flows, effective thermal regulation is crucial for applications such as cooling/heating systems and chemical processing. The incorporation of nanoparticles and porous media has been shown to enhance thermal conductivity and increase surface area for effective heat dissipation [26], addressing some of these challenges. Efficient energy utilization is essential in the face of global energy challenges and environmental concerns [27], with heat transfer playing a pivotal role in energy conservation [28]. This is particularly important in microchannel systems, where excess heat can cause reliability issues [29] and increase operational costs [30,31]. However, high entropy generation often hinders efficient energy conversion [32]. To address this, a multi-objective Pareto front approach can be employed to balance the maximum heat transfer rate with minimum entropy generation, leading to more efficient and sustainable system designs [33].

1.1. Fundamentals of electrical double layers (EDL)

Electrokinetic effects arise from the interaction between fluid movement and electrical currents within porous materials composed of minerals such as silicates, oxides, and carbonates, as shown in Fig. 1.1. These phenomena arise due to the development of an electrical double layer (EDL) at the solid-liquid boundary, where charged interactions occur between solid substrates and ionic fluid media [34]. When materials come into contact with aqueous environments, surface charges naturally develop. While many electrokinetic studies acknowledge these charges without extensively analyzing their origins, their formation remains a crucial aspect to consider. Surface charging occurs through various mechanisms, including surface group ionization, ion adsorption from the surrounding solution, and structural irregularities within the mineral lattice.

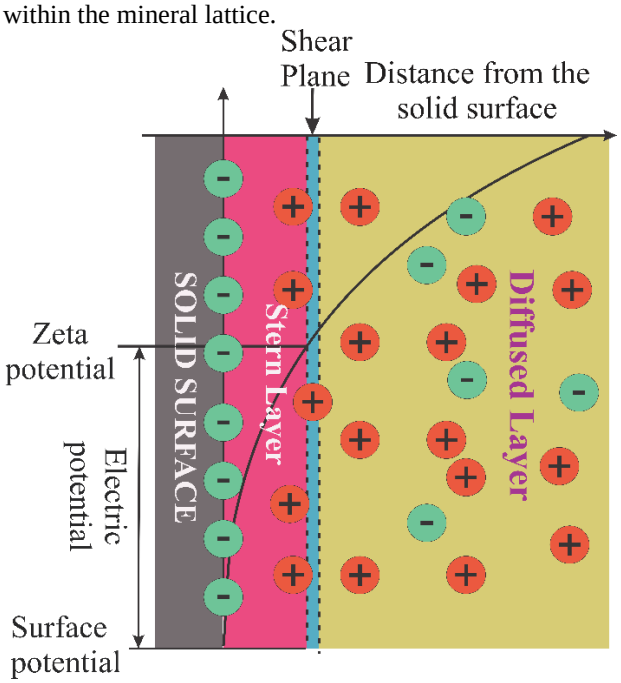

Fig. 1.1 Electrical double layer effect

To better understand the origin of surface charge, the physical chemistry occurring at a silica surface in the presence of aqueous fluids is examined. Silica is considered due to its abundance in the Earth's crust, making it a primary component of rocks [35]. Chemical reactions at silica surfaces in contact with aqueous solutions. Two types of neutral surface groups on silica have been identified: doubly coordinated siloxal $>Si_2O^0$ and singly coordinated silanol $>SiOH^0$, where > represents the mineral lattice, and the superscript "0" indicates a neutral charge [36]. The siloxal group $>Si_2O^0$ remains chemically unreactive, whereas silanol groups $>SiOH^0$ readily

undergo surface reactions, leading to charge formation. Under highly acidic conditions, where pH falls below the point of zero charge ($\left(pH < pH_{pzc} = 2-3\right)$, protonation leads to the formation of positively charged sites $\left(> SiOH_2^+\right)$. In contrast, at pH levels exceeding the pH_{pzc}, the removal of protons (deprotonation) creates anionic surface sites $\left(> SiO^-\right)$.The pH_{pzc} represents the specific pH at which the concentrations of $> SiOH_2^+$ and $> SiO^-$ are equal, ensuring an electrically neutral surface.

For simplification, silica grains interacting with a 1:1 electrolyte solution, such as sodium chloride (NaCl), within a pH range of 6 to 8 are considered. At this interface, the behavior of silanol groups significantly influences charge development. The deprotonation of silanol groups follows the reaction:

$$> SiOH^0 \rightleftharpoons > SiO^- + H^+ \tag{1.1}$$

The adsorption of cations onto silica surfaces is expressed as:

$$> SiOH^0 + Mo^+ \rightleftharpoons > SiOMo^0 + H^+ \tag{1.2}$$

where Mo^+ represents monovalent cations such as Na^+ or K^+. It is important to note that for pH values above 6, the positively charged $> SiOH_2^+$ species do not form at the silica-electrolyte interface. Instead, three surface species remain: the negatively charged $> SiO^-$, along with two neutral groups, $> SiOH^0$ and $SiOMo^0$. Similar reactions occur in systems involving other electrolyte solutions.

The equilibrium state of these reactions can be analyzed using the law of mass action, with equilibrium constants given by:

$$K_- = \frac{\varpi^0_{SiO^-}\alpha^0_{H^+}}{\varpi^0_{SiOH}} \tag{1.3}$$

$$K_{Mo} = \frac{\varpi^0_{SiOMo^-}\alpha^0_{H^+}}{\varpi^0_{SiOH}\alpha^0_{Mo^+}} \tag{1.4}$$

where K_- represents the dissociation constant of silanol groups, K_{Mo} denotes the adsorption constant for cations, ϖ_0 is the surface site density, expressed in sites per square meter, and ϖ_i^0 refers to the density of surface sites for species i, measured in $\left(sites/m^2\right)$, and α_i^0 refers to the activity of ionic species in close proximity to the mineral interface.

The total surface site density $\left(\varpi_s^0\right)$ remains constant and is described by the equation:

$$\varpi_s^0 = \varpi^0_{SiOH} + \varpi^0_{SiO^-} + \varpi^0_{SiOMo} \tag{1.5}$$

Eq. (1.5) acts as a conservation equation for mineral surface groups. By solving Eqs. (1.3) -(1.5), the density of sites $\varpi^{0}_{SiO^{-}}$ and can be determined. The total electric charge distributed over a given surface area, commonly represented as σ (sigma), is termed the surface charge density at a material interface in $\left(C/m^{2}\right)$ is determined by the concentration of charged surface groups and follows the equation:

$$\sigma = -e\varpi^{0}_{SiO^{-}} \tag{1.6}$$

where e represents the elementary charge of an electron.

The earliest experimental evidence of electroosmotic motion was reported by Reuss [37], who observed fluid transport in a water–clay system subjected to an electric field. This observation later motivated Helmholtz [38] to conceptualize the existence of an interfacial electrical structure arising at the boundary between a charged solid surface and an electrolyte. His formulation explained how such interfacial charge arrangements could generate fluid motion within narrow capillaries under an applied electric potential. Building upon this framework, Smoluchowski [39] refined the theory by establishing a quantitative relationship for electroosmotic velocity.

Subsequently, Gouy [40] and Chapman [41] proposed that the interfacial charge distribution is not confined to a rigid layer but instead extends into the fluid domain. Their model described a diffuse cloud of ions whose spatial distribution follows Boltzmann statistics, gradually decaying with distance from the solid boundary. To reconcile the rigid interfacial structure proposed by Helmholtz with the diffuse nature described by Gouy and Chapman, Stern [42] introduced a unified model that incorporates both regions at the solid-liquid interface. In aqueous environments, many solid surfaces acquire electrical charge due to surface reactions such as ion adsorption, dissociation, or chemical association. Materials such as clays, quartz, ceramics, sand, and surfaces exposed to specific pH conditions commonly exhibit negative surface charges. As a consequence, these charged interfaces attract oppositely charged ions from the surrounding electrolyte while repelling ions of like charge. This electrostatic sorting results in the formation of a structured interfacial region characterized by spatial charge separation adjacent to the solid surface.

The resulting electrical double layer (EDL) is a fundamental feature governing interfacial transport phenomena and plays a crucial role across a wide range of scientific and technological fields, including colloidal stability, polymer processing, biological systems, medical diagnostics, and separation technologies such as membrane filtration, wastewater treatment, and biomolecular separation [43,44]. Structurally, the EDL consists of two distinct regions: a compact, immobile Stern (or Helmholtz) layer where counter-ions are strongly bound to the surface, and an adjacent diffuse layer in which ions remain mobile and distributed within the fluid. The boundary separating these regions is commonly referred to as the shear plane.

When an external electric field is applied parallel to the surface, the ions within the diffuse layer experience an electrostatic force and begin to migrate, dragging the surrounding fluid with them. This ion-driven motion gives rise to electroosmotic flow, as schematically illustrated in Fig. 1.3. These surface phenomena are crucial in shaping electrokinetic characteristics by affecting fluid motion, ionic migration, and

charge behavior at the interface. The arrangement of ions and electrostatic potential within the diffuse region are modeled by the Poisson-Boltzmann (PB) equation [45], which equilibrates Coulombic interactions and thermal motion influences. In a unidirectional configuration normal to a planar boundary, the linearized PB equation's solution yields a potential gradient diminishing nearly exponentially with separation from the interface, as visualized in Fig. 1.3. Within the bulk fluid, cation and anion concentrations equilibrate, maintaining charge neutrality. The shear boundary, marking the onset of hydrodynamic motion near the solid surface, defines the slip interface where the zeta potential (ξ) critical to electrokinetic phenomena is measured. Reservoir substrates typically exhibit anionic surface charge and resultant negative (ξ) potentials in aqueous environments. The Debye screening length (λ_D), representing the exponential decay range of the electrical double layer (EDL) potential, is determined exclusively by liquid-phase properties (ionic strength, temperature) and independent of surface charge/potential. It is given by [46]:

$$\lambda_D = \sqrt{\left(\varepsilon k_B T_a\right) \Big/ \left(2 n_0 e^2 z_v^{\,2}\right)} \tag{1.7}$$

where ε is the permittivity, ρ_e is the charge density, e denotes electronic ionic charge density, and z_v is symmetric electrolyte with an equal distribution of charge valence. The symbol n_0 represents the equilibrium ion concentration in the bulk solution, k_B denotes the Boltzmann constant, and, and T_a indicates the absolute temperature measured on the Kelvin scale. For monovalent electrolytes like NaCl or KCl, with concentrations ranging from 1 mM to 0.1 M (typical for aqueous solutions in rocks or soils), the Debye length varies between 10 nm and 1 nm at 25°C [47]. This length scale is generally much smaller than the pore sizes found in most rocks and soils. As a result, the solid-liquid interface within pores can often be treated as a planar, semi-infinite surface for practical purposes.

1.2. Theory of electrokinetic phenomena in microfluidics

Electrokinetic phenomena encompass interconnected mechanisms originating from the interplay of externally imposed electric fields or pressure differentials with the charge-segregated interfacial layer at the boundary of a solid material and an ionic solution. This group of mechanisms encompasses electroosmosis, particle migration, flow-induced potential, and settling-induced potential. Particle migration and electroosmosis are activated by external electrical fields, resulting in charged particle displacement or collective fluid movement, respectively [48]. In contrast, streaming potential and sedimentation potential are driven by an applied pressure gradient, which induces fluid or particle motion and generates an electric field as a result. Based on the driving force, electrokinetic
phenomena are broadly classified into two categories: **(i) electrically actuated processes** (e.g., electrophoresis and electroosmotic flow) and **(ii) mechanically driven phenomena** (e.g., streaming potential and sedimentation potential). These phenomena are fundamental to understanding the behavior of charged systems and are widely applied in fields such as microfluidics, colloidal science, and membrane technology.

1.2.1. Electroosmosis

Within the charge-segregated interfacial zone, an externally applied electrical potential parallel to the boundary induces Coulombic forces on mobile ions of opposite charge within the interfacial region, prompting their directional migration. Conversely, ions sharing the surface's charge polarity are repulsed by the interfacial charge, remaining largely within the bulk liquid phase. Although these co-ions are more abundant in the bulk, their uniform spatial arrangement minimizes their hydrodynamic influence. The migration of counter-ions under the electric field's influence transfers momentum to proximate fluid molecules via viscous coupling, culminating in bulk fluid motion termed electroosmotic transport. This flow, arising from a resultant pressure differential and ion-to-fluid momentum transfer, enables precise manipulation of fluid dynamics without moving parts [49,50]. This capability has made EOF a cornerstone where precision and miniaturization are paramount.

1.2.2. Electrophoresis

In electrically driven fluid transport, electrophoresis refers to the motion of charged particles suspended in a liquid under the influence of an applied electric field. When a potential difference is applied, electrically active particles such as ions, colloids, or macromolecules experience an electrical force, expressed in vector form as $\mathbf{F}_e = q_p\mathbf{E}$, where q_p is the total charge of the particle and $\mathbf{E}$ is the applied electric field. This force drives cations toward the cathode and anions toward the anode. As particles move through the fluid, they encounter viscous resistance from the medium, resulting in a drag force given by $\mathbf{F}_d = -f_d\mathbf{v}$, where f_d is the drag coefficient and $\mathbf{v}$ is the particle velocity vector. At steady state, the electrical and viscous forces balance, allowing the particle to reach a terminal velocity known as the electrophoretic velocity, $\mathbf{v} = \mu_m\mathbf{E}$, where μ_m is the electrophoretic mobility. The value of μ_m depends on particle properties such as size, shape, and surface charge, as well as fluid characteristics including viscosity μ, dielectric permittivity, and ionic strength. In microfluidic or capillary systems, electrophoresis often acts together with electroosmotic flow to enable precise control and enhanced separation of charged species. This combined mechanism is widely employed in applications such as DNA sequencing, protein analysis, and lab-on-a-chip devices, where accurate manipulation of particle motion is essential [51].

1.2.3. Streaming potential

In microscale fluidic devices, spontaneous and effective fluid propulsion methods are advantageous for studying hydrodynamic behavior. A key mechanism in such systems is the generation of an electrical potential gradient due to pressure-driven flow, observed when an ionic solution is forced through a microscale conduit under a hydraulic pressure differential. As the fluid moves, the charged walls of the channel perturb the ion distribution within the interfacial charge layer, leading to an accumulation of oppositely charged ions in the mobile region adjacent to the surface.

This imbalance drives the convective transport of these ions along the flow direction, establishing an axial electrical potential. This induced potential, termed the streaming potential, produces a counter-current (streaming current) opposing the pressure-driven flow [52]. The streaming potential initiates two counteracting ionic fluxes: one from free ions in the bulk liquid and another from immobilized charges in the rigid interfacial layer. Both fluxes resist the primary flow direction. Collectively, these interactions diminish the net flow velocity, as the induced potential generates an electrokinetic retarding force. This opposition stems from electrohydrodynamic coupling, where electrical interactions within the interfacial charge layer amplify the fluid's viscous resistance [53].

1.2.4. Sedimentation potential

Sedimentation potential emerges when electrically charged particles suspended in a liquid move relative to the surrounding fluid under the action of body forces, such as gravity or centrifugal acceleration. This relative motion causes a spatial separation of charge between the particles and the fluid, which in turn gives rise to an induced electric field, denoted as E_{sed}. At the level of individual particles, the process is controlled by the total charge carried by each particle, q_p, which is related to the ionic valence through the relation $q_p = ez_v$. Here, z_v denotes the ionic valence (number of elementary charges associated with the particle), and e represents the elementary charge. This form of the charge appears explicitly in particle-scale force balances that account for gravitational, viscous, and electrical forces. In contrast, continuum descriptions of ionic transport, including the Boltzmann distribution and the Nernst-Planck framework, are more naturally expressed in terms of the valence-based quantity ez_v. When the problem is viewed from a macroscopic electrokinetic perspective, the influence of particle charge is conveniently represented by the zeta potential ξ, which characterizes the electrical double layer at the particle-fluid interface. Using this description, the sedimentation-induced electric field follows the scaling $E_{\mathrm{sed}} \propto (\xi\varepsilon\Delta\rho g c)/\mu$, where εdenotes the fluid permittivity, μ is the dynamic viscosity, $c$represents the particle concentration, $\Delta\rho$ is the density difference between the particles and the carrier fluid, and g is the gravitational acceleration [54]. While the electric field can formally be written as the gradient of the sedimentation potential, $E_{\mathrm{sed}} = -\partial\psi_{\mathrm{sed}}/\partial y$, this compact form alone does not reveal how material properties and particle characteristics govern the magnitude of the field. It is also important to distinguish sedimentation potential from streaming potential, which arises from fluid flow past fixed charged surfaces rather than from particle motion. In typical microfluidic configurations, sedimentation-induced effects are often weak because gravitational settling is minimal at low Reynolds numbers ($Re \ll 1$); nevertheless, in systems involving vertical channel orientations, centrifugal actuation, or density-based particle manipulation, sedimentation potential can play a measurable role in electrokinetic response and particle transport [55].

1.3. Theory of electro-hydrodynamic (EHD) flow

Electro-Hydrodynamic (EHD) interactions significantly affect electroosmotic flow (EOF) and streaming potential flow, improving fluid transport, energy conversion, and electrokinetic stability. These effects manifest in various ways, enhancing the functionality of microfluidic and nanofluidic systems. Unlike traditional electrokinetic flow mechanisms, which rely solely on the EDL or pressure-driven ion movement, EHD effects introduce bulk fluid motion, enhancing both flow control and efficiency.

1.3.1. EHD effects in electroosmotic flow

Electroosmotic flow (EOF) in Newtonian fluids typically exhibits a uniform plug-like velocity profile while in non-Newtonian fluids the flow behavior varies depending on the shear rate. Electrohydrodynamic (EHD)-driven EOF offers enhanced control by modulating shear-dependent viscosity through adjustments in electric field gradients leading to more predictable and controllable fluid motion. EHD enhances fluid mixing by using transverse electric fields to generate secondary vortices. These vortices disrupt laminar flow patterns, resulting in improved homogenization [56]. Charge injection mechanisms further influence flow dynamics by creating localized conductivity variations promoting recirculation and reducing dispersion in microchannels, an effect particularly advantageous in biochemical assays where uniform mixing ensures accurate reaction kinetics [57,58]. In biofluid transport such as in microfluidic devices EHD-driven EOF effectively manages viscoelastic properties facilitating precise sample movement. Moreover, this approach enables voltage-controlled fluid transport no dependence on mechanical pumps [59]. The dynamic modulation of surface charge density also enhances fluid handling in miniaturized diagnostic platforms which is crucial for point-of-care devices where controlled sample transport ensures reliable detection and analysis.

1.3.2. EHD effects in streaming potential flow

Electrohydrodynamic (EHD) phenomena inherently arise in streaming potential flow due to the coupling between pressure-driven fluid motion and self-generated electric fields. However, these effects are weak in highly resistive or dielectric fluids, where conventional streaming potential mechanisms underperform. By applying an external transverse electric field, EHD effects are amplified: enhanced ion drift and Coulomb force optimize charge separation, suppress viscous dissipation, and stabilize ion transport to overcoming limitations of streaming potential flow, such as low energy conversion efficiency and non-uniform conductivity [60]. This synergy enables precise control over fluid dynamics, minimizes energy losses, and mitigates electrokinetic instabilities caused by concentration gradients. As a result, EHD-enhanced systems achieve superior performance in applications such as biosensors devices, and self-powered microsystems (e.g., wearable sensors), where reliability, efficiency, and precision are critical [61].

1.4. Theory of electro-magneto-hydrodynamic (EMHD) flow

Electro-Magnetohydrodynamics (EMHD) integrates the interaction of electric and magnetic fields, where fluid motion is governed by the combined electromagnetic force per unit volume, expressed as, $\mathbf{F} = \rho_e \mathbf{E} + \mathbf{J} \times \mathbf{B}$. Here, $\mathbf{F}$ represents the electromagnetic body force per unit volume, ρ_e denotes the net charge density, $\mathbf{E}$ is the electric field vector, $\mathbf{J}$ is the current density vector, and $\mathbf{B}$ is the magnetic field, which typically acts perpendicular to the flow direction [62]. Unlike EHD, which relies solely on Coulombic forces, EMHD introduces magnetic field-driven directional control over ionized fluids. This stabilizes flows in high-resistance media (e.g., non-polar solvents) and viscoelastic fluids (e.g., polymer melts) by suppressing charge aggregation and turbulence. A key benefit of EMHD in microscale systems is its capacity for non-contact fluid control through external magnetic fields [63]. In biochemical applications, this principle allows selective biomolecule isolation, where localized magnetic fields assist in targeted separation and retrieval. Magnetic forces play a crucial role in controlling magnetically responsive components, such as functionalized particles, tagged cellular structures, and ferrofluidic segments, within microchannels, providing precise control over fluidic processes.

1.4.1. EMHD effects in electroosmotic flow

In EOF, magnetic fields counteract charge screening effects in the EDL by aligning ion trajectories via the Lorentz force, stabilizing flow against instabilities (e.g., electroconvection). This is critical for transporting viscoelastic biofluids (e.g., mucus, plasma), where shear-thinning and elastic recoil disrupt conventional EOF [64]. Magnetically induced MHD vortices further enhance mixing by generating chaotic advection, breaking diffusion-limited barriers in microreactors. Adjusting the magnetic field's orientation and strength tailors mixing intensity without increasing Joule heating, a key advantage for temperature-sensitive assays [65].

1.4.2. EMHD effects in streaming potential flow

Coulombic and magnetic interactions significantly amplify charge segregation, enhancing the efficacy of energy extraction from electrokinetic processes. Within electro-magnetohydrodynamic systems, the minimization of ionic losses and charge neutralization renders these systems optimally adapted for microscale energy harvesting platforms. The influence of the magnetic field optimizes ion drift, reducing resistance and enhancing charge mobility, which further contributes to efficient energy conversion. Additionally, the presence of the Lorentz force in EMHD lowers the required electric field strength, leading to reduced energy consumption and minimizing unwanted thermal effects an essential advantage for delicate biological and chemical processes. The EMHD stabilize ion distribution, improving the precision of electrochemical sensors. Furthermore, EMHD effectively suppresses unwanted charge accumulation, thereby enhancing measurement accuracy in lab-on-a-chip platforms [66,67].

1.5. Thermophysical phenomena and heat transfer

Resistive heating, frictional energy losses, and radiative heat emission synergistically govern thermal transport dynamics and thermodynamic irreversibility in thermal energy systems. Resistive heating and frictional energy losses function as intrinsic thermal sources, whereas radiative heat transfer mediates energy redistribution through electromagnetic wave propagation. Their interaction shapes temperature gradients, increases thermodynamic irreversibility, and impacts system efficiency critical for optimizing processes in microfluidics, aerospace, and power generation.

1.5.1. Primary effects of Joule heating

Resistive heating, termed ohmic heating, arises from the flow of electrical current through a resistive material, producing thermal energy due to the medium's opposition to charge movement [68]. In microscale electrohydrodynamic systems, this phenomenon introduces critical thermal and hydrodynamic considerations, especially under the influence of interfacial charge layers and externally applied electrical potentials [69]. The primary effect of Joule heating is the generation of heat in the fluid due to electrical resistance. The rate of heat generation is governed by Joule's law and is given by $j = \sigma_e \mathbf{E^2}$, where σ_e is the fluid's electrical conductivity and $\mathbf{E}$ is the electric field vector. [70]. This localized heating induces a temperature rise within the fluid, establishing non-uniform temperature distributions characterized by axial
(streamwise) and radial (transverse) gradients [71]. The resulting thermal gradients directly modify fluid properties: viscosity decreases with temperature, reducing flow resistance; electrical conductivity increases, altering ion migration rates; and density variations may induce buoyancy-driven convection. These property changes perturb electrokinetic behaviours such as electroosmotic flow velocity profiles, streaming potentials, and ion mobility [72]. For instance, temperature-dependent conductivity amplifies current density in warmer regions, creating feedback loops that exacerbate inhomogeneous heating. In microscale systems, where surface-to-volume ratios are high, radial temperature gradients become significant, leading to asymmetric flow patterns and reduced separation efficiency in electrophoretic applications. Furthermore, excessive Joule heating can degrade thermally sensitive biomolecules or compromise the structural integrity of polymer based microchannels [73], underscoring the need for thermal management strategies in electrokinetic device design [74]. To construct Fig. 1.2, data have been taken from the published papers [75,76] The electric current passes through the buffer solution in the capillary, which strongly influences the Joule current resistance. The findings demonstrate that resistive heating amplifies current flow by 66.5% compared to scenarios without thermal effects. This increase occurs because resistive heating elevates the buffer layer's temperature during current conduction, correlating quadratically with the applied electric field intensity in microscale systems.

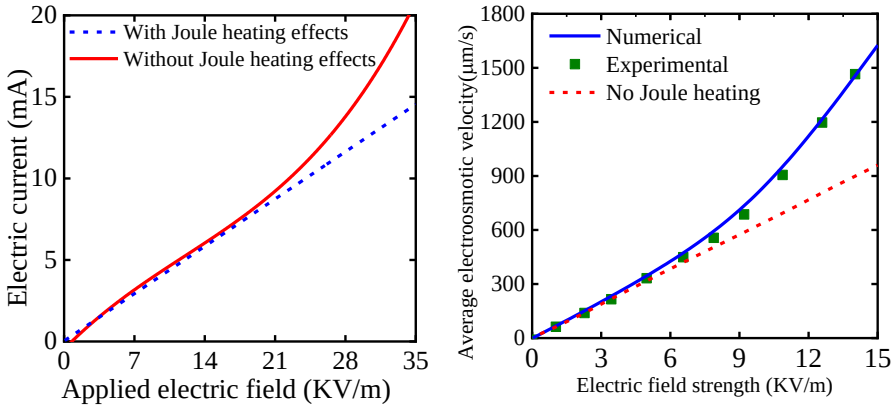

(a) (b)

Fig. 1.2 Impact of resistive thermal effects: (a) Current flow in the buffer layer under resistive heating versus non-thermal conditions [75]; (b) Comparison of numerically and experimentally obtained electroosmotic flow rates across varying field intensities, recorded 15 seconds post-field application, including flow velocities with and without thermal coupling [76].

1.5.2. Primary effects of viscous dissipation

Viscous dissipation in microchannels converts fluid friction into heat, critically shaping temperature fields, velocity profiles, and heat transfer. The Brinkman number (Br), representing viscous heating relative to conduction, governs bulk temperature rise even at low values due to microscale thermal confinement [77]. Axial heating reduces dynamic viscosity (μ), decreasing (Br) by 50 % downstream. This decline indirectly lowers the Nusselt number (Nu) via thermal boundary layer distortion (termed the secondary effect) [78]. Temperature-dependent μ dominates liquid behavior, creating asymmetric velocity profiles: accelerated flow in warmer zones (lower μ) and deceleration in cooler regions [79]. Microchannel geometry (d_h) amplifies viscous dissipation, coupling temperature and velocity fields through feedback loops (e.g., reduced μ enhances flow, intensifying heating). Such nonlinear interactions demand advanced models for microscale thermal-fluidic design [80]. Fig. 1.3 illustrates the impact of the Brinkman number (Br*)* on thermal transport in a triangular microchannel under steady-state thermal and hydrodynamic equilibrium for non-Newtonian fluids governed by the power-law model, incorporating viscous dissipation under fixed thermal boundary conditions. At specific Br and power-law indices (n=0.8) in forced convection, viscosity-amplifying fluids exhibit shorter hydrodynamic development lengths compared to viscosity-reducing fluids, regardless of thermal constraints. Viscous dissipation effects are more pronounced in viscosity-amplifying fluids than in viscosity-reducing fluids under identical flow configurations, as demonstrated in Fig. 1.3a [81]. Chen and Tso [82] explored the effect of porous medium permeability on convective heat transfer by examining variations in the Nusselt number over a range of Brinkman numbers

for both Newtonian and non-Newtonian fluids. Their study identified a permeability-dependent transition in thermal behavior, wherein shear-thickening fluids exhibit higher heat transfer rates than shear-thinning fluids in low-permeability regimes (Da < 0.3), while the opposite trend emerges as permeability increases beyond this threshold. The numerical results further revealed that viscous dissipation becomes increasingly pronounced in non-Newtonian fluids within the low-permeability range (0.0001 < Da < 0.1), indicating a strong sensitivity of thermal transport to internal friction effects. At a moderate permeability level near Da ≈ 0.2, the Nusselt numbers for Newtonian and non-Newtonian fluids converge, as illustrated in Fig. 1.3b. For small Brinkman numbers, numerical analysis shows that once Da > 1, viscous heating controls the thermal behavior of non-Newtonian flows, emphasizing the relevance of dissipation effects in high-permeability media.

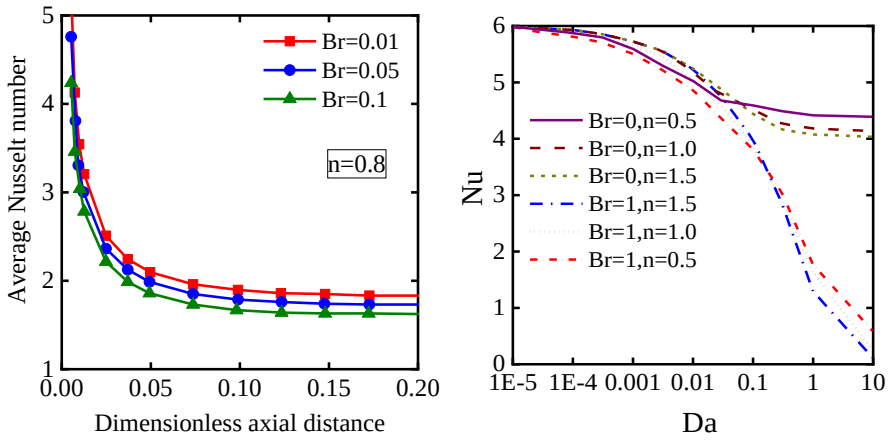

(a) (b)

Fig. 1.3 Variation with Brinkman number: (a) average Nusselt number vs. dimensionless axial distance in a triangular microchannel [81]; (b) Nusselt number vs. Darcy number in a parallel-plate microchannel [82]

1.5.3. Primary effects of thermal radiation

Thermal radiation in microchannels governs energy transfer via electromagnetic waves, particularly in systems with participating media (e.g., fluids or solids that absorb or emit radiation) [83]. Minimal thermal gradients between the conduit surface wall (T_w) and ionic medium (T) drives radiative heat flux, approximated by the Rosseland diffusion model for optically thick media [84],

$$q_r = -\left(4\sigma/3\tilde{k}\right)\frac{\partial T^4}{\partial y} \tag{1.8}$$

In this context, Stefan-Boltzmann constant (σ), Rosseland mean absorption coefficient $(\tilde{k})$, and T determines the fluid's thermal state. This linearizes the

inherently nonlinear T^4 dependence by expanding T^4 around T_w using a Taylor series:

$$T^4 = T_w^4 + 4T_w^3(T - T_w) + O\left((T - T_w)^2\right) \quad (1.9)$$

where higher-order terms $O\{(T\text{-}T_w)^2\}$ are neglected for small temperature differences $(T - T_w \ll T_w)$, simplifying to $T^4 \approx 4T_w^3 T - 3T_w^3$. This approximation enables tractable modeling of radiative-convective-conductive coupling at boundaries, altering thermo-responsive fluid attributes (e.g., viscosity, conductivity) and reshaping velocity profiles [85]. In microelectronics cooling,
radiation enhances heat dissipation under constant T_w by amplifying thermal gradients, while in micropumps or microreactors, electromagnetic interactions introduce Joule heating effects distinct from radiative transfer. Radiation dominates in high-temperature or low-velocity flows but requires iterative solvers due to T^4 nonlinearity [84]. Neglecting radiation risks underestimating heat transfer in MEMS devices or overheating biomolecules in lab-on-a-chip systems, highlighting its dual role as a thermal enhancer and design constrain.

1.6. Enhancing microchannel mixing and separation

Microfluidic mixing processes are optimized through active or passive methods, each exploiting distinct physical principles. Active micromixers, conversely, apply external forces such as magnetic [86], acoustic [87], electrical [88], and mechanical [89] to perturb flows, enabling techniques like droplet-based [90], time-periodic mixing [91]. Active systems, though complex, achieve tunable mixing in dynamic environments [92], balancing energy input, efficiency, and operational flexibility [93]. Passive designs dominate chemical [94] and biological [95] applications due to their fabrication simplicity and scalability, exemplified by pesticide detection chips that mix enzymes with samples cost-effectively [96]. Passive micromixers are categorized into lamination-based and chaotic advection-based designs without external energy input. Lamination-based mixers, such as T-shaped [97] and Y-shaped [98] geometries, split and recombine fluid streams to enhance interfacial contact via the split-and-recombine principle. Passive strategies rely on laminar flow and molecular diffusion, augmented by geometries like serpentine channels [99], obstacles [100], zigzag paths [101], staggered herringbones [102], or patterned blocks [103]. These structures intensify fluid interactions by inducing secondary flows (e.g., dean vortices in curved channels) or chaotic advection (irregular fluid trajectories) [104], stretching and folding fluid layers to reduce diffusion distances [105,106]. This addresses the inherent challenge of mixing at low Reynolds numbers, where diffusion alone is insufficient.

1.7. Hydrodynamic slip and thermal jump at boundaries

Transport processes at micro- and nano-length scales depart significantly from classical macroscopic behavior because fluid–solid interactions become increasingly dominant as the characteristic dimensions shrink. This enhanced influence arises

from the large surface-to-volume ratio, which amplifies molecular effects and alters the overall flow response. Helmholtz [107] was among the first to suggest that liquid slip may occur at solid boundaries by considering the order of magnitude of molecular motion. In this context, the molecular thermal velocity is expressed as $\left(u_m = \sqrt{3k_B T_w / m}\right)$. where u_m denotes the thermal velocity of molecules, $k_B$is the Boltzmann constant, T_a represents the absolute temperature, and mis the molecular mass. Although such interfacial slip effects are negligible in macroscale systems, they become increasingly relevant when flow domains approach microscopic dimensions. At small length scales, boundary conditions are no longer universal and are highly sensitive to surface and interfacial characteristics. Parameters such as wettability, surface charge, dissolved gas content, imposed shear rates, nanoscale roughness, pressure gradients, interfacial friction, and fluid–structure interactions near the wall collectively govern the near-wall flow behavior [108]. The degree of slip is commonly quantified using the slip length, which is defined as the extrapolated distance below the solid surface at which the tangential fluid velocity would theoretically vanish [109,110]. While this quantity does not correspond to a physical length, it serves as a practical measure of interfacial slip.

The flow behavior at microscale is primarily classified using the Knudsen number (Kn), defined as the ratio of the molecular mean free path to a characteristic channel dimension. Based on this criterion, flow regimes are categorized as continuum flow for Kn < 0.001, slip flow for 0.001 < Kn < 0.1, transition flow for 0.1 < Kn < 10, and free molecular flow for Kn > 10 [111]. When the Knudsen number exceeds 0.1, conventional continuum-based models become inadequate, necessitating higher-order slip boundary formulations to capture rarefaction effects accurately [112]. Within the slip-flow regime, the classical Navier–Stokes equations must therefore be modified by incorporating velocity slip conditions at the fluid-solid interface.

The Navier slip boundary condition provides a widely adopted framework for modeling liquid slip, relating the tangential velocity at the wall to the local velocity gradient normal to the surface through a proportionality constant known as the slip length. It is expressed as. u+ $adu/dy|_{y=h}$=0 [113]. This formulation demonstrates that slip may persist even when the interfacial shear rate remains below a critical value [114,115]. Consequently, the extent of deviation from the classical no-slip assumption is strongly governed by the Knudsen number and interfacial dynamics.

In Newtonian fluids, slip arises from molecular-scale interactions at interfaces. True slip comes at the liquid-solid boundary when weak adhesion (e.g., lyophobic surfaces or molecular roughness mismatches) enables tangential sliding of fluid molecules, violating the no-slip condition and reducing viscous drag. Apparent slip, observed at a fluid-fluid interface, involves slip over secondary layers such as cavitation-induced gas bubbles (under critical shear stress), molecularly ordered structures near surfaces, or engineered textures (e.g., shark-skin riblets) that decouple near-wall flow. These principles are applied in microfluidic serpentine mixers (chaotic advection and biomedical catheters (lyophobic coatings minimizing blood drag) [116].

In non-Newtonian fluids, slip at solid boundaries is largely influenced by the behavior of polymer chains under shear. On surfaces modified with grafted polymers, the near-wall flow can be divided into three regimes. At low shear rates, the polymer chains

remain attached to the surface, resulting in little or no slip. As the shear increases beyond a critical point, the chains begin to detach partially, allowing some sliding of the fluid along the wall. At even higher shear rates, the polymer chains detach almost completely, and the bulk flow effectively decouples from the surface, producing full slip. This shear-dependent response is particularly useful in applications such as injectable gels for drug delivery and surfaces engineered to reduce drag [117].

Slip behavior is also observed in gas flows, where it was first explained by Maxwell using kinetic theory for monoatomic gases [118]. In his model, gas molecules are treated as rigid spheres that constantly collide with both the wall and each other. When molecules strike a surface, some exchange momentum with the wall and re-emit at a velocity corresponding to the wall's thermal state, while the rest reflect without losing tangential momentum. The fraction of molecules that equilibrate with the wall is described by the tangential momentum accommodation coefficient, σ_v. A value of $\sigma_v = 0$corresponds to purely elastic or specular reflection, where no momentum is transferred to the surface, while $\sigma_v = 1$represents full diffuse reflection, with complete momentum transfer to the wall. Smoluchowski experimentally verified the temperature jump conditions $(T-T_w)+d(dT/dy)|_{y=h}=0$ model's thermal discontinuities at walls relates to the inter-collision distance (λ_m) and $(\partial u/\partial n)_{wall}$ is a velocity gradient normal to the wall. For instance, Deissler's model incorporates higher-order terms:

$$u_{slip} = u_{gas} - u_{wall} = \frac{2-\sigma_v}{\sigma_v}\lambda_m \left(\partial u/\partial n\right)_{wall} + \frac{3}{4}\frac{\mu}{\rho T_{gas}}\left(\partial u/\partial n\right)_{wall} \tag{1.10}$$

Similar to the concept of slip velocity in momentum transfer, a portion of gas molecules, denoted by σ_T, interacts with the wall and exchanges energy, allowing the wall to adjust their mean thermal energy to match its own. This fraction of molecules effectively reflects from the surface with thermal energy corresponding to the wall temperature, while the remaining fraction, $1-\sigma_T$, rebounds with its original incident energy. The dimensionless coefficient $\sigma_T$is referred to as the thermal accommodation coefficient, which quantifies the extent of energy exchange between the gas and the solid surface [107,119]. Using this concept and applying an energy balance at the interface, the temperature jump condition at the wall. Recognizing the Taylor series expansions, the boundary conditions were derived by Deissler [120] as given in Eqs. (1.11) and (1.12), and the boundary conditions recommended by Karniadakis et al. [121] and Gad-el-Hak [122] are in Eqs. (1.13) and (1.14).

$$u\big|_{y=h} = \left(\frac{2-\sigma_v}{\sigma_v}\right)\lambda_m \frac{\partial u}{\partial y} - \frac{9}{8}\lambda_m^2\left(\frac{\partial^2 u}{\partial x^2} + \frac{1}{2}\frac{\partial^2 u}{\partial y^2} + \frac{1}{2}\frac{\partial^2 u}{\partial z^2}\right) + u_c \tag{1.11}$$

$$\begin{aligned} T\big|_{y=h} - T_w = &\left(\frac{2-\sigma_T}{\sigma_T}\right)\left(\frac{2\gamma_r}{\gamma_r+1}\right)\frac{\lambda_m}{\mathrm{Pr}}\frac{\partial T}{\partial y} \\ &-\frac{9}{128}\lambda_m^2\left(\frac{177\gamma_r - 145}{\gamma_r+1}\right)\left[\frac{\partial^2 T}{\partial x^2} + \frac{1}{2}\frac{\partial^2 T}{\partial y^2} + \frac{1}{2}\frac{\partial^2 T}{\partial z^2}\right] \end{aligned} \tag{1.12}$$

$$u_{gas} - u_{wall}\big|_{y=h} = \frac{(2-\sigma_v)}{\sigma_v}\left[\lambda_m \frac{\partial u}{\partial y} + \frac{\lambda_m^2}{2}\frac{\partial u^2}{\partial y^2}\right] + u_c \tag{1.13}$$

$$T\big|_{y=h} - T_w = \frac{(2-\sigma_T)}{\sigma_T}\left(\frac{2\gamma_r}{\gamma_r+1}\right)\frac{1}{Pr}\left[\lambda_m \frac{\partial T}{\partial y} + \frac{\lambda_m^2}{2}\frac{\partial^2 T}{\partial y^2}\right] \tag{1.14}$$

where γ_r is the specific heat capacity ratio, λ_m is the mean free path between two successive collisions. $Pr=\mu c_p/k_T$ is the Prandtl number.

The momentum and thermal accommodation coefficients, which quantify the degree of momentum and energy exchange between a fluid and a solid surface, can vary between 0 and 1. Accurate specification of interfacial boundary conditions is not only fundamental to fluid dynamics but also critical for modeling modern applications, including MEMS devices, biological systems, and colloidal chemistry. In microchannel flows, fluid slip plays a key role in reducing flow resistance and is often linked to enhanced permeability within porous media. This property is exploited in microscale pumps used for targeted drug delivery and microelectronic cooling, where different degrees of slip can be engineered to optimize performance [123].

In gaseous flows, slip phenomena are particularly important in applications such as hard-disk drives, where the gas layer at the head-disk interface governs performance. Kinetic theory provides a framework for describing gas-solid slip, while thermal resistance at the interface manifests as a temperature discontinuity due to imperfect energy transfer. This effect arises because acoustic waves propagate much faster in solids than in liquids, and abrupt changes in molecular structure create a significant impedance mismatch between the two media [124]. The resulting temperature jump reflects the interruption in energy transport across the interface. Molecular dynamics simulations have further shown that the magnitude of this jump depends on surface characteristics, including microstructural texture and wettability, highlighting the importance of surface engineering in controlling interfacial thermal phenomena.

1.8. Physical aspects of electroosmotic flow dynamics and heat transfer

Imposing a pressure gradient in microchannels modifies flow and thermal dynamics compared to purely electroosmotic flow (EOF) [125]. Unlike pressure-driven flow, EOF arises from electric double layer (EDL) interactions, producing distinct plug-like velocity profiles under uniform zeta potential and electric fields. Key parameters like electroosmotic mobility (governed by wall zeta potential, fluid viscosity, and dielectric constant) and applied voltage dictate flow behavior, with viscosity variations and non-uniform surface potentials further altering velocity distributions. These flows significantly influence thermal transport through Joule heating (volumetric heat from ionic current) and viscous dissipation (shear-induced energy loss), critically shaping temperature profiles [126]. In hybrid electroosmotic-pressure-driven flows, velocity profiles emerge from competing electric and pressure forces. For Newtonian fluids [127], pure EOF exhibits a flat velocity profile due to

EDL-driven motion, while superimposed pressure gradients introduce parabolic distortions. For non-Newtonian fluids [128], shear-dependent viscosity (e.g., couple stress Casson, Maxwell, and Oldroyd-B models) further distorts the profile, as viscous stresses nonlinearly couple with electric and pressure forces.

1.8.1. Newtonian fluid transport in microchannels

In microfluidic systems, Newtonian fluids (exhibiting a linear shear stress–shear rate relationship) can experience electroosmotic flow (EOF) and magnetohydrodynamic (MHD) effects when orthogonal electric and magnetic fields generate a Lorentz force $\left(\mathbf{F}=\mathbf{J}\times\mathbf{B}\right)$, altering flow dynamics. Based on the Debye-Hückel assumption (valid for low zeta potentials, ξ<25 mV), the electrical double layer (EDL) drives EOF, producing a near-uniform plug-like velocity profile determined by electroosmotic Helmholtz-Smoluchowski velocity $\left(u_{HS}=-\varepsilon\xi E_x/\mu\right)$, which depends on wall zeta potential (ξ), reference velocity (u_{HS}), fluid permittivity (ε), and viscosity (μ) [129]. EOF efficiency is modulated by ionic strength (governing EDL thickness) and channel geometry. Thermal transport involves Joule heating and viscous dissipation, with temperature distributions impacting fluid properties and stability. The Nusselt number, derived from bulk and wall temperatures, quantifies convective heat transfer critical for optimizing lab-on-a-chip and biomedical devices [130]. The synergy between charge-mediated fluidic phenomena and magnetic field-induced interactions facilitates precise regulation of hydrodynamic and thermal behavior in microscale systems.

1.8.2. Viscoelastic fluid characteristics flow in microscale systems

In microscale systems, viscoelastic fluids which exhibit both viscous dissipation and elastic energy storage demonstrate flow behaviors distinct from Newtonian fluids due to their time-dependent stress response [131]. These fluids are governed by intrinsic material parameters such as relaxation time governing stress decay after deformation and retardation time associated with delayed strain recovery. Unlike Newtonian flows, viscoelastic effects in microchannels can induce phenomena like flow asymmetry, elastic instabilities, and stress driven secondary flows [132].
In electrokinetically driven flows, the EDL at the channel walls interacts with the fluid's viscoelasticity. When zeta potential effects are considered without invoking the Debye Hückel approximation (valid only for low or high surface potentials), the interplay between EDL polarization and viscoelasticity alters velocity and concentration profiles. For instance, in confined microchannel flows of Oldroyd B fluids (a canonical viscoelastic model), time periodic electroosmotic forcing can induce mass separation: a phenomenon where solute species migrate asymmetrically due to competing elastic and viscous stresses. This effect arises from the coupling of fluid elasticity, EDL dynamics, and oscillatory electric fields leading to spatially nonuniform concentration gradients even in the of bulk pressure differences [91].

1.9. Physical aspects of streaming flow dynamics and heat transfer

Pressure-driven flow in microchannels interacts with the EDL at the channel walls. This hydrodynamic shear mobilizes ions within the EDL generating a streaming current. Charge neutrality is restored through the spontaneous formation of a streaming potential which opposes the flow via an induced electric field. The resulting interplay between pressure-driven advection and electroosmotic backflow creates velocity profiles deviating from conventional hydrodynamic behavior.
Key factors governing the streaming potential include wall zeta potential (surface charge), fluid ionic strength (modulating EDL thickness through Debye screening) and channel geometry (influencing field gradients). These parameters collectively dictate flow retardation and velocity distribution [133].
Thermal transport is shaped by three mechanisms: Joule heating from ionic current, viscous heating from shear deformation and thermal radiation from electromagnetic energy transfer. These energy dissipation processes generate temperature gradients that alter heat transfer efficiency. Such coupled flow-thermal phenomena are critical for optimizing microscale energy harvesting systems and biomedical diagnostics where controlled thermal management ensures device reliability or enhances biomolecular interactions [67].

1.9.1. Viscoplastic fluid flow in microchannels

In microchannel flows, viscoplastic fluids such as couple-stress Casson fluids demonstrate unique dynamics under EMHD forces and streaming potentials. These fluids combine yield stress behavior (characteristic of Casson models) [134] with microstructural couple-stress effects [113], leading to nonlinear flow profiles and altered thermal transport in confined geometries. The interplay of EMHD forces generated by the interaction of electric currents and magnetic fields with streaming potentials (electric fields induced by pressure-driven ion transport) governs energy conversion efficiency. This efficiency quantifies the system's ability to transform mechanical energy from fluid motion into electrical energy through electrokinetic coupling [135]. Key factors such as the couple-stress parameter (reflecting micro-rotational resistance) [136], Casson yield stress (defining flow initiation thresholds) [137], and slip-modified zeta potential (influencing interfacial charge distribution) [138] critically determine energy harvesting performance in applications like microscale power generation.
Thermal performance in such systems is evaluated via the Nusselt number (Nu), which characterizes convective heat transfer relative to conduction. For couple-stress Casson fluids, Nusselt number is modulated by the fluid's viscoplasticity (e.g., shear-thinning and yield stress) and EMHD induced secondary flows. Concurrently, entropy generation analysis reveals thermodynamic irreversibility arising from viscous dissipation, Joule heating, and thermal gradients. Parameters like the couple-stress coefficient and Casson yield stress directly impact entropy production rates, guiding optimization strategies for minimizing energy losses in microfluidic thermal management and energy conversion systems [67].

1.9.2. Viscoelastic fluid characteristics flow in microscale systems

In microscale systems, viscoelastic fluids like transient Maxwell [128] and time periodic Oldroyd-B [139] fluids exhibit unique dynamics shaped by their relaxation times, polymer microstructure, and boundary interactions. During transient flow initiation, elastic stresses dominate until the relaxation timescale allows viscous effects to equilibrate the system. In pressure-driven flows with slip-dependent zeta potentials, the interplay between hydrodynamic shear and electrokinetic slip at the wall redistributes ions in the electrical double layer (EDL), altering streaming potential generation. This ion redistribution enhances electrokinetic energy conversion efficiency by modulating local conductivity and counterion mobility. Under constant heat flux boundary conditions, viscous dissipation (from shear-thinning behavior) and Joule heating (from induced currents) create temperature gradients that reduce convective heat transfer efficiency. The Nusselt number quantifies this thermal performance, while entropy generation driven by thermal gradients and fluid friction identifies irreversible losses critical for optimizing microscale energy harvesters [140].

For time-periodic Oldroyd-B fluids, which incorporate both relaxation and retardation times, oscillatory pressure-driven flows amplify viscoelastic memory effects. The periodic deformation of polymer chains in the fluid microstructure generates phase-lagged stresses, influencing velocity profiles and mass transport [91]. The resulting streaming potential varies cyclically, coupling fluid elasticity to energy conversion efficiency. Time-averaged mass transport rates depend on the elasticity number (ratio of fluid relaxation time to flow timescale), which dictates whether elastic or viscous effects dominate. Under constant wall temperature conditions, energy dissipation from viscous heating (shear-rate-dependent) and Joule heating (frequency-dependent) redistributes thermal energy, altering the Nusselt number's dependence on viscoelastic parameters. Entropy generation analysis reveals that polymer chain alignment under oscillatory shear minimizes viscous losses but amplifies thermal irreversibility, guiding designs for applications requiring frequency-tunable energy conversion.

These insights into fluid microstructure, transient kinetics, and boundary-driven electrokinetics advance microfluidic technologies such as adaptive lab-on-a-chip platforms, microscale energy harvesters, and biomedical sensors requiring precise thermal and flow control.

1.10. Numerical simulation of desalination via electroosmotic flow

Desalination in a hyperbolic nanochannel integrated with a cation exchange membrane (CEM) relies on selective ion transport driven by electroosmotic phenomena. The CEM's fixed negative charge groups facilitate selective transport of Na^+ ions while electrostatically repelling Cl^- ions, enabling ion separation. When an external electrical potential is applied, electroosmotic transport is generated within the nanoscale conduit via the coupling of the field with the interfacial charge in the charge-segregated zone along the walls This EOF advects both bulk fluid and dissolved Na^+ ions toward the membrane. Concurrently, electromigration direct ion

motion driven by the electric field enhances Na^+ transport through the CEM, while Cl^- ions are retained due to the membrane's perm-selectivity [141].
The system leverages ion concentration polarization (ICP), a phenomenon where ion depletion and enrichment zones form at the CEM-nanochannel interface. This ICP creates a localized electric field gradient, further amplifying ion selectivity and separation efficiency [142]. By restricting Cl^- permeation and optimizing Na^+ transport through coupled EOF and electromigration, the configuration achieves desalination by effectively separating salt ions from the feed solution.

1.11. Multi-objective optimization framework for electrokinetic system design

Designing electrokinetic systems often requires balancing multiple conflicting objectives. Two effective algorithms for such multi-objective optimization problems are the Non-Dominated Sorting Genetic Algorithm II (NSGA-II) and the Non-Dominated Sorting Grey Wolf Optimization Algorithm (NSGWOA). Both aim to identify a set of Pareto-optimal solutions, offering designers a range of optimal trade-offs between objectives.
Below are the structured steps for each algorithm:

1.11.1. Non-Dominated Sorting Genetic Algorithm II (NSGA-II) Steps:

The NSGA-II algorithm is analyzed through the following steps [143],
(i) Initialization: Generate an initial population of potential solutions with random decision variables within predefined bounds.
(ii) Evaluation: Assess each individual's performance by calculating the values of the objective functions.
(iii) Non-Dominated Sorting: Rank individuals based on Pareto dominance, categorizing them into different fronts where the first front consists of non-dominated individuals, the second front is dominated by the first but not by others, and so on.
(iv) Crowding Distance Assignment: For each individual, compute the crowding distance, which measures the density of solutions surrounding it in the objective space, aiding in maintaining solution diversity.
(v) Selection: Use a tournament selection mechanism that considers both rank (from non-dominated sorting) and crowding distance to choose parents for reproduction.
(vi) Crossover and Mutation: Apply genetic operators such as crossover (combining pairs of parents to produce offspring) and mutation (introducing small random changes) to generate a new offspring population.
(vii) Elitism: Form a combined population of current and offspring individuals, then select the next generation by choosing the best individuals based on rank and crowding distance, ensuring the preservation of high-quality solutions.
(viii) Termination check: Stop when Pareto front stabilizes or maximum iterations are reached.

1.11.2. Non-Dominated Sorting Grey Wolf Optimization Algorithm (NSGWOA) Steps:

The operational framework of the NSGWOA algorithm is outlined in the following steps [144],

(i) Initialization: Initialize a population of grey wolves (archive size) with random positions (decision variables) within the search space.

(ii) Evaluation: Evaluate each wolf's position by computing the objective function values.

(iii) Non-Dominated Sorting: Organize the wolves into different non-dominated fronts based on Pareto dominance relationships.

(iv) Crowding Distance Calculation: Calculate the crowding distance for each wolf to maintain diversity in the solution set.

(v) Leadership Hierarchy Establishment: Identify: the alpha (best solution), beta, and delta wolves based on non-dominated sorting and crowding distance.

(vi) Position Update: Update the positions of the remaining wolves by mimicking the hunting behavior, moving towards the positions of alpha, beta, and delta wolves.

(vii) Termination check: Halt when the Pareto front converges or iteration limits are met.

1.12. Multicriteria decision-making (MCDM) for pareto-optimal solution selection

The Technique for Order of Preference by Similarity to Ideal Solution (TOPSIS) is a widely used MCDM method to rank and select the most suitable solution from a set of Pareto-optimal alternatives. In multi-objective optimization (e.g., using NSGA-II or NSGWOA), Pareto fronts provide a spectrum of trade-offs between conflicting objectives (e.g., maximizing electroviscous heat transfer vs. minimizing thermal irreversibility). TOPSIS helps decision-makers systematically prioritize solutions by evaluating their relative closeness to an ideal "best" solution and distance from an anti-ideal "worst" solution [145].

1.13. Machine learning driven prediction of pareto-optimal solutions in thermal management

The integration of Artificial Neural Networks (ANNs) and Adaptive Neuro-Fuzzy Inference Systems (ANFIS) into multi-objective thermal management enables rapid prediction of Pareto-optimal solutions by learning complex relationships between design parameters, thermal performance metrics, and energy efficiency. These machine learning (ML) tools act as surrogate models, reducing computational costs associated with iterative simulations or experiments while maintaining accuracy in identifying optimal trade-offs.

1.13.1. Artificial Neural Networks (ANNs)

ANNs are computational models inspired by the human brain's neural structure, consisting of interconnected nodes (neurons) organized in layers. They process input data to identify underlying patterns and relationships. In thermal management

applications, ANNs can be trained to predict outcomes such as pressure loss, and thermal resistance based on various design parameters. Once trained, ANNs can rapidly evaluate potential designs, aiding in the swift identification of Pareto-optimal solutions without the need for extensive simulations [146].

(i) Define Network Architecture: Define the architecture by aligning the input layer neuron count with the input feature dimensions, configuring the quantity and dimensionality of intermediate layers to model intricate nonlinear relationships, and assigning neurons in the final layer to mirror the target output specifications.

(ii) Initialize Parameters: Set initial weights and biases, typically with random values, to prepare the network for training.

(iii) Forward Propagation: Feed input data through the network, applying activation functions (such as sigmoid or Rectified Linear Unit) at each neuron to generate output predictions. Measure the discrepancy between the predicted outputs and actual target values using an appropriate loss function, like mean squared error.

(iv) Compute Loss: Measure the discrepancy between the predicted outputs and actual target values using an appropriate loss function, like mean absolute percentage error, root mean squared error.

(v) Backpropagation and Parameter Update: Compute the gradients of the loss function with respect to each weight using backpropagation, then update the weights and biases using optimization techniques like stochastic gradient descent (SGD) or the Adam optimizer.

(vi) Iterate Training: Repeat the forward propagation, loss computation, and backpropagation steps over multiple epochs until the network's performance reaches the desired level.

1.13.2. Adaptive Neuro-Fuzzy Inference Systems (ANFIS)

The Adaptive Neuro-Fuzzy Inference System (ANFIS) is a hybrid machine learning framework that integrates fuzzy logic principles with neural network adaptability. By combining the interpretability of fuzzy systems with the learning capabilities of neural networks, ANFIS effectively models complex nonlinear relationships. Its architecture consists of five layers that map inputs to outputs through fuzzy rules, membership functions, and parameter optimization. Below are the key steps for implementing ANFIS [147]:

(i) Define Fuzzy Inference System (FIS) Structure: Specify input and output variables, assign membership functions to each input variable, and formulate fuzzy if-then rules based on the input variables.

(ii) Initialize Parameters: Set initial parameters for membership functions and rule consequents, often based on domain knowledge or predefined methods.

(iii) Train ANFIS Model: Introduce the training dataset into the computational framework and utilize a combined optimization strategy that integrates quadratic loss minimization and iterative gradient-based parameter refinement to optimize model coefficients.

(iv) Validate Model: Evaluate the model’s predictive accuracy on a holdout dataset to verify its robustness and consistency when exposed to new, previously unencountered data sample.

Chapter 2. Literature review

2.1. Overview of microscale transport phenomena

An in-depth and sequential review of the literature has been carried out to explore the modelling approaches for electroosmotic flow and streaming potential, with a special focus on recent innovations targeting energy-efficient system designs. The latest progress in this area has been thoroughly evaluated to uncover emerging trends and technological advancements. Through this analysis, unresolved challenges and knowledge gaps have been identified, serving as a basis for defining clear directions for future research efforts.

2.2. Electroosmotic microflows: modelling and parametric insights

Electroosmotic phenomena have garnered significant attention in contemporary fluid dynamics research, particularly in studies investigating coupled flow fields and heat transfer mechanisms. Analytical and numerical models have been rigorously applied to characterize key parameters, including velocity profiles, temperature gradients, Nusselt number variations, concentration fields, and time-averaged mass transport rates. Recent advancements have further explored hybrid modelling frameworks tailored to both high-zeta-potential and low-zeta-potential regimes, offering nuanced insights into the interplay between surface charge dynamics and flow behavior. These methodological innovations underscore the versatility of electroosmotic systems in addressing complex transport phenomena across diverse engineering applications.

2.3. Steady-state EMHD flow with thermal effects in microfluidic systems in Newtonian fluid dynamics

The relentless miniaturization of portable electronics intensifies thermal management challenges, as shrinking surface areas struggle to dissipate escalating heat fluxes, risking performance degradation and failure [148]. Conventional cooling methods like air-cooled heat sinks are ineffective at microscales, necessitating advanced microchannel based systems [149]. However, laminar microchannel flows governed by low Reynolds numbers and restrictive thermal boundary layers limit heat exchange [150].

Electromagnetohydrodynamic (EMHD) micropumps address this by leveraging Lorentz forces from interactions between electric currents in fluids and applied magnetic fields, enhancing flow without mechanical components [62]. Hybrid actuation combining electric and magnetic fields [151], offers superior control over micro/nanofluidic dynamics compared to purely electroosmotic systems [63], while simultaneously minimizing Joule heating and achieving higher flow rates [64]. Jang and Lee [53] reported the EMHD micropump acting along the flow of an electrically

conducting liquid in the imposed electric and magnetic fields in the perpendicular direction. According to Kundu and Saha [124] further reported that even weak magnetic fields significantly enhance volumetric flow rates. Recent advancements in EMHD flow and heat transfer have significantly enhanced the understanding of microscale transport phenomena by incorporating slip effects, rarefaction, and electromagnetic forces. These studies have progressively evolved from conventional no-slip models to higher-order slip conditions, capturing complex interactions involving Joule heating, viscous dissipation, and electrokinetic effects. Furthermore, analytical and numerical frameworks have been expanded to incorporate realistic boundary conditions and Newtonian fluid behavior.

Microfluidic instabilities, such as jet breakup, often persist despite geometric or flow rate optimizations, necessitating stabilization through externally applied fields (magnetic [152], electromagnetic [153], acoustic [154], electric [154]). Electromagnetic fields excel in precision control when paired with superhydrophobic surfaces featuring slip boundary conditions, where reduced friction and amplified surface charge enhance electroosmotic effects [152]. Sarkar et al. [155] demonstrated that combining EMHD pressure-driven flow with electrokinetic slip effectively mitigates electrical double layer (EDL) resistance, improving flow rates.

In pure electroosmotic flow systems, higher electric fields are generally required to drive electrolyte solutions often, inducing excessive Joule heating that damage thermally sensitive biological samples. Ranjit et al. [136] investigated the impact of first-order slip and jump conditions on the thermal characteristics of EMHD laminar flow, observing an increase in Nusselt numbers.

Sadeghi and Saidi [127] reported the thermally fully developed analytical study in parallel plate microchannels without electromagnetic effects Their findings demonstrated that increasing the viscous dissipation parameter reduces the Nusselt number, underscoring its thermal impact. Chakraborty et al. [129] explored coupled electroosmotic and pressure-driven flows during thermal development in microchannels, incorporating both viscous dissipation and resistive heating effects under combined electric and magnetic field exposure.

In micro heat exchangers, external electric fields simultaneously induce electroosmotic flow (EOF) and Joule heating [156–158]. Elevated electrolyte concentrations or strong fields amplify Joule heating, altering fluid properties such as viscosity and conductivity. These changes disrupt uniform EOF velocity profiles and intensify viscous dissipation near channel walls within the EDL [159,160].

Joule heating and viscous friction act synergistically to govern the thermal performance of microchannel heat exchangers, critically defining their heat transfer dynamics. In microscale geometries with high surface-area-to-volume ratios, radiative heat flux can dominate over conduction or convection, making thermal radiation a critical parameter. Lopez et al. [161] analyzed heat transport in a magneto-hydrodynamic nanofluid through a porous vertical microchannel with nonlinear thermal radiation, solving the governing equations numerically using Runge-Kutta and shooting techniques. Their research underscores the coupling of convection and radiation in heat transfer dynamics, where the Nusselt number is modulated by nonlinear radiative processes, viscous energy dissipation, and ohmic heating. This

underscores the critical need to incorporate radiative mechanisms in microfluidic systems exposed to extreme thermal conditions or optical activity.
Sadeghi et al. [127] concluded that in the presence of a thick EDL, viscous dissipation has a greater impact on heat transfer in EOF than ohmic heating.
Beyond internal heat transfer mechanisms, transverse conduction across microchannel walls has emerged as a key factor in thermal regulation, enabling precise temperature profile management [162]. Yang et al. [130] studied EMHD flow with Joule heating and viscous dissipation under no-slip/no-jump conditions.
For rarefied gas flows, Navier-Stokes equations remain valid up to Knudsen numbers $(Kn \leq 0.1)$ under Maxwell/Smoluchowski slip and temperature jump conditions [122]. Colin et al. [163] studied the second-order slip flow model predicts higher flow rates than the first-order slip flow model, with a difference of about 13% for a square duct at Knudsen number $Kn \leq 0.1$. While both models agree up to $Kn \leq 0.05$, significant differences arise at higher Knudsen numbers, with S2 showing better alignment with experimental data up to $Kn \leq 0.05$. Beyond this point, although second order model remains closer to experimental results than 1st order model, the agreement is not as precise. Colin et al. [164] further showed that neglecting second-order terms underestimates flow rates by 10–13% at $Kn \leq 0.1$, particularly in high-aspect-ratio ducts, necessitating higher-order corrections for accurate microscale flow predictions.

2.3.1. Research gaps in steady-state EMHD flow.

Existing research emphasizes the use of theoretical and computational approaches to evaluate the spatial variation of interfacial charge layer potentials, velocity distributions, thermal profiles, and Nusselt number values. These factors critically shape the performance of microscale fluidic systems, largely due to frictional energy losses and resistive heating effects, as observed in EMHD frameworks operating without radiative heat transfer. Subsequent studies, however, integrated frictional losses, resistive heating, and radiative mechanisms while disregarding electromagnetic forces in electrokinetically driven flow configurations. Predominant theoretical frameworks in microscale flow analysis adopt zero-slip and zero-jump boundary constraints for Newtonian fluids within microchannels. Later advancements incorporated primary-order velocity slip and thermal discontinuity conditions on water-repellent surfaces, neglecting radiative heat transfer and resistive heating effects. Scholarly attention has centered on primary-order slip with zero-jump constraints alongside radiative heat transfer, viscous energy losses, and resistive heating parameters, where the Nusselt number is commonly resolved via discrete numerical techniques. However, comprehensive analytical investigations integrating the Nusselt number with radiative exchange, viscous dissipation, resistive heating, and secondary-order hydrodynamic and thermal slip constraints for velocity and temperature profiles in EMHD flows through rectangular microchannels remain disconnected and insufficient.

2.4. Oscillatory flow characteristics of Oldroyd-B fluids in confined microchannel environments

In recent years, the rheology of viscoelastic fluid has advanced with greater attention to researchers due to the numerous applications of this particular fluid in various engineering fields. The fluid above has additional properties such as memory, normal stress, and yield stress [165,166]. For the above fundamental aspects, viscoelastic fluid differs from the Newtonian fluid. The complex model of the viscoelastic fluid analyzes biofluids [167], long-chain molecules [168], colloidal suspensions [169], DNA separation [170], and Lab scale device [171].

In this context, the P-B equation governs the electroosmotic flow for electrical-potential distributions. However, the solution of this equation is more complex to study the accurate and realistic cases for the presence of highly nonlinear source terms. Vasu and De [172] introduced the electrokinetic width (K) range for no overlapped EDL at a high zeta potential. The slip velocity at the liquid-solid interface affects the electroosmotic flow [173]. The slip velocity occurs in numerous applications in industrial and medical sciences, such as blood through stenosed arteries [174], polishing artificial heart valves [175], production of paint [176], shampoo [176], foam [177], and polymer melts [178]. Many studies based on Maxwell and Oldroyd-B constitutive models have analyzed slip and no-slip flow in parallel plate [128,179], circular [180], and rotating [181,182] microchannels with small zeta potential. For isothermal conditions, viscosity usually appears as a constant factor. However, in non-isothermal conditions under an electroosmotic flow, the ions of the electrolyte solution circulate in fluids. Therefore, the absolute viscosity is not constant; it depends on temperature, and as a result, the thermal state influences slippage conditions [183]. Matías et al. [184] studied the influence of slip on a hydrophobic surface for a non-isothermal electroosmotic-viscoelastic fluid flow in a microchannel.

Wang et al. [185] examined the electroosmotic transport of the fractional viscoelastic Oldroyd-B fluid in a rectangular microchannel, maintaining a high surface charge constraint. In contrast, Liang et al. [186] investigated the effect of slip on the rotating electroosmotic flow of Oldroyd-B fluid in a microchannel under high zeta potential. Time-modulated electroosmotic flow has been shown to enhance mixing efficacy and interfacial functionalization [187–189].

Investigations into oscillatory EHD flow have focused on both viscous Newtonian [190] and viscoelastic Jeffrey's fluids [191] within microscale channels, incorporating the influence of ion-depleted interfacial regions.

The Maxwell model for time-periodic electroosmotic flow was studied in a parallel plate [131,192] and circular [193] microchannel with a low zeta potential and no-slip condition. Ding and Jian [139] investigated the resonance phenomena of the Oldroyd-B fluid for electrokinetic oscillation flow. They provided a detailed analysis in a linear regime with no-slip boundary conditions at low zeta potential. In these circumstances, the mass transport mechanism for passive solute is essential in investigating microfluidic components analysis and design. The performance of a lab-on-a-chip depends on so many factors, viz. mixing [194], electroosmotic pumping [195], sample collection [196], detection of bacteria and viruses [197], separation of

chemical species [198,199], removal of toxic metal ions [200], and flow control elements [201]. Oscillatory pressure gradients have enhanced the mass transport due to the oscillatory flow. Electrokinetic pumps [202] maintain a useful pressure gradient in the combined pressure-driven and electroosmotic flow.

Hydrodynamic dispersion refers to the combined effects of molecular diffusion and bulk fluid flow due to the non-uniformity of velocity through a channel is analyzed based on the Taylor dispersion [203]. Aris [204] determined the apparent diffusion coefficient by incorporating the effect of axial molecular diffusion. Ramon et al. [205] found that the existence of the electrical double layer enhances the mass transfer. Their study also suggests that an oscillatory-electroosmotic flow could have the optimal species separation conditions. The oscillating flow of viscoelastic fluid [206] and power-law fluid [207] increments the transport of a non-reacting solute.

Baños et al. [208] demonstrated that the velocity slip boundary condition might not enhance mass transport rate and cross-over phenomena for separating different species of shear-thickening fluids. Chatwin [209] showed that the longitudinal pressure gradient creates the flow to fluctuate harmonically with time. Watson [210] demonstrated enhanced mass transfer efficiency of a dissolved solute within a cylindrical conduit through the application of oscillatory movement in the surrounding liquid medium. Kurzwer and Jaeger [211] investigated an improved mass transfer method utilizing oscillatory motion of gases in capillary arrays under axial concentration differentials to isolate gaseous components at elevated flow rate differentials. Later, Kurzweg [212] proposed a general analytical solution of enhanced diffusional separation of dilute liquid solution in oscillatory-liquid flow within open-ended capillary tubes. Mass transfer of electroosmotic flow under the periodic electric field with the asymmetric zeta potential in microchannels was studied [213,214].

Muñoz et al. [215] investigated the dispersion in a microcapillary tube with slippage conditions at the wall under oscillatory-electroosmotic flow. Mederos et al. [216] analysed time-integrated solute transport in extended microchannels with reactive interfaces for a chemically passive Jeffrey's fluid at varying molarities of uncharged species. Under spatially heterogeneous interfacial potential distributions. With the asymmetric zeta potential, Hoshyargar et al. [217] analysed the transport characteristics of late-time solute of hydrodynamic-dispersion (HD) in electroosmotic flow through a slit microchannel.

2.4.1. Identified research gaps in time-periodic Oldroyd-B fluid flow

Existing studies predominantly employ linearized electrostatic screening models under weak interfacial potential conditions simplifying charge distribution analyses in the EDL. Also, a few researchers determined the electrical-potential distribution in microchannels for no overlapped EDL with the high zeta potential. Furthermore, no attempt has been made to explore studies about the no overlapped EDL with low and high zeta potentials. Researchers have not focused on determining velocity and concentration profiles in microchannels under slip conditions for the inherent complexity of periodic-oscillatory Oldroyd-B fluid subjected to the electroosmotic flow. The real fact is to provide always the time-periodic analysis of

microchannel flow in the separation of chemical species. The flow transitions to a steady oscillatory regime once transient dynamics diminish. These observations underpin the rationale for the current investigation.

2.5. Non-Newtonian fluid behavior in thermal transport in streaming potential-driven microflows: a modelling perspective

Beyond steady Newtonian electromagnetohydrodynamic (EMHD) flow, realistic modelling of non-Newtonian fluids is pivotal for designing high-efficiency microfluidic systems with minimal energy dissipation. Analytical studies of couple-stress Casson fluid rheology reveals that interfacial electrokinetics significantly influence pressure-driven transport in systems governed by streaming potential dynamics. Among non-Newtonian fluid models, the Maxwell and Oldroyd-B frameworks are prominent. The Maxwell model is often favored over the Oldroyd-B model due to its computational simplicity and ability to represent materials governed by a single relaxation time. The Maxwell framework is particularly effective for fluids exhibiting viscoelasticity dominated by a single relaxation mechanism, such as dilute polymer solutions or low-viscosity melts. In contrast, the Oldroyd-B model incorporates both relaxation and retardation times, enabling the simulation of complex viscoelastic phenomena like stress overshoot and normal stress differences. However, this added complexity comes at a substantially higher computational cost.

Streaming potential dynamics in viscoelastic fluids further underscore the necessity of integrating oscillatory effects into microchannel flow analysis. For example, the Oldroyd-B model has demonstrated utility in optimizing species separation for targeted drug delivery. Among existing viscoelastic flow frameworks, the Maxwell and Oldroyd-B models remain widely adopted. Emerging research highlights their growing relevance in advanced fluid dynamics, particularly in applications requiring a balance between model fidelity and computational feasibility.

2.6. Steady state Couple stress Casson fluid model in a microchannel

The enormous contribution of fluid and ion transport via miniature systems has made it an attractive area for researchers. Understanding the physics of small-scale confined liquid flow explains many natural and artificial processes and allows researchers to use the concept in various advanced technologies. It has extensive applications based on microfluidic diagnostic devices such as micro-reactors for biological cell analysis [5], liquids containing long-chain molecules as polymeric suspensions [8], mass flow controller [9], reduction of mixing time for sampling [10], lowering of bleeding during surgeries [11], blood pumping machine [218], feeding vessels for cancer tumors [13], cell separation with development of magnetic devices [12], and many more.

A voltage gradient emerges along the fluidic conduit due to pressure-driven flow, inducing an electrical current that opposes the primary flow direction. This interaction reduces the effective flow velocity aligned with the pressure gradient. The generated voltage gradient consistently opposes the flow, creating a counteracting

electrokinetic force that impedes fluid movement. This resistance stems from amplified viscous forces and electrohydrodynamic interactions, as outlined in prior studies [53].

Integrated electromagnetic fields are extensively applied in EMHD microscale pumping systems to assess fluidic transport properties, leveraging advantages such as fabrication simplicity, non-mechanical operation, reduced power requirements, and bidirectional flow generation capacity [219]. These forces use alone or in appropriate combinations to efficiently activate the flow in microchannels. Zhao et al. [220] investigated thermally stabilized flow within planar microscale conduits exposed to concurrent pressure gradients and magnetic forces. Their work rigorously analysed nanoparticle laden fluid dynamics influenced by streaming potentials in pressure-driven systems. As a result, contemporary investigations have increasingly prioritized the use of non-Newtonian fluid models to better capture the complex, nonlinear dependencies between shear stress and deformation rates. Numerous applications, including blood [14], colloid suspensions [15], protein suspensions [16], DNA [17], salivary fluids [18], and synovial lubricants [19] demonstrate rheological properties inconsistent with Newtonian fluids, where conventional Newtonian models fail to describe stress-strain relationships. To address these complexities, advanced rheological models are employed to simulate flow dynamics under electromagnetic fields. Studies have explored viscoelastic fluids models like Maxwell fluid [221], Oldroyd-B [91], Phan-Thien-Tanner fluid [133], Casson [222], and Couple-stress [223] fluids in microchannels. Kumar et al. [224] analysed pulsatile streaming potential flow in a time periodic pressure gradient between two parallel plates microchannel. The model of Casson fluid was developed by Casson [225] for the flow behavior of pigment oil suspension of the printing ink type. Casson fluid behaves like an elastic solid having a low-shear strain.

When the stress is high, Casson behaves like a Newtonian fluid. According to the definition, this fluid shows shear-thinning behavior with infinite viscosity at zero rates of shear and zero viscosity at an infinite rate of shear. Subsequently, many researchers studied the electroosmotic flow transport of Casson's electrolyte solution [226]. Saleem et al. [227] investigated the behavior of an electroosmotically driven Casson fluid in a cylindrical geometry with contracting and relaxing sinusoidal walls. Bag and Bhattacharyya [228] investigated electrokinetically driven transport of yield-stress fluids within microscale conduits. They compared the results for velocity distributions of three viscoplastic materials, like Casson, Herschel–Bulkley, and Bingham plastic fluids. The rotating electroosmotic flow in a microchannel for a Casson and Bingham plastic fluid was analyzed by Qi and Ng [229]. Rajaram et al. [230] reported a detailed numerical and theoretical analysis of electroosmotic transient state Casson fluid flow for the influence of EMHD free convection stream passed through an exponentially accelerated plate.

However, a couple-stress fluid (CSF) has a noticeable non-Newtonian behavior. Researchers developed many theories to explain the properties of this fluid.

Stokes [231] developed the couple stress fluid model from the fundamental idea of non-Newtonian fluid. This framework prioritizes the inclusion of microparticle interactions, a factor omitted in classical Newtonian viscous analyses. The non-Newtonian formulation incorporates directional microstructural effects,

body torque interactions, and asymmetric stress contributions to modulate flow dynamics. Adding higher-order terms, its equation of motion is identical to the classical Navier-Stokes theory. The stress tensor is non-symmetric, and the couple-stress tensor is additional. Siva et al. [232] analysed the electrokinetic transport of viscoelastic couple-stress materials within a spinning microscale conduit.

In contrast, Sridhar et al. [233] examined velocity profiles and thermal gradients in such fluids under electroosmotic conditions, revealing that higher values of the rheological parameter correlate with diminished axial flow velocities. Ding et al. [234] explored pressure-driven couple stress fluid flow between two parallel plates microchannel with streaming potential effects at a low zeta potential.

By developing various portable devices for the harvested energy from different resources in domestic contexts, the dependency of contemporary society on centralized power sources reduces. A substantial portion of hydroelectricity is produced by large turbines using advanced technologies based on electromagnetic induction from mechanical inputs. Conversely, a notable green power source converts into water's mechanical energy. However, the physical requirements of mighty dams and infrastructure restrict their suitability as a dispersed energy source. Therefore, the slip-dependent zeta potential electro-magneto-hydrodynamic force for the non-Newtonian viscoplastic fluid in narrow microfluidic devices is employed for alternative energy sources [20]. The streaming current offers the possibility of converting hydraulic power generated by pressure into electrical power within the fluid system. The quantification of the streaming potential relies on the principle of electro-neutrality conservation.

The emergence of electrokinetic technology has led to a growing interest in electrokinetic energy conversion. This clean energy harvesting system in solid-liquid interface via streaming potential enriches On-chip laboratory system based on micro power generators referred to as the EKEC efficiency. It may open the exploration of new renewable energy [21] and can significantly impact studies of harvesting electrical power, the desalination process, and self-power sensors [22]. Microfluidic energy harvesting involves integrating electrokinetic energy systems into microfluidic devices, enabling the electricity generation by moving small liquid volumes. This electricity can then be utilized to power micro-electromechanical systems (MEMS) or micro-sensors. Electrokinetic energy systems can aid in desalination processes by implementing the streaming potential effect using carbon tubes, leading to increased energy efficiency in these operations. Electrokinetic energy systems can power sensors and monitoring devices in remote locations or areas with limited access to traditional power sources. These self-powered sensors, such as water quality or groundwater level measurements, can be used for environmental monitoring. Therefore, many researchers have theoretically and experimentally studied the EKEC efficiency in pure pressure-mediated flow in confinements [235]. In circular [236] and parallel plate [237] microchannels, the pressure-dependent viscosity on flow for Newtonian fluid demonstrates the decline in EKEC efficiency. Chen and Jian [238] showed that the rotational effect can improve the electrokinetic conversion efficiency in a parallel plate microchannel. The soft nanochannel exhibits a 25% increase in electrokinetic energy conversion efficiency, attributed to the resonance effect [239]. Due to slip effects, electrokinetic

energy efficiency is greatly amplified [240]. Xie [241] demonstrated that the maximum EKEC efficiency in stratified fluid configurations exceeds that of homogeneous systems in core-annular flow. Chandra et al. [242] revealed the increment of the electrokinetic energy efficiency (2.5-3%) for flow in a soft nanochannel compared to the rigid one at low zeta potential. Liu et al. [66] found the electrokinetic conversion efficiency in a curved nanochannel amplified by 17% compared to a straight nanochannel under specific parameters. Xie and Jian [135] analyzed the EKEC efficiency of nanoparticle-laden magnetohydrodynamic flow under streaming potential effects, incorporating slip velocity constraints at the microscale conduit surface.

Chen et al. [243] explored thermal transport dynamics in streaming potential-mediated flow within microscale channels subjected to electromagnetic fields, rigorously assessing thermal gradients and heat transfer coefficients under fixed thermal boundary conditions using velocity profiles and streaming potential data. Zhao et al. [244] evaluated the thermal performance of thermally stabilized nanoparticle suspensions in planar microchannels under concurrent pressure gradients and streaming potentials. Narayana et al. [245] computationally modeled three-dimensional magnetohydrodynamic flow of viscoplastic Casson fluids with microstructural stresses over elongating surfaces, incorporating radiative heat transfer mechanisms.

Entropy generation is an essential topic in thermal systems because it guides how to control or reduce irreversibility [246]. Entropy can be generated in various flow systems, particularly in thermal management systems, due to the irreversible heat transfer, resistive heating, hydrodynamic forces, and viscous dissipation. The Bejan number, a dimensionless metric, quantifies the dominance of thermal over frictional irreversibilities in such systems [247]. Abolbashari et al. [137] examined entropy production in viscoplastic nanofluid flow over elongating substrates, omitting interfacial charge layer interactions. Escandón et al. [248] quantified irreversibility rates in electrokinetically driven non-Newtonian fluid flow within planar microchannels. Xie and Jian [249] explored heat transfer and entropy dynamics in a dual-layer fluid system under combined electromagnetic and electroosmotic forces. Later, Xie and Jian [250] extended their work by introducing one layer composed of non-conducting viscoelastic fluid. Ibáñez et al. [251] researched the optimum slip length value that minimizes the entropy generation in parallel plate microchannels.

2.6.1. Key research gaps and unexplored aspects in Couple stress Casson fluid dynamics

Recent studies have investigated strategies to optimize streaming potential, flow velocity, energy conversion efficiency, and thermal profiles in microscale systems. Viscoelastic fluids demonstrate superior performance in streaming potential generation and energy conversion compared to Newtonian fluids. Electromagnetic hydrodynamic interactions and hybrid methodologies have been identified as effective means to control hydrodynamic behavior, thermal regulation, and reduce

thermodynamic losses. Initial investigations, however, focused primarily on Newtonian fluid dynamics under streaming potential conditions.

The combined rheological effects of couple-stress and Casson fluids in pressure-driven streaming potential flows remain unexplored in microchannel applications. Slip-modulated surface charge dynamics and thermal discontinuity conditions in non-Newtonian systems may critically influence flow optimization and thermal management in microscale environments. While couple-stress models fall short in simulating hemodynamic conditions during arterial constriction, integrating Casson fluid behavior addresses these limitations by accommodating variable rheological properties in microscale flows.

The synergistic coupling of couple-stress and Casson rheological frameworks in planar microchannel geometries remains unaddressed, likely owing to the computational challenges posed by streaming potential interactions. Future research should prioritize analyzing thermal gradients, heat transfer coefficients, and irreversibility metrics in microchannels featuring asymmetric, slip-influenced surface charge distributions. Visco-plastic materials are pivotal in biomedical and microengineering applications, enabling precise control of hydrodynamic and thermal behaviors in pressure-driven microfluidic systems leveraging streaming potential phenomena.

2.7. Transient Streaming Potential Flow of Maxwell Fluids in Microscale Domains

Microscale and nanoscale fluidic platforms provide adaptable and economical solutions for integrated diagnostic chips [252], energy conversion technologies [6], and and targeted therapeutic delivery systems [253]. When an insulating electrolytic medium interacts with a solid substrate, an interfacial charge-separated zone develops [124]. During pressure-induced flow, surplus counterions within this zone are convectively transported, inducing an axial voltage gradient [133]. This potential induces a conduction current opposite to fluid flow, creating electroosmotic force in reverse to pressure-driven flow. Magnetohydrodynamics (MHD) enhances microchannel transport by interacting with magnetic fields to induce streaming potential [52]. The Lorentz force generates Hall currents and ion slip, boosting collision frequency [254]. Magnetic nanoparticles with tunable properties enable nanofluids for applications like magnetic cell separation and drug delivery [255]. MHD flow operates without electrode contact, preventing fouling and biocompatibility issues, and applies to polar and non-polar fluids [256]. It also improves mixing particle trapping and heat transfer, especially for non-conductive fluids [257].

In the context of miniaturized diagnostic devices, understanding streaming potential phenomena in non-Newtonian fluids is essential for rheological analyses. This study selects the Maxwell fluid model over the Oldroyd-B fluid due to its computational simplicity. It represents a material with a single relaxation time. It suitable for modeling fluids with viscoelastic behavior dominated by a single stress response, such as low viscosity or simple polymer melts [91]. In contrast, the Oldroyd-B fluid includes both relaxation and retardation times, capturing more complex behaviors like shear-thinning but with a more significant computational cost

[180]. Therefore, the Maxwell fluid is ideal for modeling systems with more straightforward, single-relaxation processes. Streaming potential flow, driven by fluid motion across charged surfaces, aids efficient transport through porous media. A slip boundary condition in hydrophobic channels enhances streaming potential [258]. Porous media, comprising interconnected solid matrix voids, disrupt fluid flow [259], impacting systems like gallbladders and coronary arteries [260]. However, irregular flow velocity in porous media promotes mixing [261]. But, adopting porous material into microchannels significantly increases shear stress [262]. Lodhi and Ramesh [263] explored magnetohydrodynamic electroosmotic Jeffrey fluid under Hall effects in porous microchannels.

Renewable energy sources like wind, solar, and geothermal power can reduce greenhouse gas emissions but face limitations due to geographical and weather constraints [264]. Electrokinetic energy conversion (EKEC) converts hydrodynamic energy into electricity via streaming current, offering a scalable, compact, reliable, and environmentally friendly alternative [21,265,266]. There are many factors, such as the slip factor [240], channel size [267], surface charge density [235], and shape [52] influence EKEC efficiency. Ren and Stein [268] found the slip factor amplified the EKEC efficiency by 37% in a nanochannel, whereas Berli [269] showed the EKEC efficiency improved in a polymer solution compared to a Newtonian fluid. Xie et al. [270] demonstrated a ballistic micro-droplet-based electrostatic generator with an EKEC efficiency of almost 46%. Liu et al. [271] predicted a 50% increase in EKEC efficiency with the steric effect. Xie and Jian [135] showed a 16% increase in power by adding 5% nanoparticles. Saha and Kundu [67] analyzed the influence of EMHD streaming potential dynamics on thermal transport in microscale channels, underscoring the pivotal role of interfacial double-layer potential and slip boundary conditions in optimizing EKEC efficacy and thermal irreversibility.

Enhancing heat transfer in microscale magnetohydrodynamic flows is crucial for cooling and chemical systems. Nanoparticles and porous media improve thermal conductivity and surface area for heat dissipation [272]. Dewanjee and Kundu [273] recently reviewed thoroughly green nanofluids, emphasizing the enhancement of thermal performances of solar collectors, eco-friendly nanoparticles (e.g., olive leaf, barley husk), economic aspects, and the way to improve the stability of the nanofluid. Sayed et al. [274] found the Nusselt number enhancement with an increasing concentration of single-walled carbon nanotube particles in EMHD electroosmotic flow in a corrugated microchannel. However, thermodynamic irreversibility leads to energy loss. Liu et al. [275] found that the steric effect enhances heat transfer, while a large curvature ratio of rectangular curved nanochannel reduces entropy generation. Siva et al. [276] illustrated thermal field and thermodynamic irreversibility in viscoelastic materials with microstructural stresses subjected to EMHD electrokinetic flow, revealing that slip boundary conditions and rheological parameters could mitigate thermodynamic losses. Pabi et al. [277] demonstrated the viscoelastic effect to minimize entropy generation. Ibáñez et al. [251] optimized slip length to reduce thermal irreversibility. Efficient energy utilization is essential due to global energy challenges and environmental concerns [27]. Heat transfer is crucial for energy conservation [28] and is particularly important in microchannel systems where excess heat can lead to reliability issues [29] and increased operational costs [30,31]. High

entropy generation hinders efficient energy conversion [32]. Table 1 displays some important literature works connected with streaming potential and electroosmotic flow for Newtonian, Maxwell, and Oldroyd-B fluids in microchannels by mentioning critical determinations.

Table 1
Summary of some important literatures

Flow Mechanism	Types of Fluid	Flow Actuation	State of Flow	Main findings of the Studied	Refs.
Streaming potential	Newtonian	No External fields	Steady state	Evaluated streaming potential, velocity, and EKEC efficiency.	[66,236–238,241]
Streaming potential	Newtonian	Without/with magnetic field	Steady state	Evaluated streaming potential, velocity, temperature, Nusselt number, and entropy.	[220,243,244,278–280]
Electroosmotic	Newtonian	Electromagnetic field, Hall current, ion slip	Steady state	Evaluated velocity, temperature, Nusselt number.	[281–283]
Streaming potential	Newtonian, Maxwell	magnetic field	Time periodic pressure driven	Evaluated streaming potential, velocity, and EKEC efficiency.	[221,284]
Streaming potential	Maxwell, Oldroyd-B	No external fields	Transient effects vanished	Evaluated streaming potential, velocity, and EKEC efficiency.	[139,239]
Electroosmotic	Newtonian	External electric and magnetic fields	Unsteady and steady	Evaluated transient velocity and steady temperature, Nusselt number, entropy generation.	[285]
Electroosmotic	Oldroyd-B	External electric and magnetic fields	Unsteady	Evaluated transient velocity and steady temperature, Nusselt number.	[132]
Electroosmotic	Maxwell	No external fields	Unsteady	Evaluated transient velocity.	[128,286,287]

2.7.1. Identified Research Gaps in Maxwell Fluid flow

Recent research has invented innovative approaches to improve microchannel streaming potential flow and EKEC efficiency. However, those studies have mainly focused on steady-state flow conditions and Newtonian fluids, neglecting Hall current and ion slip in microchannels. Newtonian models also cannot describe non-Newtonian fluids used daily, such as biofluids, long-chain molecules, etc. Additionally, although some studies have examined unsteady electroosmotic flow for

Newtonian fluids and viscoelastic fluids, they have either neglected the streaming potential effect or assumed streaming potential for time-periodic oscillating flow when transient effects die out. Therefore, studies with transient behavior provide information on the actual flow velocity and EKEC efficiency in microchannels in real-world applications, especially for viscoelastic Maxwell fluids with slip-dependent zeta potential. However, existing studies have already focused on the steady-state temperature distribution and the effect of streaming potential for Newtonian fluids. The intricate structure of porous media, with diverse pore sizes and geometries, requires careful consideration for accurately determining thermal conductivity, accounting for grain size distribution, and finite area contact. This is crucial, especially regarding the solid-to-fluid thermal conductivity ratio, as it examines the combined impact of nanofluids and porous media on microchannel heat transfer. Nevertheless, more work is necessary on the effects of relaxation time on heat transfer during transient states, particularly near initial and short time under jump boundary conditions.

2.8. Time periodic EMHD flow of Oldroyd-B fluid model in microfluidic domains

Microfluidics drives advancements in Micro-total Analysis Systems (μTAS) and lab-on-a-chip (LOC) devices, with applications in microvalves [288], biochips [289], micropumps [290], environmental monitoring [291], energy harvesting [292], chemical separation [293], and biomedical diagnostics [294], to name a few. Flow regulation uses pressure gradients [295], concentration gradient [296], external magnetic field [220], external electromagnetic fields [67], and their innovative combinations. In electrolyte-filled microchannels, an electrical double layer (EDL) forms at charged surfaces. Pressure differences drive flow generating an electric current and a streaming potential which induces an opposing electroosmotic force that reduces flow rate. This effect known as the electroviscous effect mimics higher fluid viscosity [297]. Newtonian and viscoelastic fluids exhibit distinct flow behaviors, with viscoelastic fluids in biological systems [298], polymer solutions [299], and colloidal suspensions [300], causing instabilities in microdevices due to the interaction of elastic and viscous forces. Gong et al. [301] studied electroviscous forces in Newtonian fluids at low zeta potential, while Buren et al. [302] extended this to high zeta potentials in parallel-plate microchannels. EMHD micropumps use Lorentz forces to propel conductive liquids through microchannels, offering precise control [67]. Liu and Jian [303] demonstrated that flow-induced electrical potential and charge-induced viscous phenomena intensify with higher hydrodynamic slip coefficients, exhibiting reduced prominence in Newtonian fluids relative to Maxwell fluids.

The rapid industrialization and heavy reliance on fossil fuels have significantly increased greenhouse gas emissions, raising concerns about climate change and environmental degradation [304]. Electrokinetic energy conversion (EKEC) efficiently transforms hydrodynamic energy into electricity via streaming currents, offering a scalable and sustainable alternative [305,306]. Microfluidic systems leveraging electrokinetic have gained traction for next-generation energy conversion, with applications in MEMS, self-powered sensors, and portable power

sources. Xie et al. [305] found that pressure-dependent viscosity reduces EKEC efficiency, while Liu et al. [307] demonstrated that boundary slip enhances output power and efficiency, achieving 2.7 pW and 30%, respectively. Berli [269] showed improved efficiency in polymer-based power-law fluids. Gillespie [308] suggested that large ion arrangements in nanofluidic channels could enable over 50% efficiency. Jian et al. [239] reported a 25% efficiency for Maxwell fluids in time-periodic flow through soft nanochannels. Ding et al. [139] observed a 19% efficiency increase in Oldroyd-B fluids at resonance frequency compared to Newtonian fluids.

Fluid flow is crucial for efficient solute transport in microfluidic systems, ensuring precise dispersion, mass flow rate regulation, and separation process effectiveness. Taylor's [203] longitudinal dispersion equation and Aris's [204] mathematical formulation describe how solute bands broaden due to hydrodynamic dispersion. This affects mass transfer, fluid mixing, and separation in microfluidic devices for tasks like sample preparation, reactions, and chemical processes. Peralta et al. [193] explored electroosmotic flow in Maxwell fluid to enhance mixing and separation in a micro-annulus. Mederos et al. [216] mass transport in a microcapillary with a reactive wall, where oscillatory electroosmotic flow of a Jeffreys fluid moved an electroneutral solute between reservoirs of differing concentrations.

Fluid maldistribution in microchannels hampers heat exchanger efficiency and leads to uneven thermal performance [25]. Nanofluids particularly Fe_3O_4 based offer enhanced heat transfer benefiting applications in cooling systems drug delivery and magnetic cell separation [26,309]. The integration of MEMS technology enables precise fluid control advancing industries such as computing aerospace, nuclear energy, and hybrid vehicle [272]. Studies on Joule heating and viscous dissipation in Newtonian fluid microchannels highlight the role of electroviscous effects in boosting heat transfer [53,310]. Govindarajulu and Reddy [311] explored the MHD pulsating flow of a third-grade hybrid nanofluid in a rectangular channel, incorporating the effects of thermal radiation while disregarding electrokinetic influences.

Energy loss is a key concern in practical applications, aiming to maintain quality while minimizing energy destruction, as per the second law of thermodynamics [312]. Entropy production distribution is vital in systems like solar collectors, heat exchangers, pumps, and microelectronic cooling [313]. Key causes of entropy generation include thermal gradients, fluid friction, flow driving forces, and ohmic losses in microfluidic devices [285]. Bejan [314] developed a framework for entropy minimization in thermal design, crucial for energy optimization and assessing irreversibility. Mieczkowski et al. [315] optimized a microscale thermal management system through entropy minimization using evolutionary optimization strategies. Table 2 presents key studies on electrokinetic flow in microchannels, highlighting significant findings for Newtonian, Maxwell, and Oldroyd-B fluids.

Table 2
Summary of some important literatures

Flow Mechanism	Types of Fluid	Flow Actuation	State of Flow	Main findings of the Studied	Refs.
Streaming potential	Maxwell, Oldroyd-B	No External fields	Time periodic	Evaluated velocity, and mass transport.	[91,182, 316–318]
Streaming potential	Newtonian	Electro-magnetic field	Steady state	Evaluated streaming potential, velocity, and EKEC efficiency.	[135]
Electroosmotic	Newtonian	No external fields	Time periodic	Evaluated velocity, and mass transport.	[198,199 ,319]
Streaming potential	Newtonian, power Law, Couple stress	Electromagne tic field	Steady/unst eady	Evaluated streaming potential, velocity, and Nusselt number.	[113,243 ,320,321]
Electroosmotic	Newtonian	Electromagne tic field	Steady state	Evaluated streaming, thermal field, Nusselt number and irreversibility metrics.	[283]
Streaming potential	Newtonian	No external fields	Steady state	Evaluated transient velocity, thermal field, convective heat and irreversibility metrics.	[244]
Without Electrokinetic	Maxwell	No external fields	Time periodic	Analysed flow, thermal field, convective heat and irreversibility metrics.	[322]

2.8.1. Identified research gaps in time-periodic EMHD flow

Integrated microfluidic devices enable precise manipulation of ultra-low fluid volumes (nanoliters to picoliters), with applications spanning medical diagnostics, pharmaceutical development, environmental sensing, and tailored healthcare solutions. Prior research has predominantly analyzed oscillatory electroosmotic flow to characterize velocity and solute distribution profiles, incorporating slip velocity, thermal discontinuity constraints, and electromagnetic field interactions. However, these investigations prioritized Newtonian fluid

dynamics under electroviscous conditions, omitting external electromagnetic forces in momentum conservation frameworks. Notably, a scarcity of research exists on thermal and mass transport phenomena in oscillatory streaming potential-driven flows mediated by field-induced viscous interactions.

2.9. Ion-selective membrane desalination in electroosmotic environments within nanochannels

Access to freshwater is essential for human survival and socioeconomic development. However, the growing global population, coupled with climate change-induced water scarcity, has intensified the pressure on traditional freshwater sources [323]. Two-thirds of humanity (4 billion people) annually endure severe water scarcity for at least one month, with nearly half this population concentrated in China and India [324]. In certain coastal areas, freshwater resources are extremely scarce, necessitating the extraction of significant amounts of freshwater from saline sources or even treated waste-water [325,326]. Across the world, more than two billion people still lack access to safe drinking water, creating serious risks to public health, community well-being, and economic development [327,328]. Each year, around 485,000 deaths are linked to waterborne illnesses such as cholera and diarrhea, highlighting the pressing need to improve water safety and sanitation infrastructure globally [329]. Existing studies indicate that readily accessible freshwater resources comprise only about 2.5% of the world's total water, with significant reserves located in specific regions such as Canada, Siberia, Alaska, and Far East [330]. As the demand for freshwater continues to rise, it has become increasingly clear that new and reliable water sources are needed. One promising approach is desalination, which removes salt and other impurities from seawater or brackish water to produce clean, usable water. In recent years, desalination has gained growing attention as a practical way to help ease global water shortages [331].

In response, technologies like reverse osmosis, electrodialysis, and ion-exchange resins have been developed to treat seawater and brackish water, with the optimal choice hinging on feed water quality, energy use, and economic viability [332]. Although these conventional desalination methods each have their own advantages, they often face persistent challenges such as high energy consumption, environmental impacts, and cost inefficiency [325]. Reported efficiencies for multi-stage flash (MSF), multi-effect distillation (MED), reverse osmosis (RO), and electrodialysis (ED) are approximately 44.4%, 8.4%, 41.1%, and 6.1%, respectively [331]. Similarly, reverse osmosis [333,334], another widely used desalination method, although more energy-efficient, still demands significant energy inputs and is susceptible to fouling, leading to decreased efficiency and increased operational costs [333,335,336]. Reverse osmosis (RO) is a leading membrane-based desalination process. Its present energy demand is about 3 kWh/m^3, approaching the theoretical limit of 1 kWh/m^3 for seawater containing 35 g/kg salt at 50% recovery [333].

In response to these shortcomings, researchers have been exploring innovative desalination technologies that offer improved energy efficiency, reduced

environmental impact, and lower operational costs. One promising approach involves the use of nanochannel arrays, which leverage nanotechnology to enhance desalination processes. By manipulating the behaviour of water molecules at the nano scale, nanochannel arrays have the potential to revolutionize desalination technology, making it more sustainable and economically viable [337,338]. Innovative water purification techniques utilizing advanced physical principles remain central to addressing global freshwater scarcity, with ion-selective concentration polarization (ICP) emerging as a cutting-edge approach [338,339]. When a solid membrane comes into contact with a solution, it usually becomes electrically charged. This charge attracts ions with the opposite sign and repels ions with the same sign. As a result, an electric double layer (EDL) forms near the surface, and the collected charge can be used to produce electricity. At the micro and nano scale, membranes show unique ion transport behavior compared to large-scale systems [91]. The electrokinetic desalination process is governed by a sequence of interlinked phenomena that occur within nanoarray located at the centre of the nanochannel. Inside each of the nanoscale channels, the negatively charged walls and EDL along their surfaces where channel height is comparable to the Debye length, the EDLs from opposite walls overlap, filling most of the nanochannel cross-section with counter-ions while excluding co-ions [340]. This EDL overlap imparts strong cation selectivity to each nanochannel array, allowing mainly positively charged ions to pass through. As an electric field is applied across the system, this selective ion movement produces ion-selective transport through the nanoarray, where cations migrate easily while anions are largely blocked. The imbalance in ion flux across the selective nanoarray gives rise to ion concentration polarization (ICP) at its interfaces [341]. Near the upstream (anodic) side of the array, ions are removed faster than they are replenished, forming an ion-depleted region with significantly reduced salt concentration. On the downstream (cathodic) side, ions accumulate, creating an ion-enriched region with elevated salinity [342]. These depletion and enrichment zones extend into the adjacent portions of the nanochannel, influencing the local electric field and electroosmotic flow patterns. The depleted zone effectively acts as a desalinated region, where the ionic concentration is greatly reduced, while the enriched zone corresponds to the brine region containing concentrated ions [343–345]. Together, these coupled electrokinetic effects EDL overlap, ion-selective transport, and ICP constitute the fundamental physical mechanism of electrokinetic desalination in the negatively charged nanoarray system. The significant difference between ion concentrations on two sides of an ISM gives rise to the ion concentration polarization (ICP) phenomenon [346].

An electric field is applied across the horizonal nanochannel. Both reservoirs contain 0.1 M KCl, and the nanochannel has a negative surface charge (σ_{surf} = -0.6 C/m^2) to favour K^+ ion transport. A voltage of 5-170 V is applied across the reservoirs. The observed over-limiting current results from an increased Cl^- concentration inside the nanochannel, which enhances ionic conductivity [347]. Selective ion-exchange membranes have found extensive use across a range of applications, such as such as electro membrane processes, biomolecular separation, biosensing, and fuel cells [348–350]. Experimentally reported that the formation of strong convective vortices

on the depletion side of a nanochannel shortens the electroneutral diffusion boundary layer (DBL). This reduction in DBL thickness causes the transition from the limiting to the over-limiting resistance region [351]. An array of five nanochannels embedded within a horizontal microchannel was analysed, where the distance between neighbouring channels was varied to adjust the level of interaction. Larger spacing between channels resulted in stronger current intensification, while at higher voltages, electro-convective effects dominated and limited the interaction by suppressing diffusion layer growth [352]. A numerical simulation was performed to analyze the behavior of a U-shaped seven-nanochannel array microsystem. The study examined how external voltage and pressure influence key performance parameters such as current, maximum electric field, shear stress, and flow velocity [343]. The Poisson-Nernst-Planck (PNP) and Navier-Stokes equations were employed in a numerical simulation using a five-nanochannel array model embedded in a horizontal nanochannel to predict ion concentration, electric potential distribution, and energy consumption rate [23]. Desalination through overlapping electric double layers (EDLs) achieves the lowest power consumption of 1.2 kWh/m³ while delivering the highest desalination rate of up to 9.72 mL/min·cm², corresponding to 14 km³/day for a 1 cm² membrane area [331]. The permselective properties of ion-selective membranes have been applied to vertical nanochannels containing 10 arrays under an applied electric field. While they analyzed the velocity and concentration distributions of KCl, the economic feasibility of the system was not addressed [342].

A detailed techno-economic analysis is carried out in this study to assess the economic feasibility of using ion concentration polarization (ICP) for seawater desalination. ICP desalination offers the advantage of easily achieving partial desalination, a feature it shares with electrodialysis [353]. The minimum levelized cost of water is $25.9, $20.5, and $16.4 per m³ for concentrations of 10, 25, and 40 g/kg, respectively. A salt removal efficiency of 98.95% and an average flow velocity of 0.56 mm/s were achieved using a five-nanochannel array under an applied voltage of 0.5 V and a pressure of 100 Pa. The total treatment cost was 2.08 $/m³, making this approach economically competitive with other electro-membrane desalination techniques [23].

2.9.1. Research gaps in desalination process based on ion concentration polarization

The ICP desalination system provides notable benefits for improving sensing and biosensing techniques, advancing desalination technologies, and supporting energy-harvesting applications. Its theoretical principles are especially applicable to arrangements of nano-slots or permselective materials, enabling the study of how spacing between channels affects the overall behavior of the array. This captures the essence of inter-channel interactions in both the Ohmic and limiting current regimes, where transport is primarily driven by electro-diffusion, and electro-convection plays a minimal role. Most studies in the literature have concentrated on desalination using nanochannel arrays under electroosmotic flow, primarily

analysing velocity and concentration profiles within the system. A few works have also considered the effects of electroosmotic slip velocity boundary conditions. So far, research has not explored desalination in vertical nanochannel arrays, such as rectangular and hyperbolic shapes, where both electric fields and pressure gradients drive the flow, and there has been no comparison of how different geometries affect performance. Additionally, the economic feasibility of vertical-channel configurations for producing low-cost desalinated water with minimal electricity consumption remains unexplored.

2.10. Integration of multi-objective optimization, multi-criteria decision-making strategies, and machine learning in lab-on-a-chip technologies

A multi-objective Pareto front approach can balance maximum heat transfer rate and minimum entropy generation, leading to more efficient and sustainable system designs [33]. Rabiee et al. [354] used NSGA-II to optimize the figure of merit and minimize entropy production in a microchannel heat sink. Jangir and Jangir [144] introduced the Non-Dominated Gray Wolf Optimizer Algorithm (NSGWOA) for complex engineering challenges, optimizing fuel costs and emission efficiency. Cheng et al. [355] focused on minimizing thermal resistance and pumping power. Employing the NSGA-II multi-objective optimization algorithm and excluding streaming potential effects. Wang et al. [145] employed NSGA-II to optimize Nusselt number, and pressure loss, and utilized the Technique for Order of Preference by Similarity to Ideal Solution (TOPSIS) to identify the optimal solution. Li et al. [356] introduced the UN-based methane estimation with machine learning and multi-objective optimization, aiming to improve the efficiency and accuracy of global methane concentration mapping.

Recent research increasingly focuses on leveraging artificial intelligence (AI) tools for data analysis due to their simplicity, ease of use, and minimal memory requirements [357]. AI techniques include Artificial Neural Networks (ANN), Support Vector Machines (SVM), Adaptive Neuro-Fuzzy Inference Systems (ANFIS), and Evolutionary Algorithms. ANFIS, a hybrid technique, combines ANN's learning capabilities with Fuzzy Inference Systems (FIS) interpretability, enabling optimized and efficient modeling [358]. By minimizing an error metric, ANFIS maps inputs to outputs effectively [359]. Farahani et al. [360] explored combining jets with porous foam gradients for improved electrical efficiency, using ANFIS and Gaussian Process Regression (GPR) for accurate estimation. Nascimento et al. [361] used NSGA-III to optimize counter-flow plate-fin heat exchangers, achieving 55.4% and 72.3% pressure drop reductions on the hot and cold sides, respectively, validated by

TOPSIS with CFD-generated datasets and ANN, ensuring accuracy and efficiency. Larranaga et al. [362] optimized unrestricted micro-fin geometries to minimize the performance evaluation criterion (PEC) while validating designs with machine learning models for accuracy and reliability. Baghban et al. [363] employed ANN to forecast nanofluid properties. Khan et al. [364] utilized ANN to investigate the electroosmotic flow of nanofluids. Nandagopal et al. [365] explored using advanced neural networks to predict liquid-liquid flow patterns. Naphonet al.

[366,367] applied ANN and ANFIS to study nanofluid flow characteristics under various conditions.

2.10.1. Research gaps in the combined application of multi-objective optimization, TOPSIS, and ML

The existing literature lacks studies on micro-heating/cooling systems designed to simultaneously maximize electroviscous heat transfer and minimize normalized entropy generation in microchannels. Furthermore, the NSGA-II algorithm's potential for optimizing electrokinetic energy conversion (EKEC) efficiency while reducing entropy generation remains unexplored in this context. Notably, no studies have compared multi-objective optimization using a Non-Dominated Gray Wolf Optimizer Algorithm (NSGWOA) and NSGA-II; this study addresses this gap by employing a Pareto-optimal solution to optimize the electroviscous heat transfer rate and entropy production. Current decision-making frameworks, such as TOPSIS, provide only suboptimal solutions, highlighting the need for advanced multi-objective strategies.

A critical gap persists in modeling time-periodic streaming potential flows (e.g., Maxwell and Oldroyd-B fluids) for normalized heat transfer and entropy generation. While ANN predict Nusselt numbers in electroosmotic flows, machine learning methods like ANN and ANFIS have not been applied to analyze thermal irreversibility or entropy dynamics in these non-Newtonian fluids. Additionally, no comparative studies evaluate ANN and ANFIS for improving predictive accuracy in such systems.

Resolving these challenges could redefine thermal control in microfluidic systems, advancing low-energy thermal regulation and thermodynamic efficiency enhancement for integrated microscale diagnostic platforms.

Chapter 3. Thermal transport in EMHD-driven Newtonian electroosmotic flow: second-order slip/jump effects

3.1. Objectives of the chapter

This study investigates heat transport behavior in electroosmotically driven microchannel flows under varying boundary conditions. The hydrodynamic analysis evaluates velocity profiles under hydrodynamic adherence (no-slip), linear slip velocity (first-order), and quadratic slip corrections (second-order) boundary regimes. Concurrently, thermal behavior is assessed for continuity of thermal fields (no-jump), linear temperature discontinuity (first-order), and nonlinear interfacial thermal resistance (second-order), all subjected to constant thermal flux boundary constraints. The governing equations for velocity, temperature, and heat transport are rigorously derived by incorporating pressure, electric, and magnetic forces.
Key phenomena such as viscous dissipation, Joule heating, and thermal radiation are explored to quantify their impact on heat transfer dynamics. Analytical solutions and parametric insights provide a comprehensive framework for understanding microscale flow fundamentals, bridging critical gaps in design optimization. By consolidating these findings, this work advances knowledge in microscale thermal management, offering foundational insights to address emerging challenges in microfluidic devices and energy-efficient systems.

3.2. Mathematical modelling and governing equations

3.2.1. Physical formulation

This study investigates the interplay of pressure-induced electrokinetic flow under electromagnetic fields within a rectangular microscale channel. The geometry comprises two parallel plates (height (2h), width (w) and length (L>>2h, w), enabling an infinite parallel-plate approximation (See Fig. 3.1). A coordinate system is adopted where the y-axis is normal to the channel walls, and the x-axis aligns with the flow direction. Due to symmetry about the y-axis, mathematical analysis is confined to the upper half ($0 \le y \le h$). The dielectric electrolyte (permittivity ε), flows between uniformly charged walls under an axial pressure gradient ($-dp/dx$), an electric field (E_x). A uniform magnetic field (B_y) is oriented orthogonally to the flow direction, while uniform heat flux (q_w) at the walls and an externally applied lateral electric field (E_z) are implemented. The study assumes a small aspect ratio ($w \gg\gg 2h$, $L \gg\gg 2h$, w), enabling the approximation of the microchannel as an infinite parallel-plate system with negligible end effects.

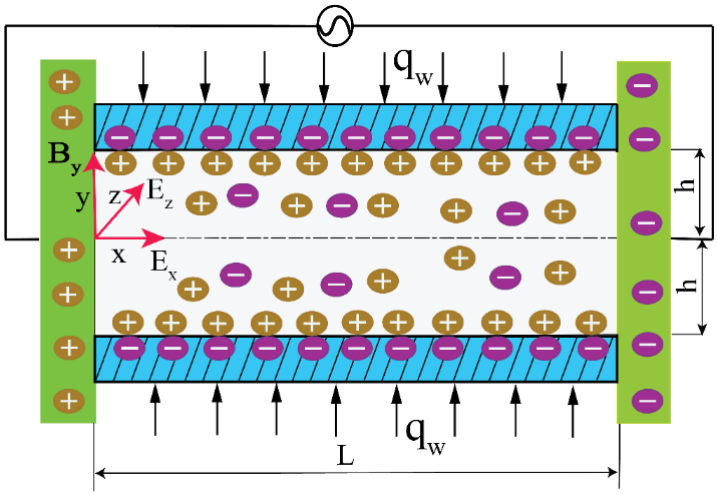

Fig. 3.1 Graphical illustration of a rectangular microchannel.

3.2.2. Determination of EDL potential

Some important assumptions are taken to present a mathematical analysis to establish the steps required for the theoretical estimation:
(i) Streamline, incompressible, and developed flow.
(ii) Constant thermo-physical properties.
(iii) The channel walls satisfy a constant heat flux.
(iv) The mathematical analysis is performed only in the upper half of the channel ($0 \le y \le h$) due to symmetry about the x-axis.
(v) Weak interfacial potentials are imposed to maintain consistency with the linearized electrostatic screening framework, ensuring analytical tractability in resolving EDL phenomena.
(vi) The ion distribution within the electric double layer is governed by the Boltzmann equilibrium model.

The spatial variation of electric potential within the interfacial charge layer is governed by the Poisson equation, which mathematically relates charge density (ρ_e) to electrostatic potential gradients (ψ) [40,41],

$$\nabla^2\psi = -\rho_e/(\varepsilon\,\varepsilon_0) \tag{3.1}$$

One can express ρ_e as,

$$\rho_e = e(z_{v+}n_+ - z_{v-}n_-) \tag{3.2}$$

where $z_{v\pm}$ represents the valency of positively and negatively charged species. $n_{\pm}$ is the symmetric electrolyte having an equal amount of charge valency, where both co-

ions and counter ions have the same charged value. The permittivity of the medium is defined by ε, where ε_0 signifies the vacuum permittivity. The ions are idealized as volume less point charges, and their equilibrium spatial distribution follows the Boltzmann statistics, mathematically expressed as [43],

$$n_{\pm} = n_0 \exp\left(\frac{z_{v\mp} e\psi}{k_B T_a}\right) \tag{3.3}$$

Substituting Eq. (3.3) into Eq. (3.2) gives,

$$\rho_e = -2n_0 z_v e \sinh\left(e\, z_v \psi / k_B T_a\right) \tag{3.4}$$

Combining Eqs. (3.1) and (3.4) yields,

$$\nabla^2 \psi = \left(2n_0 e\, z_v / \varepsilon\, \varepsilon_0\right) \sinh\left(e\, z_v\, \psi / k_B T_a\right) \tag{3.5}$$

Eq. (3.5) exhibits strong nonlinearity. However, in most practical scenarios, the interfacial electrostatic potential remains significantly lower than the thermal potential. Under the linearized low surface potential model, the hyperbolic sine term $\sinh\left(ez_v\psi / k_B T_a\right)$ can be approximated by its argument, simplifying the equation into a linear form $\left(ez_v\psi / k_B T_a\right)$.

The mathematical formulation and material characteristics defining the Debye screening $\left(\lambda_D\right)$ length is presented in Eq. (1.7) and $\left(h/\lambda_D\right)$ characterizes the electrohydrodynamic scaling between the half-channel dimension and the Debye screening length. Eq. (3.5) is reformulated in terms of normalized variables to emphasize its dimensionless structure,

$$d^2\bar{\psi}/dY^2 - \left(K^2/\bar{\xi}\right) \sinh\left(\bar{\psi}\,\bar{\xi}\right) = 0 \tag{3.6}$$

The dimensionless parameters used to express Eq. (3.6) in a dimensionless form are as follows:

$$\bar{\xi} = e\, z_v \xi / k_B T_a \,;\; \bar{\psi} = \psi / \xi \,; \text{ and } \; K = h/\lambda_D \tag{3.7}$$

By applying the Debye-Hückel linearization assumption, Eq. (3.7) simplifies into the following form,

$$d^2\bar{\psi}/dY^2 - K^2\bar{\psi} = 0 \tag{3.8}$$

In microchannel flow, the boundary wall upholds a constant zeta potential. It decreases progressively from the wall towards the center of the channel and reaches a minimum at the channel center. Consequently, the mathematical representations for the boundary conditions of the zeta potential are:

$$\bar{\psi}\big|_{Y=1} = \bar{\xi} \;,\; d\bar{\psi}/dX\big|_{Y=0} = 0 \tag{3.9}$$

Applying the boundary conditions (Eq. 3.9), the dimensionless EDL potential distribution is,

$$\bar{\psi} = \bar{\xi} \cosh\left(KY\right)/\cosh\left(K\right) \tag{3.10}$$

As a result, the local total charge density can be calculated using Eqs. (3.4) and (3.10) in the following manner,

$$\rho_e = -K^2 \frac{\varepsilon\varepsilon_0 \bar{\xi}}{h^2} \frac{\cosh(KY)}{\cosh(K)} \tag{3.11}$$

3.2.3. Velocity field

The fundamental conservation laws for mass and momentum within the fluid domain are expressed in vector notation as [129],

$$\mathrm{div}\,\mathbf{U} = 0 \tag{3.12}$$

and,

$$\rho(\mathbf{U}\cdot\nabla\mathbf{U}) = -\nabla P + \mu\,\nabla^2\mathbf{U} + \mathbf{F} \tag{3.13}$$

where ρ is the fluid density, p is the hydrostatic pressure, dynamic viscosity of the fluid is denoted by μ. The velocity vector is given as, **U**≡(u,0,0), aligned along the axial direction. The electromagnetic body force per unit volume acting on a conducting fluid is governed by the generalized Lorentz force expression as,

$$\mathbf{F} = \mathbf{J}\times\mathbf{B} + \rho_e\mathbf{E} \tag{3.14}$$

The total current density **J** incorporates both Ohmic and convective contributions:

$$\mathbf{J} = \sigma_e\mathbf{E} + \sigma_e(\mathbf{U}\times\mathbf{B}). \tag{3.15}$$

Here, **B** is the magnetic field vector perpendicular to the flow direction. In the present model, the fluid is subjected to an externally applied electric field vector $\mathbf{E} = (E_x, 0, -E_z)$, and a transverse magnetic field $\mathbf{B} = (0, B_y, 0)$. Rewriting Eq. (3.13) in scalar form under the influence of a hydrodynamic electromagnetic field in the x-direction yields,

$$-\frac{dp}{dx} + \mu\frac{d^2u}{dy^2} + \rho_e E_x + \sigma_e E_z B_y - \sigma_e u B_y^2 = 0 \tag{3.16}$$

To address Eq. (3.16), the boundary conditions incorporate second-order velocity slip constraints. Given the symmetrical velocity profile relative to the channel's central axis (Y-axis), the velocity gradient at the central axis vanishes, expressed in non-dimensional form as,

$$\left(U + \bar{a}_1\frac{dU}{dY} - \bar{a}_2\frac{d^2U}{dY^2}\right)\Bigg|_{Y=1} = 0, \left(\frac{dU}{dY}\right)\Bigg|_{Y=0} = 0 \tag{3.17}$$

where $U = u/u_{HS}$, u_{HS} represents the reference electro-osmotic velocity, also known as the Helmholtz-Smoluchowski velocity. Here, $\bar{a}_1 (= a_1/h)$, and

$\bar{a}_2 \left(= a_2/h\right)$ denotes the dimensionless slip length for first order and second order respectively.

Now, Eq. (3.16) is in dimensionless form as follows,

$$\frac{d^2U}{dY^2} - Ha^2U + \Omega Ha + \Gamma + K^2 \frac{\cosh\left(KY\right)}{\cosh\left(K\right)} = 0 \tag{3.18}$$

where, $Ha = hB_y\sqrt{\sigma_e/\mu}$ is the Hartmann number, $\Gamma = h^2\left(-\frac{dp}{dx}\right)\Big/\mu u_{HS}$ is a dimensionless pressure gradient. The transverse electric field magnitude is defined by $\Omega = hB_y\sqrt{\sigma_e/\mu}$. The non-dimensional velocity distribution is then derived by solving Eq. (3.18) using the boundary conditions provided in Eq. (3.17).

$$U = A_1 + A_4\cosh\left(HaY\right) - A_3\cosh\left(KY\right) \tag{3.19}$$

where

$$A_1 = \frac{\left(Ha\Omega + \Gamma\right)}{Ha^2};\ A_2 = \frac{K^2}{\left(K^2 - Ha^2\right)};\ A_3 = \frac{A_2}{\cosh\left(K\right)};$$

$$A_4 = \frac{A_2 - A_1 - A_2K^2\bar{a}_2 + A_3K\bar{a}_1\sinh\left(K\right)}{\cosh\left(Ha\right) + \bar{a}_1Ha\sinh\left(Ha\right) - \bar{a}_2Ha^2\cosh\left(Ha\right)} \tag{3.20}$$

3.2.4. Energy equation and heat transfer

This research investigates heat transfer dynamics in microscale channels under coupled electromagnetic and hydrodynamic interactions for Newtonian fluids. To achieve this, the governing energy conservation equation is employed to model temperature response,

$$\rho c_p u\frac{\partial T}{\partial x} = k_T\left(\frac{\partial^2 T}{\partial x^2} + \frac{\partial^2 T}{\partial y^2}\right) - \frac{\partial q_r}{\partial y} + \mu\left(\frac{\partial u}{\partial y}\right)^2 + j \tag{3.21}$$

The isobaric specific heat capacity $\left(c_p\right)$, local thermal field (T) and volumetric resistive heating rate $\left(j\right)$ define the thermal properties. Dimensionless thermal constraints at walls include a quadratic temperature discontinuity. Owing to symmetry in the temperature profile about the Y-axis, the central boundary condition enforces a vanishing thermal gradient,

$$\left(\theta + \bar{d}_1\frac{d\theta}{dY} - \bar{d}_2\frac{d^2\theta}{dY^2}\right)\Big|_{Y=1} = 0,\ \left(\frac{d\theta}{dY}\right)\Big|_{Y=0} = 0 \tag{3.22}$$

When the flow attains thermal equilibrium (thermally fully developed), the axial temperature gradient becomes invariant, satisfying: This condition can be expressed as $\partial^2 T/\partial x^2 = 0$. Here, $\bar{d}_1 = d_1/h$ and $\bar{d}_2 = d_2/h$ are dimensionless first order jump and second order parameters respectively. The mean velocity across the channel is calculated by averaging the velocity profile over the channel height a, $U_{av} = \frac{1}{h}\int_0^h u dy$

The average velocity, $U_{av} = u_{av}/u_{HS}$ is obtained from Eq. (3.19),

$$U_{av} = A_1 + A_5 \sinh(Ha) - A_6 \sinh(K) \tag{3.23}$$

where, $A_5 = A_4/Ha$ and $A_6 = A_3/K$ (3.24)

The viscous energy dissipation is from of the following expression:

$$a_0 = \int_0^1 (dU/dY)^2 \, dY \tag{3.25}$$

Eq. (3.25) is integrated using Eq. (3.19):

$$\begin{aligned} a_0 &= F_1 \sinh(2Ha) + F_2 \sinh(2K) - F_3 \\ &- F_4 \cosh(K)\sinh(Ha) + F_5 \cosh(Ha)\sinh(K) \end{aligned} \tag{3.26}$$

where

$$F_1 = A_7^2/4Ha;\ F_2 = A_8^2/4K;\ F_3 = \left(A_7^2/2 + A_8^2/2\right);\ F_4 = 2A_7A_8K/\left(K^2 - Ha^2\right);$$
$$F_5 = 2A_7A_8Ha/\left(K^2 - Ha^2\right);\ A_7 = HaA_4;\ A_8 = KA_3 \tag{3.27}$$

The thermal equilibrium analysis for an infinitesimal fluid segment spanning a differential axial length(dy) of the channel is expressed as,

$$\frac{dT_M}{dy} = \frac{\left[q_w(1+Nr) + h\,j + \frac{\mu u_{HS}^2}{h}\int_0^1 \left(\frac{dU}{dY}\right)^2 dY\right]}{\left(h\rho c_p U_{av}\right)} \tag{3.28}$$

where, $Nr = 16T_3^3\sigma_e/3\tilde{k}k_T$ is a dimensionless thermal radiation parameter [67]. The governing physical parameters for thermal radiation phenomena are comprehensively defined within the derived framework in Eq. (1.8). The non-dimensional energy equation can be written from Eqs. (3.21), (3.25), (3.26), and (3.28) in the following form:

$$\frac{d^2\theta}{dY^2} = \frac{U}{U_{av}}\left[1 + \frac{J_h}{(1+Nr)} + \frac{Bra_0}{(1+Nr)}\right] - \frac{J_h}{(1+Nr)} - \frac{Br}{(1+Nr)}\left(\frac{dU}{dY}\right)^2 \tag{3.29}$$

The dimensionless Joule heating coefficient $J_h\,(= jh/q_w)$ characterizes the ratio of ohmic dissipation to the prescribed constant wall heat flux. The Brinkman number

(Br) quantifies viscous energy losses relative to conductive thermal transport. Eq. (3.29) is solved for the dimensionless temperature profile using the boundary conditions defined in Eqs. (3.29) and (3.22).

$$\begin{aligned}\theta &= H_1 Y^2 + H_2\cosh(HaY) - H_3\cosh(KY) - H_4\cosh(2HaY) - H_5\cosh(2KY)\\ &+H_6\sinh(HaY)\sinh(KY) - H_7\cosh(HaY)\cosh(KY)\\ &+H_8\sinh(HaY)\sinh(KY) + C_1\end{aligned} \tag{3.30}$$

where,

$$\begin{aligned}C_1 &= -\bar{a}_1\left(A_{10} + A_{11}\sinh(Ha) - A_{12}\sinh(K) - A_{13}\sinh(2Ha) - A_{14}\sinh(2K)\right.\\ &\left.+A_{15}\sinh(Ha)\cosh(K) - A_{16}\cosh(Ha)\sinh(K)\right)\\ &+\gamma_2\left(A_{10} + A_{17}\cosh(Ha) - A_{18}\cosh(K) - A_{19}\cosh(2Ha) - A_{20}\cosh(2K)\right.\\ &\left.+A_{21}\sinh(Ha)\sinh(K)\right) - H_1 - H_2\cosh(Ha) + H_3\cosh(K)\\ &+H_4\cosh(2Ha) + H_5\cosh(2K) - H_6\sinh(Ha)\sinh(K)\\ &+H_7\cosh(Ha)\cosh(K) - H_8\sinh(Ha)\sinh(K)\end{aligned}$$

where, $A_9 = \dfrac{1+\dfrac{J_h}{1+Nr}+\dfrac{Bra_0}{1+Nr}}{U_{av}}$; $A_{10} = \left(A_1A_9 - \dfrac{J_h}{1+Nr} + \dfrac{F_3Br}{1+Nr}\right)$; $A_{11} = \dfrac{A_9A_4}{Ha}$

$$A_{12} = \frac{A_3A_9}{K};\ A_{13} = \frac{BrA_5^2}{4Ha(1+Nr)};\ A_{14} = \frac{A_6^2Br}{4K(1+Nr)};\ A_{15} = \frac{2A_5A_6KBr}{\left(K^2-Ha^2\right)(1+Nr)};$$

$$A_{16} = \frac{2A_5A_6HaBr}{\left(K^2-Ha^2\right)(1+Nr)};\quad A_{17} = A_{11}Ha;\quad A_{18} = A_{12}K;\quad A_{19} = 2HaA_{13};$$

$$A_{20} = 2KA_{14};\quad A_{21} = KA_{15};\quad A_{22} = HaA_{15};\quad A_{23} = KA_{16};\quad A_{24} = HaA_{16};$$

$$H_1 = \frac{A_1A_9}{2} - \frac{J_h}{2(1+Nr)} + \frac{F_3Br}{2(1+Nr)};\ H_2 = \frac{A_9A_4}{Ha^2};\ H_3 = \frac{A_3A_9}{K^2};$$

$$H_4 = \frac{BrA_5^2}{8(1+Nr)Ha^2};\ H_5 = \frac{BrA_6^2}{8K^2(1+Nr)};\ H_6 = \frac{2A_5A_6K^2Br}{\left(K^2-Ha^2\right)^2(1+Nr)};$$

$$H_7 = \frac{4A_5A_6KBrHa}{\left(K^2-Ha^2\right)^2(1+Nr)};\ H_8 = \frac{2A_5A_6Ha^2Br}{\left(K^2-Ha^2\right)^2(1+Nr)} \tag{3.31}$$

The mean thermal profile across the flow domain is determined by evaluating the integral derived from Eqs. (3.30) and (3.31)

$$\int_0^1 U\theta dY = \frac{A_1H_1}{3} + \frac{A_1H_2}{Ha}\sinh(Ha) - \frac{A_1H_3}{K}\sinh(K) - \frac{A_1H_4}{2Ha}\sinh(2Ha) - \frac{A_1H_5}{2K}\sinh(2K)$$

$$+\left(A_1H_6 + A_1H_8\right)\left[\frac{K}{\left(K^2 - Ha^2\right)}\cosh(K)\sinh(Ha) - \frac{Ha}{\left(K^2 - Ha^2\right)}\cosh(Ha)\sinh(K)\right]$$

$$-\left(A_1H_7 + A_4H_3 + A_3H_2\right)\left[\begin{array}{l}\dfrac{K}{\left(K^2 - Ha^2\right)}\cosh(Ha)\sinh(K) \\ -\dfrac{Ha}{\left(K^2 - Ha^2\right)}\sinh(Ha)\cosh(K)\end{array}\right]$$

$$+A_1C_1 + \frac{A_4H_2}{2}\left[1 + \frac{\sinh(2Ha)}{2Ha}\right]$$

$$+A_4H_1\left[\frac{\sinh(Ha)}{Ha} - \frac{2}{Ha^2}\cosh(Ha) + \frac{2}{Ha^3}\sinh(Ha)\right]$$

$$-A_4H_4\left[\frac{2}{3Ha}\cosh(Ha)\sinh(2Ha) - \frac{1}{3Ha}\sinh(Ha)\cosh(2Ha)\right]$$

$$-\left(A_4H_5 - \frac{A_3H_7}{2}\right)\left[\begin{array}{l}\dfrac{2K}{\left(4K^2 - Ha^2\right)}\cosh(Ha)\sinh(2K) \\ -\dfrac{Ha}{\left(4K^2 - Ha^2\right)}\sinh(Ha)\cosh(2K)\end{array}\right]$$

$$+\left(\frac{A_4H_6}{2} + \frac{A_4H_8}{2}\right)\left[\begin{array}{l}\dfrac{K}{\left(K^2 - 4Ha^2\right)}\sinh(2Ha)\cosh(K) \\ -\dfrac{2Ha}{\left(K^2 - 4Ha^2\right)}\cosh(2Ha)\sinh(K)\end{array}\right]$$

$$-\left(\frac{A_4H_7}{2} - A_3H_4\right)\left[\begin{array}{l}\dfrac{2Ha}{\left(4Ha^2 - K^2\right)}\cosh(K)\sinh(2Ha) \\ -\dfrac{K}{\left(4Ha^2 - K^2\right)}\sinh(K)\cosh(2Ha)\end{array}\right]$$

$$-\frac{A_4H_7}{2K}\sinh(K)+\frac{A_4C_1}{Ha}\sinh(Ha)-A_3H_1\left[\begin{array}{l}\dfrac{\sinh(K)}{K}-\dfrac{2}{K^2}\cosh(K)\\+\dfrac{2}{K^3}\sinh(K)\end{array}\right]$$

$$+\frac{A_3H_3}{2}\left[1+\frac{\sinh(2K)}{2K}\right]+A_3H_5\left[\frac{2}{3K}\cosh(K)\sinh(2K)-\frac{1}{3K}\sinh(K)\cosh(2K)\right]$$

$$-\left(\frac{A_3H_6}{2}+\frac{A_3H_8}{2}\right)\left[\begin{array}{l}\dfrac{Ha}{\left(Ha^2-4K^2\right)}\sinh(2K)\cosh(Ha)\\-\dfrac{2K}{\left(Ha^2-4K^2\right)}\cosh(2K)\sinh(Ha)\end{array}\right]$$

$$+\frac{A_3H_7}{2Ha}\sinh(Ha)-\frac{A_3C_1}{K}\sinh(K) \tag{3.32}$$

The dimensionless bulk-mean temperature is obtained from the following mathematical expression:

$$\theta_m=\int_0^1 U\theta dY\Big/\int_0^1 UdY \tag{3.33}$$

Eq. (3.34) defines the Nusselt number (Nu) using the hydraulic mean diameter as follows

$$Nu=h_cd_h/k_T=-4/\theta_m \tag{3.34}$$

where h_c refers to the coefficient of convective heat exchange. The findings, derived from this study, will be elaborated in subsequent sections to provide comprehensive insights into the role of second-order slip/jump conditions in convective heat transfer. This work bridges a critical gap in non-equilibrium flow modeling and establishes a benchmark for future research in microscale thermal engineering.

3.3. Results and discussion

This investigation performs a systematic review of existing research on microscale fluid dynamics and constructs an exact analytical model to analyse EMHD flow in rectangular microchannels, integrating pressure-driven and electroosmotic mechanisms. The framework calculates dimensionless velocity, temperature distributions, and heat transfer efficiency (Nusselt number) by incorporating second-order boundary conditions for velocity slip and temperature discontinuity. The model also includes energy contributions from viscous friction, electrical resistive heating, and radiative heat transfer. All dimensionless parameters adhere to permissible validated ranges, ensuring relevance to practical microdevice engineering. Variables such as externally applied magnetic fields, transverse electric potentials,

electrokinetic dimensions, and energy dissipation factors are analysed to quantify their impact on flow and thermal performance.

In this work, Ha varies from 0.01 to 0.1 for the permissible EMHD micropumps (10 for the maximum permissible range), h~100 μm, σ_e~10 S/m, the spectrum of applied magnetics flux density (B_y) is 1 to 100T, Ω varies from 0 to 10 (100 for the maximum permissible limit), u_{HS}~100 μms^{-1}, μ~10^{-3} Pa-s, O(E_z)~1 Vm^{-1}, Brinkman number (Br) is 0-0.01, K=5-40, Γ=1, and Nr=0-2 which are taken from the published literature with the physical acceptability [127,129].

3.3.1. Validation and verification

In order to validate the present analysis, Fig. 3.2a is depicted the velocity distribution determined by the present study and the published work [129] with the different magnitudes of Hartman number (Ha), ignoring the electric field, and no-slip boundary conditions i.e., $\bar{\alpha}_1$=0, and $\bar{\alpha}_2$=0. The exact matching of results indicates the correctness of the velocity distribution predicted by the present study. The figure demonstrates that elevated Ha suppress electroosmotic velocity, with higher Ha values correlating to reduced flow magnitudes. It highlights from this figure that, an increase in Hartman number declines the electroosmotic flow velocity.

A numerical validation approach applies the finite difference technique to compute dimensionless velocity and temperature profiles, as well as the Nusselt number, to verify the accuracy of the analytical model under slip boundary effects. Governing Eqs. (3.18) and (3.29) are approximated using a second-order spatial discretization scheme. The discretized system is computationally resolved via a Gauss-Seidel iteration protocol, integrating multiscale slip kinematics and interfacial thermal resistance phenomena. Fig. 3.2b depicts the temperature distribution evaluated by the present analysis and the numerical method based on the finite-difference approach for the pure electroosmotic flow. Here, pressure gradient, transverse electric field, thermal radiation, and viscous dissipation (Γ=0, Ω=0, Nr=0, Br=0) have been considered in no-jump boundary conditions, with a small magnetic field (Ha=0.01) employed to maintain the generality of the analysis. The results determined by Sadeghi and Saidi [127] are also plotted in the same figure for the comparative information. A good agreement of results among the different prediction methods shows the authentication of the present analytical results in rectangular microchannels.

The subsequent sections will explore the outcomes of this investigation, evaluating velocity distributions, thermal gradients, and heat transfer performance under electromagnetic field interactions. These analyses employ experimentally validated ranges of dimensionless flow parameters and incorporate higher-order slip boundary effects, ensuring alignment with microscale flow dynamics. Detailed insights into the interplay of electro-magneto-hydrodynamic forces and slip mechanisms will be presented to advance understanding of non-equilibrium transport phenomena.

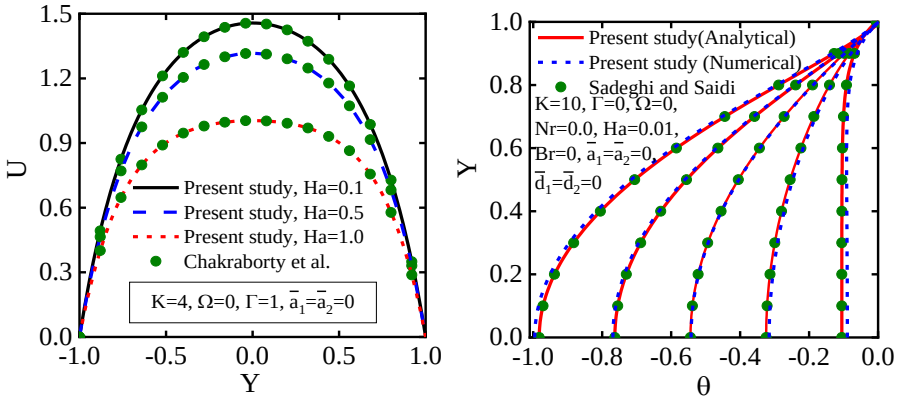

(a) (b)

Fig. 3.2 Validation of the present analysis: (a) velocity distribution determined by present analysis and published work [129], and (b) temperature distribution determined by present analytical and numerical analyses, and published work [127] in microchannels.

3.3.2. Fluid flow of Newtonian fluids

(i) Velocity distribution

Figure 3.3 evaluates the interplay of electromagnetic coupling on velocity distributions across hydrodynamic slip regimes (no-slip, first-order, and second-order slip). At low Ha, Γ modulate velocity via Lorentz force interactions, with peak velocities concentrated along the channel centre-line. Under elevated Ha and second-order slip (Fig. 3.3a), velocity amplification occurs due to intensified electromagnetic contributions. This behavior stems from competing axial pressure gradients, flow-enhancing $\sigma_e E_z B_y$ and flow-impeding $\sigma_e u B_y^2$ components as defined in Eq. (3.16), which collectively dictate velocity morphology. These trends underscore how electromagnetic parameters and interfacial slip govern microscale hydrodynamics, emphasizing non-equilibrium phenomena in advanced fluidic systems.

In high Γ regimes (Γ=10), the dominance of flow-assisting forces boosts bulk velocity, while no-slip conditions (Kn<0.001) anchor flow stagnation at walls due to molecular adhesion. Comparative analysis of slip models reveals distinct behaviours: first-order slip ($\bar{a}_1$=0.12 and $\bar{a}_2$=0) moderately elevates near-wall velocity, whereas second-order slip ($\bar{a}_1$=0.12 and $\bar{a}_2$=0.0048) further enhances flow by accounting for transitional rarefaction effects $0.001 \le Kn \le 0.01$. The Knudsen number (Kn) emerges as a critical factor, governing slip magnitude through molecular mean free path dynamics, higher Kn reduces intermolecular collisions, amplifying wall slip as molecules interact more with boundaries. At Kn=0.08, second-order slip predicts intermediate velocities between no-slip and first-order models under Ha=1, highlighting transitional sensitivity to slip approximations. This

bridging behavior underscores the necessity of higher-order models in capturing nuanced momentum transfer where electromagnetic forces and rarefaction coexist. Enhanced slip conditions (Kn≥0.001) reduce viscous drag, increasing throughput by mitigating wall resistance, while molecular interactions at boundaries create velocity gradients critical for microscale systems as shown in Fig.3.3b. These insights emphasize the role of electromagnetic-thermal coupling, interfacial slip, and molecular rarefaction in optimizing microfluidic design, particularly in applications requiring precise flow control, such as lab-on-a-chip devices or MEMS/NEMS technologies operating near molecular flow regimes.

.

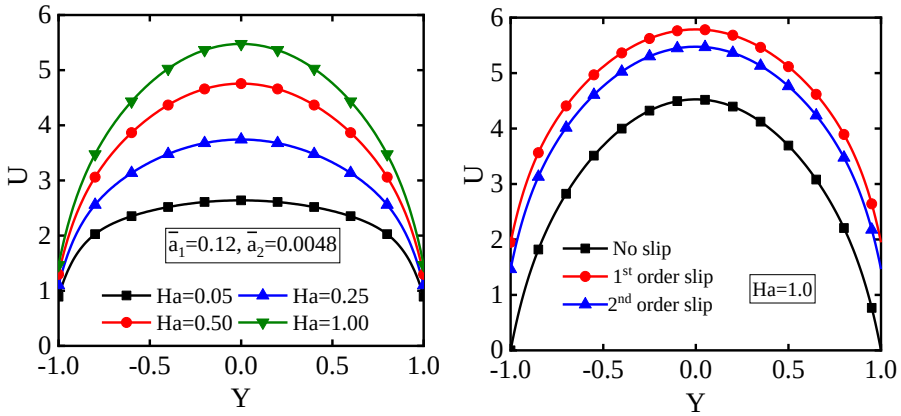

(a) 2nd order-slip

(b) Comparison of no-slip, 1st order, and 2nd order-slips at Ha=1

Fig. 3.3 Velocity profile dependence on hydrodynamic slip regimes in microchannels under fixed parameters (K=10, Ω=10, and Γ=1): (a) 2nd order slip dynamics, and (b) comparative assessment of adherent, linear-shear, and curvature-dependent boundary regimes.

Figure 3.4 examines the velocity profile of an EMHD flow under varying Ω with a focus on hydrodynamic slip effects. Increasing Γ elevates flow velocity significantly, particularly under second-order slip regimes, as shown in Fig. 3.4a. However, at Ω=0, a velocity reduction near the channel center arises due to the absence of lateral electric forces, leaving magnetic damping (Ha) as the primary flow-impeding mechanism. Under no-slip conditions (Fig. 3.4b), minimal molecular rarefaction (Kn≈0) restricts flow near walls, while slip boundaries enhance velocity by reducing viscous drag through near-wall molecular interactions (Knudsen layer effects). Rarefaction effects (Kn) amplify mass flow rates by promoting slip, critical in microscale systems dominated by surface phenomena. Comparative analysis (Fig. 3.4b) confirms that slip boundaries boost throughput by mitigating wall resistance. These insights underscore the interplay of electromagnetic forces, molecular-scale interactions, and boundary conditions in modulating microscale transport, offering pathways to optimize microfluidic systems through parameter tuning for enhanced energy efficiency and mass transfer in applications like lab-on-a-chip devices.

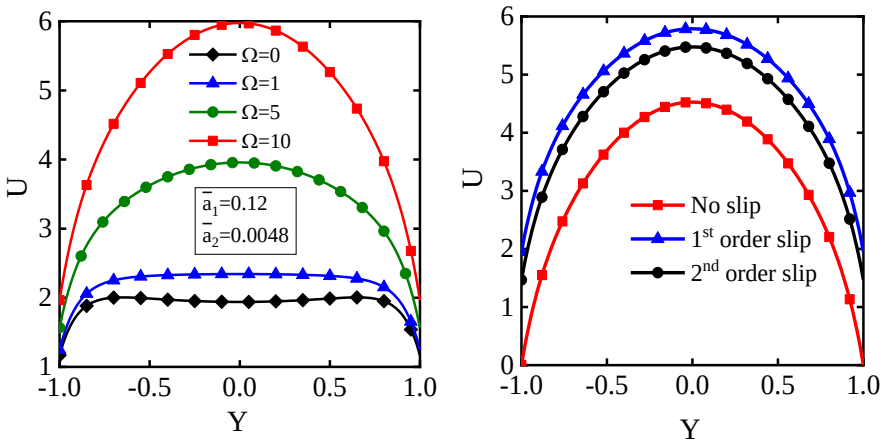

(a) 2nd order-slip

(b) Comparison of no-slip, 1st order, and 2nd order-slips at Ω=10

Fig. 3.4 Influences of on velocity distributions in microchannels for K=10, Ha=1, and Γ=1: (a) 2nd order interfacial dynamics, and (b) comparative assessment of adherent, linear-shear, and curvature-dependent boundary regimes at Ω = 10.

3.3.3. Thermal analysis of Newtonian fluids

(i) Temperature field

Figure 3.5 analyses temperature profiles in microchannels under varying Ha and boundary conditions. For second-order temperature jump (Fig. 3.5a), low Ha without transverse electric fields suppresses flow-aiding forces, leaving only resistive components. Higher Ha reduces velocity (due to electromagnetic resistance) and elevates fluid temperature, as slower advection weakens convective cooling. Dimensionless temperature rises at elevated Ha due to faster reduction in the denominator (scaling term) compared to the numerator (thermal energy).

Temperature gradients intensify slightly under jump conditions versus no-jump cases (Fig. 3.5b), as thermal energy transfer to the fluid increases with boundary discontinuities. These trends highlight how electromagnetic forces and boundary thermal dynamics jointly govern microscale heat transfer.

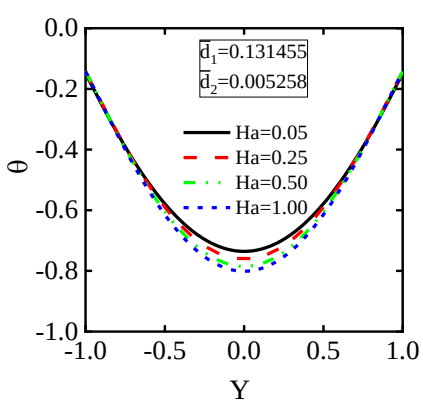

(a) 2nd order jump

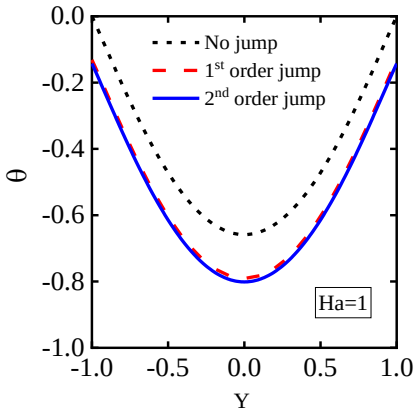

(b) Comparison of no-jump, 1st order-jump, and 2nd order-jump at Ha=1.0

Fig. 3.5 Effects of Hartmann number on temperature distributions in microchannel flow at K=10, **Ω**=0, Br=0.01, J_h=1, Γ=1, Nr=1, $\bar{d}_1$=0.12, and $\bar{d}_2$=0.0048: (a) 2nd order jump, and (b) comparison of no-jump, 1st order jump, and 2nd order jump at Ha = 1.

Figure 3.6 analyse thermal dynamics in microchannels under electromagnetic and rarefied flow regimes with the transverse electric field disabled (**Ω**=0). In this scenario, thermal gradients are governed primarily by magnetic damping (Ha), where elevated Ha (>1) flattens velocity profiles, enhancing conductive heat transfer and reducing temperature gradients across the channel as depicted in Fig.3.6a. At lower Ha (0.05≤Ha≤1), the absence of lateral electric forces results in velocity stagnation near walls (See Fig.3.4a), diminishing advective cooling and elevating local temperatures compared to **Ω**>0 cases. Under no-slip/no-jump conditions (Kn=0.08), symmetric thermal profiles exhibit sharp near-wall gradients due to rarefaction-induced molecular disequilibrium, where sparse fluid-wall collisions limit energy exchange. First and second-order slip conditions ($\bar{d}_1$=0.12, and $\bar{d}_2$ =0.0048) partially mitigate interfacial thermal contrasts, though reduced electromagnetic complexity (**Ω**=0) yields milder stratification than systems with active lateral fields. Elevated Kn (≥0.001) amplifies slip effects, increasing mass flow while moderating temperature disparities in the absence of competing electromagnetic forces as shown in Fig.3.6b. These insights emphasize optimizing Ha and Kn for thermal management in systems prioritizing electromagnetic simplicity, such as lab-on-a-chip devices requiring balanced conductive-advective heat transfer under rarefied, non-equilibrium conditions.

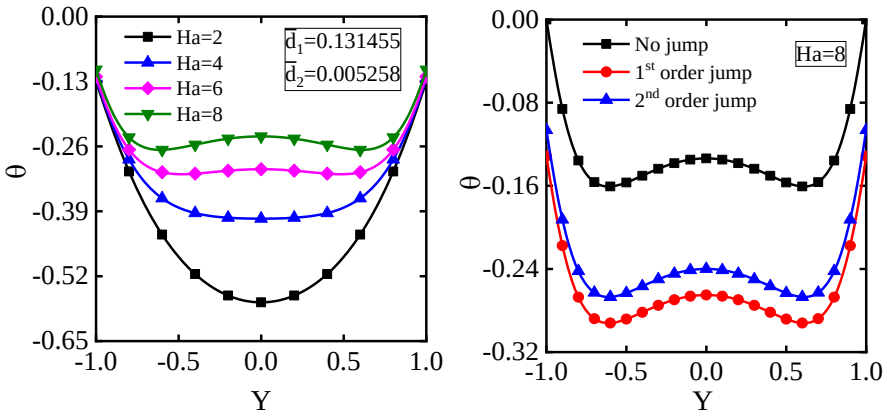

(a) 2nd order-jump

(b) Comparison of no-jump, 1st order-jump, and 2nd order-jump at Ha=8.0

Fig. 3.6 Variation of temperature profiles in microchannels with different Ha at K=10, Ω=0, Br=0.01, J_h=1, Γ=1, Nr=1, $\bar{d}_1$=0.12, and $\bar{d}_2$ =0.0048: (a) 2nd order jump, and (b) comparison of no-jump, 1st order jump, and 2nd order jump at Ha = 8.0.

Figure 3.7 illustrates the normalized temperature profile across the system under varying intensities of Nr). The results highlight the significant influence of radiative heat transfer on temperature distribution patterns. When Joule heating (energy from electrical resistance) and viscous dissipation (heat from fluid friction) are present, increasing the thermal radiation parameter (Nr) correlates with a reduction in normalized temperature values. This trend arises because thermal radiation introduces energy into the fluid, elevating its local temperature. However, the non-dimensional scaling framework used in the analysis accounts for this energy input in a way that inversely relates radiative effects to the normalized temperature metric. Thus, while radiation physically amplifies thermal energy, its representation in the non-dimensional system reflects a balancing mechanism that reduces the scaled temperature parameter. This interplay underscores the importance of radiative heat transfer in modulating thermal behavior under combined electromagnetic and viscous effects.

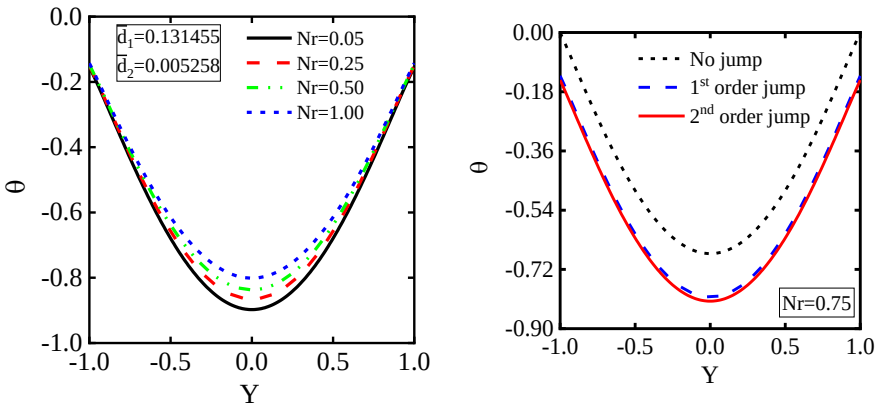

(a) 2nd order-jump

(b) Comparison of no-jump, 1st order-jump, and 2nd order-jump at Nr=0.75

Fig. 3.7 Dependence of thermal profile on Ha in microchannel flow under specified conditions at K=10, Ω=10, Br=0.01, Ha=1, J_h=1, Γ=1, $\bar{\boldsymbol{d}}_1$=0.12, and $\bar{\boldsymbol{d}}_2$ =0.0048: (a) Second-order jump, and (b) comparative analysis of no-jump, 1st order jump, and 2nd order jump at Nr = 0.75.

(ii) Nusselt number estimations for heat transfer

Figure 3.8 examines the dependence of Nu on Ha in transverse electromagnetic environments, evaluated across distinct K values. The trend of these curves for Nu initially declines with Ha, reaches a minimum value at a particular Ha, and after that, it rises with Ha, as displayed in Fig. 3.8a. Therefore, there is a critical Hartmann number (Ha_c) at which Nu becomes a minimum. In other words, Nusselt number distributions with Ha have two distinct regimes based on the critical Ha. At a constant K, the Nusselt number decreases in the first region, whereas a counteractive heat transfer response emerges in the second region. The effect of K always provides a high value of Nu. Nu has also been determined numerically, and these results have been plotted in Fig. 3.8. Additionally, boundary condition comparisons reveal that scenarios without temperature discontinuity (no-jump) achieve the highest Nu, maximizing thermal transfer capacity compared to cases incorporating temperature jump effects (Fig. 3.8b). This underscores the critical influence of boundary conditions on optimizing heat management in electromagnetohydrodynamic systems.

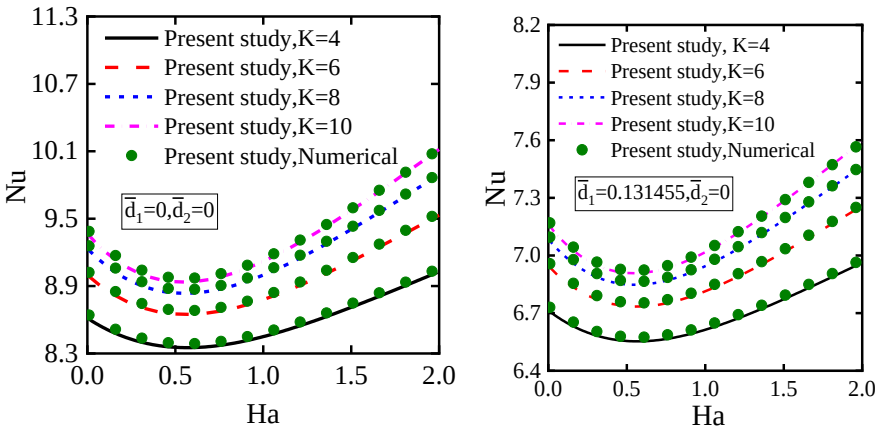

(a) No jump (b) 1st order jump

Fig. 3.8 Influence of magnetic field intensity on thermal performance (Nu) as a function of K under fixed parameters Br=0.01, Ω=3, Γ=1, J_h=1, Nr=0: (a) no jump, and (b) 1st order jump boundary conditions

3.4. Summary and outcomes

This investigation explores EMHD electroosmotic flow in rectangular microchannels through an innovative analytical framework, revealing distinctive behavioural patterns in microscale transport phenomena. The model integrates multiscale interfacial momentum anomalies and thermal discontinuity phenomena, coupled with energy dissipation mechanisms such as viscous friction, electrical resistive heating, and radiative heat transfer. Key findings demonstrate that the Hartmann number (Ha) exerts a pronounced impact on velocity profiles and thermal distributions, irrespective of the presence of transverse electric fields (Ω). At water-repellent interfaces, Ha governs flow regulation by identifying zones of reduced velocity and shear stress.

In scenarios devoid of transverse electric fields, flow velocity escalates incrementally with rising Ha at lower magnitudes. Thermal gradients intensify with increasing Ha up to a threshold of 1, beyond which an inverse relationship emerges. Conversely, under weak transverse electric fields, temperature rises monotonically with Ha. The study further examines rarefaction impacts within rectangular microchannels under second-order slip and temperature jump constraints, revealing that velocity and temperature profiles diverge markedly from those predicted by first-order or no-slip models.

Notably, under transverse electric fields, the Nu exhibits a dependency on Ha, modulated by the parameter K. Below a critical Ha threshold, Nu inversely correlates with Ha; beyond this point, the trend reverses. These revelations enhance the comprehension of thermal transport in EMHD-actuated systems, providing

actionable insights for refining thermal regulation in microfluidic platforms and energy-efficient including miniaturized biomedical or chemical analysis platforms. The analytical approach underscores the interplay between electromagnetic forces, boundary conditions, and energy dissipation, advancing predictive capabilities in non-equilibrium microscale flows.

Chapter 4. Time-periodic electroosmotic flow and mass transfer analysis for Oldroyd-B fluids

4.1. Objectives of the chapter

This study investigates oscillatory electroosmotic flow dynamics in Oldroyd-B viscoelastic fluids under sinusoidal variations of velocity, electric fields, pressure gradients, shear stress, flow rate, and concentration. A computational approach combines finite difference discretization and MATLAB's bvp4c solver to resolve electrical potential distributions without zeta potential constraints. Semi-analytical methods derive oscillatory velocity profiles in parallel-plate microchannels, incorporating slip boundary conditions and zeta potential variations (high/low). The distribution of velocity within the flow field is significantly governed by the surface electrostatic potential, the viscoelastic characteristics of the fluid, and boundary slip phenomena

A key innovation lies in optimizing mass transport of viscoelastic fluids via oscillatory field parameters under tunable zeta potentials at microchannel walls. This strategy enhances mixing and transport efficiency in microscale systems, bridging gaps in understanding viscoelastic fluid behavior under coupled electrokinetic and oscillatory forcing. The methodology and findings offer insights for designing advanced microfluidic devices leveraging time-dependent electromagnetic fields and tailored boundary conditions.

4.2. Physical aspect and mathematical formulation

This research examines oscillatory electroosmotic flow of viscoelastic Oldroyd-B fluids within a parallel-plate microchannel. The setup involves a parallel-plate microchannel, with Fig. 4.1 depicting the geometry and coordinate framework. A Cartesian coordinate system is centred midway between the plates, with the x-axis aligned along the flow direction and the y-axis perpendicular to the plates. The channel's height $2h$ and width w are negligible compared to its length (L), satisfying $L \gg 2h$ and $w \gg 2h$. Symmetry about the x-axis allows analysis to focus on the upper half $(0 \le y \le h)$.The channel contains an incompressible electrolyte with dielectric constant (ε).Channel walls maintain a uniform zeta potential. A time-periodic electric field (E_x), and oscillatory pressure gradient $(-\partial p/\partial x)$ drive fluid motion. The system links two reservoirs with distinct solute concentrations (c_1 and c_2), maintaining identical solute types. The Oldroyd-B constitutive model describes the viscoelastic fluid's stress-strain behavior, capturing nonlinear rheological responses under oscillatory electrokinetic forcing. This framework enables exploration of periodic flow dynamics influenced by viscoelasticity, electric fields, and pressure gradients in microscale geometries.

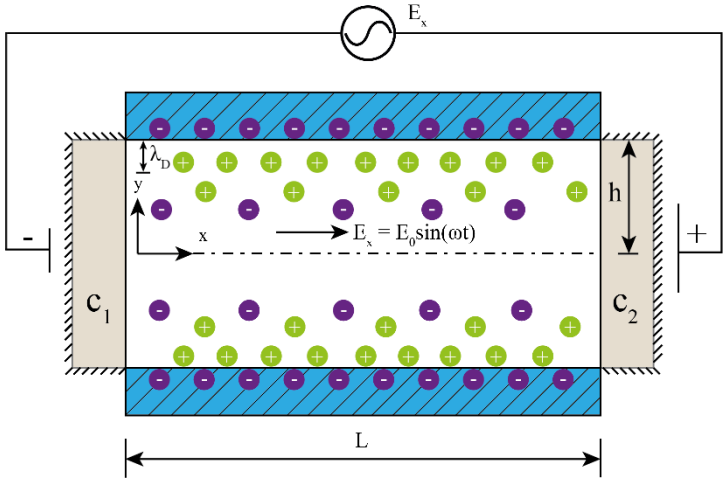

Fig. 4.1 Graphical representation of a parallel-plate fluidic microchannel.

4.2.1. EDL potential

The Poisson-Boltzmann equation determines electrical potential and charge density, balancing electrostatic and ionic diffusion effects by relating potential variations to charge distribution [49]:

$$\nabla^2\psi = -\rho_e/\varepsilon\,,\ \ \rho_e = -2n_0 z_v e \sinh\left(ez_v\psi/k_B T_{av}\right), \tag{4.1}$$

$$Y = y/h\,,\ \text{and}\ \ K = kh \tag{4.2}$$

The symbols are introduced in Eqs. (1.7), while the governing equations are outlined in Eqs. (3.1) -(3.7). By applying the transformation given in Eq. (4.2), Eq. (4.1) can be reformulated in a dimensionless form as follows,

$$\nabla^2\bar{\psi} - K^2 \sinh\left(\bar{\psi}\right) = 0 \tag{4.3}$$

Under the one-dimensional flow assumption, the necessary boundary conditions to solve Equation (4.3) are established as follows:

$$\mathrm{d}\bar{\psi}/\mathrm{dY}\big|_{Y=0} = 0\ ,\ \ \bar{\psi}\big|_{Y=1} = \bar{\xi} \tag{4.4}$$

4.2.2. Velocity distribution

This study analyses a spatially invariant, transient fluid flow, where the governing equations for mass conservation and momentum balance are formulated in a generalized framework,

$$\nabla\cdot\mathbf{U} = 0 \tag{4.5}$$

$$\rho\left(\partial\mathbf{U}/\partial t + \left(\mathbf{U}\cdot\nabla\right)\mathbf{U}\right) = -\nabla p + \nabla\cdot\boldsymbol{\sigma} + \mathbf{F} \tag{4.6}$$

The momentum balance equation for the Oldroyd-B viscoelastic fluid model incorporates rheological adjustments to account for time-dependent stress relaxation and retardation effects, as outlined [186]:

$$\rho\left(\partial\mathbf{U}/\partial t+\left(\mathbf{U}\cdot\nabla\right)\mathbf{U}\right)=-\nabla p+\nabla\cdot\boldsymbol{\sigma}_{\mathbf{1}}+2\mu\left(\lambda_2/\lambda_1\right)\nabla\cdot\mathbf{A}+\mathbf{F} \tag{4.7}$$

Eq. (4.7) is commonly utilized in the analysis of non-Newtonian fluid flow, where $\mathbf{U}$ represents the velocity vector of the viscoelastic fluid. The constitutive parameters λ_1 and λ_2 denote the relaxation and retardation times, respectively, and it is assumed $\lambda_1\geq\lambda_2$. The elastic stress tensor $\boldsymbol{\sigma}_{\mathbf{1}}$ depends on the strain rate tensor, $\mathbf{A}=\left(\nabla\mathbf{U}+\nabla\mathbf{U}^T\right)\big/2$ represents the rate of the strain tensor. The notations $\mathbf{F}$ are introduced in Eq. (3.15). An oscillatory flow by a time-harmonic applied voltage with the electric field, imposed pressure gradient, stress tensor, and volume flow rate becomes a complex form with the following exponential variables:

$$\mathrm{u}=\mathrm{Im}\left(u_0\,e^{i\omega t}\right),\ E_x=\mathrm{Im}\left(E_0\,e^{i\omega t}\right),\ \partial p/\partial x=\mathrm{Im}\left(\left(dp_0/dx\right)e^{i\omega t}\right),$$

$$\sigma_{yx}=\mathrm{Im}\left(\sigma_{yx}^{0}e^{i\omega t}\right),\ \text{and}\ q=\mathrm{Im}\left(q_0e^{i\omega t}\right) \tag{4.8}$$

In this context, Im represents the imaginary component of a complex-valued parameter, t is the time, and i symbolizes an imaginary number. u_0, E_0, $\left(dp_0/dx\right)$, σ_{yx}^{0}, and q_0 are the complex amplitude of velocity, electric field, pressure gradient, shear stress, and volumetric flow rate, respectively. ω is the angular frequency The Oldroyd-B constitutive model characterizes the rheological response of viscoelastic fluids, capturing both elastic and viscous behaviors. For unidirectional flow scenarios, the momentum balance equation specific to this model is expressed as follows [186],

$$\sigma_{yx}+\lambda_1\left(\partial\sigma_{yx}/\partial t\right)=\mu\left(1-\lambda_2/\lambda_1\right)\partial u/\partial y \tag{4.9}$$

where σ_{yx} is the shear stress. Symmetry at the channel center and hydrophobicity-induced Navier slip (slip length a) at the wall are imposed as:

$$du/dy\big|_{y=0}=0,\ \left(u+a\,du/dy\right)\big|_{y=h}=0 \tag{4.10}$$

The normalised parameters and variables used are defined as,

$$U=u/u_{HS}\ ;\ U_0=u_0/u_{HS}\ \ ;\ u_{HS}=-\left(\varepsilon\xi E_0\right)/\mu\ \ ;\tau=\omega t\ ;$$

$$\mathrm{Re}_{\omega}=\left(\rho h^2\omega\right)\big/\mu\ ;\ \bar{a}=a/h\ ;\ \Gamma=\left(-\frac{dp_0}{dx}h^2\right)\Big/\left(\mu u_{HS}\right) \tag{4.11}$$

Here, $\bar{\lambda}_1$ $\left(=\lambda_1\mu/\rho h^2\right)$ quantifies the balance between the fluid's elastic and viscous properties. A simplified form of the governing Eq. (4.7) using Eq. (4.11) can be normalized as,

$$\frac{d^2U_0}{dY^2}-\Upsilon^2U_0+\frac{\Upsilon^2\Gamma}{i\,\mathrm{Re}_\omega}+\frac{\Upsilon^2K^2}{i\,\mathrm{Re}_\omega\,\bar{\xi}}\sinh\left(\bar{\psi}\right)=0 \tag{4.12}$$

where U_0 is the dimensionless complex amplitude of velocity, $\Upsilon\left(=\sqrt{\frac{i\,\mathrm{Re}_\omega(1+i\,\mathrm{Re}_\omega\,\bar{\lambda}_1)}{\left(1+i\,\mathrm{Re}_\omega\,\bar{\lambda}_1\lambda_r\right)}}\right)$ is the dimensionless parameter, and Γ quantifies the relative strength of pressure-driven to electroosmotic driving forces, and Re_ω defined by the oscillatory flow frequency. $\lambda_r=(\lambda_2/\lambda_1)$ defines the retardation time to the relaxation time ratio. For the special case, when $\lambda_r=0$, the Oldroyd-B model becomes the Maxwell model. The dimensionless boundary conditions for Eq. (4.12), derived from Eqs. (4.8), (4.10), and (4.11), are:

$$dU_0/dY\big|_{Y=0}=0\,,\ \left(U_0+\bar{a}\,dU_0/dY\right)\big|_{Y=1}=0 \tag{4.13}$$

The solution of Eq. (4.12) is made with the help of Eqs. (4.8) and (4.13) and can be expressed by applying the complementary function and particular integral methods as,

$$U\left(Y,\tau\right)=\mathrm{Im}\left\{\mathrm{e}^{\mathrm{i}\,\tau}\left(\begin{array}{l}c_0\cosh\left(\Upsilon Y\right)+\dfrac{\Gamma}{i\,\mathrm{Re}_\omega}\\ +\dfrac{K^2\Upsilon}{2i\,\mathrm{Re}_\omega\,\bar{\xi}}\left(e^{-\Upsilon Y}\int_0^Y\sinh\left(\bar{\psi}\right)\mathrm{e}^{\Upsilon Y}\,dY-e^{\Upsilon Y}\int_0^Y\sinh\left(\bar{\psi}\right)\mathrm{e}^{-\Upsilon Y}\,dY\right)\end{array}\right)\right\} \tag{4.14}$$

$$c_0=\frac{\left[A_1\,\mathrm{e}^{\Upsilon}\int_0^1\sinh\left(\bar{\psi}\right)\mathrm{e}^{-\Upsilon Y}\,dY-A_2\,\mathrm{e}^{-\Upsilon}\int_0^1\sinh\left(\bar{\psi}\right)\mathrm{e}^{\Upsilon Y}\,dY\right]}{\left[\cosh\left(\Upsilon\right)+\Upsilon\bar{a}\sinh\left(\Upsilon\right)\right]}$$
$$-\frac{\Gamma}{i\,\mathrm{Re}_\omega\left[\cosh\left(\Upsilon\right)+\Upsilon\bar{a}\sinh\left(\Upsilon\right)\right]} \tag{4.15}$$

$$A_1=\left(K^2\Upsilon\right)\Big/\left(2i\,\mathrm{Re}_\omega\,\bar{\xi}\right)+\left(\Upsilon^2K^2\bar{a}\right)\Big/\left(2i\,\mathrm{Re}_\omega\,\bar{\xi}\right),$$
$$A_2=\left(K^2\Upsilon\right)\Big/\left(2i\,\mathrm{Re}_\omega\,\bar{\xi}\right)-\left(\Upsilon^2K^2\bar{a}\right)\Big/\left(2i\,\mathrm{Re}_\omega\,\bar{\xi}\right) \tag{4.16}$$

The dimensionless flow rate per unit width under time-periodic conditions is calculated from the velocity profile as,

$$Q(\tau)=\frac{q}{2hu_{HS}}=\int_{Y=0}^{1}U\left(Y,\tau\right)dY \tag{4.17}$$

Combining Eqs. (4.14) and (4.17) results,

$$Q(\tau)=\mathrm{Im}\left[e^{i\tau}\left\{\frac{c_0\sinh(\alpha)}{\Upsilon}+\frac{\Gamma}{i\,\mathrm{Re}_\omega}+\frac{K^2\Upsilon}{2i\,\mathrm{Re}_\omega\,\bar{\xi}}\left\{\int_0^1\left(e^{-\Upsilon Y}\int_0^Y\sinh(\bar{\psi})e^{\Upsilon Y}dY-e^{\Upsilon Y}\int_0^Y\sinh(\bar{\psi})e^{-\Upsilon Y}dY\right)dY\right\}\right\}\right] \tag{4.18}$$

4.2.3. Concentration distribution

The solute concentration field $c(x,y,t)$ and molar diffusion coefficient D govern species transport dynamics. Spatial variations in velocity profiles lead to non-uniform solute distributions across the microchannel's cross-sectional area. The framework assumes no reciprocal influence between solute transport and the surrounding electric potential field. The flow behavior is dictated entirely by the carrier electrolyte's hydrodynamic characteristics. Accordingly, the solute concentration profile is governed by the species conservation equation derived in reference [214],

$$\partial c/\partial t+u(\partial c/\partial x)=D\left(\partial^2 c/\partial x^2+\partial^2 c/\partial y^2\right) \tag{4.19}$$

Here, $c(x,y,t)$ is the solute concentration field and D denotes molar diffusion coefficient. The non-uniformity of the velocity distribution causes the concentration of species non-uniform at any cross-section of the parallel plate microchannel. An imposed flow oscillation effect on $c(x,y,t)$, due to the superposition of oscillatory influence of the velocity on the species concentration $c_u(y,t)$ and a linear concentration distribution, known as the Chatwin approximation [199,209], is written mathematically as,

$$c(x,y,t)=c_1+(c_2-c_1)x/L+c_u(y,t) \tag{4.20}$$

Conditions at the boundaries at the channel's two ends i.e., $c(x,\mathrm{y},t)\big|_{x=0}=c_1$ and $c(x,\mathrm{y},t)\big|_{x=L}=c_2$ linked to Eq. (4.20) are not satisfied in the presence of $c_u(y,t)$ .Yet by disregarding the final consequences, it is an adequate approximation because $L\gg h$.

The boundary conditions in the y-direction can be expressed as [65,368],

$$\left[c(x,y,t)+d\partial c(x,y,t)/\partial y\right]_{y=h}=0 \tag{4.21}$$

where *d* is the concentration slip length. After transient effects subsideed, one can stated Eq. (4.19) in the following scaled form for a periodic response by combining Eq. (4.20) and $c_u=\mathrm{Im}\left(c_u^0 e^{i\omega t}\right)$ as,

$$i\,\mathrm{Re}_\omega\,Sc\,C_u^0+\Lambda\,Pe_D\,U_0=d^2C_u^0/dY^2 \tag{4.22}$$

where, diffusive Pèclet number is represented by $Pe_D\left(=u_{HS}h/D\right)$, Schimdt number denoted as, $Sc\left(=\upsilon/D\right)$, the aspect ratio by $\Lambda\left(=h/L\right)$, is the dimensionless imposed flow oscillation effect on the concentration distribution, and C_u^0 is the complex amplitude of convective part of the concentration field produced by the oscillation effect. Eq. (4.22) is treated to the following scaled boundary conditions:

$$dC_u^0/dY\Big|_{Y=0}=0\ ,\ \left[C_u^0+\bar{b}\,C_u^0/dY\right]_{Y=1}=0 \tag{4.23}$$

where, $\bar{b}\ \left(=b/h\right)$ is a normalized mass slip factor.

4.2.4. Tidal displacement

The oscillatory flow is governed by the angular frequency of the additional electric field, which modifies the reference velocity. Consequently, scaled parameters dependent on this velocity exhibit frequency-dependent variation. For this reason, some dimensionless parameters vary as they have been normalized based on the reference velocity. To evaluate bulk mass transport in time periodic flows, the tidal displacement $\left(\Delta z\right)$ serves as a useful metric for comparing overall mass transport under time-dependent conditions. It is defined as the cross-stream averaged maximum axial distance travelled by fluid elements during half a cycle of oscillation [211,212].

$$\Delta z=\left|\frac{1}{h}\int_{y=0}^{h}\int_{t=0}^{\pi/\omega}u\left(y,t\right)dt\,dy\right| \tag{4.24}$$

where $\tau=2\pi/\omega$ is the periodic oscillation. By introducing dimensionless variables, the tidal displacement becomes,

$$\Delta Z=\frac{\Delta z}{h}=\frac{u_{HS}}{h\omega}\left|\int_{Y=0}^{1}\int_{\tau=0}^{\pi}U\,d\tau\,dY\right| \tag{4.25}$$

Equivalently, in terms of the function $U_0\left(Y\right)$, Eq. (4.25) changes to,

$$\Delta Z=\frac{u_{HS}}{h\,\omega}\left|2i\int_{Y=0}^{1}U_0\left(Y\right)dY\right| \tag{4.26}$$

For the flow dependent on the angular frequency, the Péclet number is redefined as,

$$Pe_\omega=\frac{\Delta Z\,Sc\,\mathrm{Re}_\omega}{\mathrm{Im}\left(2i\left\langle U_0\right\rangle\right)} \tag{4.27}$$

where $\langle U_0 \rangle$ denotes the cross-sectional average of the function $U_0(Y)$. Here, it can be noted that the time-averaged mass transport maintains always a fixed value of ΔZ for each flow.

4.2.5. Mass transport rate

The combined effects of convective and diffusive transport of the solute from the high-concentration buffer to the low-concentration buffer within the microchannel determine the net mass transfer throughout a single oscillation cycle. For a single fluctuations period, the circumference of the microchannel and the mass flow rate, summed over time, are calculated as [213,216],

$$m_x = \frac{1}{h}\frac{\omega}{2\pi}\int_{y=0}^{h}\int_{t=0}^{2\pi/\omega} J_x \, dt \, dy \tag{4.28}$$

wherein, J_x is the contemporaneous mass flux caused by diffusive and convective actions in the x-direction.

$$J_x = u(y,t)c(x,y,t) - D\left(\partial c(x,y,t)/\partial x\right) \tag{4.29}$$

The following formula can be used to get the devoid of dimensions mean mass transfer rate for the cyclic electroosmotic flow based on the velocity and concentration distributions:

$$\bar{m}_x = \frac{m_x L}{D(c_1 - c_2)} = 1 - \frac{Pe_\omega}{2\Lambda}\int_{Y=0}^{1} \mathbb{R}\left[U_0(Y)\tilde{C}_u^0(Y)\right]dY \tag{4.30}$$

where $U_0(Y)$ is the function of velocity amplitude, $\tilde{C}_u^0(Y)$ is the complex conjugate of the function of $C_u^0(Y)$ and $\mathbb{R}$ represents the real part of the product of these two functions.

4.3. Numerical scheme

In the current study, the finite-difference approach is devised for estimating the solution of the potential distribution field. Employing the Simpson's 1/3rd law, numerical integrations of Eqs. (4.14), (4.18), and (4.30) assess the semi-analytical outcomes of the time-harmonic distribution of the speed, volumetric liquid flow rate, and mass transfer rate respectively.

A finite-difference code is established to solve Eq. (4.22) with the concentration slip boundary conditions Eq. (4.23). A Tridiagonal matrix algorithm (TDMA) employs to determine all unknowns by solving the algebraic linear system of equations. The concentration is determined by the semi-analytical solution with the time-periodic electroosmotic velocity distribution.

4.4. Results and discussion

This study investigates oscillatory electroosmotic flow of viscoelastic Oldroyd-B fluids in a parallel-plate microchannel with hydrodynamic slip boundary conditions at the walls. The analysis employs a dimensionless framework to generalize the results. The following parameters governing the electroosmotic flow are adopted for quantitative evaluation: $0.1 \leq h \leq 15$ μm, $\rho \sim 10^{3}$ kgm^{-3}, $\lambda_1 \leq 0.01$ s, $\mu \sim 10^{-3}$ Pa-s, $E_0 \leq 10^{5}$ Vm^{-1}, $D \sim 10^{-9}$-10^{-10} m^{2}s^{-1}, $L \sim 10^{-2}$ m, $\varepsilon \sim 10^{-10}$ CV^{-1}m, $25 \leq \xi \leq 200$ mV, and $0.1 \leq \omega \leq 100$ rad s^{-1} [131,190,192,193]. In alignment with prior studies $E_0 \leq 10^{5}$ Vm^{-1} [205,216], Ohmic current effects are neglected in this analysis, eliminating the need to incorporate associated parameters within the energy equation. Consequently, thermal effects are excluded from the investigation. To uphold the validity of the steady-state EDL assumption, the selected relaxation time the λ_1 is constrained to be significantly shorter than the oscillation period $2\pi/\omega$ of the applied electric field. This ensures the product of the electric field frequency and relaxation time (ω) remains below $\bar{\lambda}_1 Re_\omega < 2\pi$ [131,216]. For all the present calculations, we employ $\Delta z=1$, $\Lambda=0.001$, and Sc=1000, as Ramon et al. [205] and Mederos et al. [216] considered.

4.4.1. Validation and verification

MATLAB bvp4c scheme appoints for the numerical results by solving Eq. (4.3). Fig. 4.2 compares the results for the electrical potential determined by the present and Vasista et al. [49] analyses in the case of high zeta potential for the validation purpose. This figure illustrates the accuracy of the present work by showing that the results obtained are in excellent agreement with previously reported findings.

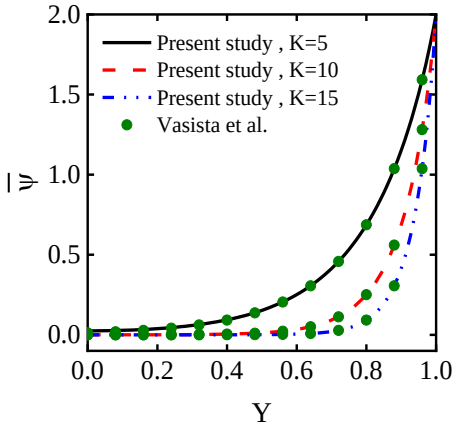

Fig. 4.2 Comparison of normalised electrical potential distribution at $\bar{\xi}=2$ predicted by the present work and Vasista et al [49].

The validation of the present velocity and concentration distributions cannot verify their accuracy directly due to the unavailability of results in the literature. Therefore, we must validate the present study separately for the above flow parameters with

some assumptions. Figs. 4.3a and 4.3b, respectively, compare the current analysis for velocity amplitude with Liu et al. [191] and Liu et al. [131] for the Newtonian and Maxwell fluid. These figures plotted in this study consider a real part of pure electroosmotic flow velocity amplitude for Newtonian and Maxwell fluids as a function of coordinate Y. A maximum deviation of 2.7% is observed compared to Liu et al. [131] at $\bar{\lambda}_1 Re_\omega = 2\pi$. Overall, a good agreement of results finds the appropriate analysis presented under the tested condition.

A comparison of mass transfer plotted in Fig. 4.4 of the current study and those reported by Mederos et al. [216] for a Newtonian fluid shows a piece of validation information. For calculating the mass transfer, non-dimensional parameters participate as $\bar{\xi}=1$, Sc=1000, $\bar{\lambda}_1 Re_\omega=0$, $\Gamma=0$, $\lambda_r=0$, $\bar{a}=0$, and $\bar{b}=0$ The mass transport rate as a proportion of angular Reynolds number is calculated in a Cartesian coordinate and compared with the cylindrical coordinate used in a previous study for qualitatively matching purposes. Again, the trend of results shown is obvious to demonstrate correct predictions.

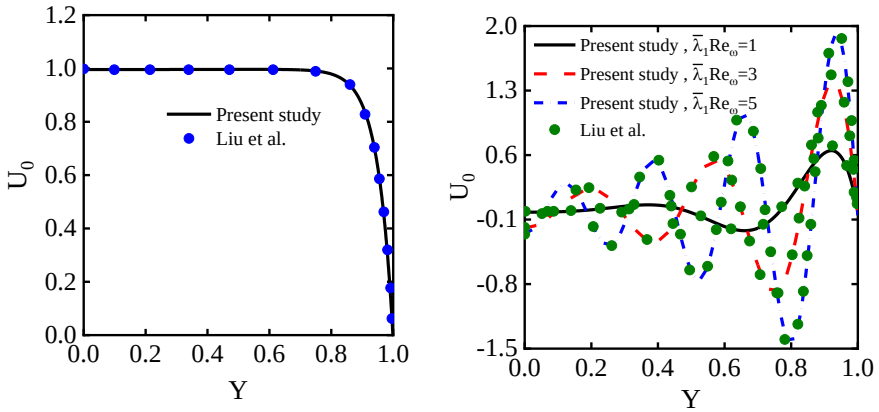

(a) K=20, $\bar{\xi}$=-1, Re_ω=0.1, $\bar{\lambda}_1 Re_\omega$=0, Γ=0

(b) K=20, $\bar{\xi}$=1, Re_ω=100, $\bar{\lambda}_1 Re_\omega=2\pi$, Γ=0

Fig. 4.3 Validation of present study for velocity amplitude at no-slip, $\bar{a}$=0: (a) Newtonian fluid with Liu et al. [191] and (b) Maxwell fluid with Liu et al. [131].

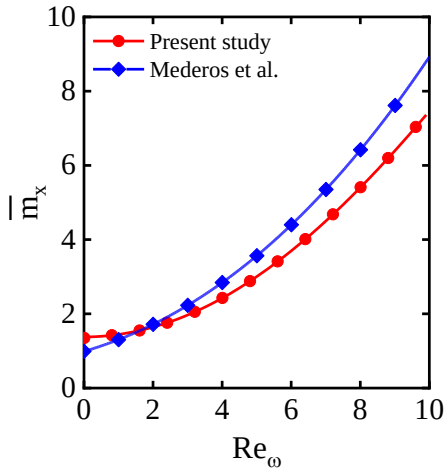

Fig. 4.4 Evaluation of current and Mederos et al. [216] results for mass transfer as function of angular Reynolds (Re_ω) number for Newtonian fluid.

(i) Velocity profile

Figure 4.5 illustrates the velocity profile of a time-periodic, pressure-driven oscillatory electroosmotic flow in an Oldroyd-B fluid under significant zeta potential, plotted as a function of the Y-coordinate. The graphical results demonstrate the effects of relaxation time, zeta potential, retardation time, and time phase on the velocity field. The flow parameters for the fixed values of K=10, Γ=1, $\bar{a}$=0.1, Re_ω=30, $\bar{\xi}$=2, λ_r=0.05, τ=π/2, and different values of $\bar{\lambda}_1$=0, 0.1, 0.15, 0.18, and 0.2 are taken to generate the results. The asymmetric plug-like velocity is observed for a Newtonian fluid, and this influence is a minimum at the center of the channel. For a particular value of λ_r=0.05 and larger values of $\bar{\lambda}_1$, the elastic nature of fluid becomes more pronounced. As the elasticity ($\bar{\lambda}_1$) increases, the velocity profile within the EDL oscillates rapidly rather than at the channel's core The oscillation period remains shorter than the characteristic diffusion time scale, limiting momentum transport to peripheral regions and preventing penetration into the flow's core. As expected, the flow velocity profile restricts only close to the channel walls in the thin EDL zone. It can be noted that the amplitude of velocity for a higher elastic fluid ($\bar{\lambda}_1$=0.18) increases by 18.45%. In the case of the $\bar{\lambda}_1$=0.2, it enhances by 21.01%. These increments are from the reference fluid having $\bar{\lambda}_1$=0.1.

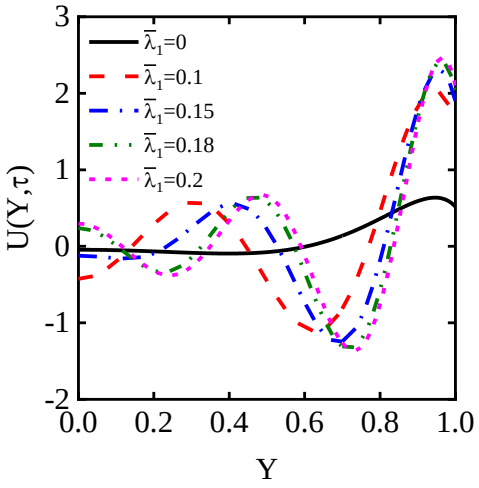

Fig. 4.5 Time-periodic velocity distribution of Oldroyd-B fluid across the channel ($\lambda_r \neq 0$) at slip conditions.

Figure 4.6 illustrates the velocity distribution along the Y axis. The $\bar{\xi}$ physically arises from ion formation within the EDL. Velocity profiles are analysed under varying $\bar{\xi}$ while, holding K=10, Γ=1, and τ=π/2 constant. The potential force close to the walls near the EDL zone is required to improve to increase the value of $\bar{\xi}$. The velocity rises near the microchannel wall and attains a maximum value for viscoelastic fluid. For varying values of $\bar{\xi}$, the peak velocity value moves away from the surface when the time cycle is present. In particular, the slip velocity has increased approximately 142.75% for the zeta potential at $\bar{\xi}$=4 compared with that at $\bar{\xi}$=0.1as illustrated in Fig. 4.6a. The generation of ions in the EDL leads to the activation of the zeta potential $\bar{\xi}$. In other words, Enhanced counterion concentration within the EDL elevates the $\bar{\xi}$. intensifying the electromotive force acting on fluid particles. Near the EDL interface, velocity amplitudes peak due to this amplified driving force. Velocity magnitudes rise proportionally with $\bar{\xi}$, until a critical threshold, beyond which nonlinear deviations emerge (Fig. 4.6a). Fig. 4.6b displays the combined effects of relaxation time, zeta potential, retardation time, and dimensionless physical time on the fluid velocity. Fig. 4.6c analyses the influence of Re_ω on velocity profile. velocity profiles remain nearly uniform throughout the channel at a lower Re_ω, indicating that the momentum diffusion time is shorter than the electric field's oscillatory time. In this situation, there is adequate time for momentum diffusion from the EDL to the centre of the channel. On the other hand, at elevated Re_ω momentum diffusion timescales exceed the oscillation period, resulting in sharp velocity gradients near the walls and heterogeneous axial flow profiles. More significant velocity gradients appear near the wall for the high value of Re_ω. Another parameter for this non-uniformity in velocity profile is elasticity, as already shown in Fig. 4.5. Next, a study is conducted for the velocity profiles for both Maxwell and Oldroyd-B fluids at a fixed value of $\bar{\lambda}_1$. Maxwell fluid's velocity amplitude is larger than Oldroyd-B fluid in the whole flow field. The Maxwell fluid only exhibits the

relaxation time effect, whereas both relaxation and retardation times are present in the Oldroyd-B fluid. Therefore, the elasticity of the Maxwell fluid is a key characteristic; the combined electroosmotic and pressure-driven force is more effective in the Maxwell fluid to increase the velocity amplitude. On the other hand, the velocity profile is more oscillating by applying an external periodic electric field for the Oldroyd-B fluid for λ_r<0.2. From the physical aspect, it is evident that the elastic effect is more outweighs than the viscous impact. Conversely, the conventional viscous effect dominates with the increase in δ value, and the velocity variations behave as a plug-like flow in the whole flow field. Fig. 4.6d investigates the influences of the velocity slip parameter on the flow velocity. An increment trend of the slip velocity occurs when the slip parameter gradually increases at the wall of the channel. Consequently, the slip-modified boundary velocity amplifies the fluid's acceleration gradient near the surface compared to free-slip scenarios. It reveals that the velocity increases gradually with $\bar{a}$ due to the more involvement of the relative motion of molecules at the interface.

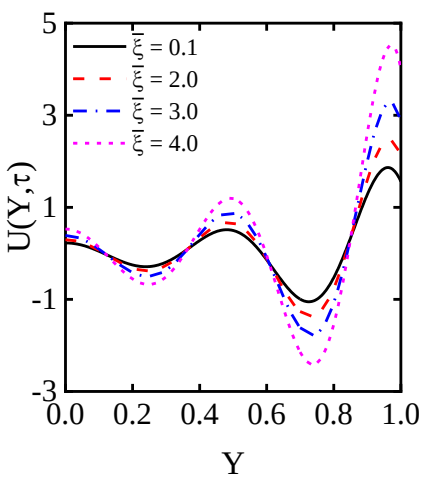

(a) λ_r=0.05, Re_ω=30, $\bar{a}$=0.1

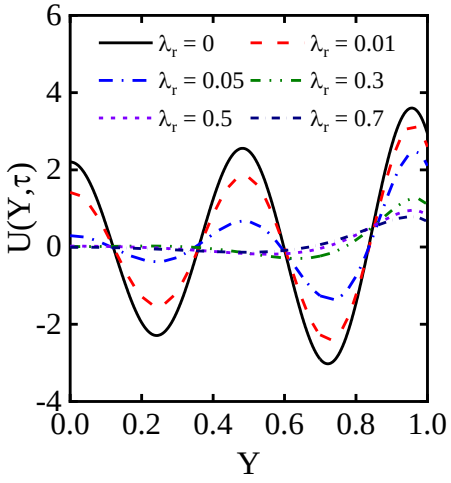

(b) $\bar{\xi}$=2, Re_ω=30, $\bar{a}$=0.1

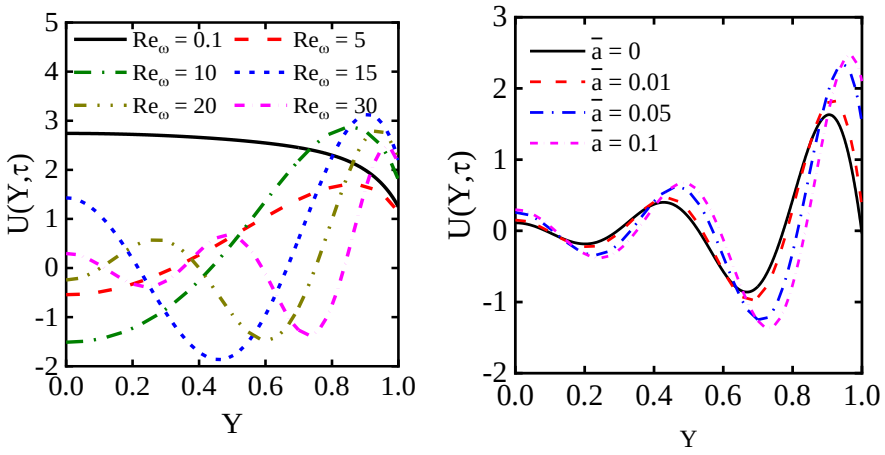

(c) $\bar{\xi}$=2, λ_r=0.05, $\bar{a}$=0.1 (d) $\bar{\xi}$=2, λ_r=0.05, Re_ω=30

Fig. 4.6 Time periodic velocity profile of Oldroyd-B fluid across the channel at slip conditions: (a) variation of $\bar{\xi}$, (b) variation of λ_r (c) variation of Re_ω , and (d) variation of $\bar{a}$.

Finally, an effort has been dedicated to plotting some results to show the importance of the present model. Figure 4.7 highlights the significance of the proposed model by comparing normalized velocity profiles of Oldroyd-B, Maxwell, and Newtonian fluids under fixed parameters K=20, $\bar{\xi}$=2, Γ=1, Re_ω =10, $\bar{\lambda}_1$=0.2, and τ=π/2 with λ_r governing rheological transitions. At λ_r=0, the Oldroyd-B model reduces to a Maxwell fluid, dominated by elastic effects, while approaching Newtonian behavior as $\lambda_r \to 1$, where viscous forces prevail. The analysis validates the framework's versatility, showing precise alignment of Maxwell and Newtonian velocity profiles with theoretical expectations under no-slip conditions, while intermediate Oldroyd-B cases (λ_r=0.05, 0.3) exhibit transitional dynamics as depicted in Fig. 4.7a. Slip effects ($\bar{a} \to 0$) markedly enhance near-wall velocities, amplified further by harmonic pressure gradients, substantial zeta potentials, and viscoelasticity is shown in Fig. 4.7b. Increasing λ_r intensifies viscous retardation, diminishing peak velocities, whereas lower λ_r emphasizes elastic relaxation, augmenting oscillatory responses. Newtonian fluids achieve maximal velocity gradients under no-slip conditions, Maxwell fluids highlight elastic lag, and Oldroyd-B fluids balance both effects, tunable via λ_r. This comparative study underscores the role of viscoelastic parameters and slips boundary in microfluidic transport, offering insights for optimizing non-Newtonian systems in applications requiring tailored flow control.

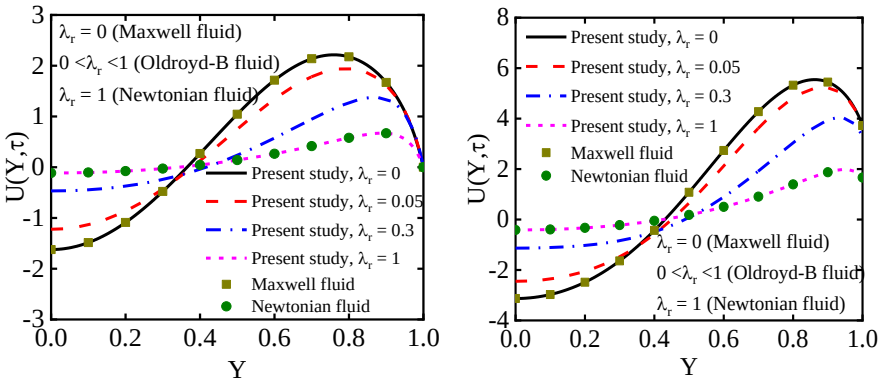

Fig. 4.7 Comparison of normalised velocity profile between Oldroyd-B ($0< \lambda_r<1$), Maxwell, and Newtonian fluids: (a) no-slip boundary conditions, and (b) slip boundary condition.

(ii) Volume flow rate

Figure 4.8 predicts the variations of dimensionless volumetric flow rate in the channel against K, evaluated at fixed values $\Gamma=1$, $\tau=\pi/2$, $\bar{\lambda}_1=0.2$, $Re_\omega=30$, and $\lambda_r=0.05$, for both low and high zeta potentials. With increased *K*, the number of active ions per unit thickness enhances. Therefore, the velocity adjacent to the wall, as well as the flow rate, amplifies. Far away from the EDL, ions are motionless. The increase in the volume flow rate for high zeta potential $\bar{\xi}=2$, 3, and 4 with respect to that for a low zeta potential $\bar{\xi}=0.1$, are 0.95%, 3.08%, and 9.32%, respectively.

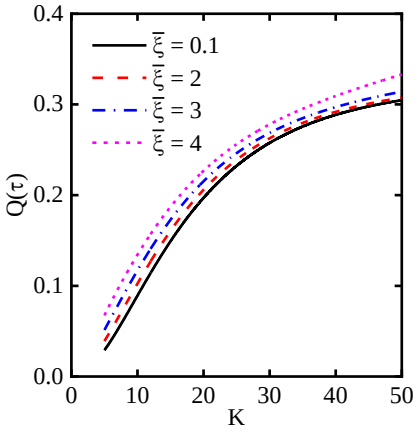

Fig. 4.8 Dimensionless volumetric flow rate under hydrodynamic slip conditions as a function of parameter K, evaluated across varying $\bar{\xi}$.

Figure 4.9 analyses Q vs Re_ω under fixed parameters K=10 K=10, $\bar{\lambda}_1$=0.2, λ_r=0.05, $\tau=\pi/2$, and $\bar{a}$=0.1 for $\bar{\xi}$=2. Here, it can be noted from the relation $\Gamma=(-dp_0/dx)/(\mu u_{HS})$ that, $\Gamma>0$ denotes an assisting pressure gradient (aligned with electroosmotic flow), while $\Gamma<0$ signifies an opposing gradient, respectively. The situation enhances flow oscillation amplitude and wall slip velocity due to synergistic pressure and electrokinetic forces, whereas an adverse pressure gradient $\Gamma<0$ suppresses flow dynamics. Notably, the pure electroosmotic case ($\Gamma=0$) exhibits minimal oscillatory effects, emphasizing the role of unidirectional electrokinetic driving forces. The volume flow rate decreases significantly as the negative pressure gradient is employed. Therefore, the volume flow rate diminishes with an adverse pressure gradient. A nearly flat (constant) volume flow rate occurs for the Oldroyd-B fluid with the increase in Re_ω.

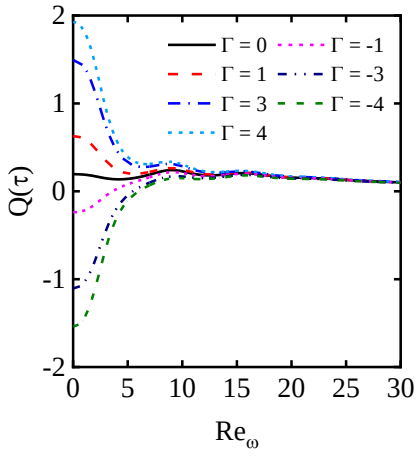

Fig. 4.9 Variation of non-dimensional volumetric flow rate with slip boundary conditions as a function of Re_ω for different values of $\bar{\xi}$.

(iii) Concentration profile

For the influence of sinusoidal pulsations, Fig. 4.10 examines solute concentration profiles along the dimensionless transverse coordinate Y under sinusoidal pulsations, with fixed parameters K=10, Γ=1, λ_r=0.05, Re_ω=30, $\bar{a}$=0.1, and $\bar{b}$=0.1. Significant transverse heterogeneity in solute distribution is observed due to pulsatile flow dynamics. Fig. 4.10a elevated $\bar{\xi}$ enhances concentration gradients, amplifying the periodic oscillations in solute distribution. Near EDL, viscous effects dominate, resulting in pronounced solute accumulation.

Increasing the relaxation $\bar{\lambda}_1$ on the concentration distribution is presented in Fig. 4.10b demonstrates that increasing $\bar{\lambda}_1$. enhances the amplitude of periodic concentration oscillations, a consequence of delayed stress relaxation in viscoelastic fluids. Higher Re_ω localize momentum diffusion near the EDL, limiting transverse dispersion and steepening velocity gradients, which intensify solute advection.

Temporal evolution of concentration profiles (Fig. 4.10c) reveals finite momentum propagation delays from the EDL to the channel core, modulated by viscoelastic memory effects that introduce phase lags in solute redistribution. For micro-mixing applications, viscoelastic fluids at elevated Re_ω exhibit superior oscillatory dispersion ($\tau=\pi/4$), leveraging chaotic advection for enhanced mixing efficiency, a stark contrast to diffusion-dominated Newtonian systems. This interplay of elastic memory, pulsatile dynamics, and electrokinetic forces underscores the potential for optimizing microfluidic devices through tailored viscoelastic working fluids.

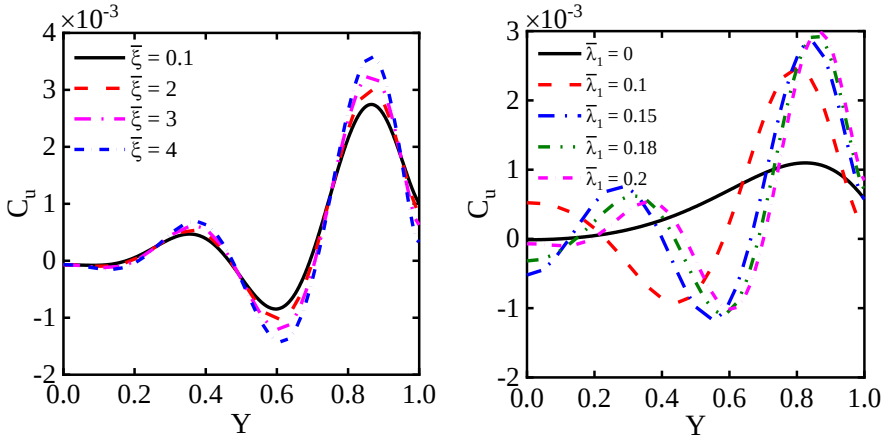

(a) $\bar{\lambda}_1$=0.2, $\tau=\pi/2$ (b) $\bar{\xi}$=2, $\tau=\pi/2$

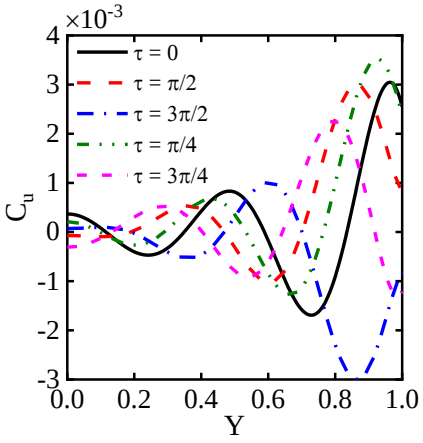

(c) $\bar{\xi}$=2, $\bar{\lambda}_1$=0.2

Fig. 4.10 Oscillatory solute distribution in Oldroyd-B viscoelastic flow with slip-enhanced mass transport: (a) effect of zeta potential $\bar{\xi}$, (b) impact of relaxation parameter $\bar{\lambda}_1$, and (c) time-dependent evolution τ.

(iv) Mass flow rate

Impact of Reω on mass transfer rate in Oldroyd-B fluid across the channel is depicted in Fig. 4.11. The parameter set adopted for mass transfer rate analysis comprises K=50, $\bar{\xi}$=2, and Γ=1. Fig. 4.11a illustrates the dimensionless mass transport of the Oldroyd-B fluid against Re_ω, which serves as a normalized frequency metric, under high zeta potential and no-slip boundary conditions. The cross-over phenomena appear for a combination of physical values of Oldroyd-B fluid. It reveals that the mass flow rate increases with Re_ω and its oscillation increases with an increase in $\bar{\lambda}_1$ due to the uneven flow velocity profiles, as shown in Figs. 4.5 and 4.6c. Fig. 4.11b contrasts the oscillatory-flow-induced mass transfer performance of Maxwell and Oldroyd-B viscoelastic fluids. At low Re_ω, inert solutes exhibit sluggish reaction kinetics, leading to amplified mass flow rates dominated by density-mediated transport phenomena when other system variables remain fixed.

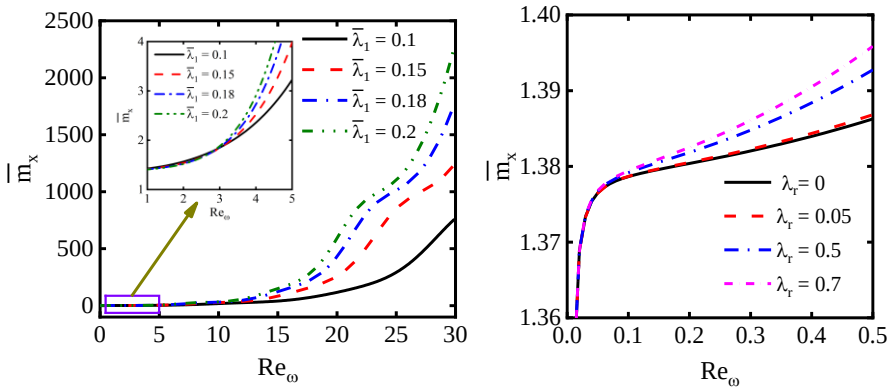

(a) λ_r=0.05 (b) $\bar{\lambda}_1$=0.2

Fig. 4.11 Variation of mass transfer rate across a channel of Oldroyd-B fluid as a function of Re_ω: (a) for different values of $\bar{\lambda}_1$, and (b) for different values of λ_r.

4.5. Summary and outcomes

This work proposes a semi-analytical framework to analyse oscillatory combined electroosmotic-pressure-driven transport of viscoelastic Oldroyd-B fluids in a planar microchannel. The fluid flow occurs at high or low zeta potential fields. The imaginary part of the complex variables provides the fluid velocity and concentration governing equations to a set of nonlinear and nonhomogeneous types. At the peak point, the velocity amplitude for a higher elasticity $\bar{\lambda}_1$=0.18 increases by 18.45% compared to that for a lower elasticity ($\bar{\lambda}_1$=0.1). A comparative analysis of Maxwell and Oldroyd-B fluid velocity profiles under fixed parameter conditions reveals distinct dynamic behaviors. The study highlights a direct correlation between zeta potential magnitudes and spatial amplification of both velocity and concentration amplitudes across the channel.

In contrast, the flow velocity is firmly dependent on viscous and elastic forces. The oscillating flow behavior is more significant for elastic force when the viscous force is an auxiliary influence. However, the viscous force reduces the oscillatory behavior when the elastic force affects secondarily. The flow velocity does not change significantly at the center of the channel, but it increases slowly with the zeta potential.

The peak speed has amplified approximately 142.75% for $\bar{\xi}$=4 with respect to $\bar{\xi}$=0.1. The volume flow rates under high zeta potentials, viz. $\bar{\xi}$=2, 3 and 4, were boosted by 0.95%, 3.08%, and 9.32%, respectively, compared to that under the low zeta potential $\bar{\xi}$=0.1. The concentration magnitude exhibits negligible fluctuations under slip-enhanced mass transport conditions.

Analysis demonstrates that oscillatory electric fields at $\tau=\pi/4$ significantly enhance mixing and dispersion efficiency within the channel. This phenomenon becomes pronounced near the electric double layer (EDL) interface, where high-amplitude electrokinetic forces dominate. Furthermore, angular Reynolds number-dependent resonant modes modulate mass transfer rates and species separation dynamics, reflecting the interplay between oscillatory flow frequencies and viscoelastic stress relaxation. Due to the elastic and viscous properties, the Oldroyd-B fluid's mass transfer rate increases compared to the Maxwell fluid. Finally, the present semi-analytical studies can provide better analysis to study the physical behavior of oscillating charged species of Oldroyd-B fluid in microchannels. A single analysis presented in this study also determines the flow properties of the Maxwell and Newtonian fluids by choosing the appropriate viscoelastic parameter. The comparative results of different fluids will identify a suitable viscoelastic fluid to obtain more mass transfer rate under the same design condition.

Chapter 5. Entropy generation in EMHD driven streaming potential flow: couple stress Casson fluid dynamic analysis

5.1. Objectives of the chapter

This investigation explores EMHD streaming potential dynamics in a planar microchannel using a Casson fluid model that incorporates couple-stress effects. Asymmetric zeta potentials, velocity slip, and thermal discontinuity conditions are imposed at the channel boundaries to simulate interfacial electrokinetic phenomena. Electromagnetic field coupling significantly modulates EKEC efficiency, particularly through slip-modulated zeta potential adjustments. Velocity field characteristics are thermodynamically coupled with temperature distributions through ohmic heating and viscoelastic stress mechanisms. External electromagnetic fields induce Joule heating, creating measurable thermal gradients within the fluid. Counteracting this, intensified thermal radiation along the channel axis elevates localized entropy generation, highlighting the system's energy dissipation mechanisms. The present results show that the couple stress and Casson parameters influence the development of streaming potential, electrokinetic energy conversion (EKEC) efficiency, temperature, Nusselt number, and Bejan number for asymmetric velocity slip and temperature jump circumstances. According to the present results, the EKEC efficiency increases with a slip-dependent zeta potential of couple stress Casson fluid, couple stress fluid, Casson fluid, and Newtonian fluid by 45.92 %, 47.10 %, 42.81 %, and 37.68 %, respectively, compared to that for the slip-independent zeta potential. At the centre of the microchannel for the jump boundary conditions, temperature increases by 2.95 % compared to no jump boundary conditions.

5.2. Physical aspects and mathematical formulations

This work examines the steady, incompressible flow of a rheologically complex fluid (Casson model with couple-stress effects) within a parallel-plate microchannel featuring non-uniform surface charges. The analysis focuses on characterizing interconnected phenomena, including streaming potential generation, EKEC efficiency, hydrodynamic velocity profiles, thermal transport, and entropy production under MHD conditions. A pressure gradient along the axial direction (x-axis) drives the flow. Fig. 5.1 provides a schematic representation of the geometry, where the channel walls are separated by 2h, with width (w) and length (L). The coordinate system aligns the x-axis parallel to the walls and the y-axis perpendicular to them.

The study assumes a small aspect ratio ($w \gg\gg 2h$, $L \gg\gg 2h$, w), enabling the approximation of the microchannel as an infinite parallel-plate system with negligible end effects. Consequently, the two-dimensional electrokinetic flow simplifies to a

one-dimensional formulation dependent solely on the y-coordinate. The microchannel is filled with an incompressible electrolyte solution (permittivity ε) and its hydrophobic walls exhibit asymmetric zeta potentials influenced by ion concentration gradients and interfacial slip lengths. In flow scenarios actuated by pressure differentials, a self-generated streaming potential (E_s) emerges opposing fluid motion, even in the absence of an externally imposed electric field aligned with the fluid's direction. A uniform magnetic field (B_y) is oriented orthogonally to the flow direction, while uniform heat flux (q_w) at the walls and an externally applied lateral electric field (E_z) are implemented. The model assumes spatially separated EDL at the channel boundaries.

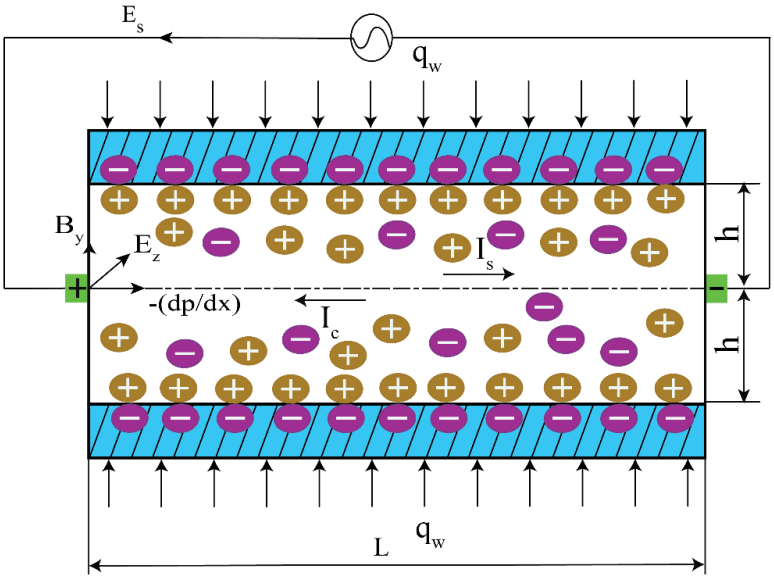

Fig. 5.1 Schematic diagram of a parallel plate microchannel flow.

5.2.1. EDL potential

The mathematical framework outlined in prior sections employs the linearized electrostatics model (low surface potential approximation) to derive the scaled electric potential profile in non-dimensional form,

$$\frac{d^2\bar{\psi}}{dY^2} - K^2\bar{\psi} = 0 \tag{5.1}$$

Normalised variables introduce below for the analysis:

$$\bar{\xi}_1=\frac{\left(e z_v \xi_1\right)}{\left(k_B T_a\right)}\ ,\ \bar{\xi}_2=\frac{\left(e z_v \xi_2\right)}{\left(k_B T_a\right)}\ ,\ Y=\frac{y}{h}\ ,\ K=\frac{h}{\lambda_D} \tag{5.2}$$

The upper and lower channel walls exhibit distinct zeta potentials ξ_1 and ξ_2, respectively. Under the linearized low surface potential model, both potentials are scaled to unity $\left(\bar{\xi}_1=\bar{\xi}_2=1\right)$ corresponding to dimensional values of $\xi_1=\xi_2\approx 25\ mV$. As noted in prior work [138] the simplified electrostatic framework remains applicable for potentials satisfying $\bar{\xi}_{a1}=\bar{\xi}_{a2}\le 2$, aligning with weakly charged surface regimes.

The analysis emphasizes that hydrodynamic slip conditions modulate interfacial potentials at the upper and lower walls due to ion redistribution within the EDL. These normalized potentials, governed by slip effects, are defined as,

$$\bar{\xi}_{a\,1}=\bar{\xi}_1\left[1+\bar{a}_1 K\frac{\sinh\left(\bar{\xi}_1\right)}{\bar{\xi}_1}\right]\text{and}\ \bar{\xi}_{a\,2}=\bar{\xi}_2\left[1+\bar{a}_1' K\frac{\sinh\left(\bar{\xi}_2\right)}{\bar{\xi}_2}\right] \tag{5.3}$$

where $\bar{\xi}_{a1}$ and $\bar{\xi}_{a2}$ are the apparent surface potential at the top and bottom boundaries.

Eq. (5.1) employs the following boundary conditions, derived from the 1D flow model,

$$\bar{\psi}\big|_{Y=1}=\bar{\xi}_{a1}\ \text{ and }\ \bar{\psi}\big|_{Y=-1}=\bar{\xi}_{a2} \tag{5.4}$$

The EDL potential distribution obtained can be written as,

$$\bar{\psi}=A\cosh\left(KY\right)+B\sinh\left(KY\right) \tag{5.5}$$

$$\text{where,}\ A=\frac{\left(\bar{\xi}_{a1}+\bar{\xi}_{a2}\right)}{2\cosh\left(K\right)}\ \text{, and}\ B=\frac{\left(\bar{\xi}_{a1}-\bar{\xi}_{a2}\right)}{2\sinh(K)} \tag{5.6}$$

5.2.2. Velocity distribution

This study employs a steady-state, fully developed flow model for a Casson fluid incorporating couple-stress effects, and generalizes the continuity and Cauchy momentum equations for this flow as [66,228,230],

$$\nabla\cdot\mathbf{U}=0$$

(5.7)

$$\rho\left(\mathbf{U}\cdot\nabla\right)\mathbf{U}=-\nabla p+(1/2)(\nabla\times\rho\mathbf{c})-\mu\left(1+p_y/\mu_B\sqrt{2\pi_c}\right)(\nabla\times\nabla\times\mathbf{U})$$
$$-\eta\left(\nabla\times\nabla\times\nabla\times\nabla\times\mathbf{U}\right)+\left(\upsilon+2\mu\right)\nabla\left(\nabla\cdot\mathbf{U}\right)+\mathbf{F} \tag{5.8}$$

where **U** denote the velocity field, **c** the mass-specific couple , ρ the fluid density, p is the hydrostatic pressure, (υ, μ) are the dynamic viscosity coefficients, and η the couple-stress viscosity. This study neglects the elements of the body couple force.

The Casson fluid model describes the viscoplastic fluid rheological behavior. The rheological model for the unidirectional flow can be described as [228],

$$\tau_{ij} = \begin{cases} 2\left(\mu_B + p_y/\sqrt{2\pi}\right)e_{ij}, & \pi > \pi_c \\ 2\left(\mu_B + p_y/\sqrt{2\pi}\right)e_{ij}, & \pi < \pi_c \end{cases} \tag{5.9}$$

The Casson rheological parameter is expressed as $\beta\left(=\mu_B\frac{\sqrt{2\pi_c}}{p_y}\right)$, where τ_{ij} and e_{ij} correspond to the shear stress and strain rate tensors, respectively. p_y represents the yield stress, π represents the scalar invariant of the strain rate tensor, and π_c signifies its critical threshold for viscoplastic behavior. The parameter μ_B characterizes the plastic viscosity of the non-Newtonian fluid under shear. The volumetric body force $\mathbf{F}$ arising from electromagnetic interactions, incorporates contributions from the Lorentz force and induced electric fields. This electromagnetic body force is defined as [124],

$$\mathbf{F} = \mathbf{J}\times\mathbf{B} + \rho_e\mathbf{E} \tag{5.10}$$

The system incorporates an induced electric field $\mathbf{E}$, and a magnetic flux density $\mathbf{B}$ oriented orthogonally to the flow direction. The current density $\mathbf{J}$,governed by Ohm's law is formulated as [124],

$$\mathbf{J} = \sigma_e\left(\mathbf{U}\times\mathbf{B}\right) + \sigma_e\mathbf{E} \tag{5.11}$$

Here, σ_e presents the electrolyte's electrical conductivity. For laminar flows with axially invariant velocity gradients (i.e., stabilized velocity profiles), the momentum equations governing a Casson fluid with couple-stress effects reduce along the *x*-direction in Cartesian coordinates to:

$$-\frac{dp}{dx} + \mu\left(1+\frac{1}{\beta}\right)\frac{d^2u}{dy^2} - \eta\frac{d^4u}{dy^4} + \rho_e E_s + \sigma_e E_z B_y - \sigma_e u B_y^2 = 0 \tag{5.12}$$

Hydrophobic effects at the channel walls are captured through Navier slip boundary conditions, with unique slip coefficients assigned to the top and bottom surfaces,

$$\left[u + a_1\left(\frac{du}{dy}\right)\right]_{y=h} = 0 \text{ , and } \left[u - a_1'\left(\frac{du}{dy}\right)\right]_{y=-h} = 0 \tag{5.13}$$

where a_1 and a_1' represent the hydrodynamic slip coefficients at the top and bottom channel boundaries, respectively. The dimensionless variables and scaling factors applied to Eq. (5.15) are formulated as:

$$\gamma = h\sqrt{\frac{\mu}{\eta}}\,,\; E = \frac{E_s}{E_{ref}}\,,\; Y = \frac{y}{h}\,,\; u_{ref} = \frac{\left(\varepsilon k_b T_a E_{ref}\right)}{\left(\mu e z_v\right)}\,,\; U = \frac{u}{u_{ref}}\,,\; \Gamma = \frac{h^2\left(-\frac{dp}{dx}\right)}{\left(\mu u_{ref}\right)}\,,$$

$$\Omega = \frac{E_z}{\left(u_{ref} B_y\right)}\;,\; Ha = B_y H\sqrt{\frac{\sigma_e}{\mu}} \tag{5.14}$$

where γ signifies the couple stress parameter, quantifying elastic effects in the fluid. $\bar{E}_s$ denotes the dimensionless streaming potential induced along the x-axis. u_{ref} serves as the reference velocity for normalization., Γ represents the non-dimensional pressure gradient driving the flow, **Ω** corresponds to the dimensionless lateral electric field parameter, Ha (Hartmann number) characterizes the relative influence of the magnetic field on viscous forces. Eq. (5.12) can be simplified using Eq. (5.14) which is in a normalised form as,

$$\frac{d^4U}{dY^4} - \gamma^2\,\Gamma - \gamma^2\left(1+\frac{1}{\beta}\right)\frac{d^2U}{dY^2} + \bar{E}_s\,K^2\,\gamma^2\,\bar{\psi} - \gamma^2\,Ha^2\,\Omega + \gamma^2\,Ha^2\,U = 0 \tag{5.15}$$

This analysis derives three limiting scenarios from the unified framework of Eq. (5.15). Case (I) Casson Fluid Limit, β=1, and γ→∞ ; The model reduces to a standard Casson fluid, eliminating couple-stress effects while retaining viscoplasticity. Case (II) Couple-Stress Fluid Limit, β→∞ and γ=1; the framework simplifies to a couple-stress fluid, preserving elastic stresses but omitting yield-stress behavior. Case (III) Newtonian Fluid Limit, γ→∞ and β→∞, Both viscoplastic and elastic effects vanish, recovering classical Newtonian dynamics. The asymmetrical boundary constraints in dimensionless form, derived from Eq. (5.15), are expressed as,

$$\left[U + \bar{a}_1\left(\frac{dU}{dY}\right)\right]_{Y=1} = 0\;,\; \left[U + \bar{a}_2'\left(\frac{-dU}{dY}\right)\right]_{Y=-1} = 0 \tag{5.16}$$

where $a_1\left(=\frac{a_1}{h}\right)$ and $\bar{a}_1'\left(=\frac{a_1'}{h}\right)$ are the upper and lower walls dimensionless slip parameters, respectively. Eq. (5.16) is solved analytically using Eq. (5.15) to obtain the velocity distribution:

$$U = c_1\cosh\left(m_1 Y\right) + c_2\sinh\left(m_1 Y\right) + c_3\cosh\left(m_2 Y\right) + c_4\sinh\left(m_2 Y\right)$$

$$+\frac{\left(\gamma^2\,\Gamma\right)}{p_2} + \frac{\left(Ha^2\,\Omega\gamma^2\right)}{p_2} - \frac{\bar{E}_s\,K^2\,\gamma^2\left(A\cosh\left(KY\right) + B\sinh\left(KY\right)\right)}{\left(K^4 - p_1K^2 + p_2\right)} \tag{5.17}$$

where, the coefficients p_1, m_1, c_1, p_2, c_2, m_2, c_3, and c_4 are defined in the Appendix A.

5.2.3. Streaming potential and streaming current

Prior studies did not provide closed-form expressions for flow velocity distributions and induced streaming potential characteristics, motivating the development of new formulations in this work. A pressure differential applied across a parallel plate microchannel induces a streaming potential, which drives the net migration of counter ions toward the downstream region of the channel within the electric double layer. This redistribution of ions establishes a downstream electric potential gradient, generating a streaming current that opposes the primary flow velocity. Concurrently, a conductive current emerges from ion migration within both the primary fluid phase and the Stern layer, opposing the flow-driven streaming phenomena. To quantify the streaming potential, the electroneutrality principle is applied, requiring that the total current, comprising streaming, conduction, and Stern layer currents, equals zero under steady state conditions. This balance ensures no net charge accumulation, allowing for the precise determination of the streaming potential magnitude [133].

$I_{net}=I_{sterm}+I_{conduction}+I_{stern}=0$ (5.18)

The electrokinetic system comprises three distinct current contributions: streaming current I_{stream} generated by bulk fluid flow transporting ions within the diffuse double layer. Conduction current $I_{conduction}$ results from ion migration under the influence of an induced electric field in the mobile electrolyte region. Stern layer current I_{stern} originates from immobilized counterions within the Stern layer adjacent to the charged surface and the expressions are given as,

$$I_{stream}=\int_{-h}^{h} ez_v\left(n_+-n_-\right)udy\,,\quad I_{conduction}=\frac{z_v^2e^2E_s\left(n_++n_-\right)}{f}\,,\quad I_{stern}=2\sigma_{stern}E_s \tag{5.19}$$

where $f\left(=\dfrac{2n_0e^2z_v^2}{\sigma_B}\right)$ is the ionic friction factor, under equilibrium conditions, charged particles distribute spatially according to a balance of thermal agitation and electrostatic interactions,

$$n_\pm=n_0\exp\left(\mp\frac{ez_v\psi}{k_BT}\right)\approx n_0\left(1\mp\frac{ez_v\psi}{k_BT_a}\right) \tag{5.20}$$

Using the scaling relationships defined in Eqs. (5.19) and (5.20), the governing equation (Eq. 5.21) is rendered dimensionless as,

$$\int_{-1}^{1}U\bar{\psi}dY-\bar{E}_s\alpha\left(\int_{-1}^{1}dY+2Du\right)=0 \tag{5.21}$$

where $\alpha\left(=\dfrac{\mu\sigma_B}{\left(2\varepsilon n_0k_BT_a\right)}\right)$ is an ionic Péclet number, Du is a Dukhin number.

The non-dimensional streaming potential is written as,

$$\bar{E}_s = \frac{R_1}{R_2 + 2\alpha(1+Du)} \tag{5.22}$$

where R_1 and R_2 are defined in the Appendix B

5.2.4. EKEC efficiency

In microscale conduits subjected to pressure-driven flow, electrokinetic current generation stems from ion displacement within the charge-segregated interfacial region near the channel boundaries. This phenomenon facilitates the transformation of mechanical energy (generated by pressure gradients) into electrical energy through streaming potential and current. The system attains peak power output when operating at 50% of its maximum streaming potential and 50% of its maximum current, balancing electrical generation efficiency. The highest electrokinetic energy conversion efficiency is quantified as the ratio of electrical power output (per unit channel width) to mechanical power input (derived from the pressure gradient). This metric reflects the effectiveness of energy harvesting in microscale systems under optimized conditions [135],

$$\eta_c = \frac{|I_s E_s|}{4\left|-\frac{dp}{dx} Q_{in}\right|} \tag{5.23}$$

where I_s is the induced electric current, E_s is the induced electric potential, $\left(\frac{-dp}{dx}\right)$ is the pressure gradient, and Q_{in} is the baseline volumetric flow rate without considering the streaming potential.

5.2.5. Temperature distribution

This study focuses on analyzing heat transfer characteristics in microscale channels for a non-Newtonian Casson fluid exhibiting both couple stress and EMHD effects. The temperature profile is modeled using the energy conservation equation, formulated as follows: [223,250],

$$\rho c_p \mathbf{U}\cdot\nabla T = k_T \nabla^2 T - \left(\frac{\partial q_r}{\partial y}\right) + \frac{\mathbf{J}\cdot\mathbf{J}}{\sigma_e} + \mu\left(1 + \frac{p_y}{\mu_B\sqrt{2\pi_c}}\right)(\nabla\mathbf{U})^2 + \eta\left(\nabla^2\mathbf{U}\right)^2 \tag{5.24}$$

Under thermally stabilized flow conditions, Eq. (5.24) reduces to

$$\overbrace{\rho c_p u \frac{\partial T}{\partial x}}^{\text{convective term}} = \overbrace{k_T\left(\frac{\partial^2 T}{\partial x^2} + \frac{\partial^2 T}{\partial y^2}\right)}^{\text{conductive term}} - \underset{\text{thermal radiation term}}{\frac{\partial q_r}{\partial y}} + \underset{\text{Joule heating term}}{\sigma_e E_s^2}$$

$$\overbrace{+\sigma_e E_z^2+\sigma_e B_y^2 u^2-2\sigma_e E_z B_y u}^{\text{electro-magnetic term}} \quad \overbrace{+\mu\left(1+\frac{1}{\beta}\right)\left(\frac{\partial u}{\partial y}\right)^2+\eta\left(\frac{\partial^2 u}{\partial y^2}\right)^2}^{\text{viscous dissipation term of viscoplastic fluid}} \tag{5.25}$$

Here, c_p denotes the constant-pressure specific heat capacity. and T represents the local fluid temperature. In a thermally stabilized flow regime, the axial temperature gradient becomes constant:

$$\partial T/\partial x = dT/dx = dT_M/dx = \text{constant} \tag{5.26}$$

From the above equation, it is obvious that $\partial^2 T/\partial X^2 = 0$. The mean velocity $u_{av}=\frac{1}{2h}\int_{-h}^{h} u\,dy$ .The non-dimensional average flow velocity, $U_{av}=\frac{u_{av}}{u_{ref}}$ is obtained from Eq. (5.17) as follows,

$$U_{av}=\frac{c_1}{m_1}\sinh(m_1)+\frac{c_3}{m_2}\sinh(m_2)+\frac{\gamma^2\Gamma}{p_2}+\frac{Ha^2\Omega\gamma^2}{p_2}-\frac{\bar{E}_s K\gamma^2 A\sinh(K)}{\left(K^4-p_1K^2+p_2\right)} \tag{5.27}$$

The thermal constraints at the channel walls are expressed in dimensionless terms to account for asymmetrical temperature discontinuity effects. For a system with non-identical boundary interactions, these constraints are formulated as:

$$\left[\theta+\bar{d}_1\left(\frac{d\theta}{dY}\right)\right]_{Y=1}=0,\quad \left[\theta+\bar{d}_1'\left(\frac{-d\theta}{dY}\right)\right]_{Y=-1}=0 \tag{5.28}$$

The dimensionless temperature θ is expressed as: $\theta=\frac{k_T(T-T_w)}{(q_w H)}$ for thermally stabilized flow regimes and T_w is the wall temperature, and k_T is the fluid's thermal conductivity, $\bar{d}_1(=d_1/h)$ and $\bar{d}_1'(=d_1'/h)$ represent the dimensionless thermal discontinuity coefficients at the upper and lower walls, respectively, accounting for interfacial thermal resistance effects.

By analysing thermal equilibrium across a differential control segment spanning the channel's axial length, the dimensionless energy equation is derived using the frameworks of Eqs. (5.29) and (5.30), yielding:

$$\frac{d^2\theta}{dY^2}=\beta_2 U-\frac{Ha^2 Br}{(1+Nr)}U^2-\frac{Br}{(1+Nr)}\left(1+\frac{1}{\beta}\right)\left(\frac{dU}{dY}\right)^2-\frac{Br}{\gamma^2(1+Nr)}\left(\frac{d^2U}{dY^2}\right)^2$$
$$-\frac{Ha^2 Br\Omega^2}{(1+Nr)}-\frac{J_h}{(1+Nr)} \tag{5.29}$$

where $Nr = \left(16T_a^3\sigma\right)\Big/\left(3\tilde{k}\,k_T\right)$ is a non-dimensional radiative heat transfer coefficient, $\tilde{k}$ is the Rosseland absorption coefficient, k_T thermal conductivity, σ is the Stefan-Boltzmann constant. $J_h\left(=\left(\sigma_e E_s^2 h\right)\Big/q_w\right)$ represents the volumetric heat generation rate from electrical resistive effects, and The Brinkman number is defined as $Br\left(=\left(\mu u_{ref}^2\right)\Big/\left(q_w h\right)\right)$ which signifies the ratio of viscous dissipation to externally applied heat flux [250]. Eq. (5.29) has been solved to determine a dimensionless temperature by applying the boundary conditions (Eq. 5.28) as,

$$\begin{aligned}\theta &= I_1\cosh\left(m_1Y\right)+I_2\sinh\left(m_1Y\right)+I_3\cosh\left(m_2Y\right)+I_4\sinh\left(m_2Y\right)+I_5Y^2\\ &-I_6\cosh\left(KY\right)-I_7\sinh\left(KY\right)-I_8\cosh\left(2m_1Y\right)-I_9\sinh\left(2m_1Y\right)\\ &-I_{10}\cosh\left(m_1Y\right)\cosh\left(m_2Y\right)+I_{11}\sinh\left(m_1Y\right)\sinh\left(m_2Y\right)-I_{12}\cosh\left(m_1Y\right)\sinh\left(m_2Y\right)\\ &+I_{13}\sinh\left(m_1Y\right)\cosh\left(m_2Y\right)+I_{14}\cosh\left(m_1Y\right)\cosh\left(KY\right)-I_{15}\sinh\left(m_1Y\right)\sinh\left(KY\right)\\ &+I_{16}\cosh\left(m_1Y\right)\sinh\left(KY\right)-I_{17}\sinh\left(m_1Y\right)\cosh\left(KY\right)-I_{18}\cosh\left(2m_2Y\right)\\ &-I_{19}\sinh\left(2m_2Y\right)+I_{20}\cosh\left(KY\right)\cosh\left(m_2Y\right)\\ &-I_{21}\sinh\left(KY\right)\sinh\left(m_2Y\right)-I_{22}\cosh\left(KY\right)\sinh\left(m_2Y\right)-I_{23}\sinh\left(KY\right)\cosh\left(m_2Y\right)\\ &-I_{24}\cosh(2KY)-I_{25}\sinh(2KY)+c_5Y+c_6\end{aligned} \tag{5.30}$$

where, the coefficients of I_1 to I_{25} , c_5 , and c_6 are given in Appendix C

The Nusselt number (Nu) is computed using the dimensionless average bulk temperature $\left(\theta_m\right)$, derived from the integral expression [244].

$$\theta_m = \frac{\int_{-1}^{1} U\theta dY}{\int_{-1}^{1} U dY} \tag{5.31}$$

The heat transfer efficiency is quantified by the Nusselt number (Nu), defined using the hydraulic diameter $\left(d_h\right)$ as,

$$Nu\left(=\frac{h_c d_h}{k_T}\right) \tag{5.32}$$

where h_c is the convective heat transfer coefficient,

Using the dimensionless bulk mean temperature derived in Eq. (5.31), Nu is calculated as:

$$Nu = -\left(\frac{4}{\theta_m}\right) \tag{5.33}$$

5.2.6. Entropy generation analysis

The volumetric entropy production rate within the microchannel is determined by integrating the hydrodynamic velocity and thermal gradient profiles. Irreversibility arises from four primary sources: thermal energy transfer due to spatial temperature variations, resistive dissipation from electric current flow, magnetohydrodynamic interactions between ionic motion and applied magnetic fields, and viscous energy losses from internal fluid friction, as detailed in prior analyses [250].

$$S_{G,H} = \frac{k_T}{T^2}\left(1+\frac{16T_a^3\sigma}{3\tilde{k}\,k_T}\right)\left(\frac{dT}{dy}\right)^2, S_{G,J} = \frac{\sigma_e E_s^2}{|T|}, S_{G,C} = \frac{2\sigma_e E_z B_y u}{|T|} + \frac{\sigma_e E_z^2}{|T|},$$

$$S_{G,M} = \frac{\sigma_e}{|T|}B_y^2 u^2,\ S_{G,\mathrm{V}} = \frac{1}{|T|}\left[\left(1+\frac{1}{\beta}\right)\mu\left(\frac{du}{dy}\right)^2 - \eta\left(\frac{d^2u}{dy^2}\right)^2\right] \tag{5.36}$$

The normalised entropy production rate, scaled by the characteristic entropy flux $\left(\frac{k_T}{h^2}\right)$ is formulated as,

$$S_G = S_H + S_J + S_C + S_M + S_V \tag{5.37}$$

where

$$S_H = \frac{(1+Nr)}{(\theta+\Theta)^2}\left(\frac{d\theta}{dY}\right)^2,\ S_J = \frac{J_h}{(\theta+\Theta)},\ S_C = \frac{2Ha^2\,\Omega\,Br\,U + Ha^2 Br\,\Omega^2}{(\theta+\Theta)},$$

$$S_M = \frac{Ha^2 Br\,U^2}{(\theta+\Theta)}, S_V = \left(1+\frac{1}{\beta}\right)\frac{Br}{(\theta+\Theta)}\left(\frac{dU}{dY}\right)^2 - \frac{Br}{(\theta+\Theta)\gamma^2}\left(\frac{d^2U}{dY^2}\right)^2 \tag{5.38}$$

The dimensionless thermal parameter $\Theta\{=(k_T T_w)/(q_w h)\}$ is derived from steady-state thermal boundary conditions (constants T_w and q_w). The total entropy generation, expressed in non-dimensional terms, is calculated by integrating the local entropy production rate over the channel domain:

$$S_{total} = \int_{-1}^{1} S_G\,dy \tag{5.39}$$

Eq. (5.39) is integrated numerically. Simson 1/3th rule-based integration technique is used by MATLAB software. 500 steps were considered for this involvement, so the results don't change up to five decimal points.

The dimensionless irreversibility ratio (Be), termed the Bejan number, quantifies the comparative influence of thermal entropy generation against total system irreversibility. It is defined as:

$$Be = \frac{S_H}{S_G} \tag{5.40}$$

The physical significance of the Bejan number (Be) acknowledges when $Be > 0.5$ thermal gradients dominate system irreversibility, whereas, $Be < 0.5$ implies viscous effects prevail as the primary source of entropy.

5.3. Results and discussion

This work constructs an exact analytical model to investigate EMHD actuated streaming potential dynamics in a planar microchannel for viscoplastic fluids incorporating couple-stress effects. The framework evaluates key dimensionless metrics, including streaming potential, velocity profiles, temperature fields, and Nusselt number, under asymmetric boundary constraints characterized by hydrodynamic slip and thermal discontinuity. The analysis integrates contributions from viscous energy dissipation, resistive Joule heating, and radiative heat transfer mechanisms [66,91,133,135,221,243,249,250]. The following electrokinetic and rheological parameters are employed to quantify the streaming potential flow behavior: $0.1 \leq h \leq 100$ μm, $\rho \sim 10^{-3}$ kgm^{-3}, $\sigma_e \sim 10$ Sm^{-1}, $T_a = 298$K, $B_y \sim 0.01$-5 T, u_{ref} 100 μm s^{-1}, $\mu \sim 10^{-3}$-10^{-2} Pa-s, $E_{ref} \sim 10^4$ Vm^{-1}, $e \sim 1.6 \times 10^{-19}$ C, $k_B = 1.381 \times 10^{-23}$ JK^{-1}, $\sigma_B \sim 0$-72 nScm^{-1} and $f \sim 10^{-12}$N s m^{-1}. The interfacial potentials at the channel boundaries ($\bar{\xi}_1$ and $\bar{\xi}_2$) are normalized to unity ($\bar{\xi}_1 \sim 1$, $\bar{\xi}_2 \sim 1$) under a low-potential linearization framework, applicable to systems with minimal surface charge density. This simplification assumes negligible ionic polarization, enabling tractable analytical solutions for electrokinetic phenomena. For flows with hydrodynamic slip at the walls, the effective interfacial potentials retain, $\bar{\xi}_1 \sim 1$ and, $\bar{\xi}_2 \sim 1$ isolating the impact of slip effects on momentum and heat transfer dynamics without conflating electrostatic contributions. The Joule heating parameter is taken as $J_h \sim 0$-10. The strength of the non-dimensional electrical parameter varies $\Omega \sim 0$-10, the magnitude of Hartmann number varies Ha~0.01-0.1 for the permissible EMHD micropumps, and the Brinkman number is set to be Br~0-0.1. The operational ranges of key parameters are highly contingent on the intrinsic properties of yield-stress fluids, including but not limited to critical yield thresholds, particulate loading, and microstructural organization. These factors collectively govern the rheological response under applied stresses. The physically possible ranges of the electrokinetic width (K) and Dukhin number (Du) for the Debye-Hückel approximation in streaming potential flow without overlap for viscoplastic fluids are K~5-40, and Du~0-10, respectively for hydrodynamic slip conditions with fixed zeta potentials. Electrokinetic width is set to change from K~5-18 satisfying the apparent zeta potential, i.e., $\bar{\xi}_a \leq 2$, The radiative heat transfer parameter is evaluated within Nr~0-10, while the ionic transport number spans $\alpha \sim 0$-10 which are taken from the published literature in accordance with the physical acceptability. For all the present calculations, we employ $\alpha = 0.2$ and, $\Gamma = 1$.

5.3.1. Fluid flow of couple stress Casson fluids

(i) Validation and verification

To assess the validity of the analytical framework, the computed electrokinetic streaming potential is benchmarked against the findings of Zhao et al. [244] under low surface potential conditions and no-slip constraints for pressure-driven flows. In the absence of electromagnetic fields, the couple-stress Casson model reduces to a Newtonian framework, enabling direct comparison with classical hydrodynamic theory. Fig. 5.2 illustrates strong concordance between the derived results and established literature values, validating the precision of the theoretical framework under these simplified conditions. This alignment underscores the analytical consistency of the methodology when applied to conventional Newtonian systems.

Fig. 5.3 contrasts the EKEC efficiency derived in this work against the reference data from Chen and Jian [238] for Newtonian fluids, serving as a validation benchmark. The analysis employs dimensionless parameters set to non-dimensional parameters participate as, $\bar{a}_1$=0, α=0.3, Du=0, $\bar{\xi}_1$=-1, $\bar{a}_1'$=0, $\bar{\xi}_2$=-1, Ha≈0, β→∞, γ→∞, and Ω=0 effectively reducing the model to a Newtonian framework under no electromagnetic field influence. Under no-slip boundary conditions and low zeta potentials in planar microchannels, the efficiency is evaluated as a function of the electrokinetic parameter K. The strong alignment between the computed results and prior studies confirms the analytical framework's accuracy under these conditions, reinforcing its applicability for Newtonian flow regimes.

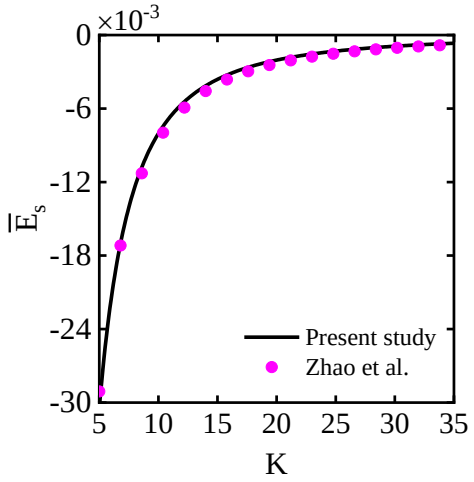

Fig. 5.2 Validation of the present results and Zhao et al. [244] results for streaming potential as a function of EDL thickness (K) for Newtonian fluids.

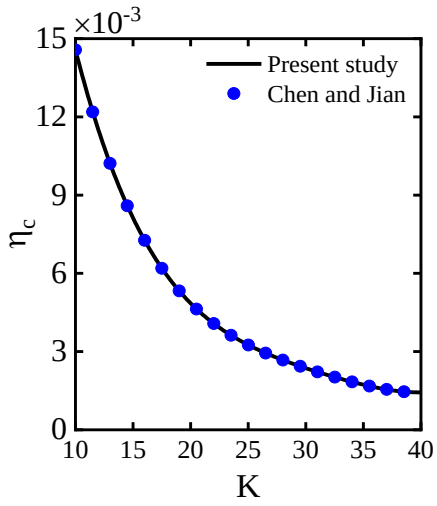

Fig. 5.3 Normalized EKEC efficiency vs K compared with Chen and Jian [238]

It is impossible to directly check the accuracy of the current velocity distributions because results have yet to be published. However, we must validate our results by assuming some flow parameters suitably. The present velocity distribution analysis compared with Zhao et al. [220] for the Newtonian fluid is plotted in Fig. 5.4. A maximum deviation of 1.7% is observed compared to Zhao et al. [220] results.

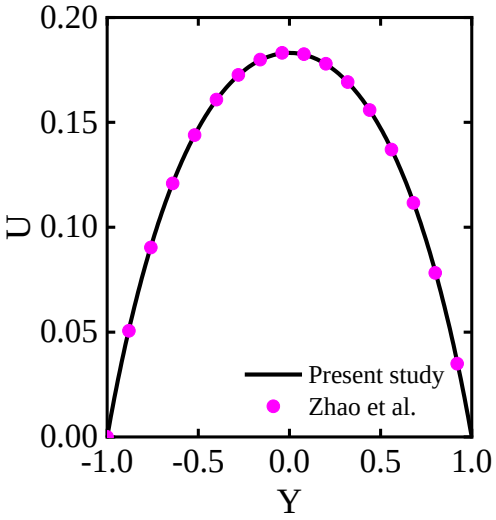

Fig. 5.4 Comparison of the present study with Zhao et al. [220] for normalised velocity distributions.

It should be mentioned that, to maintain the generality of the present physical model being addressed here K=20, $\bar{a}_1$=0, α=-0.5, Du=2, $\bar{\xi}_1$=1, $\bar{a}_1'$=0, $\bar{\xi}_2$=1, $\bar{d}_1$=0, Ha≈0, β→∞, γ→∞, Br=0.01, $\bar{d}_1'$=0, Ω=0, and J_h=1 have been considered as in our calculation procedure. The present analytical result of the temperature distribution compared with the published result of Zhao et al. [244] is plotted in Fig. 5.5. It is evident that the present analytical solution shows an excellent agreement under the tested condition.

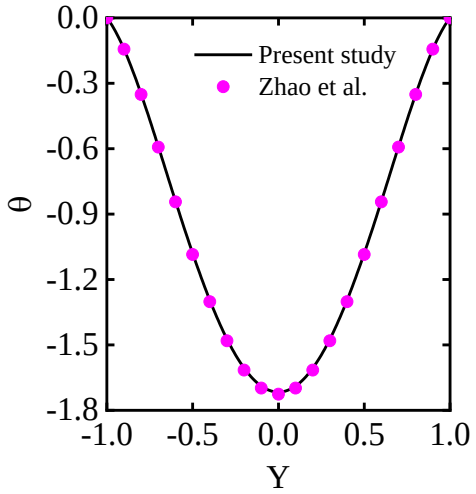

Fig. 5.5 Comparison of the present study with Zhao et al. [244] for normalised temperature distributions.

Table 3 compares the normalized velocity distributions between the current results and those obtained by Chen and Jain [238], as well as Zhao et al. [244]. The results of this comparative analysis demonstrate a negligible deviation (maximum 2.753%), affirming the validity and accuracy of the current findings.

Table 3
Comparison of the present and Chen and Jain [238], and Zhao et al. [244] normalized streaming potential for two values of α

Y	K=20, α=0.3, $\bar{\xi}_1$=-0.3, $\bar{\xi}_2$=-0.3		Absolute deviation (%)	K=20, α=0.5, $\bar{\xi}_1$=-1, $\bar{\xi}_2$=-1		Absolute deviation (%)
	Present study	Chen and Jian [238]		Present study	Zhao et al. [244]	
0	0.49335	0.49663	0.66484	0.49983	0.49547	0.87229
0.1	0.48840	0.49119	0.57125	0.49488	0.49047	0.89112
0.3	0.44880	0.45492	1.36363	0.45528	0.45047	1.05649
0.5	0.36961	0.36787	0.47076	0.37607	0.37047	1.48908
0.7	0.25087	0.25507	1.67417	0.25724	0.25048	2.62789
0.9	0.09297	0.09041	2.75357	0.09315	0.09108	2.22222

(ii) streaming potential distribution

Figure 5.6 illustrates the relationship between streaming potential and zeta potential ($\bar{\xi}_1$) under fixed parameters: K=10, Ha=0.1, $\bar{a}_1$=0.05, $\bar{\xi}_1$=1, $\bar{a}_1'$=0.01, $\bar{\xi}_2$=0.5, $\bar{d}_1$=0.05, $\bar{d}_1'$=0.01, Ω=10, β=1, and γ=1. The analysis reveals that increasing the Dukhin number (Du) reduces the streaming potential due to enhanced Stern layer conductivity. Elevated Du shifts the conduction current equilibrium toward the Stern layer, bypassing bulk fluid contributions. This creates a lower-resistance pathway for charge transport, diminishing the ionic current required to balance the streaming current and thereby lowering the induced streaming potential. For Du=2, the streaming potential decreases by 65.7% compared to Du=0. Conversely, increasing $\bar{\xi}_1$ amplifies the system's electrical potential by boosting counter-ion density in the EDL, driving a stronger streaming current aligned with the pressure gradient. However, this counter-ion accumulation further suppresses the streaming potential to maintain charge neutrality.

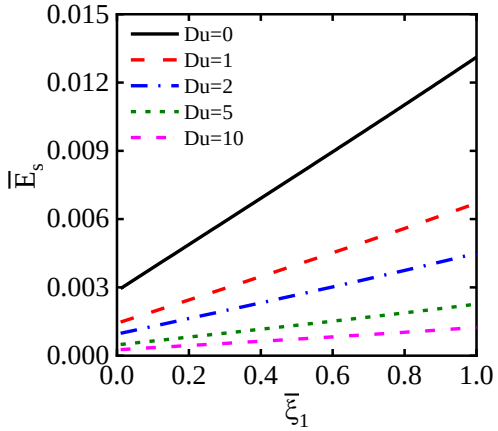

Fig. 5.6 Variation of the dimensionless streaming potential as a function of $\bar{\xi}_1$=1 with different values of Du.

(ii) Velocity distribution

Figure 5.7 examines the velocity profile of an EMHD flow for a couple-stress Casson fluid under asymmetric slip-dependent surface potentials, plotted against the transverse coordinate Y. The analysis employs fixed parameters: K=10, $\bar{a}_1$=0.05, Du=2, $\bar{\xi}_1$=1, $\bar{a}_1'$=0.01, $\bar{\xi}_2$=0.5, $\bar{d}_1$=0.05, Ha=0.1, $\bar{d}_1'$=0.01, and Ω=10. Graphical results demonstrate the impact of rheological parameters (couple-stress coefficient γ, Casson parameter β), electromagnetic forces (Ha), and slip effects on velocity distribution. A comparative assessment of four fluid models: couple-stress Casson, couple-stress, Casson, and Newtonian fluids reveals distinct velocity profiles under identical conditions.

Velocity fluctuations arise from the interplay between Coriolis forces and yield stress inherent to viscoplastic fluids, as encoded in the momentum equations. Elevated values of β=2 and γ=2 enhance flow velocity compared to β=1 and γ=1, underscoring the role of rheological complexity in accelerating fluid motion. This acceleration correlates with increased ion flux within the electric double layer (EDL), amplifying streaming current and potential. Conversely, couple-stress effects introduce additional viscous resistance, reducing velocity when γ dominates. For instance, neglecting γ (pure Casson fluid) elevates velocity due to diminished viscous damping, whereas incorporating γ (couple-stress Casson fluid) suppresses velocity through enhanced stress dissipation.

The Casson fluid exhibits higher velocity than its couple-stress counterpart, as yield stress (β) governs plasticity with minimal resistance compared to couple-stress viscosity (γ). Slip-dependent zeta potentials further modulate near-wall velocity gradients, with higher β and γ amplifying these effects synergistically with electromagnetic forces. This parametric interplay highlights the tunability of microfluidic transport through rheological and electrokinetic tailoring, offering insights for optimizing non-Newtonian fluid behavior in energy-efficient systems.

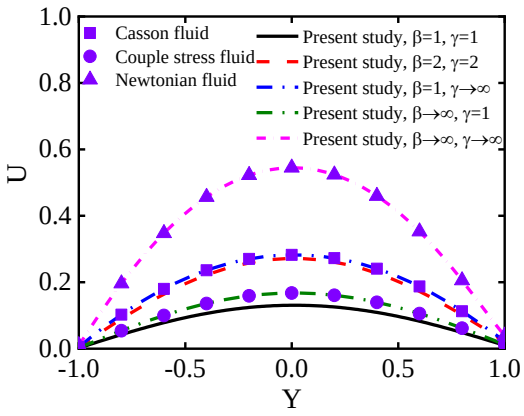

Fig. 5.7 Comparison of the present study for normalised velocity profiles of couple-stress Casson, couple-stress, Casson, and Newtonian fluids at asymmetric-slip boundary conditions in microchannels.

(iii) Electrokinetic energy conversion efficiency

Figure 5.7 contrasts the EKEC efficiency performance of four fluid models: viscoplastic Casson fluid with couple-stress effects, pure couple-stress fluid, Casson fluid, and Newtonian fluid under fixed parameters: Ha=0.1, $\bar{a}_1$=0.05, Du=2, $\bar{\xi}_1$=1, $\bar{a}_1'$=0.01, $\bar{\xi}_2$=0.5, $\bar{d}_1$=0.05, $\bar{d}_1'$=0.01, Ω=10, β=1, and γ=1. The Casson fluid with elevated couple-stress parameters (β=2, γ=2) achieves significantly higher efficiency than its baseline (β=1, γ=1), underscoring the impact of rheological complexity. The streaming potential weakens with distance from the EDL, reducing bulk ionic conductivity and increasing resistance, which necessitates a smaller induced electric

field to equilibrate currents under charge neutrality as shown in Fig. 5.7a. Enhanced β lowers flow resistance, improving energy transfer, while γ governs viscoelastic effects critical to EMHD dynamics. Transitioning to β→1, γ→∞ simplifies the model to a standard Casson fluid, governed by yield stress from its plastic behavior. For slip-dependent zeta potentials (Fig. 5.7b), efficiency increases by 45.92% (couple-stress Casson), 47.10% (couple-stress), 42.81% (Casson), and 37.68% (Newtonian) compared to slip-independent cases, with near-wall zeta potential amplified by combined β, γ and electromagnetic effects. The analysis distinguishes fluid behaviors, revealing Newtonian characteristics at extreme β, γ and highlights optimized energy conversion in tailored viscoplastic fluids.

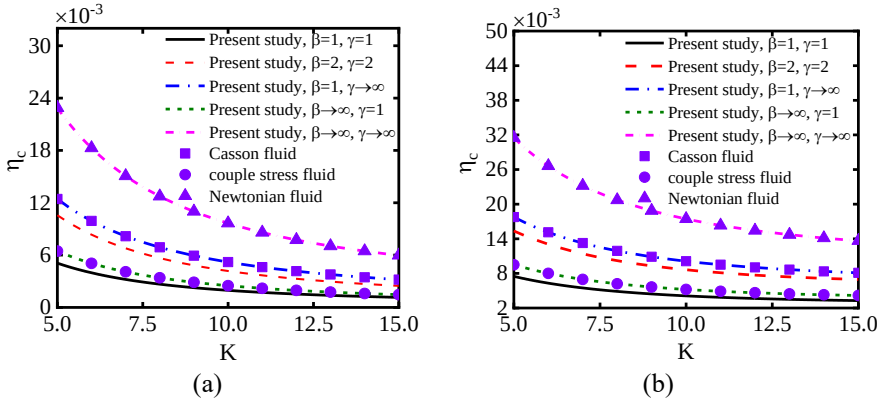

Fig. 5.8 Comparison of electrokinetic energy conversion efficiency of the present study as a function of K for different fluids: (a) slip-independent zeta potential (b) slip-dependent zeta potential.

5.3.2. Thermal analysis of couple stress Casson fluids

(i) Temperature field

Figure 5.9 analyses the scaled thermal profile under resistive heating effects for a viscoelastic Casson fluid with microstructural stresses. The flow parameters for the fixed values of K=10, $\bar{a}_1$=0.05, Du=2, $\bar{\xi}_1$=1, $\bar{a}_1'$=0.01, $\bar{\xi}_2$=0.5, $\bar{d}_1$=0.05, Ha=0.1, $\bar{d}_1'$=0.01, Ω=10, Br=0.01, and Nr=2, and Variable resistive heating intensities J_h=0,4,6 and 10 are tested to evaluate thermal behavior in pressure-driven streaming flows with radiative heat transfer. Results indicate that J_h elevated intensifies the scaled temperature across the channel, particularly under wall-heating conditions. Enhanced resistive dissipation correlates with steeper thermal gradients, reflecting the interplay between energy deposition and radiative cooling. Positive values of the normalised resistive heating term corresponding to the wall heating case amplify the temperature variation across the microchannel. Moreover, the

mathematical expression of the surface heat flux $q_w = k_T \left.\frac{dT}{dy}\right|_{y=h} = h_c\left(T_w - T_m\right)$,necessitates maintaining a constant thermal gradient at the boundary. Notably, as the Joule heating parameter (J_h) increases, both wall temperature (T_w), and mean fluid temperature (T_m) rise to preserve constant heat flux conditions. Fig. 5.9a illustrates temperature profiles for a Casson fluid with couple stress under no-jump boundary assumptions, while Fig. 5.9b demonstrates the impact of uneven thermal discontinuity at boundaries on normalized temperature distributions. Thermal slip effects arise from temperature discontinuities at fluid-wall interfaces, where significant disparities between wall and fluid temperatures occur due to limited thermal coupling. This weak interaction stems from insufficient molecular collisions between the fluid and wall, as well as within the fluid itself, leading to pronounced thermal gradients near boundary surfaces. Under jump conditions, steep temperature gradients dominate near walls, amplifying heat transfer rates. These findings highlight the critical role of boundary thermal communication in governing microscale thermal transport, particularly in systems with non-equilibrium molecular interactions and electromagnetic energy inputs. For this reason, the temperature difference increases for the temperature jump at the boundary. The influence of the thermal slip ($\bar{d}_1$) is more at the upper surface than the lower surface thermal slip ($\bar{d}_1'$) in temperature distribution. The thermal measurement at the channel's midpoint under abrupt boundary conditions demonstrates a 2.95% elevation relative to uniform boundary configurations. This behavior is applicable due to the temperature jump factor or the vertical distance in heat transfer applications like micro cooling and micro heating heat exchangers.

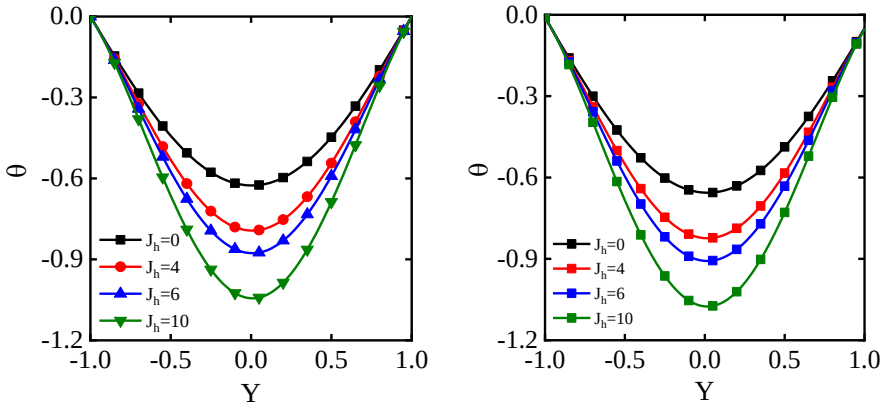

(a) $\bar{d}_1$=0, $\bar{d}_1'$=0 (b) $\bar{d}_1$=0.05, $\bar{d}_1'$=0.01

Fig. 5.9 Normalised temperature distribution with different values of J_h across a channel for couple stress Casson fluid flow at β = 1, and γ = 1: (a) no-jump conditions (b) asymmetric-temperature jump condition.

(ii) Nusselt number estimations for heat transfer

An essential dimensionless parameter in thermal flow studies is the Nusselt number (Nu). Figure 5.10 examines the dependence of the Nu on Br across varying Ha and under constant parameters: K=10, $\bar{a}_1$=0.05, Du=2, $\bar{\xi}_1$=1, $\bar{a}_1'$=0.01, $\bar{\xi}_2$=0.5, $\bar{d}_1$=0.05, Ha=0.1, $\bar{d}_1'$=0.01,Ha=0.1, Ω=10, J_h=10, and Nr=2. It is clear that a higher Ha tends to enhance the Nu when the Br remains below a critical threshold. However, as Br increases further, the magnetic field effect becomes more prominent. The thermal behavior shifts notably at elevated Br values, differing from the trends seen at lower Br. Overall, Nu shows a diminishing tendency with increasing Br and Ha. Moreover, for a fixed lateral electric field strength, Nu exhibits a downward trend.

The Ω inhibits hydrodynamic activity, modifying thermal transport dynamics. Elevated Ω magnitudes accelerate flow velocity, reducing bulk fluid temperature. To sustain constant wall heat flux under these conditions, the convective heat transfer coefficient declines as the thermal gradient (T_w-T_m) intensifies. Simultaneously, viscous boundary layer thickening under Ω exacerbates the temperature differential (T_w-T_m) diminishing both the heat transfer coefficient and Nu with increasing Br. A rise in the Ha causes an increase in magnitude of Nu for Br~0-0.003, and the opposite behaviour is noted after Br~0.003 value. The flow system is strongly dominated by fluid friction and couple-stress across the channel.

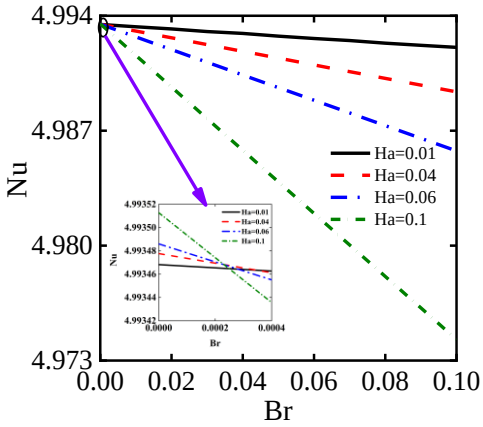

Fig. 5.10 Variation of Nu with Br for multiple Ha values in a Couple-Stress Casson fluid, evaluated at β = 1, and γ = 1.

(iii) Prediction of entropy generation

Figure 5.11 presents the spatial variation of entropy generation within the microchannel under varying radiative heat transfer intensities (Nr), keeping the parameters K=10, $\bar{a}_1$=0.05, Du=2, $\bar{\xi}_1$=1, $\bar{a}_1'$=0.01, $\bar{\xi}_2$=0.5, $\bar{d}_1$=0.05, Ha=0.1, $\bar{d}_1'$=0.01,Ha=0.1, Ω=10, J_h=10, and Br=0.01. An increase in Nr leads to a noticeable elevation in fluid temperature, with the bulk mean temperature rising more rapidly

than the wall temperature. This results in a gradual reduction in the thermal gradient (T_w-T_m), consistent with the condition of constant wall heat flux defined by $q_w=h_c(T_w-T_m)$. Within the core flow region, entropy generation remains relatively uniform; however, sharp gradients are observed near the channel boundaries, highlighting the dominant role of near-wall thermal interactions. These observations indicate that higher levels of thermal radiation mitigate thermal irreversibility in viscoplastic flow regimes, suggesting an overall enhancement in thermodynamic performance.

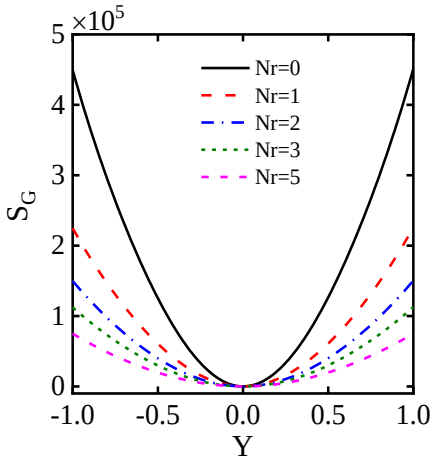

Fig. 5.11 Local entropy generation distribution across a channel for couple-stress Casson fluid flow with different radiative heat transfer parameters (Nr) at β = 1, and γ = 1.

Figure 5.12 illustrates the overall entropy generation within the microchannel in relation to variations in the lateral electric field strength Ω. The analysis is conducted using fixed dimensionless parameters: K=10, $\bar{a}_1$=0.05, Du=2, $\bar{\xi}_1$=1, $\bar{a}_1'$=0.01, $\bar{\xi}_2$=0.5, $\bar{d}_1$=0.05, Ha=0.1, $\bar{d}_1'$=0.01, J_h=10, Nr=2, and Br=0.01. The results indicate a clear upward trend in total entropy production with increasing Ω. This behavior stems from the rise in flow acceleration, which under low Ha values, promotes aiding forces that dominate over retarding ones, ultimately reducing the Nu. A decline in velocity correlates with heightened entropy generation, reflecting greater fluid irreversibility. Furthermore, as Nr increases, thermal irreversibility also intensifies, as shown in Fig. 5.12a. To better understand the influence of non-Newtonian effects, Fig. 5.12b compares entropy generation across varying values of the couple-stress and Casson fluid parameters. The findings suggest that elevated values of these stress-related parameters contribute to reduced entropy production, signifying that stronger rheological resistance diminishes viscous dissipation in the system.

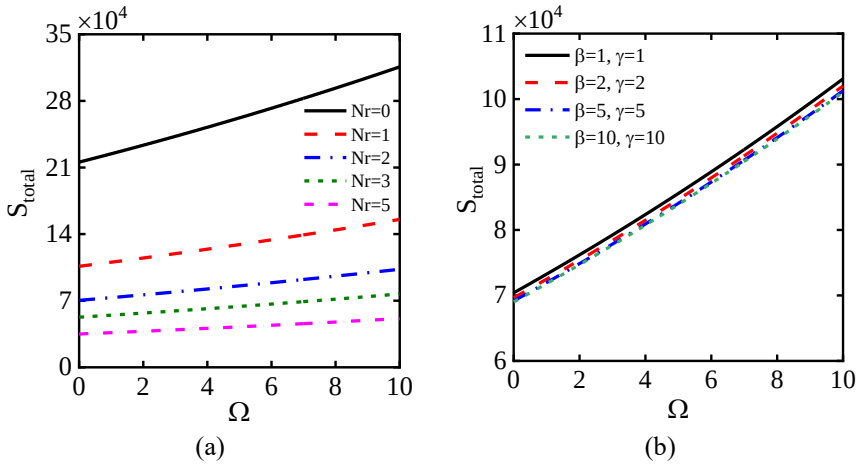

Fig. 5.12 Spatial entropy production profile for a Casson fluid with couple-stress effects across a microchannel versus Ω: (a) for varying Nr at β = 1, and γ = 1, (b) For varying rheological parameters β, and γ at Nr=2.

The distributions of Bejan number (Be) for different values of Nr is depicted in Fig. 5.13 for fixed values of K=10, $\bar{a}_1$=0.05, Du=2, $\bar{\xi}_1$=1, $\bar{a}_1'$=0.01, $\bar{\xi}_2$=0.5, $\bar{d}_1$=0.05, and $\bar{d}_1'$=0.01 are studied in this figure. The findings unambiguously demonstrate that Be increases as Nr values in the core region increase. Other than in the core region, there are very few variations in the magnitude of Bejan number distribution. It occurs because, as already noted in Fig. 5.11, which illustrates the importance of Nr in the flow domain, the magnitude of (T_w-T_m) gradually diminishes. Eventually, the entropy generation reduces in the presence of electromagnetic force. Moreover, the Bejan number increases slowly at the core of the channel.

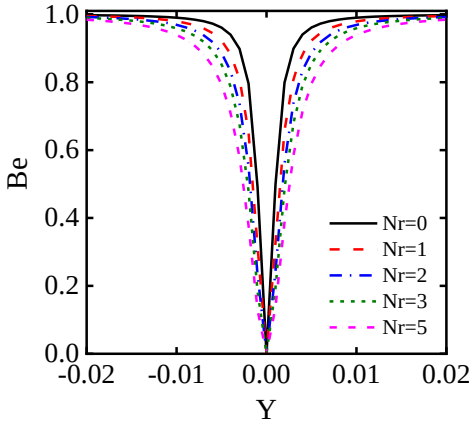

Fig. 5.13 Spatial distribution of Be across the normalized transverse coordinate Y under varying Nr.

5.4. Conclusions

This investigation examines stationary flow dynamics of a viscoplastic Casson medium with microstructural couple-stress interactions in a planar microchannel, incorporating electromagnetic coupling, pressure-induced streaming potential, and velocity-slip modulated surface charges. Closed-form formulations are obtained for critical parameters such as scaled streaming potential, EKEC efficiency, hydrodynamic profiles, thermal gradients, Nusselt number, and entropy production under asymmetric hydrodynamic slip constraints. The framework assesses the interplay of Lorentz forces, viscoelastic relaxation, and yield stress on energy efficiency, momentum transfer, and thermal regulation in ionic fluid systems. Validation against classical Newtonian benchmarks confirms predictive accuracy, with parametric comparisons showing efficiency gains of 45.92% (Casson medium with couple stress), 47.10% (couple-stress fluid), 42.81% (Casson fluid), and 37.68% (Newtonian fluid) under slip-modulated interfacial potentials. Elevated rheological parameters ($\beta = 2$, $\gamma = 2$) boost flow velocity by 107.64% relative to baseline ($\beta = 1$, $\gamma = 1$), attributed to mitigated viscoplastic drag.

Thermal gradients intensify by 2.95% near the channel core under discontinuous boundary constraints, driven by resistive heating effects. The Nusselt number exhibits abrupt deviations beyond critical thresholds of the viscous dissipation parameter (Br) and magnetic interaction number (Ha), reflecting heightened sensitivity to electromagnetic-thermal coupling. These findings refine design protocols for microsystems leveraging rheological-electromagnetic synergies.

5.5. Appendix

Appendix A:

(Velocity distribution terms)

$$p_1 = \gamma^2\left(1+\frac{1}{\beta}\right),\ p_2 = Ha^2\gamma^2,\ m_1 = \pm\sqrt{\frac{p_1+\sqrt{p_1^2-4p_2}}{2}},\ m_2 = \pm\sqrt{\frac{p_1-\sqrt{p_1^2-4p_2}}{2}},$$

$$A_1 = \frac{\left[\sinh(m_1)+\bar{a}_1 m_1\cosh(m_1)\right]}{\left[\cosh(m_1)+\bar{a}_1 m_1\sinh(m_1)\right]}\left[\cosh(m_1)+\bar{a}_1' m_1\sinh(m_1)\right]$$

$$+\left[\sinh(m_1)+\bar{a}_1' m_1\cosh(m_1)\right],$$

$$A_2 = \frac{\left[\cosh(m_2)+\bar{a}_1 m_2\sinh(m_2)\right]}{\left[\cosh(m_1)+\bar{a}_1 m_1\sinh(m_1)\right]}\left[\cosh(m_1)+\bar{a}_1' m_1\sinh(m_1)\right]$$

$$-\left[\cosh(m_2)+\bar{a}_1' m_2\sinh(m_2)\right],$$

$$A_3=\frac{\left[\sinh(m_2)+\bar{a}_1 m_2\cosh(m_2)\right]}{\left[\cosh(m_1)+\bar{a}_1 m_1\sinh(m_1)\right]}\left[\cosh(m_1)+\bar{a}_1' m_1\sinh(m_1)\right]$$
$$+\left[\sinh(m_2)+\bar{a}_1' m_2\cosh(m_2)\right],$$

$$A_4=\left[1-\frac{\cosh(m_1)+\bar{a}_1' m_1\sinh(m_1)}{\cosh(m_1)+\bar{a}_1 m_1\sinh(m_1)}\right]\left[\frac{\left(\gamma^2\Gamma\right)}{p_2}+\frac{\left(Ha^2\Omega\gamma^2\right)}{p_2}\right],$$

$$A_5=\frac{\left[\begin{array}{l}-\dfrac{K^2\gamma^2}{\left(K^4-p_1K^2+p_2\right)}\left(A\cosh(K)+B\sinh(K)\right)\\-\dfrac{\bar{a}_1K^3\gamma^2}{K^4-p_1K^2+p_2}\left(A\sinh(K)+B\cosh(K)\right)\end{array}\right]}{\left[\cosh(m_1)+\bar{a}_1 m_1\sinh(m_1)\right]}\left[\cosh(m_1)+\bar{a}_1' m_1\sinh(m_1)\right]$$
$$-\frac{K^2\gamma^2}{\left(K^4-p_1K^2+p_2\right)}\left[A\cosh(K)-B\sinh(K)\right]$$
$$+\frac{\bar{a}_1'K^3\gamma^2}{\left(K^4-p_1K^2+p_2\right)}\left[-A\sinh(K)+B\cosh(K)\right]\ ,$$

$$A_6=\left[\frac{\cosh(m_2)+\bar{a}_1 m_2\sinh(m_2)}{\cosh(m_1)+\bar{a}_1 m_1\sinh(m_1)}\right]-\left[\frac{\sinh(m_1)+\bar{a}_1 m_1\cosh(m_1)}{\cosh(m_1)+\bar{a}_1 m_1\sinh(m_1)}\right]\left(\frac{A_2}{A_1}\right),$$

$$A_7=\left[\frac{\sinh(m_2)+\bar{a}_1 m_2\cosh(m_2)}{\cosh(m_1)+\bar{a}_1 m_1\sinh(m_1)}\right]-\left[\frac{\sinh(m_1)+\bar{a}_1 m_1\cosh(m_1)}{\cosh(m_1)+\bar{a}_1 m_1\sinh(m_1)}\right]\left(\frac{A_3}{A_1}\right),$$

$$A_8=\frac{\dfrac{\left(\gamma^2\Gamma\right)}{p_2}+\left[\sinh(m_1)+\bar{a}_1 m_1\cosh(m_1)\right]\left(\dfrac{A_4}{A_1}\right)+\dfrac{Ha^2\Omega\gamma^2}{p_2}}{\left[\cosh(m_1)+\bar{a}_1 m_1\sinh(m_1)\right]},$$

$$A_9=\frac{-\left[\begin{array}{l}\dfrac{K^2\gamma^2}{K^4-p_1K^2+p_2}\left(A\cosh(K)+B\sinh(K)\right)\\+\dfrac{s_1K^3\gamma^2}{K^4-p_1K^2+p_2}\left(A\sinh(K)+B\cosh(K)\right)\end{array}\right]\left[\begin{array}{l}\sinh(m_1)\\+\bar{a}_1 m_1\cosh(m_1)\end{array}\right]\left(\dfrac{A_5}{A_1}\right)}{\cosh(m_1)+\bar{a}_1 m_1\sinh(m_1)},$$

$$A_{10}=-A_7 m_1^2\cosh(m_1)-\left(\frac{A_3}{A_1}\right)m_1^2\sinh(m_1)+m_2^2\cosh(m_2)$$

$$+\frac{\begin{bmatrix} A_6 m_1^2 \cosh(m_1) \\ +\left(\frac{A_2}{A_1}\right) m_1^2 \sinh(m_1) - m_2^2 \cosh(m_2) \end{bmatrix}\begin{bmatrix} -A_7 m_1^2 \cosh(m_1) - m_2^2 \sinh(m_2) \\ +\left(\frac{A_3}{A_1}\right) m_1^2 \sinh(m_1) \end{bmatrix}}{-A_6 m_1^2 \cosh(m_1) + m_1^2\left(\frac{A_2}{A_1}\right)\sinh(m_1) + m_2^2 \cosh(m_2)},$$

$$A_{11} = -A_8 m_1^2 \cosh(m_1) + \left(\frac{A_4}{A_1}\right) m_1^2 \sinh(m_1)$$

$$+\frac{\begin{bmatrix} -A_6 m_1^2 \cosh(m_1) \\ +m_2^2 \cosh(m_2) - m_1^2\left(\frac{A_2}{A_1}\right)\sinh(m_1) \end{bmatrix}\left[-A_8 m_1^2 \cosh(m_1) - m_1^2\left(\frac{A_4}{A_1}\right)\sinh(m_1)\right]}{-A_6 m_1^2 \cosh(m_1) + m_1^2\left(\frac{A_2}{A_1}\right)\sinh(m_1) + m_2^2 \cosh(m_2)},$$

$$A_{12} = \begin{bmatrix} -A_9 m_1^2 \cosh(m_1) \\ -\left(\frac{A_5}{A_1}\right) m_1^2 \sinh(m_1) \end{bmatrix} - \left[A\cosh(K) + B\sinh(K)\right]\frac{\left(K^4\gamma^2\right)}{\left(K^4 - p_1K^2 + p_2\right)}$$

$$+\frac{\begin{bmatrix} A_6 m_1^2 \cosh(m_1) + m_2^2 \cosh(m_2) \\ -\left(\frac{A_2}{A_1}\right) m_1^2 \sinh(m_1) \end{bmatrix}\begin{bmatrix} -A_9 m_1^2 \cosh(m_1) + m_1^2\left(\frac{A_5}{A_1}\right)\sinh(m_1) \\ -\left(A\cosh(K) - B\sinh(K)\right)\frac{\left(K^4\gamma^2\right)}{\left(K^4 - p_1K^2 + p_2\right)} \end{bmatrix}}{-A_6 m_1^2 \cosh(m_1) + m_1^2\left(\frac{A_2}{A_1}\right)\sinh(m_1) + m_2^2 \cosh(m_2)},$$

$$A_{13} = -\left(\frac{A_{11}}{A_{10}}\right),\ A_{14} = -\left(\frac{A_{12}}{A_{10}}\right),\ c_4 = A_{13} + E\,A_{14}$$

$$A_{15} = \frac{\left[A_7 m_1^2 \cosh(m_1) - \left(\frac{A_3}{A_1}\right) m_1^2 \sinh(m_1) + m_2^2 \sinh(m_2)\right]}{\left[-A_6 m_1^2 \cosh(m_1) + m_2^2 \cosh(m_2) + \left(\frac{A_2}{A_1}\right) m_1^2 \sinh(m_1)\right]} A_{13},$$

$$A_{16} = \frac{\begin{matrix} -A_9 m_1^2 \cosh(m_1) + m_1^2\left(\frac{A_5}{A_1}\right)\sinh(m_1) \\ -\left(A\cosh(K) - B\sinh(K)\right)\frac{\left(K^4\gamma^2\right)}{\left(K^4 - p_1K^2 + p_2\right)} \end{matrix}}{-A_6 m_1^2 \cosh(m_1) + m_2^2 \cosh(m_2) + \left(\frac{A_2}{A_1}\right) m_1^2 \sinh(m_1)}$$

$$+\frac{\left[-A_7 m_1^2\cosh(m_1)+\left(\frac{A_3}{A_1}\right)m_1^2\sinh(m_1)-m_2^2\sinh(m_2)\right]}{\left[-A_6 m_1^2\cosh(m_1)+m_2^2\cosh(m_2)+\left(\frac{A_2}{A_1}\right)m_1^2\sinh(m_1)\right]}A_{14}\ ,\ c_3=A_{15}-\bar{E}_s A_{16},$$

$$A_{17}=-A_{15}A_6-A_7A_{13}-A_8\ ,\ A_{18}=A_9-A_6A_{16}+A_7A_{14}\ ,\ c_1=A_{17}-\bar{E}_s A_{18},$$

$$A_{19}=-\frac{(A_2A_{15})}{A_1}-\frac{(A_3A_{13})}{A_1}+\frac{A_4}{A_1}\ ,\ A_{20}=\frac{(A_2A_{16})}{A_1}-\frac{(A_3A_{14})}{A_1}-\frac{A_5}{A_1},$$

$$c_2=A_{19}+\bar{E}_s A_{20}$$

Appendix B:

(Streaming potential terms)

$$R_1=B_1\cosh(m_1)\sinh(K)+B_3\sinh(m_1)\cosh(K)+B_5\cosh(m_2)\sinh(K)$$
$$+B_7\sinh(m_2)\cosh(K)+B_9,$$
$$R_2=B_2\cosh(m_1)\sinh(K)-B_4\sinh(m_1)\cosh(K)+B_6\cosh(m_2)\sinh(K)$$
$$-B_8\sinh(m_2)\cosh(K)-B_{10},$$

$$B_1=\frac{(2A_{17}AK)}{(K^2-m_1^2)}-\frac{(2A_{19}Bm_1)}{(K^2-m_1^2)},\ B_2=\frac{(2A_{18}AK)}{(K^2-m_1^2)}+\frac{(2A_{20}Bm_1)}{(K^2-m_1^2)}\ ,$$

$$B_3=\frac{-(2A_{17}Am_1)}{(K^2-m_1^2)}+\frac{(2A_{19}BK)}{(K^2-m_1^2)}\ ,\ B_4=\frac{(2A_{18}Am_1)}{(K^2-m_1^2)}+\frac{(2A_{20}BK)}{(K^2-m_1^2)}\ ,$$

$$B_5=\frac{(2A_{15}AK)}{(K^2-m_2^2)}-\frac{(2A_{13}Bm_2)}{(K^2-m_2^2)}\ ,\ B_6=\frac{(2A_{16}AK)}{(K^2-m_2^2)}+\frac{(2A_{14}Bm_2)}{(K^2-m_2^2)}$$

$$B_7=\frac{-(2A_{15}Am_2)}{(K^2-m_2^2)}+\frac{(2A_{13}BK)}{(K^2-m_2^2)}\ ,\ B_8=\frac{(2A_{16}Am_2)}{(K^2-m_2^2)}+\frac{(2A_{14}BK)}{(K^2-m_2^2)}$$

$$B_9=\frac{(2\gamma^2\Gamma A\sinh(K))}{(p_2K)}\ ,\qquad ,$$

$$B_{10}=\frac{(2Ha^2\Omega\gamma^2A\sinh(K))}{(p_2K)}-\frac{(K^2\gamma^2)}{(K^4-p_1K^2+p_2)}\left[A^2\frac{(1+\sinh(2K))}{2K}\right]$$

$$-\frac{(K^2\gamma^2)}{(K^4-p_1K^2+p_2)}\left[B^2\frac{(\sinh(2K)-1)}{2K}\right],$$

Appendix C:

(The temperature and Nusselt number terms**)**

$$\beta_1 = 2 + \left[\frac{\begin{array}{l} 2J_h + 2Ha^2 Br\Omega^2 + Ha^2 Br\int_{-1}^{1} U^2 dY - 2Ha^2 Br\Omega\int_{-1}^{1} U dy \\ +\left(1+\frac{1}{\beta}\right)Br\int_{-1}^{1}\left(\frac{dU}{dy}\right)^2 dy + \frac{Br}{\gamma^2}\int_{-1}^{1}\left(\frac{d^2U}{dY^2}\right)^2 dY \end{array}}{(1+Nr)} \right],$$

$$\beta_2 = \frac{\beta_1}{(2U_{av})} + \frac{\left(2Ha^2 Br\,\Omega\right)}{(1+Nr)},$$

$$F_1 = \frac{\left(Ha^2 Br\right)}{(1+Nr)}\left(\frac{c_1^2}{2} - \frac{c_2^2}{2} + \frac{c_3^2}{2} - \frac{c_4^2}{2}\right) + \left[\frac{\left(c_1^2 m_1^4\right)}{2} - \frac{\left(c_2^2 m_1^4\right)}{2} + \frac{\left(c_3^2 m_2^4\right)}{2} - \frac{\left(c_4^2 m_2^4\right)}{2}\right]\left[\frac{Br}{\left(\gamma^2(1+Nr)\right)}\right]$$

$$+\left[\frac{\left(Ha^2 Br\right)}{(1+Nr)}\right]\left[\left(\frac{Ha^2\Omega\gamma^2}{p_2}\right)^2 + \left(\frac{\gamma^2\Gamma}{p_2}\right)\left(\frac{\gamma^2\Gamma}{p_2} + \frac{\left(2Ha^2\Omega\gamma^2\right)}{p_2}\right)\right]$$

$$+\left[\frac{\left(Ha^2 Br\right) - \frac{\left(K^4 Br\right)}{\gamma^2}}{(1+Nr)}\right]\left[\frac{\left(\bar{E}_s K^2\gamma^2\right)}{\left(K^4 - p_1K^2 + p_2\right)}\right]^2\left(\frac{A^2}{2} - \frac{B^2}{2}\right),$$

$$F_2 = \left[\frac{\left(Ha^2 Br + \frac{\left(m_1^4 Br\right)}{\gamma^2}\right)}{(1+Nr)}\right]\left[\frac{\left(c_1^2 + c_2^2\right)}{(4m_1)}\right], F_3 = \frac{(c_1 c_2)}{(2m_1 + 2m_1 Nr)}\left[Ha^2 Br + \frac{\left(m_1^4 Br\right)}{\gamma^2}\right],$$

$$F_4 = \left[\frac{(2c_1c_3m_2 - 2c_2c_4m_1)}{\left(m_2^2 - m_1^2\right)}\right]\left[\frac{\left(Ha^2 Br\right) + \frac{\left(m_1^2 m_2^2 Br\right)}{\gamma^2}}{(1+Nr)}\right],$$

$$F_5 = \left[\frac{\left(2c_1c_3m_1 - 2c_2c_4m_2\right)}{\left(m_2^2 - m_1^2\right)}\right]\left[\frac{\left(Ha^2Br\right) + \frac{\left(m_1^2m_2^2Br\right)}{\gamma^2}}{\left(1+Nr\right)}\right],$$

$$F_6 = \left[\frac{\left(2c_1c_4m_2 - 2c_2c_3m_1\right)}{\left(m_2^2 - m_1^2\right)}\right]\left[\frac{\left(Ha^2Br\right) + \frac{\left(m_1^2m_2^2Br\right)}{\gamma^2}}{\left(1+Nr\right)}\right],$$

$$F_7 = \left[\frac{\left(2c_1c_4m_1 - 2c_2c_3m_2\right)}{\left(m_2^2 - m_1^2\right)}\right]\left[\frac{\left(Ha^2Br\right) + \frac{\left(m_1^2m_2^2Br\right)}{\gamma^2}}{\left(1+Nr\right)}\right],$$

$$F_8 = \frac{\left(2c_1\gamma^2\Gamma Ha^2Br + 2c_1\gamma^2Ha^4Br\Omega\right)}{\left[a_2m_1\left(1+Nr\right)\right]},$$

$$F_9 = \left[\frac{\left(Ac_1K - Bc_2m_1\right)}{\left(1+Nr\right)}\right]\left[\frac{\left(2EK^2\gamma^2\right)}{\left(K^4 - a_1K^2 + a_2\right)}\right]\left[\frac{Ha^2Br + \frac{\left(K^2m_1^2Br\right)}{\gamma^2}}{\left(K^2 - m_1^2\right)}\right],$$

$$F_{10} = \left[\frac{\left(Ac_1m_1 - Bc_2K\right)}{\left(1+Nr\right)}\right]\left[\frac{\left(2EK^2\gamma^2\right)}{\left(K^4 - a_1K^2 + a_2\right)}\right]\left[\frac{Ha^2Br + \frac{\left(K^2m_1^2Br\right)}{\gamma^2}}{\left(K^2 - m_1^2\right)}\right],$$

$$F_{11} = \left[\frac{\left(Bc_1K - Ac_2m_1\right)}{\left(1+Nr\right)}\right]\left[\frac{\left(2EK^2\gamma^2\right)}{\left(K^4 - a_1K^2 + a_2\right)}\right]\left[\frac{Ha^2Br + \frac{\left(K^2m_1^2Br\right)}{\gamma^2}}{\left(K^2 - m_1^2\right)}\right],$$

$$F_{12} = \left[\frac{\left(Bc_1m_1 - Ac_2K\right)}{\left(1+Nr\right)}\right]\left[\frac{\left(2EK^2\gamma^2\right)}{\left(K^4 - a_1K^2 + a_2\right)}\right]\left[\frac{Ha^2Br + \frac{\left(K^2m_1^2Br\right)}{\gamma^2}}{\left(K^2 - m_1^2\right)}\right],$$

$$F_{13} = Ha^2 Br\left[\frac{\left(c_2\gamma^2\right)}{\left(a_2 m_1\right)}\right]\left[\frac{\left(2\Gamma + 2Ha^2\Omega\right)}{\left(1+Nr\right)}\right], F_{14} = \left[\frac{\left(Ha^2 Br + \frac{\left(m_2^4 Br\right)}{\gamma^2}\right)}{\left(1+Nr\right)}\right]\left[\frac{c_3^2}{\left(4m_2\right)} + \frac{c_4^2}{\left(4m_2\right)}\right],$$

$$F_{15} = \left[\frac{\left(Ha^2 Br + \frac{\left(m_2^4 Br\right)}{\gamma^2}\right)}{\left(1+Nr\right)}\right]\left[\frac{\left(c_3 c_4\right)}{\left(2m_2\right)}\right], F_{16} = \left[\frac{\left(Ha^2 Br\right)}{\left(1+Nr\right)}\right]\left[\frac{\left(2c_3\gamma^2\right)}{\left(p_2 m_2\right)}\right]\left(\Gamma + Ha^2\Omega\right),$$

$$F_{17} = \left[\frac{\left(Ac_3 m_2 - Bc_4 K\right)}{\left(1+Nr\right)}\right]\left[\frac{\left(2\bar{E}_s K^2\gamma^2\right)}{\left(K^4 - p_1 K^2 + p_2\right)}\right]\left[\frac{Ha^2 Br + \frac{\left(K^2 m_2^2 Br\right)}{\gamma^2}}{\left(K^2 - m_2^2\right)}\right],$$

$$F_{18} = \left[\frac{\left(Ac_3 K - Bc_4 m_2\right)}{\left(1+Nr\right)}\right]\left[\frac{\left(2\bar{E}_s K^2\gamma^2\right)}{\left(K^4 - p_1 K^2 + p_2\right)}\right]\left[\frac{Ha^2 Br + \frac{\left(K^2 m_2^2 Br\right)}{\gamma^2}}{\left(K^2 - m_2^2\right)}\right],$$

$$F_{19} = \left[\frac{\left(Bc_3 K - Ac_4 m_2\right)}{\left(1+Nr\right)}\right]\left[\frac{\left(2\bar{E}_s K^2\gamma^2\right)}{\left(K^4 - p_1 K^2 + p_2\right)}\right]\left[\frac{Ha^2 Br + \frac{\left(K^2 m_2^2 Br\right)}{\gamma^2}}{\left(K^2 - m_2^2\right)}\right],$$

$$F_{20} = \left[\frac{\left(Bc_3 m_2 - Ac_4 K\right)}{\left(1+Nr\right)}\right]\left[\frac{\left(2\bar{E}_s K^2\gamma^2\right)}{\left(K^4 - p_1 K^2 + p_2\right)}\right]\left[\frac{Ha^2 Br + \frac{\left(K^2 m_2^2 Br\right)}{\gamma^2}}{\left(K^2 - m_2^2\right)}\right],$$

$$F_{21} = \left[\frac{\left(Ha^2 Br\right)}{\left(1+Nr\right)}\right]\left[\frac{\left(2c_4\gamma^2\right)}{\left(p_2 m_2\right)}\right]\left(\Gamma + Ha^2\Omega\right),$$

$$F_{22} = \left[\frac{\left(2A\bar{E}_s K\gamma^4\right)}{\left(K^4 - p_1 K^2 + p_2\right)}\right]\left[\frac{\left(Ha^2 Br\right)}{\left(1+Nr\right)}\right]\left[\frac{\Gamma}{p_2} + \frac{\left(Ha^2\Omega\right)}{p_2}\right],$$

$$F_{23}=\left[\frac{\left(Ha^2Br\right)}{\left(1+Nr\right)}\right]\left[\frac{\left(2B\bar{E}_sK\gamma^4\right)}{\left(K^4-p_1K^2+p_2\right)}\right]\left[\frac{\Gamma}{p_2}+\frac{\left(Ha^2\Omega\right)}{p_2}\right],$$

$$F_{24}=\left[\frac{\left(\bar{E}_sK^2\gamma^2\right)}{\left(K^4-p_1K^2+p_2\right)}\right]^2\left[\frac{Br}{\left(1+Nr\right)}\right]\left[Ha^2+\frac{K^4}{\gamma^2}\right]\left[\frac{\left(A^2+B^2\right)}{\left(4K\right)}\right],$$

$$F_{25}=\left[\frac{\left(\bar{E}_sK^2\gamma^2\right)}{\left(K^4-p_1K^2+p_2\right)}\right]^2\left[\frac{\left(2ABBr\right)}{\left(1+Nr\right)}\right]\left[\frac{\left(Ha^2+\frac{K^4}{\gamma^2}\right)}{2K}\right],$$

$$G_1=\frac{m_1}{4}\left(c_1^2+c_2^2\right),\ G_2=\frac{m_1^2}{2}\left(c_1^2-c_2^2\right)+\frac{m_2^2}{4}\left(c_3^2-c_4^2\right)+\left[\frac{\left(\bar{E}_sK^3\gamma^2\right)}{\left(K^4-p_1K^2+p_2\right)}\right]^2\left(\frac{A^2}{2}-\frac{B^2}{2}\right),$$

$$G_3=\frac{\left(c_1c_2m_1\right)}{2}\ ,\ G_4=\frac{\left(c_3c_4m_2\right)}{2},\ G_5=\frac{\left(c_3^2m_2\right)}{4}+\frac{\left(c_4^2m_2\right)}{4},$$

$$G_6=\frac{\left[\left(2c_1c_3m_1m_2^2\right)-\left(2c_2c_4m_1^2m_2\right)\right]}{\left(m_2^2-m_1^2\right)},\ G_7=\frac{\left[\left(2c_1c_3m_1^2m_2\right)-\left(2c_2c_4m_1m_2^2\right)\right]}{\left(m_2^2-m_1^2\right)},$$

$$G_8=\frac{\left[\left(2c_1c_4m_1m_2^2\right)-\left(2c_2c_3m_1^2m_2\right)\right]}{\left(m_2^2-m_1^2\right)},\ G_9=\frac{\left[\left(2c_1c_4m_1^2m_2\right)-\left(2c_2c_3m_1m_2^2\right)\right]}{\left(m_2^2-m_1^2\right)},$$

$$G_{10}=\frac{\left(2\bar{E}_sK^3\gamma^2m_1\right)\left[Ac_1K-Bc_2m_1\right]}{\left(K^4-p_1K^2+p_2\right)\left(K^2-m_1^2\right)},G_{11}=\frac{\left(2\bar{E}_sK^3\gamma^2m_1\right)\left[Ac_1m_1-Bc_2K\right]}{\left(K^2-m_1^2\right)\left(K^4-p_1K^2+p_2\right)},$$

$$G_{12}=\frac{\left(2\bar{E}_sK^3\gamma^2m_1\right)\left[Bc_1K-Ac_2m_1\right]}{\left(K^2-m_1^2\right)\left(K^4-p_1K^2+p_2\right)},G_{13}=\frac{\left(2\bar{E}_sK^3\gamma^2m_1\right)\left[Bc_1m_1-Ac_2K\right]}{\left(K^2-m_1^2\right)\left(K^4-p_1K^2+p_2\right)},$$

$$G_{14}=\frac{\left(2\bar{E}_sK^3\gamma^2m_2\right)\left[Ac_3K-Bc_4m_2\right]}{\left(K^4-p_1K^2+p_2\right)\left(K^2-m_2^2\right)},G_{15}=\frac{\left(2\bar{E}_sK^3\gamma^2m_2\right)\left[Ac_3m_2-Bc_4K\right]}{\left(K^4-p_1K^2+p_2\right)\left(K^2-m_2^2\right)},$$

$$G_{16}=\frac{\left(2\bar{E}_sK^3\gamma^2m_2\right)\left[Bc_3K-Ac_4m_2\right]}{\left(K^2-m_2^2\right)\left(K^4-p_1K^2+p_2\right)},G_{17}=\frac{\left(2\bar{E}_sK^3\gamma^2m_2\right)\left[Bc_3m_2-Ac_4K\right]}{\left(K^2-m_2^2\right)\left(K^4-p_1K^2+p_2\right)},$$

$$G_{18}=\left[\frac{\left(\bar{E}_sK^3\gamma^2\right)}{\left(K^4-p_1K^2+p_2\right)}\right]^2\left[\frac{\left(AB\right)}{\left(2K\right)}\right],G_{19}=\left[\frac{\left(\bar{E}_sK^3\gamma^2\right)}{\left(K^4-p_1K^2+p_2\right)}\right]^2\left[\frac{A^2}{\left(4K\right)}+\frac{B^2}{\left(4K\right)}\right],$$

$$H_1=\frac{\left(c_1\beta_2\right)}{m_1}-F_8,\ H_2=\frac{\left(c_2\beta_2\right)}{m_1}-F_{13},\ H_3=\frac{\left(c_3\beta_2\right)}{m_2}-F_{16},\ H_4=\frac{\left(c_4\beta_2\right)}{m_2}-F_{21},$$

$$H_5=\frac{\left(\gamma^2\Gamma\beta_2+Ha^2\Omega\gamma^2\beta_2\right)}{p_2}-\frac{\left[F_1+J_h-\left(1+\frac{1}{\beta}\right)BrG_2\right]}{(1+Nr)},\ H_6=\left[\frac{\left(A\beta_2\bar{E}_s K\gamma^2\right)}{\left(K^4-p_1K^2+p_2\right)}\right]-F_{22}$$

$$,\ H_7=\left[\frac{\left(B\beta_2\bar{E}_s K\gamma^2\right)}{\left(K^4-p_1K^2+p_2\right)}\right]-F_{23},\ H_8=F_2+\left(1+\frac{1}{\beta}\right)\left[\frac{\left(BrG_1\right)}{(1+Nr)}\right],$$

$$H_9=F_3+\left(1+\frac{1}{\beta}\right)\left[\frac{\left(BrG_3\right)}{(1+Nr)}\right],\ H_{10}=F_4-\left(1+\frac{1}{\beta}\right)\left[\frac{\left(BrG_7\right)}{(1+Nr)}\right],$$

$$H_{11}=F_5-\left(1+\frac{1}{\beta}\right)\left[\frac{\left(BrG_6\right)}{(1+Nr)}\right],\ H_{12}=F_6-\left(1+\frac{1}{\beta}\right)\left[\frac{\left(BrG_9\right)}{(1+Nr)}\right]\qquad ,$$

$$H_{13}=F_7-\left(1+\frac{1}{\beta}\right)\left[\frac{\left(BrG_8\right)}{(1+Nr)}\right],\ H_{14}=F_9-\left(1+\frac{1}{\beta}\right)\left[\frac{\left(BrG_{11}\right)}{(1+Nr)}\right],$$

$$H_{15}=F_{10}-\left(1+\frac{1}{\beta}\right)\left[\frac{\left(BrG_{10}\right)}{(1+Nr)}\right],\ H_{16}=F_{11}-\left(1+\frac{1}{\beta}\right)\left[\frac{\left(BrG_{13}\right)}{(1+Nr)}\right],$$

$$H_{17}=F_{12}-\left(1+\frac{1}{\beta}\right)\left[\frac{\left(BrG_{12}\right)}{(1+Nr)}\right],\ H_{18}=F_{14}+\left(1+\frac{1}{\beta}\right)\left[\frac{\left(BrG_5\right)}{(1+Nr)}\right],$$

$$H_{19}=F_{15}+\left(1+\frac{1}{\beta}\right)\left[\frac{\left(BrG_4\right)}{(1+Nr)}\right],\ H_{20}=F_{17}-\left(1+\frac{1}{\beta}\right)\left[\frac{\left(BrG_{14}\right)}{(1+Nr)}\right],$$

$$H_{21}=F_{18}-\left(1+\frac{1}{\beta}\right)\left[\frac{\left(BrG_{15}\right)}{(1+Nr)}\right],\ H_{22}=F_{19}-\left(1+\frac{1}{\beta}\right)\left[\frac{\left(BrG_{17}\right)}{(1+Nr)}\right],$$

$$H_{23}=F_{20}-\left(1+\frac{1}{\beta}\right)\left[\frac{\left(BrG_{16}\right)}{(1+Nr)}\right],\ H_{24}=F_{24}+\left(1+\frac{1}{\beta}\right)\left[\frac{\left(BrG_{19}\right)}{(1+Nr)}\right],$$

$$H_{25}=F_{25}+\left(1+\frac{1}{\beta}\right)\left[\frac{\left(BrG_{18}\right)}{(1+Nr)}\right].$$

$$I_1=\frac{H_1}{m_1}\ ,\ I_2=\frac{H_2}{m_1}\ ,\ I_3=\frac{H_3}{m_2}\ ,\ I_4=\frac{H_4}{m_2}\ ,\ I_5=\frac{H_4}{m_2}\ ,\ I_6=\frac{H_6}{K}\ ,\ I_7=\frac{H_7}{K}\ ,$$

$$I_8=\frac{H_8}{(2m_1)}\ ,\ I_9=\frac{H_9}{(2m_1)}\ ,\ I_{10}=\frac{(H_{10}m_2+H_{11}m_1)}{\left(m_2^2-m_1^2\right)}\ ,\ I_{11}=\frac{(H_{10}m_1+H_{11}m_2)}{\left(m_2^2-m_1^2\right)},$$

$$I_{12}=\frac{\left(H_{12}m_2+H_{13}m_1\right)}{\left(m_2^2-m_1^2\right)},\ I_{13}=\frac{\left(H_{12}m_1+H_{13}m_2\right)}{\left(m_2^2-m_1^2\right)},\ I_{14}=\frac{\left(H_{14}K+H_{15}m_1\right)}{\left(K^2-m_1^2\right)},$$

$$I_{15}=\frac{\left(H_{14}m_1+H_{15}K\right)}{\left(K^2-m_1^2\right)},\ I_{16}=\frac{\left(H_{16}K+H_{17}m_1\right)}{\left(K^2-m_1^2\right)},\ I_{17}=\frac{\left(H_{16}m_1+H_{17}K\right)}{\left(K^2-m_1^2\right)},$$

$$I_{18}=\frac{H_{18}}{\left(2m_2\right)},\ I_{19}=\frac{H_{19}}{\left(2m_2\right)},\ I_{20}=\frac{\left(H_{20}m_2+H_{21}K\right)}{\left(K^2-m_2^2\right)},\ I_{21}=\frac{\left(H_{20}K+H_{21}m_2\right)}{\left(K^2-m_2^2\right)},$$

$$I_{22}=\frac{\left(H_{22}m_2+H_{23}K\right)}{\left(K^2-m_2^2\right)},\ I_{23}=\frac{\left(H_{22}K+H_{23}m_2\right)}{\left(K^2-m_2^2\right)},\ I_{24}=\frac{H_{24}}{\left(2K\right)},\ I_{25}=\frac{H_{25}}{\left(2K\right)}$$

$$J_1=\left(\bar{d}_1+\bar{d}_1'\right)H_2,\ J_2=\left[2I_2+\left(\bar{d}_1-\bar{d}_1'\right)H_1\right],\ J_3=\left(\bar{d}_1+\bar{d}_1'\right)H_4,\quad J_4=\left[2I_4+\left(\bar{d}_1-\bar{d}_1'\right)H_3\right],$$

$$J_5=\left(\bar{d}_1-\bar{d}_1'\right)H_5,\ J_6=2I_6+\left(\bar{d}_1-\bar{d}_1'\right)H_7,\ J_7=2I_7+\left(\bar{d}_1+\bar{d}_1'\right)H_6,\ J_8=\left(\bar{d}_1+\bar{d}_1'\right)H_9,$$

$$J_9=2I_9+\left(\bar{d}_1-\bar{d}_1'\right)H_8,\ J_{10}=\left(\bar{d}_1+\bar{d}_1'\right)H_{12},\ J_{11}=\left(\bar{d}_1+\bar{d}_1'\right)H_{13},\ J_{12}=2I_{12}+\left(\bar{d}_1-\bar{d}_1'\right)H_{10}$$

$$,\ J_{15}=\left(\bar{d}_1+\bar{d}_1'\right)H_{17},\ J_{17}=2I_{17}+\left(\bar{d}_1-\bar{d}_1'\right)H_{15},\ J_{18}=\left(\bar{d}_1+\bar{d}_1'\right)H_{19},$$

$$J_{19}=2I_{19}+\left(\bar{d}_1-\bar{d}_1'\right)H_{18},\ J_{21}=\left(\bar{d}_1+\bar{d}_1'\right)H_{23},\ J_{22}=2I_{22}+\left(\bar{d}_1-\bar{d}_1'\right)H_{20},$$

$$J_{24}=\left(\bar{d}_1+\bar{d}_1'\right)H_{25},\ J_{25}=2I_{25}+\left(\bar{d}_1-\bar{d}_1'\right)H_{24}$$

$$c_5=\frac{-1}{\left(2+\bar{d}_1+\bar{d}'\right)}\left[\begin{matrix}J_1\cosh\left(m_1\right)+J_2\sinh\left(m_1\right)+J_3\cosh\left(m_2\right)\\+J_4\sinh\left(m_2\right)+J_5-J_6\cosh\left(K\right)\end{matrix}\right.$$

$$-J_7\sinh\left(K\right)-J_8\cosh\left(2m_1\right)-J_9\sinh\left(2m_1\right)-J_{10}\cosh\left(m_1\right)\cosh\left(m_2\right)$$

$$+J_{11}\sinh\left(m_1\right)\sinh\left(m_2\right)-J_{12}\cosh\left(m_1\right)\sinh\left(m_2\right)+J_{13}\sinh\left(m_1\right)\cosh\left(m_2\right)$$

$$+J_{14}\cosh\left(m_1\right)\cosh\left(K\right)-J_{15}\sinh\left(m_1\right)\sinh\left(K\right)+J_{16}\cosh\left(m_1\right)\sinh\left(K\right)$$

$$-J_{17}\sinh\left(m_1\right)\cosh\left(K\right)-J_{18}\cosh\left(2m_2\right)-J_{19}\sinh\left(2m_2\right)$$

$$+J_{20}\cosh\left(K\right)\cosh\left(m_2\right)-J_{21}\sinh\left(K\right)\sinh\left(m_2\right)-J_{22}\cosh\left(K\right)\sinh\left(m_2\right)$$

$$\left.+J_{23}\sinh\left(K\right)\cosh\left(m_2\right)-J_{24}\cosh\left(2K\right)-J_{25}\sinh\left(2K\right)\right],$$

$$c_5\left(1-\bar{d}_1'\right)-c_6=\left[\begin{matrix}L_1\cosh\left(m_1\right)-L_2\sinh\left(m_1\right)+L_3\cosh\left(m_2\right)\\-L_4\sinh\left(m_2\right)+L_5-L_6\cosh\left(K\right)\end{matrix}\right.$$

$$+L_7\sinh\left(K\right)-L_8\cosh\left(2m_1\right)+L_9\sinh\left(2m_1\right)-L_{10}\cosh\left(m_1\right)\cosh\left(m_2\right)$$

$$+L_{11}\sinh\left(m_1\right)\sinh\left(m_2\right)+L_{12}\cosh\left(m_1\right)\sinh\left(m_2\right)-L_{13}\sinh\left(m_1\right)\cosh\left(m_2\right)$$

$$+L_{14}\cosh\left(m_1\right)\cosh\left(K\right)-L_{15}\sinh\left(m_1\right)\sinh\left(K\right)$$

$$-L_{16}\cosh\left(m_1\right)\sinh\left(K\right)+L_{17}\sinh\left(m_1\right)\cosh\left(K\right)-L_{18}\cosh\left(2m_2\right)+L_{19}\sinh\left(2m_2\right)$$

$$+L_{20}\cosh\left(K\right)\cosh\left(m_2\right)-L_{21}\sinh\left(K\right)\sinh\left(m_2\right)+L_{22}\cosh\left(K\right)\sinh\left(m_2\right)$$

$$\left.-L_{23}\sinh\left(K\right)\cosh\left(m_2\right)-L_{24}\cosh\left(2K\right)-L_{25}\sinh\left(2K\right)\right],$$

$$L_1=\left(I_1-\bar{d}_1'H_2\right),\ L_2=\left(I_2-\bar{d}_1'H_1\right),\ L_3=\left(I_3-\bar{d}_1'H_4\right),\ L_4=\left(I_4-\bar{d}_1'H_3\right),$$

$L_5 = \left(I_5 + \bar{d}_1' H_5\right), L_6 = \left(I_6 - \bar{d}_1' H_7\right), L_7 = \left(I_7 - \bar{d}_1' H_6\right), L_8 = \left(I_8 - \bar{d}_1' H_9\right), \; L_9 = \left(I_9 - \bar{d}_1' H_8\right),$
$L_{10} = \left(I_{10} - \bar{d}_1' H_{12}\right), L_{11} = \left(I_{11} - \bar{d}_1' H_{13}\right), L_{12} = \left(I_{12} - \bar{d}_1' H_{10}\right), L_{13} = \left(I_{13} - \bar{d}_1' H_{11}\right),$
$L_{14} = \left(I_{14} - \bar{d}_1' H_{16}\right), L_{15} = \left(I_{15} - \bar{d}_1' H_{17}\right), L_{16} = \left(I_{16} - \bar{d}_1' H_{14}\right), L_{17} = \left(I_{17} - \bar{d}_1' H_{15}\right),$
$L_{18} = \left(I_{18} - \bar{d}_1' H_{19}\right), L_{19} = \left(I_{19} - \bar{d}_1' H_{18}\right), L_{20} = \left(I_{20} - \bar{d}_1' H_{22}\right), L_{21} = \left(I_{21} - \bar{d}_1' H_{23}\right),$
$L_{22} = \left(I_{22} - \bar{d}_1' H_{20}\right), \; L_{23} = \left(I_{23} - \bar{d}_1' H_{21}\right), \; L_{24} = \left(I_{24} - \bar{d}_1' H_{25}\right), \; L_{25} = \left(I_{25} - \bar{d}_1' H_{24}\right)$

Chapter 6. Dynamic Maxwell streaming potential irreversibility flow

6.1. Objectives of the chapter

This study investigates time-dependent velocity distributions in microchannels through the separation of variables technique, addressing both stationery and time-varying flow regimes. The analysis evaluates the influence of viscoelastic relaxation time, interfacial charge density, Hall currents, and ion-slip phenomena on hydrodynamic performance. The available literature shows no prior analysis for streaming potential pressure-driven unsteady flow for the Maxwell fluid model, the requirement for actual flow, heat transfer, and thermal irreversibility in microfluidic sustainability. A time-resolved thermal analysis incorporates discontinuous boundary constraints, resistive Joule heating, and viscous energy dissipation, revealing enhanced heat transfer efficiency in electromagnetic environments. Results show a 1.92% reduction in streaming current with 2% nanoparticles and a promising 809.91% increase in electrokinetic energy conversion efficiency for slip-dependent zeta potential compared to slip-independent zeta potential. The interplay of Hall currents and ion-slip effects further amplifies thermal transport, particularly in systems with tailored electromagnetic field orientations. These insights highlight the potential for precision control of microscale thermal-fluidic systems through multi-physical parameter modulation.

6.2. Physical aspect and mathematical formulation

This research examines heat transfer dynamics in MHD driven streaming flows through a parallel-plate microchannel infused with magnetic-responsive nanofluids. The nanoparticles, uniformly dispersed along the channel walls, attenuate the EDL thickness, altering electrokinetic interactions. Leveraging geometric symmetry, the analysis is confined to the upper half-region ($0 \leq y \leq h$) (see Fig. 6.1). Hydrophobic surfaces with slip-dependent zeta potentials induce a counter-flow streaming potential (E_s), while an externally applied transverse magnetic field (B_y) interacts orthogonally with the flow direction. The porous medium within the channel imposes a Darcy-type drag force, further modulating nanofluid motion. Magnetic nanofluids exhibit fluid-like molecular behavior, enabling precise control via external magnetic fields. This tunability enhances their suitability for applications requiring directed thermal management. Key findings reveal that nanoparticle distribution and magnetic field orientation critically influence thermal gradients, EDL suppression, and hydrodynamic resistance, factors pivotal for optimizing microscale energy systems.

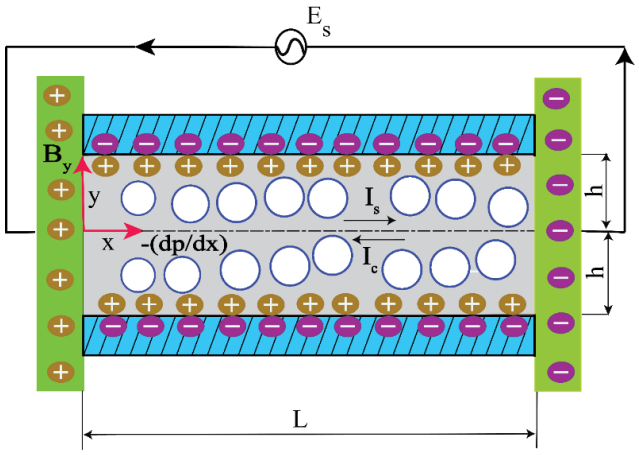

Fig. 6.1 Diagram depicting a microchannel with parallel plates.

6.2.1. EDL potential field

The variation of the EDL potential (Ψ), characterized by a non-variable permittivity, depends on a consistent charge density and is determined by the Poisson-Boltzmann equation [135],

$$\nabla^2\psi = -\left(\frac{\rho_e}{\varepsilon_{eff}}\right); \quad \rho_e = -2n_0 z_v e \sinh\left(\frac{e\, z_v \psi}{k_B T_a}\right) \tag{6.1}$$

In Table 4 outlines the key thermophysical properties, ε_s indicates the dielectric constant of the magnetic particles, whereas ε_f corresponds to that of the base fluid. The densities of the base fluid and magnetic particles are represented by ρ_f , and ρ_s respectively. The electrical conductivities of the nanofluid and the base fluid are expressed by σ_s , σ_f , respectively. The parameter μ_f stands for the viscosity of the base fluid. Additionally, $(k_T)_s$ and $(k_T)_f$ refer to the thermal conductivities of the nanoparticles and the base fluid, respectively.

Table 4
The quantitative relationship between base fluid and magnetic nanoparticles (Fe_3O_4) with volume fraction (ϕ).

The effective permittivity of nanofluids $\left(\varepsilon_{eff}\right)$ is [135],	$\varepsilon_{eff} = \varepsilon_f \left(1 + \dfrac{2\left(\dfrac{\varepsilon_s}{\varepsilon_f} - 1\right)\phi}{\left(\dfrac{\varepsilon_s}{\varepsilon_f} + 2\right) - \left(\dfrac{\varepsilon_s}{\varepsilon_f} - 1\right)\phi} \right)$
The overall density of the nanofluid $\left(\rho_{eff}\right)$ is expressed as [135],	$\rho_{eff} = \rho_f \left((1-\phi) + \dfrac{\rho_s}{\rho_f}\phi \right)$
The overall heat capacity $\left(c_p\right)_{eff}$ of nanofluids is estimated using a heat balance equation [282],	$\left(c_p\right)_{eff} = \dfrac{\left(\rho c_p\right)_f}{\rho_{eff}} \left((1-\phi) + \phi \dfrac{\left(\rho c_p\right)_s}{\left(\rho c_p\right)_f} \right)$
The expression for the effective viscosity of the nanofluids $\left(\mu_{eff}\right)$ is derived from the Brinkmann equation [135],	$\mu_{eff} = \dfrac{\mu_f}{(1-\phi)^{2.5}}$
The effective electrical conductivity of the nanofluids $\left(\sigma_{eff}\right)$, based on the Maxwell model, is defined as [135],	$\sigma_{eff} = \sigma_f \left(1 + \dfrac{3\left(\dfrac{\sigma_s}{\sigma_f} - 1\right)\phi}{\left(\dfrac{\sigma_s}{\sigma_f} + 2\right) - \left(\dfrac{\sigma_s}{\sigma_f} - 1\right)\phi} \right)$
The expression for the effective thermal conductivity of the nanofluids, $\left(k_T\right)_{eff}$, in the Maxwell model is provided as [282],	$\left(k_T\right)_{eff} = \dfrac{\left(k_T\right)_f \left(\dfrac{\left(k_T\right)_s}{\left(k_T\right)_f} + 2 - 2\left(1 - \dfrac{\left(k_T\right)_s}{\left(k_T\right)_f} \right)\phi \right)}{\dfrac{\left(k_T\right)_s}{\left(k_T\right)_f} + 2 + \left(1 - \dfrac{\left(k_T\right)_s}{\left(k_T\right)_f} \right)\phi}$

For the normalization, the following dimensionless parameters are defined as,

$$\bar{\psi} = \left(\frac{e z_v \psi}{k_B T_a} \right) ; \ \bar{\xi} = \left(\frac{e z_v \xi}{k_B T_a} \right) ; \ Y = \left(\frac{y}{h} \right) ; \ K = \left(h/\lambda_D \right) ; \text{ and } \ \varepsilon_r = \left(\frac{\varepsilon_{eff}}{\varepsilon_f} \right) \quad (6.2)$$

Where $\bar{\psi}$ represents the normalised electrical double layer potential, ξ and h are surface potential and half-height of the microchannel shown in Fig. 6.1, respectively. y and Y refer to the dimensional and normalised coordinate perpendicular to flow direction, respectively. K signifies the electrokinetic width and ε_r denotes the ratio of the effective permittivity of the nanofluids to the permittivity of the base fluid.

The notations introduced in Eq. (1.7), along with the governing equations detailed in Eqs. (3.1) to (3.7), provide the foundational framework. Utilizing the transformation defined in Eq. (5.1), Eq. (6.1) is recast into the following scaled representation,

$$\left(\frac{d^2\bar{\psi}}{dY^2}\right)-\left(\frac{K^2}{\varepsilon_r}\right)\bar{\psi}=0 \tag{6.3}$$

The normalization of the slip-induced effects on the surafce potential at the wall is given by, $\bar{\xi}_a=\bar{\xi}\left[1+\left(\bar{a}\,K/\sqrt{\varepsilon_r}\right)\left(\sinh\left(\bar{\xi}\right)/\bar{\xi}\right)\right]$, where The measured surface potential, $\bar{\xi}_a$ varies due to the velocity slip (a) at the microchannel wall, where $\bar{a}\ (=a/h)$ signifies a slip parameter. As noted in prior work [138] the simplified electrostatic framework remains applicable for potentials satisfying $\bar{\xi}_a\le 2$, aligning with weakly charged surface regimes.

Here, $\bar{\psi}|_{Y=1}=\bar{\xi}_a$ is the pertinent boundary condition involving one-dimensional flow for solving Eq. (6.3). The distribution of the EDL potential is then as follows:

$$\bar{\psi}=\bar{\xi}_a\frac{\cosh\left(\frac{K\,Y}{\sqrt{\varepsilon_r}}\right)}{\cosh\left(\frac{K}{\sqrt{\varepsilon_r}}\right)} \tag{6.4}$$

6.2.2. Velocity distribution

The analysis targets the midsection of an elongated microchannel, sufficiently distant from inlet and outlet regions to ensure fully developed, single-directional flow. For non-compressible nanoparticle suspensions under uniform electromagnetic fields, the mass and momentum conservation laws are formulated using vector calculus, as outlined in prior studies [135,239,282],

$$div\,\mathbf{U}=0 \tag{6.5}$$

$$\rho_{eff}\left(\frac{\partial\mathbf{U}}{\partial t}+(\mathbf{U}\cdot\nabla)\mathbf{U}\right)=-\nabla p+\nabla\cdot\boldsymbol{\sigma}-\mu_{eff}\left(\frac{\mathbf{U}}{\kappa_p}\right)+\mathbf{F} \tag{6.6}$$

Where $\mathbf{U}=\left(\hat{\mathbf{i}}u+\hat{\mathbf{j}}v+\hat{\mathbf{k}}w\right)$ denotes the induced velocity vector, t denotes time, $\boldsymbol{\sigma}$ symbolizes the stress tensor. The overall force exerted on fluid-element results from the induced electrical and applied magnetic fields, commonly called the Lorentz force. This force is called an electromagnetic body force $\mathbf{F}=\rho_e\mathbf{E}+\mathbf{J}\times\mathbf{B}$, in which $\mathbf{E}$ represents the electric field generated by charge separation within the fluid. In this context, the system is influenced by an electromagnetic force generated by the superposition of a uniform electric field $\mathbf{E}(\mathrm{E_s},0,0)$ oriented along the flow direction

(x-axis), and a perpendicular magnetic field $\mathbf{B}\left(0, \mathrm{B}_y, 0\right)$ applied vertically along the y-axis.
The Ohm's law provides a current density vector **J** as [281],

$$\mathbf{J} = \sigma_{eff}\left(\mathbf{E}+\mathbf{U}\times\mathbf{B}\right)-\frac{\omega_e\tau_e}{B_y}\left(\mathbf{J}\times\mathbf{B}\right)+\frac{\omega_e\tau_e\alpha_s}{B_y^2}\left[\left(\mathbf{J}\times\mathbf{B}\right)\times\mathbf{B}\right] \tag{6.7}$$

Here, τ_e is the electron collision time. $\omega_e\left(=eB_y/m_e\right)$ is the cyclotron frequency, m_e is the electron mass, α_s represents the ion displacement factor, and $\alpha_e\left(=\omega_e\tau_e\right)$ defines the Hall effect strength.
The expressions for current density component are as follows,

$$J_x = \alpha_1\sigma_{eff}B_y u+\alpha_2\sigma_{eff}B_y E_s,\ J_y = 0\text{, and } J_z = -\alpha_1\sigma_{eff}B_y E_s+\alpha_2\sigma_{eff}B_y u \tag{6.8}$$

where $\alpha_1 = \dfrac{\alpha_e}{\left(1+\alpha_e\alpha_s\right)^2+\alpha_e^2}$,and $\alpha_2 = \dfrac{1+\alpha_e\alpha_s}{\left(1+\alpha_e\alpha_s\right)^2+\alpha_e^2}$ are the constant. Eq. (6.8) captures the interplay of electric field, magnetic field, and fluid velocity, comprehensively describing current density in magnetohydrodynamic systems.

Simplifying Eq. (6.6) in the presence of the hydrodynamic electromagnetic field in the x-direction yields,

$$\rho_{eff}\left(\frac{\partial u}{\partial t}\right) = -\frac{\partial p}{\partial x}+\frac{\partial\sigma_{xy}}{\partial y}+\rho_e E_s+\alpha_1\sigma_{eff}B_y E_s-\alpha_2\sigma_{eff}B_y^2 u-\mu_{eff}\left(\frac{u}{\kappa_p}\right) \tag{6.9}$$

Where u is a y-component fluid speed. Different models are used to explain the constitutive behavior of a viscoelastic non-Newtonian fluid. E_s is the streaming potential, B_y is the magnetic force in y direction, and K represents the permeability within the porous matrix. σ_{xy} refers to shear stress in xy plane.
In this study, we opted for the Maxwell model [239], represented as,

$$\sigma_{xy}+\lambda_1\left(\partial\sigma_{xy}/\partial t\right) = \mu_{eff}\left(\partial u/\partial y\right) \tag{6.10}$$

where λ_1 is the relaxation time. The following are the definitions of the normalized parameters and variables used in the transport equation,

$$U = \frac{u}{u_{ref}}\ ;\ Ha = hB_y\sqrt{\frac{\sigma_f}{\mu_f}}\ ;\ \Gamma = \frac{h^2\left(-\partial p/\partial x\right)}{\left(\mu_f u_{ref}\right)}\ ;\ \tau = \frac{\left(t\,\mu_f\right)}{\left(\rho_f h^2\right)}\ ;\ \Omega = \frac{E_{ref}}{\left(u_{ref}B_y\right)}\ ;$$

$$Da = \frac{\kappa_p}{h^2}\ ;\ \sigma_r = \frac{\sigma_{eff}}{\sigma_f}\ ;\ \mu_r = \frac{\mu_{eff}}{\mu_f}\ ;\text{and } \bar{E}_s = \frac{E_s}{E_{ref}} \tag{6.11}$$

where u_{ref} is a reference velocity, U represents the dimensionless flow velocity, Within the analytical framework, the term $\left(-\partial p/\partial x\right)$ signifies the axial pressure gradient propelling fluid motion in the positive x-direction. The dimensionless parameter Γ reflects the proportional interplay between pressure-driven and electroosmotic forces. Ω characterizes the scaled electric field component induced by Hall current dynamics, while τ is the normalised physical time. The ratios ρ_r , μ_r σ_r describe the relative effective properties of the nanofluid compared to the base fluid. For density ρ_r , for dynamic viscosity μ_r , and σ_r for electrical conductivity. These ratios are critical for modeling the enhanced thermophysical behavior of nanofluids under electromagnetic fields. Hartmann number is denoted as Ha , and Darcy number is represented by Da . $\bar{E}_s$ normalised induced electric field by streaming potential.

The constitutive Maxwell Eq. (6.10) in its dimensionless form is expressed as,

$$T_{xy}+\bar{\lambda}_1\frac{\partial T_{xy}}{\partial \tau}=\mu_r\frac{\partial U}{\partial Y} \tag{6.12}$$

where $\mathrm{T}_{xy}=\left(\sigma_{xy}\,h\right)\Big/\left(\mu_f\,u_{ref}\right)$ is the normalized shear stress. The parameter $\bar{\lambda}_1=\left(\lambda_1\,\mu_f\right)\Big/\left(\rho_f\,h^2\right)$ is expressed as the ratio between a fluid's relaxation and viscous time. Analyzing this parameter's characteristic values enables the relative significance of the elastic and viscous effects in the fluid to be determined. For this case, the Maxwell model reduces to the Newtonian model when $\bar{\lambda}_1=0$. Moreover, we assume that the fluid is not in motion at the beginning of the process.

We simplify Eq. (6.9) using Eqs. (6.10), and (6.11), and express it in a normalized form,

$$\rho_r\left(\frac{\partial U}{\partial \tau}\right)=\Gamma+\frac{\partial T_{xy}}{\partial Y}+\alpha_1\,\sigma_r\,\bar{E}_s\,\Omega\,Ha^2-\alpha_2\,\sigma_r\,Ha^2\,U$$
$$-\mu_r\left(\frac{U}{Da}\right)-\frac{K^2\,\bar{E}_s\bar{\xi}_a\cosh\left(K\,Y\Big/\sqrt{\varepsilon_r}\right)}{\cosh\left(K\Big/\sqrt{\varepsilon_r}\right)} \tag{6.13}$$

Hence, the dimensionless initial condition is utilized to solve Eq. (6.13), $U\big|_{\tau=0}=0$ and $\left(\partial U/\partial\tau\right)\big|_{\tau=0}=0$. The speed satisfies a mirror image concerning the axis passing through the midpoint along the conduit. Under such conditions, the flow speed gradient at that section vanishes, $\left(\partial U/\partial Y\right)\big|_{Y=0}=0$. Furthermore, the condition accounting for wall slip can be applied to represent the slip velocity (b) at the inner surface of the channel wall, expressed as $U+\bar{a}\left(\partial U/\partial Y\right)\big|_{Y=1}=0$. Utilizing the Maxwell constitutive equation, we can exclusively express momentum written in Eq. (6.13) in terms of the velocity field. To solve Eq. (12), we used non-dimensional

initial boundary conditions of shear stress, $T_{xy}\big|_{\tau=0}=0$. To achieve this, we derive the Maxwell constitutive equation concerning the dimensionless transverse coordinate once, resulting in,

$$\frac{\partial T_{xy}}{\partial Y}+\bar{\lambda}_1\frac{\partial^2 T_{xy}}{\partial Y\partial\tau}=\mu_r\frac{\partial^2 U}{\partial Y^2} \tag{6.14}$$

The combination of Eqs. (6.13) and (6.14) yields the subsequent equation,

$$\rho_r\frac{\partial^2 U}{\partial\tau^2}=\Gamma+\left(\mu_r\frac{\partial^2 U}{\partial Y^2}-\bar{\lambda}_1\frac{\partial^2 T_{xy}}{\partial Y\partial\tau}\right)-\mu_r\left(\frac{U}{Da}\right)+\alpha_1\sigma_r\bar{E}_s\Omega Ha^2$$
$$-\alpha_2\sigma_r Ha^2U-\frac{K^2\bar{E}_s\,\bar{\xi}_a\cosh\left(KY/\sqrt{\varepsilon_r}\right)}{\cosh\left(K/\sqrt{\varepsilon_r}\right)} \tag{6.15}$$

Differentiating Eq. (6.13) with respect to normalized time and substituting the result into Eq. (6.15) yields the subsequent non-homogeneous momentum equation is expressed in a modified form for the Maxwell model as follows:

$$\rho_r\left(\frac{\partial U}{\partial\tau}\right)=\Gamma+\mu_r\left(\frac{\partial^2 U}{\partial Y^2}\right)-\left(\bar{\lambda}_1\rho_r\right)\left(\frac{\partial^2 U}{\partial\tau^2}\right)-\bar{\lambda}_1\left(\frac{\mu_r}{Da}\right)\left(\frac{\partial U}{\partial\tau}\right)-\left(\alpha_2\sigma_r\bar{\lambda}_1 Ha^2\right)\left(\frac{\partial U}{\partial\tau}\right)$$
$$+\alpha_1\sigma_r\bar{E}_s\Omega Ha^2-\alpha_2\sigma_r Ha^2U-\mu_r\left(\frac{U}{Da}\right)-\frac{K^2\bar{E}_s\,\bar{\xi}_a\cosh\left(KY/\sqrt{\varepsilon_r}\right)}{\cosh\left(K/\sqrt{\varepsilon_r}\right)} \tag{6.16}$$

The superposition property is employed for the separation of variables and to obtain an exact analytical solution for Eq. (6.16). Achieving this solution is necessary to convert the homogeneous equations using new variables, such as $U(Y,\tau)=U_1(Y)+U_2(Y,\tau)$, where the components of the flow speed $U(Y,\tau)$ can be described as $U_1(Y)$ plus $U_2(Y,\tau)$ corresponding to the steady state and transient velocity, respectively. Utilizing the separation of dependent variables based on Eq. (6.16) can be expressed as follows:

$$\frac{d^2U_1}{dY^2}-C_1^2U_1+C_2-\frac{K^2\bar{E}_s\,\bar{\xi}_a\cosh\left(KY/\sqrt{\varepsilon_r}\right)}{\mu_r\cosh\left(K/\sqrt{\varepsilon_r}\right)}=0 \tag{6.17}$$

and,

$$\frac{\partial^2 U_2}{\partial Y^2}-\left(\bar{\lambda}_1C_1^2+C_3\right)\left(\frac{\partial U_2}{\partial\tau}\right)-C_3\bar{\lambda}_1\left(\frac{\partial^2 U_2}{\partial\tau^2}\right)-C_1^2U_2=0 \tag{6. 18}$$

The conditions at the beginning and boundaries of the problem are outlined as follows:

$$\left(U_1 + \bar{a}\frac{dU_1}{dY}\right)\Big|_{Y=1} = 0 \text{ and } \left(\frac{dU_1}{dY}\right)\Big|_{Y=0} = 0 \tag{6.19}$$

$$U_2|_{\tau=0} = 0\,,\ \left(\frac{\partial U_2}{\partial Y}\right)\Big|_{Y=0} = 0\,, \text{and } \left(U_2 + \bar{a}\frac{\partial U_2}{\partial Y}\right)\Big|_{Y=1} = 0 \tag{6.20}$$

where $C_1 = \sqrt{\left(\left(\alpha_2\,\sigma_r\,Ha^2\right)/\mu_r + 1/Da\right)}$ and $C_2 = \left(\Gamma + \alpha_1\,\sigma_r\,\bar{E}_s\,Ha^2\,\Omega\right)/\mu_r$ are the non-dimensional parameters. While imposing boundary conditions in Eq. (6.19) to solve Eq. (6.17), the steady-state velocity is obtained as,

$$U_1 = A_1\cosh\left(C_1 Y\right) + \frac{C_2}{C_1^2} - A_3\cosh\left(\frac{K\,Y}{\sqrt{\varepsilon_r}}\right) \tag{6.21}$$

The values of A_1, A_2, and A_3 are introduced specifically to simplify the mathematical formulation of Eq. (6.21). These constants reduce the equation's complexity by consolidating multiple terms into a more compact and computationally efficient form.

$$A_1 = \frac{A_2}{\cosh\left(C_1\right) + \bar{a}\,C_1\sinh\left(C_1\right)}\,,$$

$$A_2 = -\frac{C_2}{C_1^2} - \frac{\tanh\left(\dfrac{K}{\sqrt{\varepsilon_r}}\right)\left(\bar{a}\,K^3\,\bar{E}_s\,\bar{\xi}_a\,\sqrt{\varepsilon_r}\right)}{\mu_r\left(K^2 - C_1^2\,\varepsilon_r\right)} - \frac{\left(K^2\,\varepsilon_r\,\bar{E}_s\,\bar{\xi}_a\right)}{\mu_r\left(K^2 - C_1^2\,\varepsilon_r\right)}\,,$$

$$\text{and } A_3 = \frac{K^2\varepsilon_r\bar{E}_s\bar{\xi}_a}{\mu_r\left(K^2 - C_1^2\varepsilon_r\right)\cosh\left(\dfrac{K}{\sqrt{\varepsilon_r}}\right)} \tag{6.22}$$

The product method can be applied to solve Eq. (6.18) to determine $U_2(Y,\tau)$. The product method assumes that $U_2(Y,\tau)=F(Y)G(\tau)$. Using the relationship above, Eq. (6.18) can be expressed by separating the two variables as follows:

$$\frac{d^2F}{dY^2} + \lambda^2 F = 0\,,\ \left(\frac{dF}{dY}\right)\Big|_{Y=0} = 0\,, \text{ and } \left(F + \bar{a}\frac{dF}{dY}\right)\Big|_{Y=0} = 0 \tag{6.23}$$

$$\frac{d^2G}{d\tau^2} + \frac{\left(\bar{\lambda}_1 C_1^2 + C_3\right)}{\left(\bar{\lambda}_1 C_3\right)}\left(\frac{dG}{d\tau}\right) + G\frac{\left(\lambda^2 + C_1^2\right)}{\left(C_3\bar{\lambda}_1\right)} = 0 \text{ and } \left(\frac{dG}{d\tau}\right)\Big|_{\tau=0} = 0 \tag{6.24}$$

The following relationship is derived from Eq. (6.23) as $\cot(\lambda_n) - \bar{a}\lambda_n = 0$, where $C_3(=\rho_r/\mu_r)$ is a constant parameter. The Newton-Raphson iterative method is employed for solving the transcendental equation and obtaining the Eigenvalues λ_n. Arbitrary constants m_1, and m_2 can be obtained from Eq. (6.24) as,

$$m_1 = -\Delta + i\chi \; ; \; m_2 = -\Delta - i\chi \; ; \; \Delta = \frac{\left(\bar{\lambda}_1 C_1^2 + C_3\right)}{\left(2C_3\bar{\lambda}_1\right)} \; ;$$

$$\Delta = \frac{\left(C_1^2 + \lambda_n^2\right)}{\left(2C_3\bar{\lambda}_1\right)} \; ; \text{and} \; \chi = \sqrt{\left(2\Delta - \Pi^2\right)} \tag{6.25}$$

So, the determined transient velocity component $U_2(Y,\tau)$ is from combining Eqs. (6.23), (6.24), and (6.25) as,

$$U_2(\mathrm{Y},\tau) = \sum_{n=1}^{\infty} d_n \cos\left(\lambda_n Y\right) e^{-\Pi\tau}\left(\cos\left(\chi\tau\right) + \frac{\Delta}{\chi}\sin\left(\chi\tau\right)\right) \tag{6.26}$$

Where d_n is determined using the orthogonality property associated with the separation of variables method as follows:

$$d_n = \frac{-4\lambda_n}{2\lambda_n + \sin\left(2\lambda_n\right)}\left(\begin{array}{l} A_3\left\{\begin{array}{l}\dfrac{\varepsilon_r\lambda_n\cosh\left(\dfrac{K}{\sqrt{\varepsilon_r}}\right)\sin\left(\lambda_n\right)}{\left(\varepsilon_r\lambda_n^2 + K^2\right)} \\ + \dfrac{\sqrt{\varepsilon_r}K}{\left(\varepsilon_r\lambda_n^2 + K^2\right)}\left(\sinh\left(\dfrac{K}{\sqrt{\varepsilon_r}}\right)\cos\left(\lambda_n\right)\right)\end{array}\right\} \\ + A_1\left\{\begin{array}{l}\dfrac{\lambda_n\cosh\left(C_1\right)\sin\left(\lambda_n\right)}{\left(\lambda_n^2 + C_1^2\right)} \\ + \dfrac{C_1}{\left(\lambda_n^2 + C_1^2\right)}\sinh\left(C_1\right)\cos\left(\lambda_n\right)\end{array}\right\} \\ + \dfrac{\mathrm{C}_2\sin\left(\lambda_n\right)}{C_1^2\lambda_n}\end{array}\right) \tag{6.27}$$

The combination of Eqs. (6.21), and (6.26) results in an analytical expression for the non-dimensional velocity:

$$U(Y,\tau)=A_1\cosh(C_1Y)+\frac{C_2}{C_1^2}-A_3\cosh\left(\frac{KY}{\sqrt{\varepsilon_r}}\right)$$
$$+\sum_{n=1}^{\infty}d_n\cos(\lambda_nY)e^{-\Pi\tau}\left(\cos(\chi\tau)+\frac{\Delta}{\chi}\sin(\chi\tau)\right) \quad (6.28)$$

We used the integration approach about the variable to obtain the following expression for the normalized volumetric flow rate per unit width of the channel,

$$Q(\tau)=\frac{q(t)}{2hu_{ref}}=\int_{Y=0}^{1}U(Y,\tau)dY \quad (6.29)$$

where $q(t)$ is the volume flow rate per unit width as a function of time, derived from Eqs. (6.28) and (6.29).

$$Q(\tau)=\frac{A_1}{C_1}\sinh(C_1)+\frac{C_2}{C_1^2}-\frac{A_3\sqrt{\varepsilon_r}}{K}\sinh(K)$$
$$+\sum_{n=1}^{\infty}\frac{d_n}{\lambda_n}\sin(\lambda_n)e^{-\Pi\tau}\left(\cos(\chi\tau)+\frac{\Delta}{\chi}\sin(\chi\tau)\right) \quad (6.30)$$

6.3. Streaming potential and efficiency of EKEC

Imposing a pressure differential across a planar microchannel configuration triggers an electrokinetic streaming potential. To compute this potential, the previously resolved velocity profiles are utilized. Within the electric double layer (EDL), advective transport drives excess counter-ions toward the flow direction, establishing an axial potential gradient. This streaming current is counteracted by the conduction current contributions (bulk electrolyte and Stern layer), which facilitate opposing charge transfer. The streaming potential magnitude is derived under the global electroneutrality constraint, ensuring that under steady-state conditions, the net ionic flux across the channel vanishes [133],

$I_{net}=I_{sterm}+I_{conduction}+I_{stern}=0$ (6.31)

The details of I_{sterm}, $I_{conduction}$, I_{stern} are provided in Eqs. (5.19) -(5.21)
Eq. (5.21) is integrated and expressed as,

$$\bar{E}_s=\frac{B_1}{\alpha(1+Du)-B_2} \quad (6.32)$$

The coefficients B_1, and B_2 in Eq. (6.32) are defined, respectively as,

$$B_1=\left(\frac{\Gamma}{\mu_rC_1^2\left(\cosh(C_1)+\bar{a}C_1\sinh(C_1)\right)}\right)(-C_4+C_5)+\frac{(\Gamma C_6)}{\mu_r}\text{ and}$$

$$B_2 = \frac{1}{\left(\cosh\left(C_1\right)+\bar{a}C_2\sinh\left(C_1\right)\right)}\left[\begin{array}{l}\dfrac{\left(\alpha_1\sigma_r Ha^2\Omega\right)}{\left(\mu_r C_1^2\right)}\left(-C_4+C_5\right)\\ -\dfrac{\bar{\xi}_a K^2}{\left(K^2-C_1^2\varepsilon_r\right)}\begin{pmatrix}-\varepsilon_r C_4-\bar{a}K\sqrt{\varepsilon_r}C_4\\ +\varepsilon_r C_5+\bar{a}K\sqrt{\varepsilon_r}C_5\end{pmatrix}\end{array}\right]$$

$$+\frac{\left(C_6\alpha_1\sigma_r Ha^2\Omega\right)}{\mu_r} \tag{6.35}$$

where the notations C_4, C_5, C_6, C_7, and C_8 are used to simplify Eq. (6.35) as follows:

$$C_4 = \frac{\left(\bar{\xi}_a K\sqrt{\varepsilon_r}\right)}{\left(K^2-C_1^2\varepsilon_r\right)}\tanh\left(\frac{K}{\sqrt{\varepsilon_r}}\right)\cosh\left(C_1\right),\ C_5 = \frac{\left(\bar{\xi}_a C_1\varepsilon_r\right)}{\left(K^2-C_1^2\varepsilon_r\right)}\sinh\left(C_1\right),$$

$$C_6 = \frac{\left(\bar{\xi}_a\sqrt{\varepsilon_r}\right)}{\left(C_1^2K\right)}\tanh\left(\frac{K}{\sqrt{\varepsilon_r}}\right),\ C_7 = \frac{K^2\varepsilon_r\bar{\xi}_a^2}{2\mu_r\cosh^2\left(K/\sqrt{\varepsilon_r}\right)\left(K^2-C_1^2\varepsilon_r\right)}\text{, and}$$

$$C_8 = \frac{\left(K\bar{\xi}_a^2\varepsilon_r\sqrt{\varepsilon_r}\right)}{2\mu_r\left(K^2-C_1^2\varepsilon_r\right)}\tanh\left(\frac{K}{\sqrt{\varepsilon_r}}\right) \tag{6.36}$$

where $\alpha\left(=\dfrac{\mu_f\sigma_B}{\left(2n_0\varepsilon_f k_b T_a\right)}\right)$ is the ionic Péclet number and $Du\left(=\dfrac{\sigma_{stern}}{h\sigma_B}\right)$ is a Dukhin number. Eqs. (6.34), (6.35), and (6.36) reflect the influence of the non-dimensional streaming potential, ionic friction factor, and Dukhin number on the system's behavior.

Streaming potential is essential to calculate the electrokinetic energy conversion, which converts mechanical energy into electrical power. Electrokinetic energy conversion is a promising technology, which designing energy converters with a high conversion efficiency is highly desirable [237],

$$\eta_c = \frac{\mathrm{P}_{out}}{\mathrm{P}_{in}} = \frac{\left|\dfrac{I_s}{2}\dfrac{E_s}{2}\right|}{\left|-\dfrac{dp}{dx}q\right|_{E_s=0}\Big|} \tag{6.37}$$

where P_{out}, P_{in}, and $q\big|_{E_s=0}$ represent the output power, input power, and volume flow rate, respectively without the influence of streaming potential.

6.3.1. Temperature distribution

Employing the velocity distribution of a Maxwell fluid, we can address the energy balance equation to derive the temperature distribution within the microchannel. The thermal equation for the electrolyte solution in the microchannel is as follows [282],

$$\rho_{eff}\left(c_p\right)_{eff}\left(\frac{\partial T}{\partial t}+\mathbf{U}\cdot\nabla T\right)=\left(k_T\right)_{eff}\nabla^2 T+\frac{\mathbf{J}\cdot\mathbf{J}}{\sigma_{eff}}+\Phi \tag{6.38}$$

Φ represents the viscous dissipation of the nanofluid in accordance with the Darcy flow model for porous media, which can be articulated as [282], $\Phi=\boldsymbol{\sigma}:\Delta\mathbf{U}+\mu_{eff}\frac{\left(\mathbf{U}\right)^2}{\kappa_p}$. In the case of transient flow, Eq. (6.38) transforms to,

$$\underbrace{\rho_{eff}\left(c_p\right)_{eff}\frac{\partial T}{\partial t}}_{\text{local term}}=\underbrace{\left(k_T\right)_{eff}\frac{\partial^2 T}{\partial y^2}}_{\text{conductive term}}+\underbrace{\boldsymbol{\sigma}:\Delta\mathbf{U}}_{\text{viscous dissipation term of Maxwell fluid}}+\underbrace{\mu_{eff}\frac{\left(\mathbf{U}\right)^2}{k_p}}_{\text{porous media term}}+\underbrace{\left(\alpha_1^2+\alpha_2^2\right)}_{\text{Hall current and ion slip terms}}\left(\underbrace{\sigma_{eff}E_s^2}_{\text{Joule heating term}}+\underbrace{\sigma_{eff}B_y^2u^2}_{\text{magnetic term}}\right) \tag{6.39}$$

Here, c_p represents the specific heat at constant pressure and T denotes the local temperature of the fluid. We employed a subsequent non-dimensional initial boundary condition to solve Eq. (6.39), $\theta\big|_{\tau=0}=0$. Symmetric and thermal boundary conditions for a jump length (d) at the surface become as follows: $\left(\partial\theta/\partial Y\right)\big|_{Y=0}=0$ and $\theta+\bar{d}\left(\partial\theta/\partial Y\right)\big|_{Y=1}=0$. The dimensionless temperature is defined as $\theta=\left(k_T\right)_f\left(T_w-T\right)/\left(q_w h\right)$ and $\bar{d}$=d/h is a dimensionless jump parameter. T_w is the surface temperature and q_w is the constant wall heat flux. Therefore, the above non-dimensional parameters provide a non-dimensional energy equation obtained from Eq. (6.39) as,

$$\rho_r\left(c_p\right)_r\mathrm{Pr}\frac{\partial\theta}{\partial\tau}=k_r\frac{\partial^2\theta}{\partial Y^2}-\beta_1\sigma_r J_h-\beta_1\sigma_r Ha^2 BrU^2 -\mu_r Br\left(\frac{\partial U}{\partial Y}\right)^2+\bar{\lambda}_1\frac{\partial U}{\partial Y}\frac{\partial T_{xy}}{\partial\tau}-\frac{\mu_r}{Da^2}BrU^2 \tag{6.40}$$

where, $\mathrm{Pr}=\left(\mu\ c_p\right)_f/\left(k_T\right)_f$ refers the Prandtl number, $\left(c_p\right)_r=\left(c_p\right)_{eff}/\left(c_p\right)_f$ is the proportionality between the nanofluid's effective heat capacity,

$k_r = \left((k_T)_{eff} / (k_T)_f \right)$ denotes relative effective heat conduction capacity of the nanofluid to the base fluid, $J_h = \left(\sigma_f E_s^2 h \right) / q_w$ represents the volumetric heat generation rate from electrical resistive effects, and The Brinkman number is defined as, $Br = \left(\mu_f u_{ref}^2 \right) / (q_w h)$. The Nusselt number (Nu) is computed using the dimensionless average bulk temperature (θ_m), derived from the integral expression [132],

$$\theta_m = \int_0^1 U\theta dY \Big/ \int_0^1 U dY \tag{6.41}$$

The energy transfer parameter depends on the expression for the Nusselt number $Nu \left(= h_c h / (k_T)_f \right)$. Here, h_c refers to the coefficient of convective heat exchange. The Nusselt number at the wall of the microchannel referenced to its half-height is determined by the following expression:

$$Nu = -\frac{(k_T)_r}{\theta_m} \left(\frac{\partial \theta}{\partial Y} \right) \Bigg|_{Y=1} \tag{6.42}$$

To assess the influence of streaming potential on heat transfer, a dimensionless parameter η_h is evaluated, represented by the ratio of the Nusselt number considering streaming potential $\left(Nu|_{\bar{E}_s \neq 0} \right)$ to the Nusselt number when no streaming potential is present $\left(Nu|_{\bar{E}_s = 0} \right)$. This ratio provides a quantitative measurement of how electroviscous effects influence heat transfer performance [243],

$$\eta_h = \frac{Nu|_{\bar{E}_s \neq 0}}{Nu|_{\bar{E}_s = 0}} \tag{6.43}$$

6.3.2. Entropy generation analysis

The entropy production rate in parallel plate microchannels, a measure of thermodynamic irreversibility, is determined by the velocity and temperature profiles under combined contributions from of thermal gradients, resistive heating, electro-magnetic field, and viscous friction force, respectively [285].

$$s_g = \frac{k_{eff}}{T^2} \left(\frac{\partial T}{\partial y} \right)^2 + \frac{\beta_1 \sigma_{eff} E_s^2}{|T|} + \frac{\beta_1 \sigma_{eff} B_y^2 u^2}{|T|} + \frac{\sigma_{xy}}{|T|} \frac{\partial u}{\partial y} + \frac{\mu_{eff}}{|T|} \left(\frac{u^2}{k_p} \right) \tag{6.44}$$

The characteristics entropy transfer rate $(k_T)_f / h^2$ is employed to derive the normalized entropy generation rate from Eq. (6.44) as follows:

$$S_G = \frac{s_g h^2}{(k_T)_f} = \frac{k_r}{(\theta-\Theta)^2}\left(\frac{\partial\theta}{\partial Y}\right)^2 + \frac{\beta_1 \sigma_r J_h}{|(\theta-\Theta)|} + \frac{\beta_1 \sigma_r Ha^2 Br U^2}{|(\theta-\Theta)|} + \frac{\mu_r Br}{|(\theta-\Theta)|}\left[\left(\frac{\partial U}{\partial Y}\right)^2 + \frac{U^2}{Da^2}\right] + \frac{\bar{\lambda}_1}{|\theta-\Theta|}\left[\left(\frac{\partial U}{\partial Y}\right)\left(\frac{\partial T_{xy}}{\partial \tau}\right)\right] \tag{6.45}$$

Where Θ is the temperature ratio, $(k_T)_f T_w / (q_w h)$. The overall cumulative entropy generation (S_G) of thermodynamic systems, acquired through the integration of total entropy production over the entire domain, is normalized as follows:

$$S_{total} = 2\int_0^1 S_G \tag{6.46}$$

The Bejan number (*Be*), a crucial irreversibility parameter, is defined as the ratio of entropy generation from heat transfer to the global entropy generation rate,

$$Be = \frac{\dfrac{k_r}{(\theta-\Theta)^2}\left(\dfrac{\partial\theta}{\partial Y}\right)^2}{S_G} \tag{6.47}$$

The Bejan number quantifies the relative irreversibility of heat transfer and fluid friction and ranges from 0 to 1. Also, $Be > 0.5$ indicates that entropy generation due to heat transfer is the dominant mode of irreversibility in the system, while a $Be < 0.5$ indicates that fluid friction irreversibility prevails.

Eqs. (6.40), (6.45), and (6.47) are solved, simultaneously through an implicit solution employing the finite difference method. We employed TDMA to determine all the unknowns by solving the complete algebraic linear system equations. The numerical integration of Eqs. (6.41) and (6.46) is carried out using the Simpson 1/3rd rule. An introduced tolerance of 10^{-6} ensures result stability, confirming that the results remain consistent up to six decimal places.

The implicit scheme of discretization is unconditionally stable for the energy Eq. (6.40). The global error is proportional to $O(\Delta Y^2, \Delta\tau)$, where reducing ΔY and $\Delta\tau$ ensures correct results. To confirm the necessary convergence, the results are verified by checking the difference between successive time steps j and j+1 at grid point p.

$$\left(\theta_p^{j+1} - \theta_p^j\right) < tolerance \tag{6.48}$$

To ensure convergence, the Nusselt number and entropy generation values in Eqs. (6.42), and (6.45) are checked for successive grid refinements as,

$$\left(Nu_{p+1} - Nu_p\right) < tolerance\,,\ \left(S_{G,p+1} - S_{G,p}\right) < tolerance \tag{6.49}$$

6.4. Parameter estimation

This study considers the working nanoparticle and base fluid as Fe_3O_4 and water, respectively. These magnetic oxide nanoparticles are relatively small, they can be easily controlled by combined Hall parameters, ion slip, and magnetic parameters. Table 5 presents the quantitative relationship between the base fluid and magnetic nanoparticles (Fe_3O_4) with the volume fraction of nanoparticles. For the numerical calculation of the present study, the typical values of physical parameters for transient Maxwell fluid flow in a porous microchannel are considered, as described in Table 6 and Table 7, unless they have expressly been stated in respective figures. The range of the Hartmann number varies as, $0 \le Ha \le 5$ [132] and the range of the dimensionless quantity of induced electric field changes as, $0 \le \Omega \le 10$ [124]. Dukhin and Darcy's numbers are varied as, $0 \le Du \le 10$ [133], and $0 \le Da \le 1$ [282], respectively. The relaxation time can be assumed to span a broad range as $10^{-3} \le \lambda_1$ [132] and the range of normalized relaxation time sets as, $\bar{\lambda}_1$~0-1. The slip parameter is varied from $0 - 0.04$ for the maximum zeta potential $\bar{\xi}$=1 [138].

With the above ranges, the extreme value of apparent zeta potential is prescribed as, $\bar{\xi}_a \le 2$. The Hall and ion slip parameters are varied as $0 \le \alpha_e \le 1.5$ and $0 \le \alpha_s \le 4$, respectively [281]. Based on the practical design elements, the normalized physical parameters are within the physically acceptable range.

Table 5
Thermo-physical properties of base fluids and magnetic nanoparticles [135,272].

Properties	Substance	
	Base fluids	Magnetic nanoparticles (Fe_3O_4)
$\rho(kgm^{-3})$	1.025×10^{3}	5.18×10^{3}
$\varepsilon(C^2N^{-1}m^{-2})$	6.95×10^{-10}	80
$\mu\ (kgm^{-1}s^{-1})$	1.09×10^{-3}	-
$\sigma\ (sm^{-1})$	0.1	25000
$k_T\ (Wm^{-1}K^{-1})$	0.613	401

Table 6
Typical values of physical parameters taken in the analysis.

Parameters	Values	Unit	Ref.
strength of magnetic field (B_y)	0.01-5	T	[243]
electron charge (e)	1.6×10^{-19}	C	[241]
characteristics half channel height (h)	100	nm	[237]
Boltzmann constant (k_B)	1.381×10^{-23}	JK^{-1}	[135]
characteristics channel length (L)	10^{-2}	m	[237]
electron mass (m_e)	9.1×10^{-31}	kg	[281]
bulk ionic concentration (n_0)	1	$molm^{-3}$	[135]
absolute temperature (T_a)	298	K	[135]
ion valence (z_v)	1	-	[135]
electron collision time (τ_e)	10^{-14}	s	[281]
zeta potential (ξ)	0.025	V	[135]

We calculated the velocity distribution (U) from Eq. (6.28) using the parameters mentioned in Table 7 and they have been defined in Eq. (6.11). The parameters α_e and α_s are explained in Eq. (6.8). The expression of $\bar{\lambda}_1$ is in Eq. (6.12). These dependent parameters are then used to evaluate the streaming potential field. The Du and α parameters determined from the electroneutrality condition in Eq. (6.34), are then used to calculate the streaming potential ($\bar{E}_s$).

The temperature distribution (θ) is determined using the finite difference implicit scheme. For this, we use several key parameters of velocity along with Pr, $\bar{d}$, J_h, and Br. The velocity expressed in Eq. (6.28) is used to compute the temperature distribution, which is then applied to solve the energy equation (Eq. 6.40).

Using the local temperature gradient at the wall, the Nusselt number is determined as a measurement of the convective heat transfer relative to co nductive heat transfer. This heat transfer parameter provides valuable insights into the efficiency of heat transmission within the system, enabling a deeper understanding of thermal performance under the given conditions. The Nusselt number (Nu) distribution as a function of time is calculated based on the temperature distribution provided in Eq. (6.40).

The entropy generation distribution (S_G), outlined in Eq. (6.45) is determined by combining the velocity values from Eq. (6.28), and the temperature values from Eq. (6.40), which has been computed using the Simpson 1/3rd rule for the numerical integration.

Table 7
Normalized values of key physical parameters used in the present results

Parameters	Range/Value	$\bar{\psi}$	$\bar{E}_s$	U	θ	Nu
Electrokinetic width (K)	5-40	√	√	√	√	√
Hartmann number (Ha)	0-5	-	√	√	√	√
Induced electric field (Ω)	10	-	√	√	√	√
Ionic Péclet number (α)	0.5	-	√	√	√	√
Magnetic nanoparticles (Fe_3O_4) volume fraction (ϕ)	0-0.02	√	√	√	√	√
Slip parameter ($\bar{a}$)	0-0.04	√	√	√	√	√
Zeta potential ($\bar{\xi}$)	1	√	√	√	√	√
Hall current parameter (α_e)	0-1.5	-	√	√	√	√
Ion slip parameter (α_s)	0-2	-	√	√	√	√
Dukhin number (Du)	0-10	-	√	√	√	√
Darcy number (Da)	0-1	-	√	√	√	√
Imposed pressure gradient (Γ)	1	-	√	√	√	√
Physical time (τ)	0-20	-	√	√	√	√
Relaxation time ($\bar{\lambda}_1$)	0-1	-	√	√	√	√
Prandtl number (Pr)	7.43	-	-	-	√	√
Temperature jump parameter ($\bar{d}$)	0-0.04	-	-	-	√	√
Brinkmann number (Br)	0-0.1	-	-	-	√	√
Joule heating parameter (J_h)	0-10	-	-	-	√	√
Temperature ratio (Θ)	20	-	-	-	-	-
Governing equations		Eq. (6.4)	Eq. (6.32)	Eq. (6.28)	Eq. (6.40)	Eq. (6.42)

6.5. Validation and verification

Before continuing the comprehensive investigation to generate results, comparing the results with the published literature is essential for correctness purposes. The present study can only be indirectly validated since no prior literature works are available for direct comparison. Hence, certain assumptions have been made for the flow parameters to evaluate the present study uniquely. This study also involves transient

effects, but this influence becomes dry out with increasing time and the analysis approaches to steady-state conditions at a higher time. Figs. 6.2a and 6.2b compare the streaming potential distribution by considering Al_2O_3-water nanofluid properties for the Newtonian fluid ($\bar{\lambda}_1$=0) determined by the present study and investigated by Zhao et al. [220,244] for magnetohydrodynamic flow and the pure pressure-driven flow, respectively. Calculating the normalized streaming potential involves fixing the non-dimensional parameters at specific values, participates as, $\bar{\xi}$=-1, $\bar{\alpha}$=0, Ω=0, $\bar{\lambda}_1\approx$0, Da→∞, α_e=0, and α_s=0. For the pressure-driven flow, the dimensionless parameters are ϕ=0 and Ha≈0. On the other hand, for the magnetohydrodynamic flow, the design parameter is K=30 and the calculated α value is -0.6541. These figures show an excellent correlation between the current results and the existing results. Comparing the results with Zhao et al. [244], the maximum deviation presented in Table A located in Appendix A, is 0.35%. The comprehensive agreement of findings identifies the proper analysis performed in the tested situation, indicating a correctness aspect.

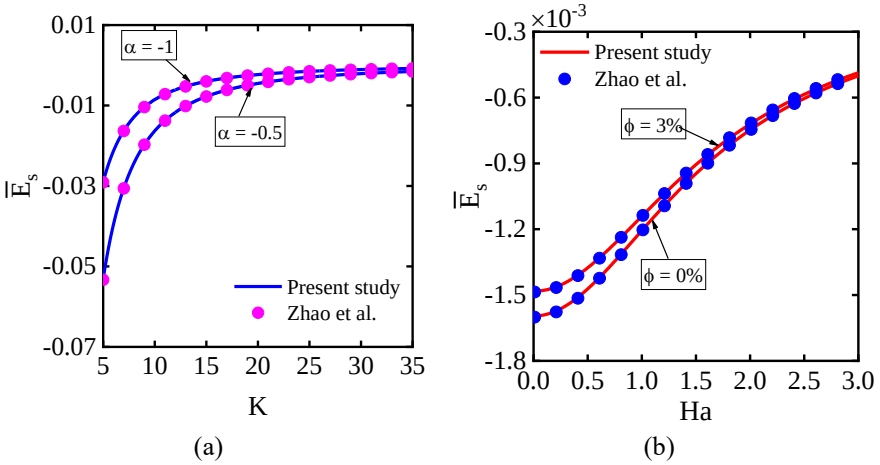

Fig. 6.2 Validation of dimensionless streaming potential: (a) different α with Zhao et al. [244] and (b) different ϕ with Zhao et al. [220].

Figure 6.3 verifies the study's applicability by comparing the velocity results obtained in the current research under the streaming potential flow to the values obtained by Zhao et al. [220,244] analyses, assuming a no-slip state. The findings are validated by utilizing the flow parameters, selecting constant values of $\bar{\xi}$=-1, $\bar{\alpha}$=0, Ha≈0, Ω=0, $\bar{\lambda}_1\approx$0, Da→∞, α_e=0, and α_s=0 while different ϕ (at K=20, and Ha≈0) and Ha (at K=30, and ϕ=0) are used. The velocity profile is calculated for Newtonian fluid and compared with the previous studies. This figure demonstrates the results from the current research align closely with the published data, highlighting the accuracy of the current study. Table B in Appendix B compares velocity at different locations determined by the current study and Zhao et al. [220]. This comparative study shows an insignificant deviation (maximum 0.202%), indicating the current results' accuracy to establish the model.

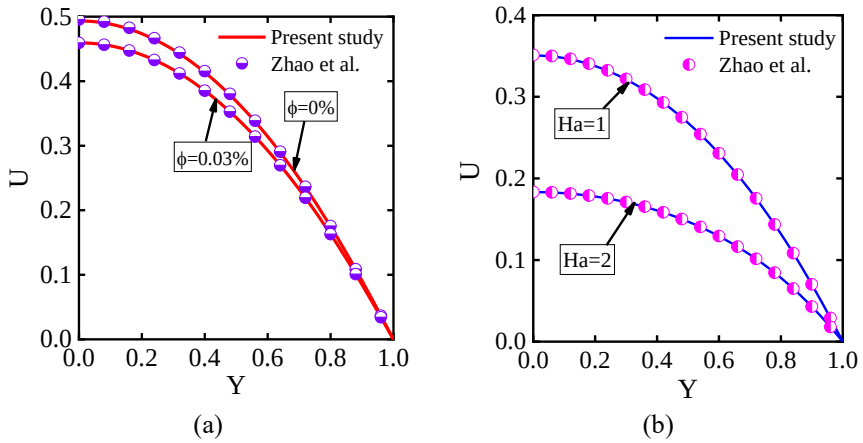

Fig. 6.3 Validation of the present study for velocity distribution for (a) various ϕ with Zhao et al. [244] and (b) various Ha with Zhao et al. [220].

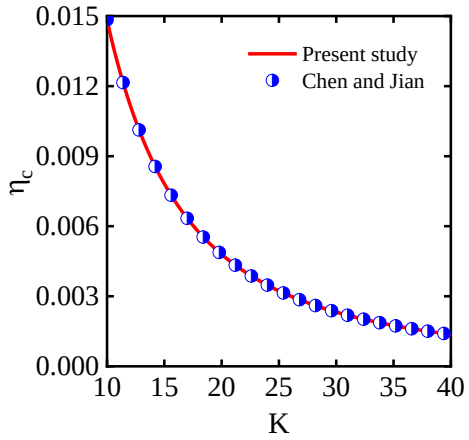

Fig. 6.4 Comparative analysis of the electrokinetic energy conversion efficiency in the current study with that of Chen and Jian [238].

A notable validation is to compare the electrokinetic energy conversion (EKEC) efficiency depicted in Fig. 6.4 of the present findings with the results illustrated by Chen and Jian [238] for a Newtonian fluid. The evaluated EKEC efficiency depends on the non-dimensional parameters as, α=0.3, $\bar{\xi}_a$=1, $\bar{\alpha}$=0, Ha≈0, Ω=0, $\bar{\lambda}_1$≈0, ϕ=2%, Da→∞, α_e=0, and α_s=0. The EKEC efficiency is subsequently computed based on the electrokinetic thickness and compared to the results of a previous study. Furthermore,

the findings robustly substantiate the accuracy of the predictions, revealing a consistent and discernible pattern.

6.6. Results and discussion

This study investigates the transient electrokinetic nanofluid flow inside a parallel plate microchannel with slip dependent zeta potential at the channel walls. The interactive influence of relaxation time, external magnetic field, Hall current, and ion slip is studied graphically on the flow analysis in a hydrophobic microchannel. The variable separation technique is used for fluid flow to conduct analytical research. The analysis determines the normalized distributions of streaming potential, velocity, flow rate, EKEC efficiency, temperature, Nusselt number, and entropy generation as a function of time. A multi-objective optimization process conducts a range of decision variables to maximize the electroviscous heat transfer rate and minimize the total entropy generation. The analysis is carried out as dependent dimensionless variables and parameters.

6.6.1. Fluid flow of Fe_3O_4-water nanofluids

(i) Streaming potential distribution

Figure 6.5 shows a variation of streaming potential with the Dukhin number (Du) for Maxwell fluid. The plotting is made with various Darcy numbers (Da) under slip-dependent zeta potential to provide a basis for comparison. As the Da amplifies, the flow interruption diminishes, leading to a decline in the magnitude of fluid friction within the porous medium, as shown in Fig. 6.5a. With a surge in Du, the conductivity of the Stem layer rises. The conduction current passes through the Stern layer, and the bulk liquid flow undergoes an amplification. With an elevated Stern layer conductivity, it forges a pathway offering diminished resistance for the flow of conduction current. Streaming and conduction currents through the stern layer reach a state of equilibrium. Hence, a lower streaming potential stabilizes the streaming current and ensures electro-neutrality. As a result, the streaming potential decreases because of the Du while keeping other parameters unchanged. Next, the study focuses on the streaming potential flow of Maxwell fluid for comparison of slippage and no-slippage zeta potentials with the variation of Du for constant parameters of Ha=4, Da=0.1, α_e=0.5, and α_s=1.5. The mathematical relation $\bar{\xi}_a = \bar{\xi}\left[1+\bar{a}\left(K/\sqrt{\varepsilon_r}\right)\sinh\left(\bar{\xi}\right)/\bar{\xi}\right]$ illustrates that $\bar{a}$ increases the electrostatic actuation force. A zeta potential near the EDL zone leads to the generation of ions. Therefore, the flow field exerts a greater driving force on fluid particles and causes an increment of the streaming potential with slip parameters. For Du=0, the peak streaming potential is at $\bar{a}=0.04$. In particular for Du=5, velocity increases significantly by approximately 23.15% in the slip-dependent zeta potential at $\bar{a}=0.01$, compared to that at $\bar{a}=0$, as shown in Fig. 6.6b.

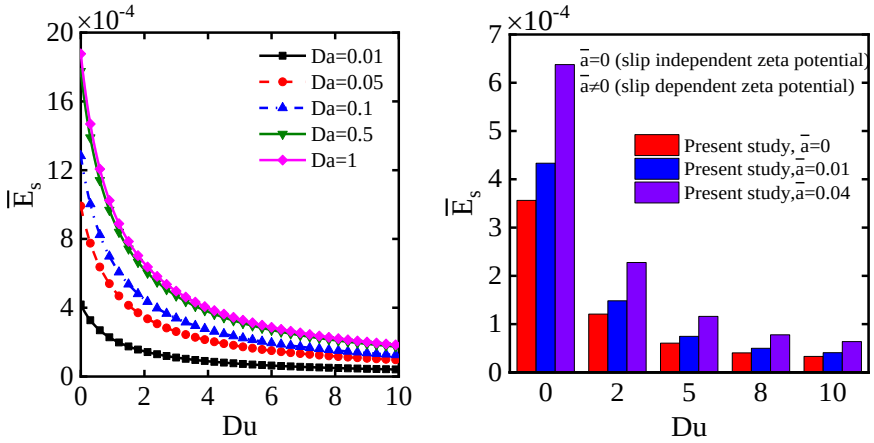

Fig. 6.5 Variation of the streaming potential distribution at slip dependent porous medium channel as a function of Du for K=20, α=0.5, ϕ=2%, α_e=0.5, α_s=1.5, and Ha=4 (a) for different values of Da, (b) comparison of slip dependent and slip independent zeta potentials.

To illustrate the impact of nanoparticle volume fraction, Fig. 6.6 depicts the distribution of streaming current with Hall current and ion slip. An increase in the volume fraction of nanoparticles declines the streaming current. The streaming current for adding 2% nanoparticles decreases by 1.92% at α_e=0.5 and α_s=1.5 compared without nanoparticles in base fluid. This trend is primarily because of the elevated concentration of nanoparticles increased the nanofluid's effective viscosity under the influence of shear rate. The Hall effect appears due to the Lorentz force acting on the moving charges in the presence of a magnetic field, which is presented in Fig. 6.6a. In the context of a fluid with charge particles flow through a microchannel, the interplay of the magnetic field and the moving charges can lead to an increase in streaming current. Conversely, ion slip occurs from an external magnetic field that generates an electric field effectively boosting the mobility of ions and thereby increasing the streaming potential (Fig. 6.6b).

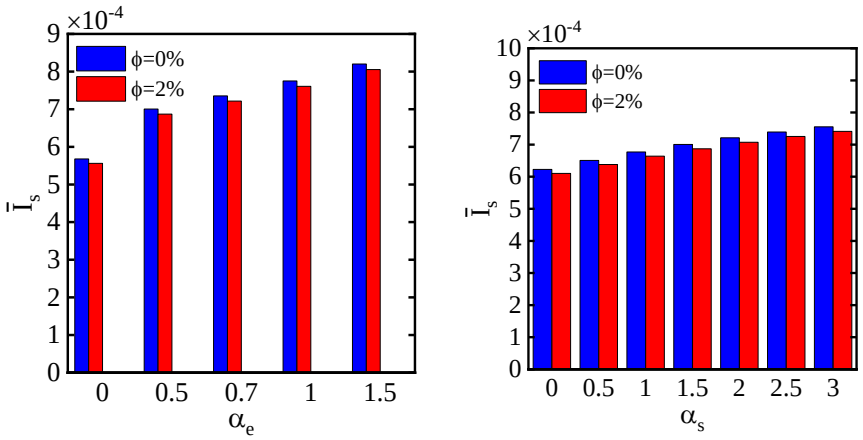

(a) α_s=1.5 (b) α_e=0.5

Fig. 6.6 The variation of normalised streaming current at different nanoparticle volume fraction for K=20, α=0.5, ā=0.01, Ha=4, Da=0.1, and Du=5: (a) with Hall current, and (b) with ion slip.

(ii) Velocity distribution

Figure 6.7 depicts the transient velocity distribution of a Maxwell fluid, varying with the Y-coordinate, while Ha=4, Da=0.1, α_e=0.5, and α_s=1.5 are kept constant. Now, the influence of relaxation time, Hartman number, electric force, slip-dependent zeta potential, Hall effects, and ionic slip on the velocity in a porous channel can be studied as all the parameters are included in the analysis. The validation of the present velocity cannot be verified directly in the transient state due to the unavailability of existing results. Therefore, we can verify the analytical results with numerical ones in the transient state. The results show an excellent agreement under the influence of relaxation and physical times. A significant variation in velocity with these two parameters occurs across the channel orthogonal to the fluid flow direction. Fig. 6.6a portrays the effect of small relaxation time on the velocity field. The velocity gradient is crucially generated with the relaxation time. The flow velocity increases at the core region when relaxation time increases. Eq. (6.12) provides the term for relaxation time $\bar{\lambda}_1$, which affects the stress tensor T_{xy}. The phenomenon of fading memory occurs due to the limited recollection ability of the Maxwell fluid, which can only vaguely remember events from the distant past. At larger $\bar{\lambda}_1$, the elastic nature of the fluid emphasizes over the viscous nature. A plausible explanation for this trend is that shorter relaxation times lead to lower elasticity. In comparison, longer relaxation times result in increased elasticity and a reduced ability of the fluid to recover its original state, as plotted in Fig. 6.6b. In physical terms, the elastic effect becomes increasingly noticeable as the relaxation time increases. Therefore, the dynamics of Maxwell fluids become increasingly comparable to a solid. The maximum velocity attained by the fluid flow during the transient period exhibits a notable increase with increasing $\bar{\lambda}_1$, attributable to the heightened elastic effects. It can reduce the motion

of fluid and boundary layer thickness at the EDL zone. Thus, the velocity profile has a higher magnitude when the dimensionless relaxation time is $\bar{\lambda}_1$=1. Following this, the velocity profile demonstrates a rising trend as time progresses. It also shows from Fig. 6.6c that fluid velocity diminishes near the channel's central region as time increases, while the trend reverses at the EDL region of the microchannel. Fig. 6.6d also reveals that the fluid velocity reaches a steady state at τ=6; beyond this time, there is no change in the velocity profile. Therefore, this time is sufficient for diffusing in the central region rather than the EDL region of the channel.

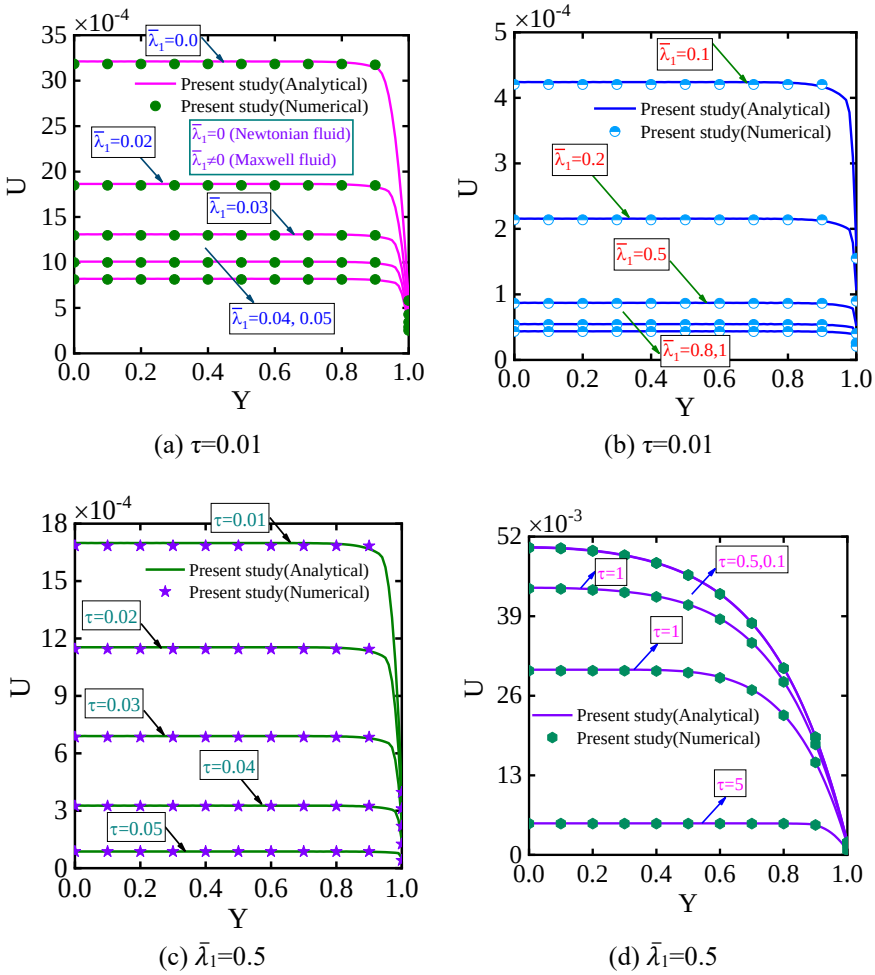

Fig. 6.7 Transient velocity distribution across a channel for Maxwell fluid with slip dependent zeta potential compared with the present analytical and numerical studies at K=20, α=0.5, ϕ=2%, $\bar{\alpha}$=0.01, α_e=0.5, α_s=1.5, Ha=4, Da=0.1, and Du=5: (a-b) different values of $\bar{\lambda}_1$, and (c-d) different values of τ.

(iii) Volume flow rate

Figure 6.7 illustrates the variation of the dimensionless discharge rate with normalized time for a magnetohydrodynamic streaming potential flow. Combined influences of relaxation time, electric field, magnetic field, Hall current, and ion slip on volume flow rate are taken with the slip boundary condition. The comparison of Maxwell and Newtonian fluid's volume flow rate calculations is made under the conditions of Ha=4, α_e=0.5, and α_s=1.5 in Fig. 6.7a. The variations of normalized discharge rate for different values of $\bar{\lambda}_1$ = 0.01, 0.2,0.5, 0.8, and 1.0 are taken to plot the results. The volume flow rate decreases significantly when the relaxation time increases.

The increase in relaxation time of viscoelastic fluid leads to more resistance to the motion of the fluid. An increased viscosity of flowing liquid increases relaxation time parameters. It highlights that for $\bar{\lambda}_1$=0, the behavior of the fluid changes from that of a Maxwell fluid to a Newtonian fluid. A higher of $\bar{\lambda}_1$ amplifies the elastic effects of the fluid. The precise agreement between the outcomes indicates the present analysis's ability to accurately calculate the Newtonian fluid's volume flow rate. An external magnetic field (Ha) interacts between body forces and the effects of Hall current and ion slip in a hyperbolic microchannel, which generates an electric field (Ω). The increase in the Hartman number leads to a significant reduction in the flow velocity, as observed. From the physical perspective, the Lorentz force, as described by Eq. (6.9), acts in the axial direction and has a magnitude corresponding to the aiding component ($\sigma_f B_z E_{ref}$) and a flow-opposing component ($\sigma_f u B_z^2$) Fig. 6.8b displays that the opposing component is more pronounced than the aiding component in the flow system. As the Hartman number increases, the normalized discharge rate experiences a decrement. Fig. 6.8c shows how the volume flow rate is affected by the Hall parameter. The Hall parameter enhances the flow rate. It is because the effective electric conductivity decreases as the Hall parameter rises, resulting in a decay in magnetic force and an increase in the flow rate. Fig. 6.8d demonstrates the impact of the ion slip parameter on the volume flow rate, with the variation of the τ. Similar behavior is observed for increasing the ion slip parameter, as shown in Fig. 6.8c. An increase in the slip parameter results in an increased velocity adjacent to the wall. This trend is because of the relatively high motion of molecules at the interfacial section and the subsequent reduction in effective electrical conductivity. It also reveals a higher flow rate in the presence of ion slip.

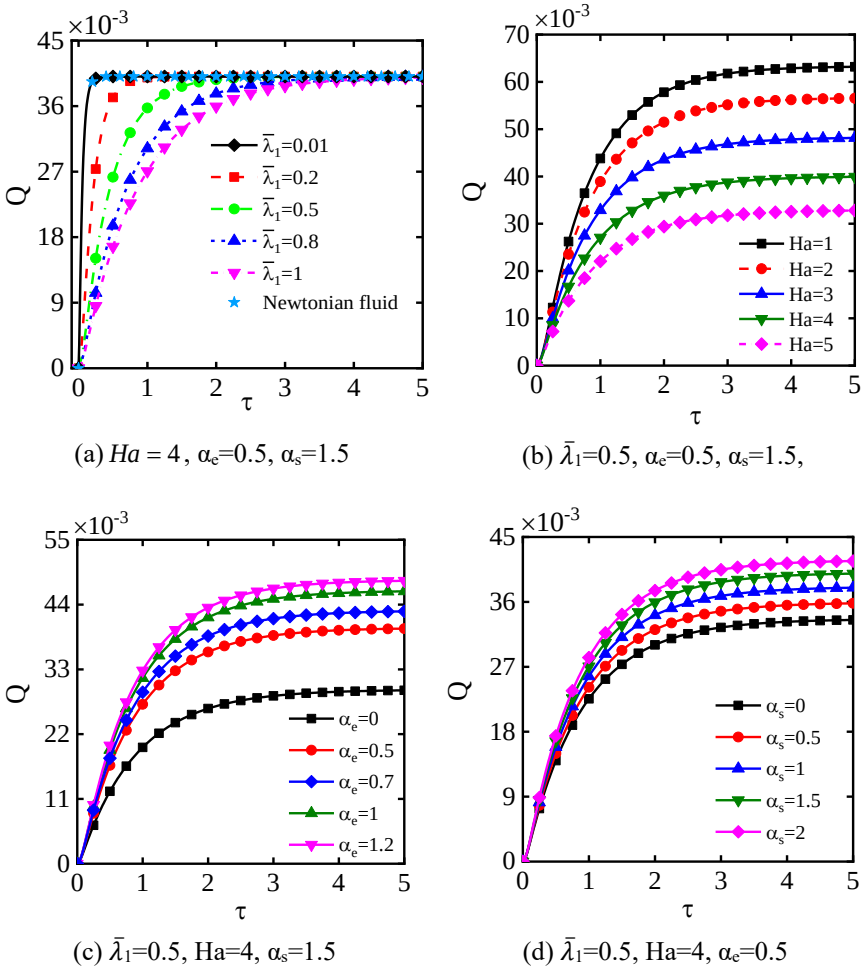

(a) $Ha = 4$, α_e=0.5, α_s=1.5 (b) $\bar{\lambda}_1$=0.5, α_e=0.5, α_s=1.5,

(c) $\bar{\lambda}_1$=0.5, Ha=4, α_s=1.5 (d) $\bar{\lambda}_1$=0.5, Ha=4, α_e=0.5

Fig. 6.8 Fluctuation of non-dimensional volumetric flow rate at slip boundary conditions with respect to τ for K=20, ϕ=2%, $\bar{\alpha}$=0.01, Ha=4, Da=0.1, and Du=5: (a) between Maxwell and Newtonian fluids for variation of $\bar{\lambda}_1$, (b) different values of Ha, (c) for variation of α_e, and (d) different values of α_s.

(iv) Electrokinetic energy conversion efficiency

Considerable effort has been devoted to determining results that highlight the significance of the current analysis. The present study explores the contrast in EKEC efficiencies between the slip-independent and slip-dependent zeta potential, as shown in Fig. 6.9. It is evident that EKEC efficiency at K=20 and Du=5 predicts greater amplification for the slip-independent zeta potential compared to the slip-dependent zeta potential, which is precisely 809.91%. According to Fig. 6.5, the streaming

potential decreases when Du increases. When the EDL becomes thinner, fewer mobile ions are present, leading to a smaller accumulation of excess ions and a weaker streaming potential, as depicted in Fig. 6.9a. The enhancement of EKEC efficiency with increasing $\bar{\alpha}$ is attributed to the increased movement of fluid molecules near the channel walls. As the normalized zeta potential rises, electrostatic interactions become stronger, drawing more counter-ions toward the charged surfaces, as shown in Fig. 6.9b. This intensifies the EDL, resulting in a greater potential difference within the fluid. As a result, the streaming potential increases. Therefore, when the zeta potential is influenced by slip conditions, it leads to a noticeable rise in the streaming potential.

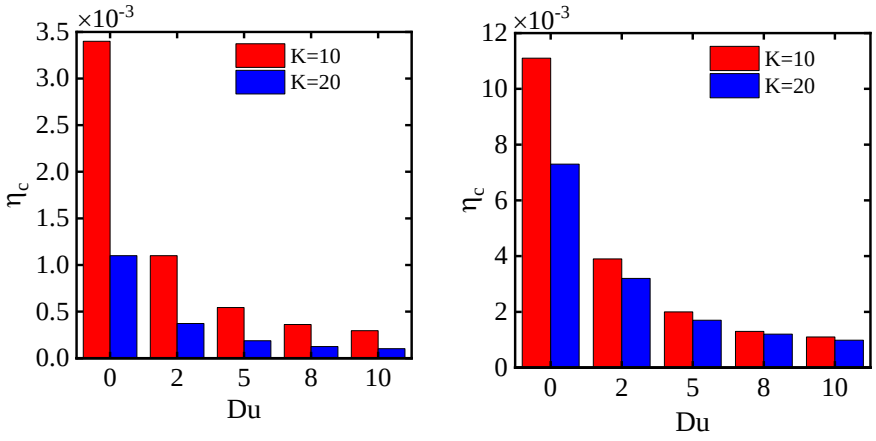

(a) Slip-independent zeta potential (b) Slip-dependent zeta potential

Fig. 6.9 Comparison of electrokinetic energy conversion efficiency as a function of Dukhin number (Du) between slip-independent zeta potential ($\bar{\alpha}$=0) and slip-dependent zeta potential ($\bar{\alpha}$=0.01) at K=20, ϕ=2%, α_e=0.5, α_s=1.5, Ha=4, and Da=0.1.

6.6.2. Thermal analysis of Fe_3O_4-water nanofluids

(i) Temperature field

Figure 6.10 illustrates the temperature distribution of magnetohydrodynamic flow of transient Maxwell fluid with Hall current and ion slip as a function of coordinate. The impact of the Joule heating effect on the dimensionless temperature distribution is illustrated in Fig. 6.10a. To conduct our analysis, we set the flow parameters at τ=0.01, and various J_h=1, 2, 5, 8, and 10 are employed to produce the results. The analysis unveils the transient temperature distribution for Maxwell fluid with Hall effects and ion slip for pressure-driven streaming potential flow for various values of Joule heating parameters.

It's noteworthy that with an increase in the Joule heating parameter, the magnitude of the dimensionless temperature also rises. When the dimensionless Joule heating term is positive, it signifies a scenario where the wall is heated, resulting in a more significant temperature difference across the microchannel. Consequently, this leads to a corresponding increase in the thermal energy generation rate within the microchannel. From a physical perspective, the negative values observed in temperature are attributed to the condition where $\theta=(k_T)_f(T_w-T)/(q_w h)$ gradually becomes negative as T always less than T_w. The central temperature of the channel experiences a 100% increase under jump boundary conditions when compared to $J_h=2$ with respect to $J_h=1$. Figs. 6.10b and 6.10c illustrate the changes in various τ with respect to the Y-coordinate in a microchannel. Our investigation adopts a fixed parameter approach, setting $J_h=10$ and Br=0.01. We systematically varied the time evolution interval (τ=0.01, 0.02, 0.03, 0.04 and 0.05) to elucidate its impact on the system's behaviour. The temperature magnitude remains low at low values of time. However, with minor changes in time, the temperature undergoes amplified, as illustrated in Fig. 6.10b. Streaming potential in microchannel flow is often associated with generating an electric potential due to fluid movement within a porous medium. As time progresses (τ=0.5, 1,2,5,10,15, and 20), the effects of joule heating (associated with the electrical potential) and viscous dissipation can contribute to the increase in temperature, potentially leading to a more uniform temperature distribution within the microchannel. The streaming potential, generated by the flow of the electrically conductive fluid through the channel, also plays a role in influencing the temperature distribution. The temperature of the fluid rises with an increase in τ within the boundary layer region, as illustrated in Fig. 6.10c. Much like the normalized velocity, due to the dependence of the temperature profile on the fluid flow, the temperature near the wall rises as the velocity grows. The steady state is reached when the temperature changes caused by joule heating, viscous dissipation, and other factors balance out over time. The effects of transient phenomena diminish, resulting in a stable and constant temperature distribution at τ=20.

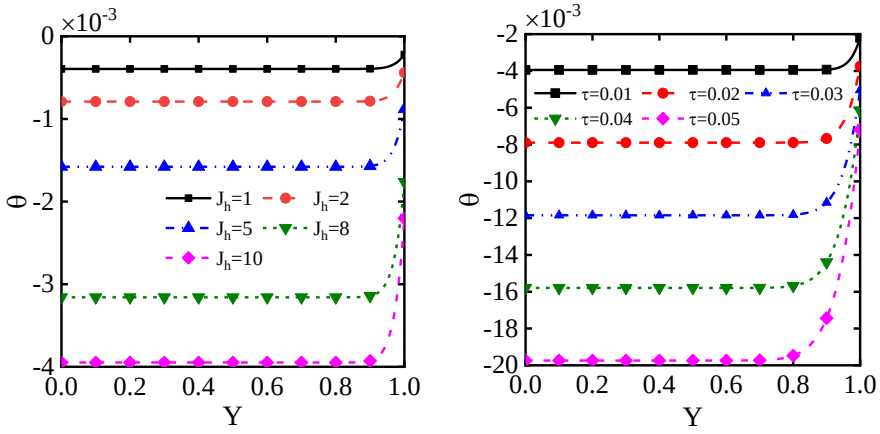

(a) τ=0.01 (b) J_h=10

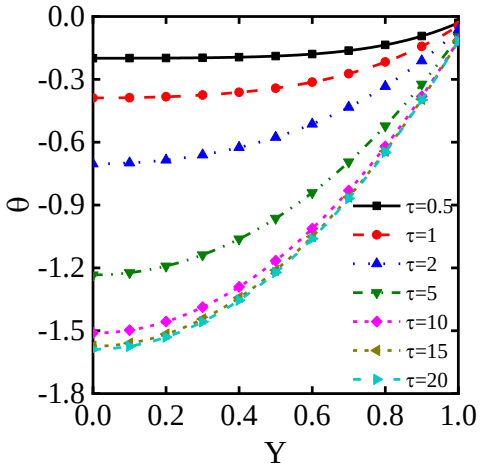

(c) J_h=10

Fig. 6.10 Transient evolution of normalised temperature distribution as a function of Y across the channel for K=20, ϕ=2%, $\bar{a}$=0.01, $\bar{\lambda}_1$=0.5, α_e=0.5, α_s=1.5, Ha=4, Da=0.1, Du=5, Br=0.01, and γ=0.04: (a) different values of J_h, (b) different low values of τ, and (c) different high values of τ.

(ii) Nusselt number estimations for heat transfer

The crucial non-dimensional parameter in thermal flow investigations is the Nusselt number (Nu). Fig. 6.11 illustrates how Nu changes concerning J_h for different γ while maintaining constant other parameters. Notably, an increase in the Joule heating

parameter leads to decreased heat transfer, resulting in alterations in temperature, as shown in Fig. 10a. Conversely, a temperature variance emerges between the surface of the channel and the fluid when thermal communication weakens. This weakness in thermal communication is attributed to a reduced frequency of collisions among molecules, both with the surfaces and among themselves. Consequently, a pronounced temperature gradient forms near the channel wall. A substantial temperature gradient manifests in the proximity of wall surfaces under temperature jump conditions. This circumstance contributes to an escalation in the temperature discrepancy at the boundary. The fluid's local temperature rises owing to heat transfer from the channel walls, Joule heating-induced heat generation, and viscous dissipation. This leads to a gradual enhancement in the bulk mean temperature as the differences between ($T-T_w$) diminish. Therefore, there is an overall decrease in heat transfer, resulting in a reduction in the Nu.

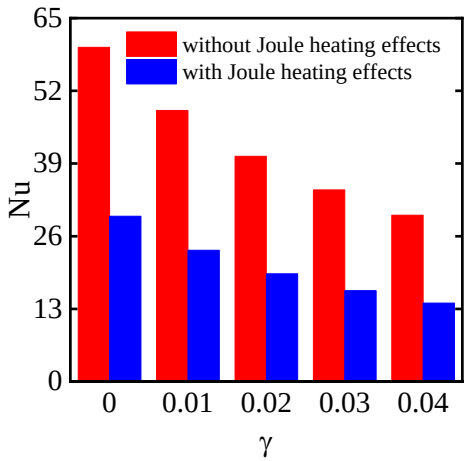

Fig. 6.11 Comparison of the Nu as a function of γ with (J_h=10) and without **(** J_h=0**)** Joule heating at K=20, ϕ=2%, $\bar{a}$=0.01, $\bar{\lambda}_1$=0.5, α_e=0.5, α_s=1.5, Ha=4, Da=0.1, Du=5, and Br=0.01.

Figure 6.12 displays the variations of η_h as a function of τ to show the transient effects within the channel. Notably, a rise in the physical time leads to increasing/decreasing trends in the electroviscous heat transfer rate, resulting in alterations in velocity and temperature, as depicted in Figs. 6.9a, and 6.12b, respectively. Maxwell fluids exhibit viscous and elastic characteristics, affecting heat transfer rates over time. Elastic effects can enhance heat transfer rate, while viscous effects can reduce it. The increased apparent viscosity due to electroviscous effects leads to lower convective heat transfer rates. The Hall effect, from magnetic fields interacting with moving charged particles, initially increases heat transfer but may decrease if the system is going to stabilize. Ion slip alters effective conductivity and velocity profiles, leading

to varying heat transfer rates due to ion concentration and distribution changes. The Darcy number indicates permeability; a higher value implies a higher fluid flow and heat transfer rates without electroviscous effects. The maximum Maxwell fluid's heat transfer rate was obtained at a small-time interval (τ=0.01) as 0.8618 at $\bar{\lambda}_1$=0.5, Ha=4, and Du=5. The rate of Nu variation with time can be linked to the Darcy number of the fluid. After τ=2, the Darcy number of the flow, the ratio of the heat transfer, and the electroviscous effect on heat transfer approach their steady-state values.

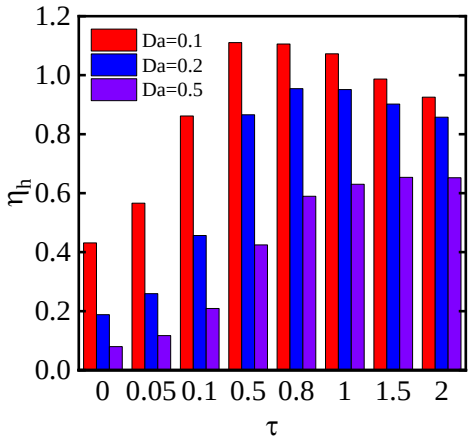

Fig. 6.12 The variation of η_c as a function of τ with different values of *Da* at

at K=20, ϕ=2%, $\bar{a}$=0.01, $\bar{\lambda}_1$=0.5, α_e=0.5, α_s=1.5, Ha=4, Du=5, Br=0.01, J_h=10, and γ=0.04.

Joule heating, viscous dissipation, electric diffusion, and magnetic interactions collectively contribute to thermal irreversibility. Fig. 6.13 illustrates the total entropy as a function of *Br* for various *Ha*. To determine the overall entropy generation, we used some fixed parameters at the initial time: γ=0.04, α_e=0.5, and α_s=1.5. Our observations indicate a clear decreasing trend in total entropy. The findings suggest that an increase in the value of *Ha* leads to a decrease in the flow rate, as mentioned in Fig. 10b, increasing irreversibility. The stronger magnetic field interaction leads to more pronounced Joule heating, boosting entropy generation. Despite the reduced flow rate, the enhanced Lorentz force increases viscous dissipation, converting energy lost to internal friction into heat and raising local temperature. These changes in temperature distribution result in larger temperature gradients, further enhancing heat transfer by conduction and contributing to higher entropy generation. Conversely, a rise in the value of Br amplifies the viscous boundary layer at Br = 0.1. This phenomenon occurs due to increase in (T_m-T_w).

(iii) Prediction of entropy generation

The total entropy generation, influenced by the parameters of Hall current and ion slip, is depicted in Fig. 6.14 to explore the tangible effects of thermal irreversibility. As the Hall current diminishes, the maximum irreversibility becomes more pronounced. Conversely, with a rise in the value of ion slip (α_s=0,0.5,1.5), a minimal change occurs in the global entropy. This variation is attributed to the increase in the flow rate for Hall current and ion slip within the flow domain, as indicated in Figs. 6.8c and 6.8d. The impact of Hall current and ion slip leads to the generation of additional streaming potential across the flow field. The magnitude (T_m-T_w) decreases at a low Br (Br = 0.01). Ultimately, the presence of the electromagnetic force leads to a reduction in the global entropy generation.

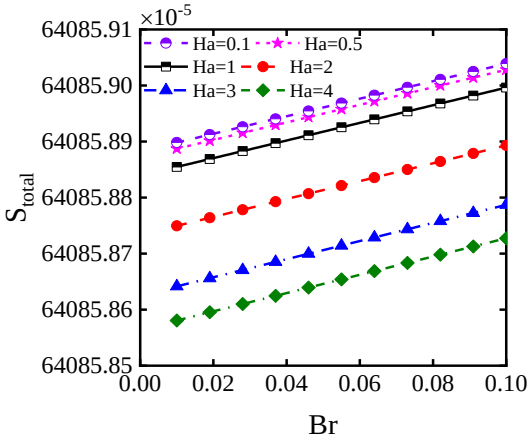

Fig. 6.13 Total entropy generation across the channel as a function of Br for various values of Ha at initial time step at K=20, ϕ=2%, $\bar{a}$=0.01, $\bar{\lambda}_1$=0.5, α_e=0.5, α_s=1.5, Da=0.1, Du=5, Br=0.01, J_h=10, γ=0.04, and τ=0.01.

The focus on the Bejan number quantifies the relative contribution of entropy generation due to heat transport compared to the overall entropy in microchannels. The distributions of the Bejan number (Be) are illustrated as a function of the Y coordinate in Fig. 6.15, exploring both small and large values of τ. The findings unambiguously show that the Bejan number rises with the progression of time (τ) in the core region, with minimal variations in its magnitude. Apart from the core region, the Bejan number along the wall rises, as plotted in Fig. 6.15a. A general observation indicates that the Bejan number (Be) is significantly smaller than 0.5 (Be<<0.5). This condition is because, at minimal values of time, viscous dissipation-induced entropy generation significantly outweighs the thermal entropy generation from heat transfer. A notable Bejan number (Be) increase is observed in scenarios with extended time durations, as evident from Fig. 6.15b. At a steady time of τ=20, near the wall, heat transfer irreversibility holds sway over fluid friction when Be>0.5. By contrast, in the

transient state slightly removed from the channel wall, fluid friction shows a more prominent role than heat transfer irreversibility when Be<0.5.

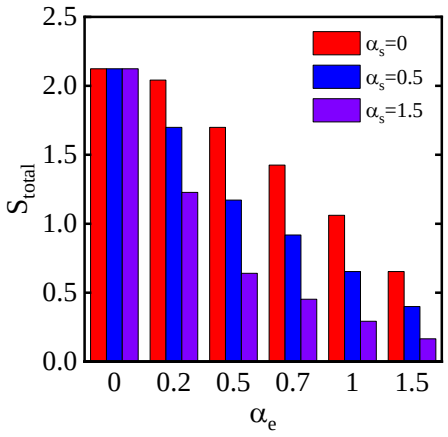

Fig. 6.14 Comparison of total entropy generation across the channel as a function of α_e for K=20, ϕ=2%, $\bar{a}$=0.01, $\bar{\lambda}_1$=0.5, Ha=4, Da=0.1, Du=5, Br=0.01, J_h=10, and γ=0.04 at different values of α_s at initial time step (τ=0.01).

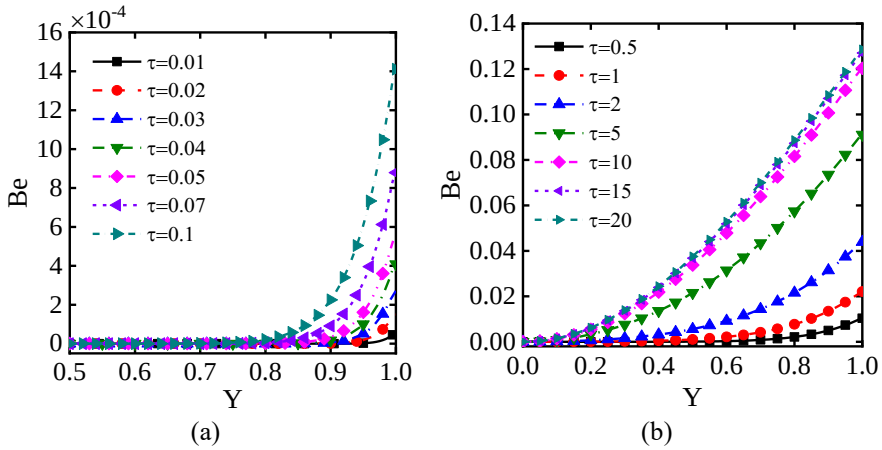

Fig. 6.15 Transient evolution of Bejan number (Be) as a function of Y across the channel for K=20, ϕ=2%, $\bar{a}$=0.01, $\bar{\lambda}_1$=0.5, α_e=0.5, α_s=1.5, Da=0.1, Du=5, Br=0.01, J_h=10, and γ=0.04 (a) low τ, and (b) high τ.

6.7. Discussion of the topic

(i) The conservative equations for maxwell flow coupling between electric, magnetic, and hydrodynamic forces become highly nonlinear, limiting analytical tractability and requiring extensive numerical computations.
(ii) Experimental validation under varying conditions, such as zeta potential dependency and electromagnetic field effects, is limited, and findings are specific to microchannel dimensions, hindering scalability to larger systems.
(iii) The Current study is unsuitable for analysing transient flow behavior for the Oldroyd-B fluid in microchannel flow.
(iv) Key factors like nanoparticle concentration, surface roughness, and non-Newtonian effects are not fully addressed, and the integration of the Nernst-Planck-Poisson framework with Navier-Stokes equations remains suboptimal, restricting practical predictions.

6.8. Conclusions with findings

This study reveals key insights into the characteristics of viscoelastic fluids' intricate rheological and heat transfer. Employing the linearized Poisson-Boltzmann equation and Debye-Hückel approximation evaluates zeta potential, wall slip, porous media, and stern layer currents. A comprehensive model was developed to analyze transient pressure-driven Maxwell fluid flow in microchannels, integrating streaming potential and magnetohydrodynamic effects. Key assessments include the flow field, volume flow rate, EKEC efficiency, temperature, Nusselt number, and entropy production. The results highlight that streaming potential significantly increases with slip parameters, exhibiting a 23.15% rise when the zeta potential depends on slip compared to no-slip conditions. Flow rate and heat transfer analysis demonstrate superior discharge and heat transfer rates for Maxwell fluids over Newtonian fluids, influenced by factors such as slippage, zeta potential, Hall current, and ion slip. Remarkably, electrokinetic energy conversion efficiency improves by 809.91% under slip-dependent zeta potential, underscoring the critical role of elastic and viscous forces.

6.9. Appendix

Appendix A

Table A
Comparison of the present and Zhao et al. [244] normalized streaming potential for two values of α

K	α=0.5		Absolute deviation (%)	α=1		Absolute deviation (%)
	Present study($\bar{E}_s$)	Zhao et al. [244] ($\bar{E}_s$)		Present study ($\bar{E}_s$)	Zhao et al. [244] ($\bar{E}_s$)	
5	-0.05316	-0.05332	0.3028	-0.02899	-0.02908	0.3380
10	-0.01630	-0.01636	0.3481	-0.00854	-0.00857	0.3555
15	-0.00775	-0.00777	0.3484	-0.00400	-0.00401	0.3519
20	-0.00450	-0.00452	0.3471	-0.00230	-0.00231	0.3495
25	-0.00294	-0.00295	0.3458	-0.00150	-0.00150	0.3478
30	-0.00207	-0.00207	0.3451	-0.00105	-0.00105	0.3457
35	-0.00153	-0.00154	0.3442	-0.00077	-0.00078	0.3452

Appendix B

Table B
Comparisons of the present and Zhao et al. [220] results for normalized velocity at two values of Ha.

Y	Ha=1		Absolute deviation (%)	Ha=2		Absolute deviation (%)
	Present study (U)	Zhao et al. [220] (U)		Present study (U)	Zhao et al. [220] (U)	
0	0.35063	0.35116	0.1490	0.18320	0.18334	0.0812
0.1	0.34739	0.34791	0.1486	0.18186	0.18201	0.0804
0.3	0.32127	0.32174	0.1456	0.17085	0.17098	0.0787
0.5	0.26797	0.26835	0.2018	0.14704	0.14715	0.0741
0.7	0.18535	0.18559	0.1306	0.10656	0.10664	0.0674
0.9	0.07013	0.07021	0.1186	0.04289	0.04292	0.0583

Chapter 7. Heat, mass, and entropy analyses in periodic electroviscous Oldroyd-B fluids

7.1. Objectives of the chapter

Research on time-periodic flow in microfluidic channels, the dynamics and energy dissipation of Fe_3O_4-water nanofluids under electromagnetohydrodynamic forces, and electroviscous effects is of prime priority nowadays. Waver streaming potential flows, critical for passive solute transport in applications such as drug delivery, diagnostics, and biomolecule separation, lack complete insights into the flow of viscoelastic Oldroyd-B fluids under pressure-driven forces. The existing literature provides no insights into the streaming potential in pressure-driven wave flow for the Oldroyd-B fluid model. However, it is vital to comprehend the flow behavior of heat transfer and thermal irreversibility in microfluidic systems. It explores the velocity field, streaming potential field, flow rate, EKEC efficiency, concentration field, mass transfer rate, heat transfer, and entropy generation under time-periodic flow conditions. Furthermore, the influence of relaxation time, retardation to relaxation time ratio, electroviscous effects, surface charge, and electromagnetic forces on fluid dynamics and thermal transport are thoroughly investigated.

7.2. Physical aspects and mathematical modelling

This study investigates the oscillatory electroviscous behavior of a non-Newtonian Fe_3O_4-water nanofluid (modeled as an Oldroyd-B fluid) within a parallel-plate microchannel under fully developed, unidirectional flow conditions. The channel geometry (length L, width W and height 2h, (L>>2h, W) ensures flow confinement to the y-axis, simplifying the system to a one-dimensional framework. A pressure-driven axial gradient ($-\nabla p$) generates a streaming potential (E_s), while externally applied electric (E_z) and magnetic (B_y) fields act perpendicular to the flow direction (z-axis). These orthogonal fields collapse the inherent two-dimensional electrokinetic dynamics into a y-dependent unidirectional flow. The microchannel interfaces with two reservoirs containing distinct solute concentrations ($c_1 \neq c_2$). To eliminate edge effects, the channel is idealized as infinitely long, enabling analytical simplification. This configuration isolates the interplay between viscoelastic stress, electromagnetic forces, and periodic pressure gradients, critical for understanding energy dissipation and mass transport in microscale non-Newtonian electrohydrodynamic systems.

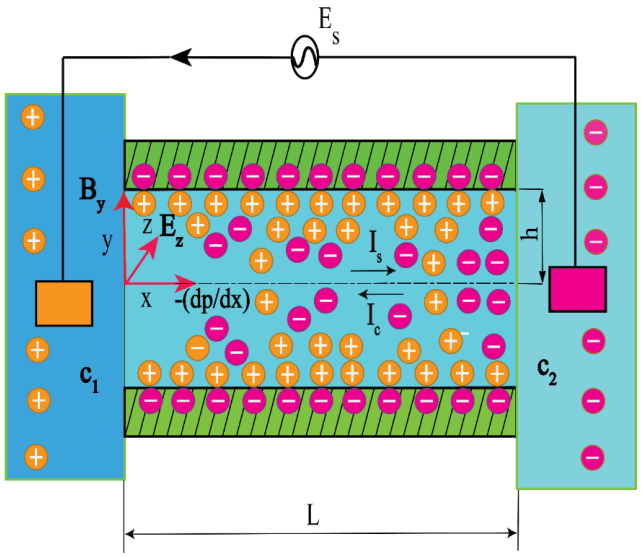

Fig. 7.1 Geometry of the physical problem

7.2.1. Electrostatics

The EDL potential profile for a symmetric electrolyte is derived by coupling Boltzmann statistics for ionic charge distribution with the Poisson-Boltzmann framework. In dimensionless terms, the defining equation for the electrostatic potential is expressed as follows, [135,305],

$$\frac{d^2\bar{\psi}}{dY^2} = \frac{K^2}{\varepsilon_r}\sinh\left(\bar{\psi}\right) \tag{7.1}$$

where $K = \left(2n_0 he^2 z_v^2\right)\Big/\left(\varepsilon_f k_B T_a\right)$, $\bar{\psi} = \left(ez_v\psi/k_B T_a\right)$, $Y = \left(y/h\right)$, $\varepsilon_r \left(= \varepsilon_{eff}/\varepsilon_f\right)$ are the dimensionless electrokinetic width, electrical potential, coordinate and ratio of the nanofluid effective permittivity to the base fluid permittivity, respectively. In the present work, K is taken to be in the range of 5 to 40 to avoid overlapping, and Eq. (1) is considered valid. Table 2 presents empirical correlations for the thermal properties of the base and magnetic nanoparticles as a function of volume fraction.

7.2.2. Fluid flow field

The current study addresses unidirectional transient flow velocity, governed by the general continuity and Navier-Stokes equations for incompressible fluids [91],

$$\nabla.\mathbf{U} = 0 \tag{7.2}$$

$$\rho_{eff}\left(\frac{\partial \mathbf{U}}{\partial t} + \left(\nabla\cdot\mathbf{U}\right)\mathbf{U}\right) = -\nabla p + \nabla\cdot\boldsymbol{\sigma} + \mathbf{F} \tag{7.3}$$

The stress-strain relationship of Oldroyd-B fluid the momentum equation modified as,

$$\rho_{eff}\left(\frac{\partial \mathbf{U}}{\partial t}+(\nabla\cdot\mathbf{U})\mathbf{U}\right)=-\nabla p+\nabla\cdot\boldsymbol{\sigma}_{\mathbf{1}}+2\mu_{eff}\left(\frac{\lambda_2}{\lambda_1}\right)\nabla\cdot\mathbf{A}+\mathbf{F} \tag{7.4}$$

where ρ is the fluid density, $\mathbf{U}$ is the flow velocity vector, t is the time, p is the hydrostatic pressure, $\boldsymbol{\sigma}_{\mathbf{1}}$ is the elastic stress tensor, $\mathbf{A}=\left(\nabla\mathbf{U}+\nabla\mathbf{U}^{T}\right)/2$ is the rate of the strain tensor.

The electromagnetic body force per unit volume acting on a conducting fluid is governed by the generalized Lorentz force expression as, $\mathbf{F}=\left(\rho_e\mathbf{E}+\mathbf{J}\times\mathbf{B}\right)$. The total current density $\mathbf{J}$ incorporates both Ohmic and convective contributions: $\mathbf{J}=\sigma_{eff}\left(\mathbf{E}+\mathbf{U}\times\mathbf{B}\right)$, and $\mathbf{B}$ is the magnetic field vector perpendicular to the flow direction. In the present model, the fluid is subjected to an externally applied electric field vector $\mathbf{E}=\left(E_s,0,E_z\right)$ and a transverse magnetic field $\mathbf{B}=\left(0,B_y,0\right)$. The velocity vector is given as, $\mathbf{U}=(u,0,0)$, aligned along the axial direction. The resulting Lorentz force becomes: $\mathbf{J}\times\mathbf{B}=-\hat{i}\,\sigma_{eff}uB_y^2-\hat{i}\,\sigma_{eff}E_zB_y$. Rewriting Eq. (7.4) in scalar form under the influence of a hydrodynamic electromagnetic field in the x-direction yields,

$$\rho_{eff}\frac{\partial u}{\partial t}=-\frac{\partial p}{\partial x}+\frac{\partial \sigma_{xy}}{\partial y}+\mu_{eff}\left(\frac{\lambda_2}{\lambda_1}\right)\frac{\partial^2 u}{\partial y^2}-\sigma_{eff}E_zB_y-\sigma_{eff}B_y^2u+\rho_eE_s \tag{7.5}$$

Here, σ_{eff} represents the effective electrical conductivity of nanofluids. The unidirectional flow the shear stress for an Oldroyd-B fluid with respect to t is denoted as $\sigma_{yx}+\lambda_1\left(\partial\sigma_{yx}/\partial t\right)=\mu_{eff}\left(1-\lambda_2/\lambda_1\right)\partial u/\partial y$, where σ_{yx} is a shear stress, λ_1 is a relaxation time, λ_2 is a retardation time, and μ_{eff} is an effective viscosity of the fluid.

An oscillatory flow, driven by a time-harmonic applied pressure gradient and influenced by an imposed voltage with an electric field (streaming potential field) and an externally applied electric field, can be represented in a complex form. This representation involves exponential variables for the pressure gradient, streaming potential, external electric field, stress tensor, velocity, and volume flow rate, respectively, as follows:

$$\partial p/\partial x=\mathrm{Im}\left(\left(\partial p_0/\partial x\right)\mathrm{e}^{i\omega t}\right),\ E_s=\mathrm{Im}\left(E_s^0e^{i\omega t}\right),\ E_z=\mathrm{Im}\left(E_z^0e^{i\omega t}\right),$$
$$\sigma_{yx}=\mathrm{Im}\left(\sigma_{yx}^0e^{i\omega t}\right),\ u=\mathrm{Im}\left(u_0e^{i\omega t}\right),\text{ and }\ q=\mathrm{Im}\left(q_0e^{i\omega t}\right) \tag{7.6}$$

where u is a y-component fluid speed, t is the physical time, ω is the angular frequency and $\left(\partial p_0/\partial x\right)$, E_s^0, E_z^0, σ_{yx}^0, and q_0 are complex amplitude of pressure

gradient, streaming potential, external electric field, shear stress, and volume flow rate, respectively [139].
Formulated the governing equations in dimensionless form for the velocity distribution, to combine Eqs. (7.5) are as,

$$\frac{d^2U_0}{dY^2}\left(\frac{1+i\,\mathrm{Re}_\omega\,\bar{\lambda}_1\lambda_r}{1+i\,\mathrm{Re}_\omega\,\bar{\lambda}_1}\right)-i\rho_r\,\mathrm{Re}_\omega U_0=-2+2\lambda\bar{E}_s^0\bar{\rho}_e+\sigma_r Ha^2\Omega+\sigma_r Ha^2U_0 \tag{7.7}$$

where $U_0\left(=u_0/u_{ref}\right)$ is dimensionless amplitude velocity. Hence, the reference velocity is established through the applied pressure gradient driving the pressure-driven transport and can be represented as, $u_{ref}=\left(-h^2/2\mu_f\right)\left(dp_0/dx\right)$. $\tau\left(=\omega t\right)$ is the normalized time, and $\bar{\lambda}_1\left(=\left(\lambda_1\mu_f\right)/\left(\rho_f h^2\right)\right)$ is the normalized relaxation time and signifies the interplay between the fluid's elastic and viscous characteristics. $Ha=h\,B_y\sqrt{\sigma_f/\mu_f}$ is the Hartmann number. The amplitude of the dimensionless streaming potential $\bar{E}_s^0\left(=E_s^0/E_{ref}\right)$ is determined by equating it to $E_{ref}=\left(-\varepsilon_f\xi/\mu_f\sigma_f\right)\left(dp_0/dx\right)$. $\Omega=E_z^0/\left(u_{ref}B_y\right)$ is the normalised external electric field. The angular Reynolds number is defined as $\mathrm{Re}_\omega\left(=\rho_f\omega h^2/\mu_f\right)$. $\lambda\left(=\varepsilon_f\xi^2/\mu_f\sigma_B\right)$ is the electroviscous parameter, signifying the relationship between the maximum electroviscous force and the pressure gradient in steady flows.

For the normalization of Eq. (7.7), the following dimensionless parameters are introduced,

$$\Upsilon=\sqrt{\frac{i\,\mathrm{Re}_\omega\left(1+i\,\mathrm{Re}_\omega\,\bar{\lambda}_1\right)\rho_r}{\left(1+i\,\mathrm{Re}_\omega\,\bar{\lambda}_1\lambda_r\right)\mu_r}},\quad \Upsilon_1=\Upsilon\sqrt{1+\frac{\sigma_r Ha^2}{i\rho_r\,\mathrm{Re}_\omega}},\quad \Upsilon_2=\Upsilon_1\sqrt{\frac{\left(2-\sigma_r Ha^2\Omega\right)}{\left(i\rho_r\,\mathrm{Re}_\omega\right)}} \tag{7.8}$$

Eq. (7.7) is rewritten in a simplified form using above normalized parameters as,

$$\frac{d^2U_0}{dY^2}-\Upsilon_1^2U_0=-\Upsilon_2^2+\frac{2\Upsilon^2\lambda\bar{E}_s^0\bar{\rho}_e}{i\rho_r\,\mathrm{Re}_\omega} \tag{7.9}$$

Eq. (7.9) encounters a Navier-slip boundary condition at the wall as, $U_0+\bar{a}\left(dU_0/dY\right)\big|_{Y=1}=0$, and a symmetric boundary condition at the channel centerline $dU_0/dY\big|_{Y=0}$. Here, $\bar{a}\left(=a/h\right)$ denotes the dimensionless slip length,

representing an extended distance from the solid surface where velocity diminishes to zero.

The normalized time-periodic velocity is expressed using an exponential form as, $U(Y,\tau) = \mathrm{Im}(U_0\, \mathrm{e}^{i\tau})$. The governing equation (Eq. 7.9) is simplified to express the solution for the time-periodic velocity in a dimensionless formula as follows,

$$U\left(Y,\tau\right) = \mathrm{Im}\left[e^{i\tau} \left\{ \begin{array}{l} c_0 \cosh\left(\Upsilon_1 Y\right) + \dfrac{\Upsilon_2^2}{\Upsilon_1^2} \\ -\dfrac{\lambda \bar{E}_s^0 \Upsilon^2}{i\,\mathrm{Re}_\omega\, \Upsilon_1} \left(e^{-\Upsilon_1 Y} \int_0^Y \sinh\left(\bar{\psi}\right) e^{\Upsilon_1 Y}\, dY - e^{\Upsilon_1 Y} \int_0^Y \sinh\left(\bar{\psi}\right) e^{-\Upsilon_1 Y}\, dY \right) \end{array} \right\} \right] \tag{7.10a}$$

$$c_0 = \frac{1}{\cosh\left(\Upsilon_1\right) + \bar{a}\,\Upsilon_1 \sinh\left(\Upsilon_1\right)} \left[\begin{array}{l} A_1 \bar{E}_s^0 e^{-\Upsilon} \int_0^1 \sinh\left(\bar{\psi}\right) e^{\Upsilon Y}\, dY \\ -A_2 \bar{E}_s^0 e^{\Upsilon} \int_0^1 \sinh\left(\bar{\psi}\right) e^{-\Upsilon Y}\, dY - \dfrac{\Upsilon_2^2}{\Upsilon_1^2} \end{array} \right] \tag{7.10b}$$

However, the constant value of complex amplitude of streaming potential $\left(\bar{E}_s^0\right)$ remains unknown in Eq. (7.10). Hence, the electro-neutrality condition can be utilized to determine its value. The streaming current is denoted by $I_s \left(= 2\int_0^h u \rho_e dy \right)$. The conduction current passing through the mobile part of the ions is represented by $I_c=2h\sigma_B E_s$. Similarly, the conduction current through the immobile part of the ions in the Stern layer is denoted by $I_{stern}=2\sigma_{stern}E_s$.The sum of the net current for steady-state conditions in the channel must be zero [67,139]. In the non-dimensional form,

$$\int_0^1 U_0 K^2 \bar{\rho}_e dY = 2\bar{E}_s^0 \left(1 + Du\right) \tag{7.11}$$

Where $Du(=\sigma_{stern}/h\sigma_B)$ Dukhin number defined as stern layer conductivity to bulk fluid conductivity. Consequently, the velocity field is fully characterized by incorporating the streaming electric field as obtained from Eq. (7.11) into Eq (7.10). In response to the induced electric field, the complex amplitude of volume flow rate can be articulated as follows $Q_0 = \int_0^1 U dY$ .The revised flow rate can be elucidated in the context of a purely pressure-driven flow uninfluenced by electrokinetic effects

mention as $q|_{E_S=0}$. The generation of streaming current (I_s) and induced electric field (E_s) converts the mechanical energy of pressure-driven flow (without streaming potential) to electric energy. The energy conversion system achieves its maximum power output at half the streaming potential and half the streaming current representing the optimal electric power generation with the electrokinetic energy conversion (EKEC) efficiency described in [139],

$$\eta_c = \frac{\left\langle \frac{I_s}{2}\frac{E_s}{2} \right\rangle}{\left\langle \frac{\partial p}{\partial x} q|_{E_S=0} \right\rangle} \tag{7.12}$$

where $\langle\cdot\rangle$ denotes the time average over a single cycle from 0 to 2π/ω.

7.2.3. Concentration distribution

The transport of a passive electroneutral solute species in an oscillatory streaming potential flow within a microchannel is examined. The aqueous electrolyte contains a nonreactive, electrically neutral solute dissolved in a dilute solution. The solute concentration is denoted $c(x,y,t)$. The microchannel is connected to two large reservoirs with different concentrations, c_1 and c_1 where $c_1 > c_2$, driving solute transport through diffusion and convection. The process is governed by the advection-diffusion equation [91,216],

$$\frac{\partial c}{\partial t} + u\frac{\partial c}{\partial x} = D\left(\frac{\partial^2 c}{\partial x^2} + \frac{\partial^2 c}{\partial y^2}\right) \tag{7.13}$$

where D is the molar diffusion coefficient of the solute in the fluid. The non-uniform velocity distribution results in a non-uniform species concentration at any cross-section within the microchannel. As evident, Eq. (7.13) does not satisfy the boundary conditions $c(0,y,t) = c_1$ and $c(L,y,t) = c_2$ due to the convective term $c_u(y,t)$ .The linear concentration distribution, mathematically represented by the Chatwin approximation [199], is expressed as: $c(x,y,t) = c_1 + (c_2 - c_1)x/L + c_u(y,t)$ .This approximation is reasonable when end effects are neglected, assuming L >> h, where L is the channel length and h is the channel height.
Once the transient phase has diminished,, the dimensionless concentration field corresponding to the oscillatory component is defined as $C_u = c_u/(c_2 - c_1)$ .Eq. (7.13) can be rewritten in its normalized form for a periodic response by combining it with incorporating $C_u = \mathrm{Im}\left(C_u^0 e^{i\tau}\right)$.

$$i\,\mathrm{Re}_\omega\, Sc C_u^0 + \Lambda Pe_D U_0 = \frac{d^2 C_u^0}{dY^2} \tag{7.14}$$

The corresponding boundary conditions for species concentration in the Y-direction can be expressed as, $dC_u^0/dY\big|_{Y=0} = 0$, and $C_u^0 + \bar{b}\left(dC_u^0/dY\right)\big|_{Y=1} = 0$.Here, the aspect ratio is given as $\Lambda\left(=h/L\right)$, with L being the length of the channel, $\bar{b}\,(=b/h)$ is the normalized concentration slip, Schmidt number is defined as $Sc\left(=\nu/D\right)$, and diffusion Peclet number is denoted as $Pe_D = u_{ref}\,h/D$.

7.2.4. Tidal displacement and mass transport rate

The reference velocity and Peclet number adapt dynamically depending on flow parameters in periodic streaming potential conditions to ensure consistent tidal displacement, a metric quantifying the maximum axial displacement of fluid parcels during half an oscillation cycle, averaged across the channel width. Tidal displacement is introduced to characterize oscillatory flow periodicity, serving as a critical measure of fluid element migration under time-dependent electromagnetic and hydrodynamic forces.[193],

$$\Delta z = \frac{1}{h}\left|\int_{y=0}^{h}\int_{t=0}^{\pi/\omega} u(y,t)\,dt\,dy\right| \tag{7.15}$$

Here, angular aspect the Peclet number is redefined from Eq. (7.15) as $Pe_\omega = \left(\mathrm{Re}_\omega\, Sc\Delta Z\right)/\mathrm{Im}\left(2i\langle U_0\rangle\right)$. Where $\langle U_0\rangle$ is the cross-sectional average velocity of complex amplitude function U_0. We can ascertain mass transport by analyzing the solutions derived from dimensionless flow velocity and concentration profiles. Rather than experiencing a lack of net flow during each time period, there is a presence of net mass flow resulting from pure diffusion and convection effects. To assess mass transport, we utilize the time-space averaged mass transfer rate written by [216],

$$m_x = \frac{1}{h}\frac{\omega}{2\pi}\left|\int_{y=0}^{h}\int_{t=0}^{2\pi/\omega} J_x\,dt\,dy\right| \tag{7.16}$$

where $J_x = -D\left(\partial c/\partial x\right) + u(y,t)c(x,y,t)$ is the instantaneous mass flux of oscillatory flow caused by convection and diffusion effects. The mass transfer rate $\left(m_x\right)$ is

scaled using $D(c_1-c_2)/L$. The normalised form of mass transfer rate for pressure mediated streaming potential flow can be analysed as follows,

$$\bar{m}_x = 1-\frac{Pe_\omega}{2\Lambda}\int_{Y=0}^{1}\mathbb{R}\left(U_0\tilde{C}_u^0\right)dY \tag{7.17}$$

Here, $\mathbb{R}$ represents the real part of the product of $U_0(Y)$, and $\tilde{C}_u^0(Y)$ is the complex conjugate of C_u^0.

7.2.5. Energy equation and heat transfer

The energy equation governs heat transfer $\tilde{C}_u^0(Y)$ in incompressible nanofluids, incorporating axial conduction, convection, Joule heating, and volumetric heat generation. Formulated under constant thermophysical properties, it is expressed in vector form to model multidimensional thermal dynamics.[67],

$$\rho_{eff}\left(c_p\right)_{eff}\left(\frac{\partial T}{\partial t}+\mathbf{U}\cdot\nabla T\right)=\nabla\cdot\left[\left(k_T\right)_{eff}\nabla T\right]-\frac{\partial q_r}{\partial y}+\frac{\mathbf{J}\cdot\mathbf{J}}{\sigma_{eff}}+\boldsymbol{\sigma}:\nabla\mathbf{U} \tag{7.18a}$$

Eq. (7.18a) can be modified based on the stress-strain relationship for the Oldroyd-B fluid as,

$$\rho_{eff}\left(c_p\right)_{eff}\left(\frac{\partial T}{\partial t}+\mathbf{U}\cdot\nabla T\right)=\nabla\cdot\left[\left(k_T\right)_{eff}\nabla T\right]-\frac{\partial q_r}{\partial y}+\frac{\mathbf{J}\cdot\mathbf{J}}{\sigma_{eff}}+\left(\boldsymbol{\sigma}_1+2\mu_{eff}\frac{\lambda_2}{\lambda_1}\mathbf{A}\right):\nabla\mathbf{U} \tag{7.18b}$$

In instances of time-periodic flow, the ohmic terms and contributions of viscous dissipation include squared terms of harmonic functions over time. Consequently, the heat source term encompasses time-harmonic components with twice the frequency of oscillation, along with a steady contribution. Using the $\theta=(T-T_w)/(T_i-T_w)$ is normalised temperature, and $\mathrm{Pr}=\mu_f\left(c_p\right)_f/\left(k_T\right)_f$ is the Prandtl number. Hence, it is reasonable to assume that the temperature is expressed in its complex form as, $\theta=\mathrm{Im}\left(\theta_0(y)e^{2i\tau}\right)$. Where $\theta_0(y)$ is the complex amplitude of the steady state temperature [369]. As a result, the normalised energy equation and its corresponding boundary conditions are stated as,

$$(k_r+Nr)\frac{d^2\theta_0}{dY^2}-\left(\rho_r c_p\right)_r\left(2i\,\mathrm{Pr}\,\mathrm{Re}_\omega\right)\theta_0=\sigma_r J_h+\sigma_r Ha^2 Br\Omega^2$$

$$+2\sigma_r Ha^2 Br\Omega U_0 + \sigma_r Ha^2 Br U_0^2 + \frac{\mu_r\left(1+i\,\mathrm{Re}_\omega\,\delta\bar{\lambda}_1\right)Br}{\left(1+i\,\mathrm{Re}_\omega\,\bar{\lambda}_1\right)}\left(\frac{dU_0}{dY}\right)^2 \tag{7.19}$$

The corresponding dimensionless symmetric and thermal boundary conditions for Eq. (7.19) at the channel surface denoted by $\left(d\theta_0/dY\right)\big|_{Y=0}=0$, and $\theta_0+\bar{d}\left(d\theta_0/dY\right)\big|_{Y=1}=0$ at $\tau>0$. Where $\bar{d}=d/h$ is the temperature jump parameter, $\left(c_p\right)_r=\left(c_p\right)_{eff}\big/\left(c_p\right)_f$ is the ratio of the heat capacity of the Fe_3O_4 to the heat capacity of the base fluid. $k_r\left(=\left(k_T\right)_{eff}\big/\left(k_T\right)_f\right)$ is the ratio of the thermal conductivity of the magnetic nanoparticles to that of the base fluid. $Br=\left(u_{ref}^2\mu_f\big/k_f\left(T_w-T_i\right)\right)$ represents the Brinkman number. $J_h=\left(\sigma_f\left(E_s^0\right)^2h^2\big/k_f\left(T_w-T_i\right)\right)$ The heat produced per unit volume due to Ohmic heating. To compute the, Nusselt number, we derive the non-dimensional bulk mean temperature using the subsequent mathematical expression $\theta_m=\int_0^1 U\theta dY\Big/\int_0^1 UdY$. Nusselt number $Nu\left(=h_c h/\left(k_T\right)_f\right)$, at the surface based on half channel height in microchannel using the subsequent mathematical expression as,

$$Nu=\mathrm{Im}\left[\left(\frac{-k_r}{\theta_m}\right)\left(\frac{d\theta}{dY}\right)_{Y=1}\right] \tag{7.20}$$

7.2.6. Entropy generation analysis

The dimensional expression for the volumetric rate of entropy generation within the system is influenced by electro-magnetohydrodynamic velocity and temperature distribution. It is typically formulated as the combined contributions of thermal gradients, viscous dissipation, electromagnetic field, magnetic field effects, and Joule heating, respectively and can be expressed mathematically as [67],

$$s_g=\left|\frac{1}{T^2}\left[\left(k_T\right)_{eff}+\frac{16\sigma T_a^3}{3\tilde{k}}\right]\left(\frac{dT}{dy}\right)^2\right|,\ s_{\mathrm{v}}=\left|\frac{\sigma_{yx}+\mu_{eff}\left(\lambda_2/\lambda_1\right)\partial u/\partial y}{T}\frac{\partial u}{\partial y}\right|,$$

$$s_c=\left|\left(\frac{2\sigma_{eff}E_zB_yu}{T}+\frac{\sigma_{eff}E_z^2}{T}\right)\right|,\ s_m=\left|\frac{\sigma_{eff}B_y^2u^2}{T}\right|,\ \text{and}\ s_j=\left|\frac{\sigma_{eff}E_s^2}{T}\right| \tag{7.21}$$

The dimensionless entropy generation rate is normalized with respect to the characteristic entropy transfer rate. $(k_T)_f / h^2$, is expressed as,

$$S_G=S_H+S_V+S_C+S_M+S_J \tag{7.22}$$

where,

$$S_H = \left|\frac{(k_r+Nr)}{(\theta+\Theta)^2}\left(\frac{d\theta}{dY}\right)^2\right|, S_V = \left|\frac{\mu_r\left(1+i\delta\,\mathrm{Re}_\omega\,\bar{\lambda}_1\right)Br}{(\theta+\Theta)\left(1+i\,\mathrm{Re}_\omega\,\bar{\lambda}_1\right)}\left(\frac{dU}{dY}\right)^2\right|,$$

$$S_C = \left|\frac{2\sigma_r Ha^2 Br\Gamma U e^{i\tau}}{(\theta+\Theta)}\right| + \left|\frac{\sigma_r Ha^2 Br\Gamma^2 e^{2i\tau}}{(\theta+\Theta)}\right|, S_M = \left|\frac{\sigma_r Ha^2 BrU^2}{(\theta+\Theta)}\right|,$$

$$S_J = \left|\frac{\sigma_r\, J_h e^{2i\tau}}{(\theta+\Theta)}\right| \tag{7.23}$$

Where $\Theta = T_w/(T_i - T_w)$ denotes the temperature ratio. By integrating the local entropy generation throughout the entire domain, the total entropy generation is calculated in its dimensionless form as,

$$S_{total} = 2\int_0^1 S_G \tag{7.24}$$

Eqs. (7.10a), (7.11), (7.15), (7.17), and (7.24) are integrated numerically using MATLAB software with the Simpson's 1/3rd rule. The computation involves 500 steps, ensuring the results remain consistent up to five decimal places.

In this study, MATLAB software is employed to solve governing equations listed in Table 8. The numerical scheme is implemented with a convergence tolerance of 10^{-6}, ensuring solution stability and accuracy up to five decimal places. The convergence is ensured through iterative updates of the solution until the residual at each grid point falls below a specified tolerance. The global error is proportional to $O(\Delta Y^2)$, ΔY is the grid spacing in the transverse direction. Convergence is confirmed by monitoring the difference between successive iterations at each grid point p. To confirm convergence, the results are verified by checking the difference between successive iteration steps j and j+1 at grid point p for momentum, advection-diffusion and energy equations in Eqs. (7.9), (7.14), and (7.19) respectively.

$$\left\{(U_0)_p^{j+1} - (U_0)_p^j\right\} < tolerance\ , \left\{\left(C_u^0\right)_p^{j+1} - \left(C_u^0\right)_p^j\right\} < tolerance\ ,$$

$$\left\{(\theta_0)_p^{j+1} - (\theta_0)_p^j\right\} < tolerance \tag{7.25}$$

A grid independence assessment was also carried out by systematically increasing the number of grid points (Ny) and observing the corresponding velocity, temperature, and concentration profiles. It is found that further refinement beyond Ny = 301 produced no significant variation in these results. This indicates that the chosen grid resolution is adequate to capture the essential physical features of the flow, ensuring accurate results while maintaining computational efficiency.

Table 8
Numerical methods utilization to solve governing equations

Governing Equation	Equation Number	Numerical Method Used
Momentum (primary form)	Eq. (7.9)	Finite difference method
Momentum (derived form)	Eq. (7.10a)	Simpson's 1/3rd rule (Numerical integration)
Advection-diffusion	Eq. (7.14)	Finite difference method
Energy	Eq. (7.19)	Finite difference method

7.3. Results and discussion

This research investigates the interplay of streaming potential generation and electroviscous phenomena in time-dependent oscillatory motion of viscoelastic Oldroyd-B fluids through a parallel-plate microchannel. The framework incorporates a magnetite Fe_3O_4-water nanofluid to assess normalized streaming potential, velocity profiles, solute concentration gradients, thermal distributions, heat transfer efficiency (Nusselt number), and entropy production under slip velocity and thermal discontinuity at boundaries. The analysis covers the influence of various non-dimensional parameters, including the Hartmann number (Ha), normalised electric field (Ω), angular Reynolds number (Re_ω), normalized relaxation time ($\bar{\lambda}_1$), Schmidt number (Sc), Joule heating parameter (J_h), viscous dissipation (Br), and thermal radiation (Nr). For the analysis in this study, the empirical relations thermo-physical nanofluids and standard values of these parameters for time-periodic Oldroyd-B fluid flow in a microchannel are used, as outlined in Tables 4 and 5. To estimate the results, we use the following parameters of streaming potential flow [91,139,243,301]: $0.1 \leq h \leq 15\ \mu m$, $e \sim 1.6\times10^{-19}$ C, $k_B \sim 1.381\times10^{-23} JK^{-1}$, $\bar{\lambda}_1 \leq 0.01$s, $D \sim 10^{-9}$-10^{-10} m^2s^{-1}, $L \sim 10^{-2}$ m, $25 \leq \xi \leq 200$ mV, $0.1 \leq \omega \leq 100$ $rads^{-1}$, $\sigma_B \sim 0$-72 $nScm^{-1}$, $f \sim 10$-12 Nsm^{-1}, $B_y \sim 0$-2.5 T. The reference electric field strength for the Joule heating effect is $E_{ref} \sim 10^4$ Vm^{-1}, a standard value for applied electric fields in EOF [243].

Table 9
Normalized values of key physical parameters used in the present results

Parameters	Range/Value	$\bar{\psi}$	U	$\bar{E}_s$	C_u	$\bar{m}_x$	θ	Nu
Electrokinetic width (K)	5-40	√	√	√	√	√	√	√
Angular Renolds number (Re_ω)	0-30	-	√	√	√	√	√	√
Hartmann number (Ha)	0-2	-	√	√	√	√	√	√
External electric field (Ω)	0-2	-	√	√	√	√	√	√
Magnetic nanoparticles (Fe_3O_4) volume fraction (ϕ)	0-0.02	√	√	√	√	√	√	√
Slip parameter ($\bar{a}$)	0.1	-	√	√	√	√	√	√
Zeta potential ($\bar{\xi}$)	0-10	√	√	√	√	√	√	√
Brinkmann number (Br)	0.02	-	-	-	-	-	√	√
Dukhin number (Du)	0-10	-	√	√	√	√	√	√
Time phrase (τ)	π/2	-	√	√	√	√	√	√
Relaxation time ($\bar{\lambda}_1$)	0-0.2	-	√	√	√	√	√	√
Ratio of retardation time to relaxation time (λ_r)	0-1	-	√	√	√	√	√	√
Concentration slip ($\bar{b}$)	0.1	-	-	-	√	√	-	-
Schmidt number (Sc)	1000	-	-		√	√	-	-
Aspect ratio (Λ)	0.001	-	-	-	√	√	-	-
Tidal displacement (ΔZ)	1	-	-	-	√	√	-	-
Prandtl number (Pr)	7.43	-	-	-	-	-	√	√
Temperature jump parameter ($\bar{d}$)	0-0.1	-	-	-	-	-	√	√
Brinkmann number (Br)	0-0.1	-	-	-	-	-	√	√
Joule heating parameter (J_h)	0-10	-	-	-	-	-	√	√
Governing equations		Eq. (7.1)	Eq. (7.10a)	Eq. (7.11)	Eq. (7.14)	Eq. (7.17)	Eq. (7.19)	Eq. (7.20)

The strength of the non-dimensional electrokinetic width number varies in streaming potential flow without overlap for Oldroyd-B fluid K~5-40 [244], When the Debye length is large (thick EDL), the diffuse charge extends farther into the channel, resulting in a broader region where there is significant electroviscous drag. In contrast, when the Debye length is small relative to the channel size (thin EDL or large K), the charge and resulting viscous drag are confined to thin boundary layers near the walls [370]. The zeta potential is assigned a range of $0 \leq \bar{\xi} \leq 10$ [133] The angular Reynolds number and normalised relaxation time are set to be $0 \leq Re_{\omega} \leq 30$, and $0 \leq \bar{\lambda}_1 \leq 0.2$ respectively [91]. The Hartmann number is varied within the range $0 \leq Ha \leq 2$ [220] to meet the requirements for EMHD micropumps, and the dimensionless external electric field parameter is set between $0 \leq \Omega \leq 2$[243]. Dukhin number is varied as $0 \leq Du \leq 10$ [67]. The ranges can vary significantly depending on the specific characteristics of the viscoelastic fluid, such as elastic stress, particle concentration, microstructure, etc. The Joule heating parameter is assigned as J_h~0-10 [244]. and the Brinkman number is set to be $Br \sim 0 - 0.1$ [220]. Ensuring a steady-state electric double layer (EDL) condition, the relaxation time ($\bar{\lambda}_1$) is chosen to be shorter than the oscillation period of the electric field $2\pi/\omega$, which makes the product of electric field frequency (ω) and relaxation time less than 2π. The velocity slip parameter, concentration slip are taken as $0 \leq \bar{a} \leq 0.1$, and $0 \leq \bar{b} \leq 0.1$, respectively [91]. The Brinkman number is set to be Br ~ 0 - 0.1[220]. Thermal radiation parameter and temperature jump are varied as $0 \leq Nr \leq 10$, and $0 \leq \bar{d} \leq 0.1$ respectively [140]. In non-dimensional form, this constraint is expressed as $\bar{\lambda}_1 Re_{\omega} < 2\pi$ [91]. Based on the practical design elements, the normalised physical parameters are within the physically acceptable range. For all the present calculations, the constant physical parameters are considered, as described in Table 9, unless they have expressly been stated in respective figures.

7.3.1. Fluid flow of Fe_3O_4-water nanofluids

(i) Validation for velocity fields

The accuracy of the current velocity distribution results cannot be directly confirmed, as no comparable data exists in the literature. To address this, we validate the findings of this study based on certain assumptions regarding the flow parameters. Fig. 7.2 presents a comparison of the velocity distribution obtained in this analysis with the results from Gong et al. [301] for a Newtonian fluid. This figure depicts the real component of the velocity amplitude in pure streaming potential flow as a function of the Y-coordinate. A maximum discrepancy of 1.3% is noted in comparison to Gong et al. [301] results. Overall, the results demonstrate good agreement, indicating that the analysis is well suited to the conditions examined.

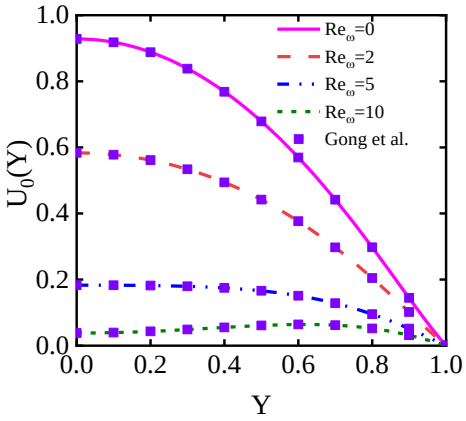

Fig. 7.2 Validation of present study for velocity amplitude at no-slip $(\bar{a}=0)$ for different values of Re_ω for Newtonian fluid (K=10, $\bar{\xi}$=1, Ω=0, λ=5, λ_r≈1, $\bar{\lambda}_1$≈0, Ha=0, Du=0), with Gong et al. [301].

(ii) Velocity distribution

Figure 7.3 illustrates the velocity of the time-periodic oscillatory streaming potential flow of Oldroyd-B fluid with high zeta potential as a function of coordinate Y. The influence of relaxation time, zeta potential, retardation time, electric field, magnetic field, and time phase on the velocity field is presented graphically. Fig. 7.3a shows the influence of $\bar{\lambda}_1$ on the velocity distribution. The flow parameters for the different values of $\bar{\lambda}_1$=0.0, 0.03, 0.08, 0.1, 0.15, and 0.2 are taken to generate the results. For a Newtonian fluid ($\bar{\lambda}_1$=0), an asymmetric plug-like velocity profile is observed, with the maximum influence at the center of the channel. As the relaxation time parameter increases, the Oldroyd-B fluid exhibits stronger elastic behavior, which influences the velocity distribution. An increase in $\bar{\lambda}_1$ enhances the polymeric contribution to the extra stress tensor, which introduces a time-delayed elastic response opposing the instantaneous acceleration induced by the oscillatory electrokinetic forcing. At intermediate values for $\bar{\lambda}_1$=0.1, there is a critical interaction between viscous and elastic forces, leading to enhanced oscillations in the velocity profile. This trend occurs because the elastic effects are strong enough to develop flow fluctuations but not dominant enough to stabilize them fully. However, for an increase in $\bar{\lambda}_1$ ($\bar{\lambda}_1$=0.2) further, the stretchy nature of the fluid becomes more pronounced, resulting in a memory effect that resists rapid variations in velocity. This suppresses oscillations rather than amplifying them, resulting in a more stable and smoother velocity profile. In this regime, the polymeric stress component becomes large enough to counteract the oscillatory momentum induced by the time-varying streaming potential, leading to damped velocity fluctuations. At this stage, the fluid behaves more like a damped spring system, where stored elastic energy counteracts sudden acceleration or deceleration. While elasticity allows the fluid to store and release energy, excessive elasticity helps dampen disturbances, reducing oscillatory

behavior in the flow field. Fig. 7.3b illustrates the impact of the angular Reynolds number on the velocity profile. The velocity distribution is uniform across the channel at a lower Re_ω=0.01, where viscous forces are dominant, allowing momentum to quickly diffuse through the channel, resulting in a more uniform (less oscillatory) velocity profile. The dominance of viscous diffusion smooths out spatial velocity gradients induced by oscillatory forcing. At these higher Re_ω values, the fluid's momentum diffusion time becomes longer than the electric field's oscillatory time. The electric field's influence is now strong enough to cause oscillations in the profile, which are no longer quickly dissipated by viscous forces. At Re_ω=30, the fluid's inertia is high enough that flow instabilities can occur. In the inertia-dominated regime, phase-lagged velocity overshoots occur and are further intensified in viscoelastic fluids due to delayed stress relaxation. These instabilities can manifest as oscillations in velocity, particularly in viscoelastic fluids, where elastic forces introduce an additional degree of freedom.

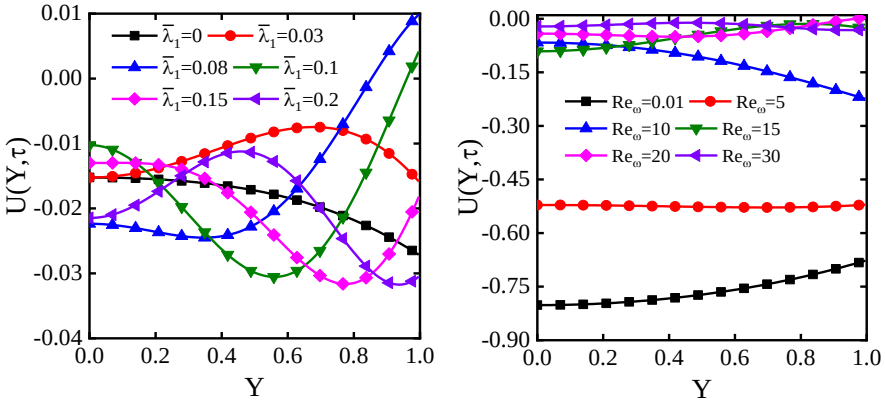

(a) Re_ω=30 (b) $\bar{\lambda}_1$=0.2

Fig. 7.3 Normalised velocity distribution as a function of Y at K=10, $\bar{\xi}$=2, Ω=1.5, λ=5, λ_r=0.05, Ha=2, Du=2, $\bar{a}$=0.1 (a) for different values of $\bar{\lambda}_1$, and (b) for different values of Re_ω.

A set of results is plotted to emphasize the significance of the current model. Figure 7.4 illustrates the variations in normalized velocity distributions for Oldroyd-B, Maxwell, and Newtonian fluids, as determined in this study, using an appropriate value of the viscoelasticity parameter, λ_r. It notes that λ_r represents the ratio of the fluid's retardation time to its relaxation time. Additional design variables highlight the combined influences of zeta potential, Hartmann number, normalized electric field, relaxation time, electroviscous parameter, and dimensionless time on fluid velocity. For λ_r=0, the Oldroyd-B fluid, the behaviour is similar to that of a Maxwell fluid. On the other hand, higher λ_r values increase the fluid's viscosity. As λ_r approaches 1, the Oldroyd-B fluid behavior qualitatively converges towards that of a Newtonian fluid in the no-slip condition plotted in Fig. 7.4a. Increasing λ_r reduces the influence of the fluid's memory effect, allowing the viscous damping to dominate over elastic recoil, which flattens the velocity profile and suppresses the high-

frequency oscillations near the centreline. Maxwell fluids exhibit a single stress response, typical of low-viscosity substances. At the same time, the Oldroyd-B model accounts for both relaxation and retardation times, offering more profound insights into microchannel flow dynamics. As the presence of slip ($\bar{a}$=0.1) is more pronounced, there is a greater asymmetry and sharper oscillations in the velocity profile, especially near the walls, as shown in Fig. 7.4b. This indicates that the slip condition allows more ions to be transported along the channel walls, resulting a in more varied ion distribution across the channel. Higher slip leads to an ion build-up closer to the walls, as ions experience less resistance from the boundary, which enhances electrokinetic effects and distorts the velocity profile more significantly. The wall slip weakens the no-shear condition at the boundary, allowing more substantial near-wall velocity gradients that amplify the local electroosmotic body force and lead to sharper velocity peaks adjacent to the walls.

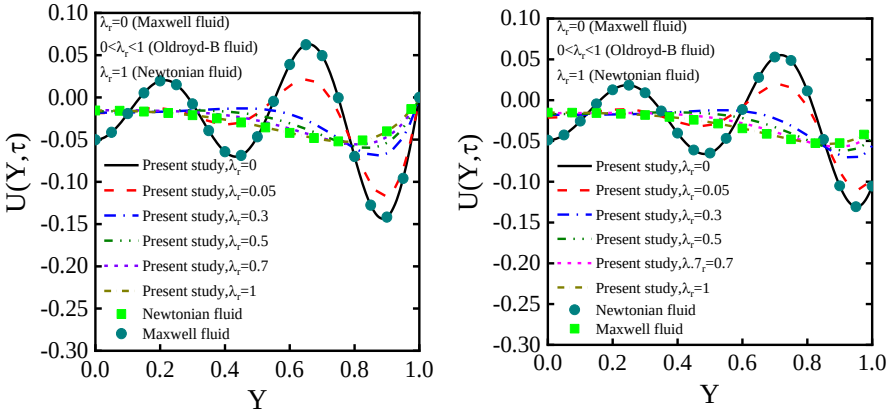

(a) Free-slip condition ($\bar{a}$=0) (b) Slip condition ($\bar{a}$=0.1)

Fig. 7.4 Comparison of present study for normalized velocity profiles among Oldroyd-B, Maxwell, and Newtonian fluids under varying boundary conditions at K=10, $\bar{\xi}$=2, Re_ω=30, $\bar{\lambda}_1$ = 0.2, Ω=1.5, λ=5, Ha=2, Du=2.

Figure 7.5 illustrates the non-dimensional velocity U (Y, τ) of an Oldroyd-B fluid subjected to a time-varying electrokinetic driving force, plotted with respect to the transverse position Y and the temporal phase angle τ. Under conditions of high zeta potential, the electrokinetic force becomes significantly stronger, leading to greater variations in the velocity profile across both space and time. The three-dimensional surface plot captures the periodic flow behavior, displaying alternating patterns that are synchronized with the imposed oscillatory field.

The velocity field responds dynamically to changes in τ, exhibiting flow reversals over different parts of the cycle. During certain phases, the velocity reaches its peak near the centreline of the channel and tapers toward the walls. In comparison, other phases have reversed flow directions, reflecting the influence of the periodically applied streaming potential and the elastic memory of the fluid. The Oldroyd-B

rheological model, which accounts for both fluid relaxation and retardation, introduces time-lags in responses. It leads to phase shifts and flow asymmetry. This viscoelastic behavior, when combined with strong electrokinetic effects due to elevated zeta potential, enhances the velocity in specific regions of the domain and at particular phases.

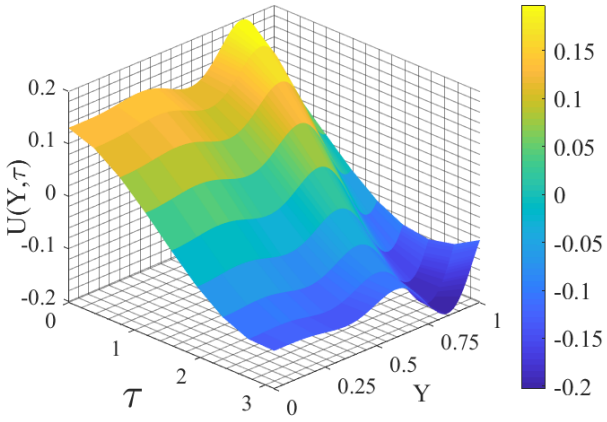

Fig. 7.5 Surface plot of normalized velocity U(Y, τ) for time-periodic electroviscous flow of an Oldroyd-B fluid, presented as a function of Y and τ at K=10, $\bar{\xi}$=2, $\bar{\lambda}_1$ = 0.2, Ω=1.5, λ=5, Ha=2, λ_r=0.05, Du=2, $\bar{a}$=0.1.

(iii) Volumetric flow rate

Figure 7.6 displays the combined effects of dimensionless Hartmann number, normalized electric field, angular Reynolds number, zeta potential, relaxation time, retardation time, and normalized physical time on the fluid flow across the channel. The variation of the volume flow rate profile for different values of Ha as a function of Re_ω is plotted in Fig.7.6a. Under the influence of the streaming potentials, the velocity changes rapidly near the walls and generates vortices and oscillations. From the physical perspective, the Lorentz force, as described by Eq. (7.5), acts in the axial direction and has a magnitude corresponding to the aiding component $\sigma_f B_y E_z^0$ and a flow-opposing component $\sigma_f u_0 B_y^2$. As lower values of Ha, adding force is more pronounced than opposing forces, which is the ratio between the electromagnetic force and the viscous force in physics, which displays that the opposing component is more pronounced than the aiding component in the flow system. The negative velocity gradients along the channel are obtained with a high value of Ha. As a result, it has a significant impact on the transport of fluids. Negative values may emerge in the volume flow rate, indicating that backflow has occurred. Increasing Ha alters the velocity distribution asymmetrically by suppressing the central core flow while amplifying secondary recirculation zones near the walls, thereby reducing the net forward throughput. Fig. 7.6b depicts the effect of Re_ω on the volume flow rate distribution with different values of τ. At a lower Re_ω, the

volume flow rate is lower, indicating that the momentum diffusion time is shorter than the oscillatory time of the electric field. The increase in Re_ω corresponds to the dominance of inertial forces. These forces would typically accelerate the flow by overcoming viscous drag. This resistance emerges not from the electric field itself, but from the viscoelastic memory stored during earlier parts of the cycle, which counters the present acceleration. At $\tau = 3\pi/2$, the flow rate may decrease because the system is at a stage of oscillation where the viscoelastic interaction ($\bar{\lambda}_1 = 0.2$) is more pronounced. This causes the system to resist changes in flow, even when inertial forces push for an increase in flow.

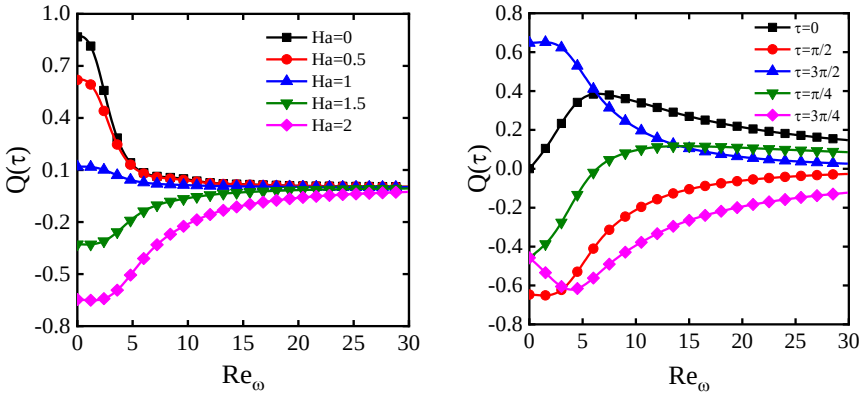

(a) $\tau = \pi/2$ (b) Ha=2

Fig. 7.6 Variation of normalised volumetric flow rate at slip boundary conditions as a function of Re_ω at K=10, $\bar{\xi}$=2, $\bar{\lambda}_1 = 0.2$, Ω=1.5, λ=5, Ha=2, λ_r=0.05, Du=2, $\bar{\alpha}$=*0.1*, (a) for different values of Ha, and (b) for different values of τ.

The combined effects of dimensionless time phase ($\tau=\omega t$) and Dukhin number (Du) significantly influence the electrokinetic volume flow rate in streaming potential-driven flows is plotted in Fig.7.7a. As τ varies from 0 to π, it captures a half-cycle of the oscillatory field, during which the direction and magnitude of the streaming potential and electric field evolve dynamically. Initially, at lower τ, the induced electric field aligns with the pressure-driven flow, enhancing the electroosmotic slip and increasing the volume flow rate. As τ progresses toward π, the direction of the field reverses, causing a phase lag in the induced streaming current and a reduction in flow, often leading to oscillatory behavior in the volume flow response.

The Dukhin number (Du), representing the ratio of surface (Stern layer) to bulk conductivity, modifies this time-dependent flow behavior by altering the conduction-streaming current balance. At low Du, the streaming current dominates, leading to higher induced electric fields and more pronounced oscillations in the flow rate. As Du increases, additional surface conduction dampens the streaming potential, reducing the net electrokinetic driving force. This damping effect is apparent during peak τ, where the flow magnitude decreases with increasing Du due to stronger electroviscous resistance. Together, τ and Du control the magnitude and timing of the volume flow oscillations. While τ determines the instantaneous electrokinetic driving

force, Du governs how effectively this force is converted into fluid motion. The surface plots demonstrate that higher Du values lead to suppressed flow amplitudes across all τ, and the phase-dependent asymmetry becomes more noticeable, especially under strong electromagnetic coupling.

Figure 7.7b illustrates the variation of normalized volume flow rate Q(τ) as a function of the Hartmann number (Ha) and the dimensionless time phase τ, for a fixed Dukhin number Du=2. The time phase (τ) spans from 0 to π, representing half of a periodic cycle of the oscillating electric field. At lower τ, the electric field and streaming current are more favourably aligned with the pressure-driven flow, leading to enhanced slip and relatively higher forward flow. As τ increases toward π, the phase difference grows, and the induced electric field begins to oppose the flow direction, resulting in a reduction or even reversal in volume flow rate. This time-varying behavior reflects the transient nature of the coupling between electrokinetic and magnetic effects.

At low Ha values, the Lorentz force is weak, and the magnetic damping is minimal, allowing the oscillatory electric field to dominate the transport. However, the flow may remain weak or even slightly negative due to phase mismatch at certain τ. As Ha increases, firmer magnetic damping initially suppresses the flow. However, the plot reveals a regime of enhanced forward flow at intermediate Ha and lower τ, indicating a constructive interaction between the induced electric field and Lorentz force. Beyond a critical Ha threshold, excessive magnetic resistance dominates, and the volume flow is reduced again regardless of time phase, demonstrating the non-monotonic impact of Ha on flow dynamics. Overall, the time phase τ plays a crucial role in modulating the volume flow rate within each oscillation cycle. The dynamic reversal and amplification effects associated with τ highlight the importance of phase timing in oscillatory driving conditions.

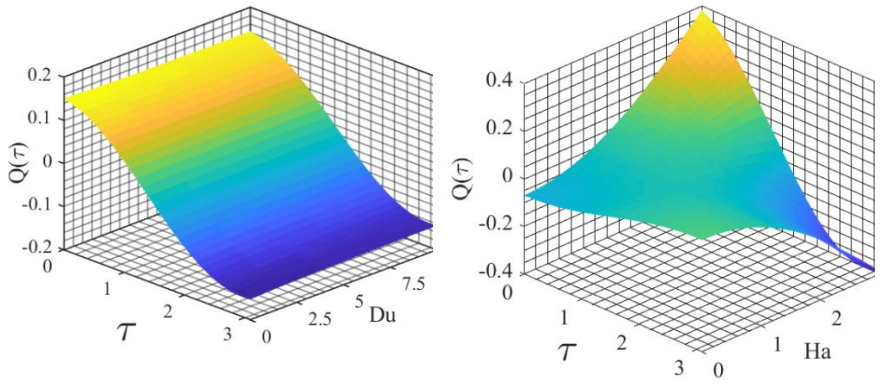

(a) Ha=2 (b) Du=2

Fig. 7.7 Surface plot of normalized volumetric flow rate for time-periodic electroviscous flow of an Oldroyd-B fluid, presented as a function of Y and τ at K=10, $\bar{\xi}$=2, $\bar{\lambda}_1$ = 0.2, Ω=1.5, λ=5, Ha=2, λ_r=0.05, $\bar{a}$=0.1.

(iv) Electrokinetic energy conversion efficiency

Figure 7.8 illustrates the variation in electrokinetic energy conversion (EKEC) efficiency for the viscoelastic Oldroyd-B fluid under different zeta potentials ($\bar{\xi}$) and the influence of the Dukhin number (Du), which characterizes Stern layer conductivity. As shown in Fig.7.8a, the EKEC efficiency initially increases with $\bar{\xi}$ due to stronger electrokinetic interactions and enhanced streaming current generation. The maximum efficiency is observed at a low zeta potential ($\bar{\xi}$=0.01), followed by $\bar{\xi}$=2, beyond which the efficiency gradually decreases for higher $\bar{\xi}$=2 values ($\bar{\xi}$>2). At very low $\bar{\xi}$=2, the electric double layer (EDL) remains weak, minimizing electroviscous drag and allowing efficient energy conversion. However, as $\bar{\xi}$=2 increases, the EDL becomes stronger, leading to increased streaming current and enhanced efficiency. Beyond a threshold ($\bar{\xi}$=2), excessive surface charge leads to greater electroviscous resistance and oscillatory losses, thereby reducing efficiency [133,370]. Figure 7.8b contrasts the impact of Stern layer conductivity by comparing cases with and without Du. Notably, at $\bar{\xi}$=4, the EKEC efficiency improves by 59.80% when Du increases from 0 to 2. This counterintuitive increase, despite a reduced streaming potential $\bar{E}_s^0$, results from the beneficial role of Stern layer conductivity. The added conduction path moderates the mismatch between streaming and conduction currents, reducing charge buildup and mitigating oscillatory losses. Although the induced field weakens, internal dissipation is suppressed, and the efficiency benefits from the (1 + Du) scaling in the normalized formulation. This behavior highlights the existence of an optimal zeta potential (around $\bar{\xi}$=4 at K=40), where the trade-off between electrokinetic force generation and viscous resistance is most favourable. Thus, incorporating Stern layer effects can significantly enhance energy conversion, particularly under thin EDL and moderate surface charge conditions, by improving current balance and reducing internal losses.

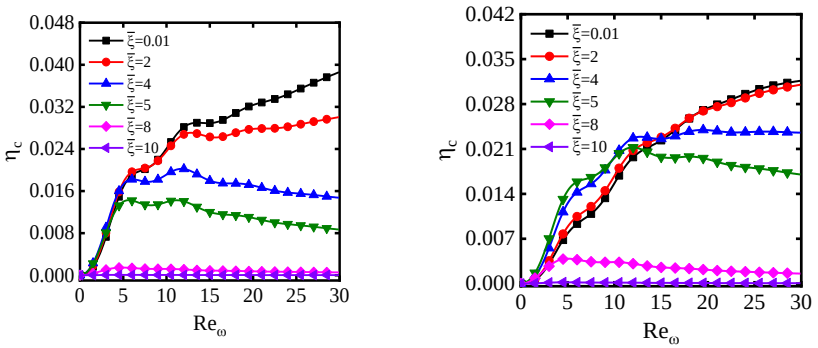

(a) Independent of stern layer (Du=0) (b) Dependent of stern layer (Du=2)

Fig. 7.8 Electrokinetic energy conversion efficiency of the present study as a function of Re_ω for different values of $\bar{\xi}$ for Oldroyd-B fluid at K = 10, Ω = 1.5, Ha = 2, $\bar{\lambda}_1$ = 0.2, λ_r = 0.05, λ = 5, τ = π/2.

(v) Concentration distribution

Figure 7.9 illustrates the effect of sinusoidal pulsations on the concentration distribution, shown as a function of the dimensionless coordinate Y. A significant variation in concentration can be observed across the channel along the transverse direction of the fluid flow. Fig. 7.9a presents the concentration distribution with the influence of λ. The electroviscous effects intensify, causing the ion concentration near the walls to oscillate. The concentration profile remains flat and symmetric across the channel centre for low λ values, as viscous forces dominate and the electric field influence is minimal. This interaction becomes most prominent in the electric double layer (EDL) near the walls, where ion accumulation occurs due to the balance between electrostatic attraction to the charged surface and thermal diffusion. As λ increases, indicating more substantial time-dependent electric field effects, the unsteady forcing amplifies the electric body force acting on the ions. This results in intensified oscillatory transport and sharper spatial concentration gradients near the walls. This interaction is most significant in the EDL near the walls, where the concentration of ions is naturally higher due to electrostatic attraction to the wall charge. Hence, higher λ values lead to more abrupt changes in concentration near the walls. This oscillation results from the enhanced electric field interaction, disturbs the ion distribution, and leads to more pronounced accumulation and depletion regions in the EDL. These oscillations in concentration near the walls are due to the competition between electrokinetic and electrostatic forces. The electric field pushes ions toward or away from the wall, creating sharp gradients in ion concentration, which are reflected as peaks and troughs in the concentration profile close to the EDL.

The variation of the concentration profile for different values of Ha is presented in Fig. 7.9b. For Ha values ranging from 0 to 1, the concentration profile remains positive, indicating that forward solute transport is dominated by streaming potential effects. However, for Ha=1.5 to Ha=2, negative values appear in the concentration profile, signifying solute backflow as mentioned in Fig. 7.6b. This shift occurs due to the increasing influence of Lorentz forces, which disrupt solute movement and lead to localized flow reversal. At elevated Ha, the magnetic field alters the curvature of velocity streamlines, compressing solute near the walls while enabling intermittent axial slippage, which results in skewed and asymmetric concentration layering. Additionally, the Oldroyd-B fluid's viscoelastic properties contribute to concentration oscillations due to the fading memory effect, further amplifying fluctuations as Ha increases. The concentration increased by 64.35% in the presence of the Hartmann number (Ha = 2) compared to the absence of the Hartmann number (Ha = 0) at the peak for Oldroyd-B fluid in the microchannel.

Figure 7.9c illustrates the effect of $\bar{\lambda}_1$ on the concentration distribution. The $\bar{\lambda}_1$ varies from 0 to 0.2. At $\bar{\lambda}_1$=0, the fluid behaves as a Newtonian fluid, where viscous forces dominate. In this case, the concentration profile remains smooth, with minimal fluctuations. Physically, a larger $\bar{\lambda}_1$ means polymer chains remain stretched longer and release elastic energy with each pulsation, causing the flow to lag and oscillate. As the relaxation time increases, elastic forces become more dominant than viscous forces. This allows the fluid to retain deformation over time, leading to oscillatory velocity behavior. These velocity fluctuations cause periodic acceleration and

deceleration of solute transport, disrupting the smooth movement of solutes. As a result, the concentration profile exhibits stronger oscillations. Near the walls, where velocity shear is more pronounced, the interaction between elastic effects and electroviscous forces further amplifies the redistribution of solutes. This creates sharper concentration gradients and enhances variations in solute transport. Additionally, the fading memory effect in viscoelastic fluids means that past deformations influence the present behavior of the fluid. Consequently, higher relaxation times increase solute transport instability, leading to a more complex and fluctuating concentration profile, particularly in regions affected by velocity shear and electrokinetic interactions.

Figure 7.9d displays the combined effects of the dimensionless Hartmann number, normalized electric field, angular Reynolds number, relaxation time, zeta potential, retardation time, and physical time on the fluid concentration for different values of the dimensionless angular Reynolds number. At Re_ω=0.01, viscous forces dominate, resulting in a stable flow with a smooth concentration profile and positive concentration values across the channel. This indicates weak convective transport and a uniform ion distribution governed primarily by diffusion. As Re_ω increases to 5, inertial forces become more significant, leading to more substantial convective transport and a smoother but adverse concentration profile. The negative values indicate solute backflow resulting from the interaction between inertial forces and the electric double layer (EDL). At Re_ω=30, inertial forces dominate, causing a highly dynamic flow with pronounced fluctuations in the concentration profile. The interaction between fluid motion and the EDL strengthens near the walls, resulting in sharp concentration gradients and regions of ion accumulation and depletion. These trends highlight the transition from diffusion-dominated transport at low Re_ω to convection-dominated, oscillatory behavior at higher Re_ω.

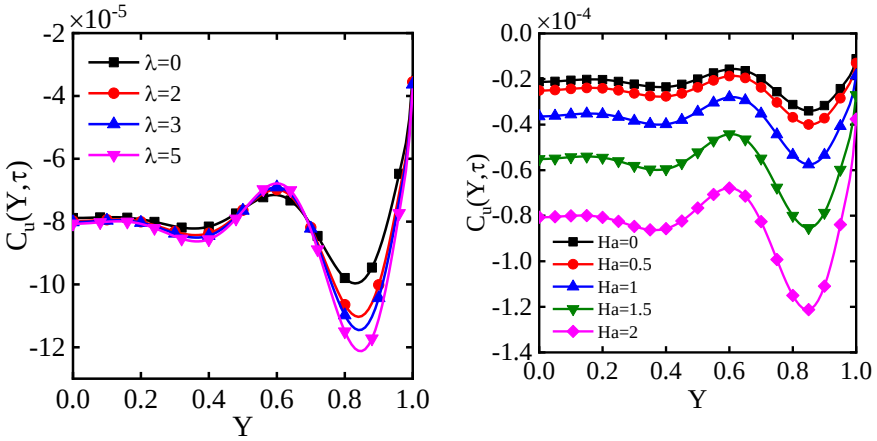

(a) Re_ω=30, Ha=2, $\bar{\lambda}_1$ = 0.2 (b) Re_ω=30, λ=5, $\bar{\lambda}_1$ = 0.2

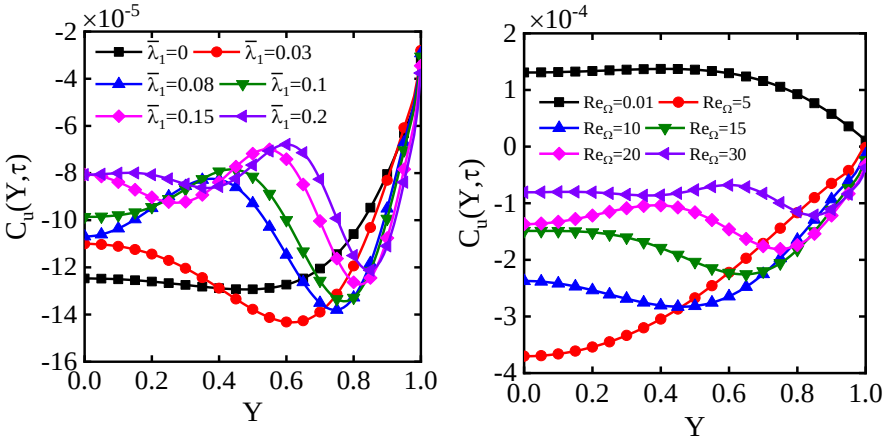

(c) Re_ω=30, λ=5, Ha=2 (d) λ=5, Ha=2, $\bar{\lambda}_1$ = 0.2

Fig. 7.9 Time-periodic concentration distribution of streaming potential flow across a channel of Oldroyd-B fluid with concentration slip conditions at K = 10, $\bar{\xi}$=2, **Ω** = 1.5, Du = 2, λ_r = 0.05, and τ = π/2, (a) for various values of λ, (b) for varying values of Ha, (c) for various values of $\bar{\lambda}_1$, and (d) for varying values of Re_ω.

(vi) Mass flow rate

Figure 7.10 shows the normalized mass flow rate for the streaming potential flow of an Oldroyd-B fluid as a function of the angular Reynolds number, considering the effects of magnetic fields. The impact of Ha on the mass transfer rate is plotted in Fig. 7.10a. The magnitude of the flow rate as a function of Re_ω increases under the conditions of Ha = 0, 0.5, and 1. In contrast, it exhibits an opposite trend under the conditions of Ha = 1.5 and 2, as shown in Fig. 7.6a. A critical Ha, in combination with appropriate conditions such as the angular Reynolds number at Du=2, facilitates the optimal dispersion of the solute. The behavior of the mass flow rate with Re_ω, Ha can be understood by considering the transition from a viscous-dominated flow regime to an inertial-dominated flow regime, along with the influence of Ha. At a low Re_ω, the flow is primarily controlled by viscous forces, and the mass flow rate decreases with increasing Ha due to the resistive effect, which acts as a braking mechanism, suppressing the motion of the conducting fluid. However, the mass flow rate increases with Re_ω because the growing inertia begins to overcome viscous resistance. As surpasses a certain threshold Re_ω~0.2, the flow enters an inertial-dominated regime, where the role of Ha changes, leading to charge separation. Here, the Lorentz force, rather than simply suppressing the motion, interacts with the flow to generate secondary vortices and enhance mass transport, increasing the mass flow rate with Ha. However, at high Re_ω, inertial effects become so dominant due to chaotic flow nature and localized recirculations, ultimately reducing the efficiency of

mass transport and causing a decrease in the mass flow rate with increasing Re_ω. This transition highlights the competing effects of viscosity, inertia, and electromagnetic forces, showing that at low Re_ω, the mass flow rate decreases with Ha but increases with Re_ω. At high Re_ω, it increases with Ha but decreases with further increases in Re_ω. This behavior demonstrates how electromagnetic forces can be used to regulate fluid motion, providing valuable insight for optimizing transport in electrically conducting Oldroyd-B fluids. In such a regime, lower values combined with higher Ha and specific Du values promote enhanced dispersion and more efficient mass transfer by maintaining a stable flow that supports the solute diffusion across the fluid. This improves the overall process by optimizing the balance between the magnetic field's effects and the fluid's flow characteristics. Fig. 7.10b shows that $\bar{m}_x$ is higher at lower Re_ω due to the dominance of viscous, elastic, and electrokinetic effects over inertial forces. At low Re_ω, the flow remains stable. At high Re_ω, the flow is influenced by the interaction between the streaming potential and the electric double layer, with a significant contribution from the Stern layer. Enhanced conductivity in the Stern layer offers a less resistive path for ionic conduction, which lowers the magnitude of the streaming potential needed to balance the streaming current and achieve electroneutrality. Lower Du values allow stronger streaming potentials to develop, maintaining coherent flow layers aligned with the axial direction, thereby enhancing $\bar{m}_x$. In viscoelastic fluids like Oldroyd-B, the elastic properties enhance the fluid's response to periodic forces, which further contributes to the higher mass transfer rate. As Re_ω increases, inertial forces disrupt this balance, diminishing the effects of the Stern layer and viscoelasticity, resulting in a decline in $\bar{m}_x$.

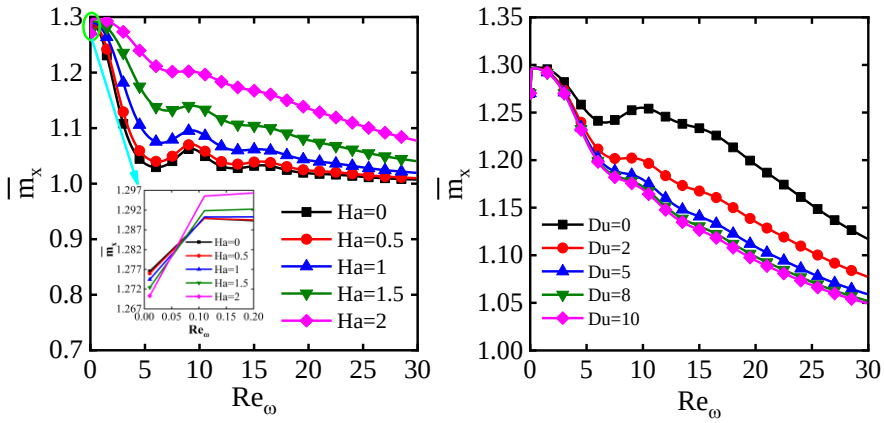

(a) Du=2 (b) Ha=2

Fig. 7.10 Mass transfer rate $\bar{m}_x$ as a function of the angular Reynolds number Re_ω across a channel for Oldroyd-B fluid with electroviscous effect at different values of Ha, Du respectively at K = 10, $\bar{\xi}$= 2, Ω = 1.5, $\bar{\lambda}_1$= 0.2, λ_r = 0.05, λ = 5, and $\tau = \pi/2$.

7.3.2. Thermal analysis of Fe3O4-water nanofluids

(i) Temperature field

Figure 7.11 depicts the normalized temperature distribution in an Oldroyd-B fluid along the Y-coordinate in a microchannel, highlighting the effects of Joule heating and thermal radiation. The influence of Joule heating effects on non-dimensional temperature distribution is shown in Fig. 7.11a, considering temperature jump boundary conditions. As the Joule heating parameter increases, more heat is generated due to converting electrical energy into thermal energy, leading to more significant temperature gradients across the channel. As the Joule heating parameter increases, more heat is generated, leading to higher temperature gradients across the channel. Heat flows from the fluid to the walls when the fluid exceeds the wall temperature ($T>T_w$), resulting in a negative dimensionless temperature (θ). This occurs because the denominator in the expression for $\theta=(T-T_w)/(T_i-T_w)$ is negative when the inlet temperature (T_i) is lower than the wall temperature (T_w). The combined effects of Joule heating and thermal radiation enhance heat transfer from the fluid to the walls, creating a more pronounced temperature distribution. It is evident that the temperature profile becomes more negative and flatter across the channel centre as J_h increases, indicating that internal volumetric heating dominates over wall conduction. The upward curvature near $Y\rightarrow1$ becomes sharper with increasing J_h, suggesting localized heat accumulation due to the temperature jump condition, which restricts thermal energy diffusion at the wall.

In Fig. 7.11b, the effect of the thermal radiation parameter (Nr) on the temperature distribution is observed across the channel. In the region (Y~0-0.8), the temperature remains nearly uniform but increases slightly with Y. As Nr increases, the fluid temperature increases due to enhanced heat absorption from radiation. This is evident as Nr=10 exhibits a higher temperature than Nr=8, and both are higher than Nr=0, indicating that radiation contributes to raising the fluid temperature in the bulk region. However, in the near-wall region ($Y\rightarrow1$), an opposite trend is observed. The temperature $\theta(Y, \tau)$ drops sharply, forming a steep thermal gradient near the wall. Interestingly, at Y=1, the case with Nr=0 has a higher temperature than Nr=8 and Nr=10. This suggests that increasing Nr enhances the heat transfer away from the wall, leading to a cooler near-wall region. The reduced temperature at the wall with increasing Nr indicates that thermal radiation facilitates heat dissipation, thereby improving the overall heat transfer efficiency. Consequently, higher radiation intensities promote a stronger thermal gradient, ensuring effective heat transport from the wall into the fluid. It is also evident that thermal radiation redistributes energy from the near-wall region to the core, causing the wall-adjacent fluid to cool faster. The steeper drop in θ near Y=1 for higher Nr values indicates enhanced radiative flux that lowers thermal resistance at the boundary.

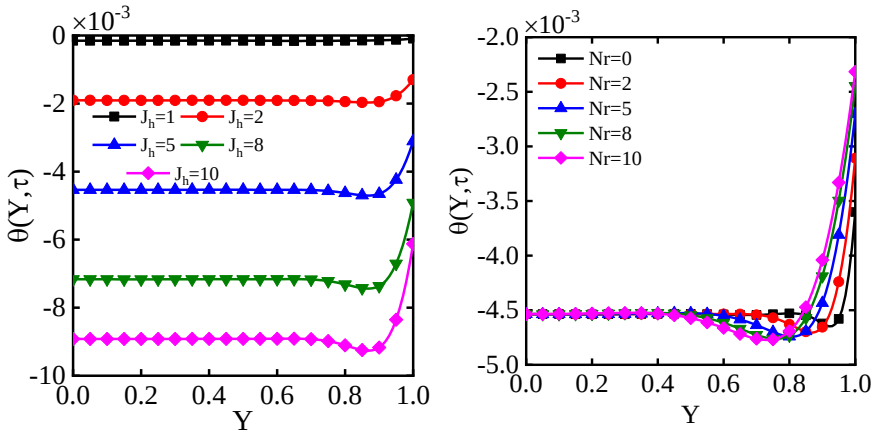

(a) Nr=2 (b) J_h=5

Fig. 7.11 Normalised temperature distribution for Oldroyd-B fluid flow across a channel for different values of J_h, Nr, and respectively at K = 10, $\bar{\xi}$= 2, Ha = 2, Du = 2, **Ω** = 1.5, $\bar{\lambda}_1$ = 0.2, λ_r = 0.05, λ = 5, τ = π/2.

(ii) Nusselt number estimations for heat transfer

Fig. 7.12 illustrates the variation of Nu as a function of K, highlighting the time-periodic effects within the channel. As K increases, the electric double layer (EDL) becomes thinner and more confined to the channel walls. This increases the number of active ions per unit thickness, enhancing the streaming potential. This results in a higher streaming potential, strengthening the electroviscous effects and modifying the bulk fluid motion. The impact of the zeta potential effect on the Nu is illustrated in Fig.7.12a by the interplay between the streaming potential, flow pulsations, viscoelastic effects, and electroviscous phenomena. Notably, changes in the zeta potential ($\bar{\xi}$) result in decreasing and increasing trends in the Nusselt number, affecting velocity and temperature gradients in the flow. At low zeta potentials ($\bar{\xi}$ =0.01), the surface charge density is minimal, resulting in a weak streaming potential that inadequately reinforces the pressure-driven flow, thereby diminishing convective heat transfer and reducing Nu. As the zeta potential increases to moderate values ($\bar{\xi}$=2 to 5), the enhanced surface charge intensifies the streaming potential, strengthening the induced electric field. This augmentation modifies flow dynamics, leading to higher velocity gradients and improved convective heat transfer coefficient, resulting in an increased Nu. The time-periodic nature of the flow further amplifies this effect by promoting better mixing through oscillatory motion. However, at very high zeta potentials ($\bar{\xi}$=10), electroviscous effects become predominant, causing a reduction in Nu. The EDL becomes more confined to the walls, increasing electroviscous resistance and suppressing velocity fluctuations essential for effective heat transport. Additionally, excessive charge accumulation near the wall further retards flow oscillations, reducing the efficiency of periodic fluid motion. Significant Joule

heating occurs, leading to localized temperature rises near the walls, disrupting the temperature gradient, and impairing convective heat transfer. The combination of high $\bar{\xi}$ and high K exacerbates these adverse effects, as the strong streaming potential near the walls interacts with the thin EDL, leading to excessive viscous dissipation and localized heating. In contrast, the system achieves an optimal balance between flow enhancement and thermal dissipation at moderate K and $\bar{\xi}$ values, maximizing Nu. Therefore, both $\bar{\xi}$ and K critically influence the heat transfer characteristics, with their combined effects determining the efficiency of convective heat transfer in streaming potential flows.

The heat transfer highlights the effect of the non-Newtonian parameter λ_r (the ratio of retardation time to relaxation time) on Nu as K increases, as shown in Fig.7.12b. At λ_r=0, representing Maxwell fluid behavior, strong elastic effects amplify the streaming potential field, resulting in an enhancement of Nu. However, as K increases, the EDL thins, leading to increased streaming potential. Consequently, Joule heating and electroviscous effects intensify due to the rise in apparent viscosity, while the contribution of elastic effects to the heat transfer rate becomes more significant. Oldroyd-B fluids exhibit intermediate viscoelastic behavior, with $0<\lambda_r<1$indicating a balance between viscous and elastic effects. In contrast, at λ_r=1, representing Newtonian fluid behavior, viscous forces dominate, leading to a significant reduction in Nu. These trends collectively highlight the intricate interplay of elastic and viscous forces, electrokinetic contributions, and the relative dominance of the EDL versus bulk flow effects in shaping the observed heat transfer behavior.

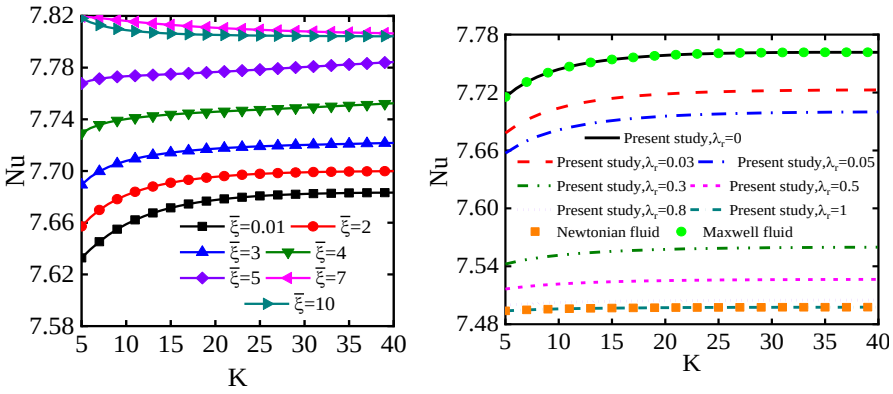

(a) λ_r =0.05 (b) $\bar{\xi}$=2

Fig. 7.12 The variation of Nu as a function of K with different values of $\bar{\xi}$, λ_r, respectively at K = 10, Ha = 2, Ω = 1.5, Du = 2, $\bar{\lambda}_1$ = 0.2, λ = 5, τ = π/2, Nr = 2, and J_h = 5.

(iii) Prediction of entropy generation

Thermal irreversibility in the system results from the combined effects of the electric field, magnetic field, Joule heating, and viscous dissipation. The influence of the K

on S_{total}. System entropy production arises from the interplay of electromagnetic forces, resistive heating, and viscous energy dissipation. Fig. 7.13 analyzes how parameter K governs total entropy (S_{total}). Fig. 7.13a maps against K for varying Du, demonstrating that a compressed EDL lowers ion density near boundaries. This reduces localized electrical conductivity and resistive heating, as shown in Fig. 7.13a. Elevating Du intensifies Stern layer conductivity, altering the equilibrium between streaming currents and conduction mechanisms. This shifts dominance to mobile conduction currents in bulk fluid, marginalizing Stern layer contributions. Concurrently, stationary conduction currents within the Stern layer amplify alongside bulk flow. The heightened Stern layer conductivity creates a low-impedance pathway for charge transport, reducing the ionic current required to neutralize streaming effects. Consequently, diminished streaming potential suffices to stabilize current equilibrium and preserve electroneutrality

In Fig. 7.13b, the effect of the elasticity parameter ($\bar{\lambda}_1$) on S_{total} is analyzed for a fixed Du = 2. The plot shows that for $\bar{\lambda}_1$=0 (Newtonian fluid), entropy generation starts at a relatively high value and decreases as K increases. As $\bar{\lambda}_1$ increases to 0.03, total entropy initially rises, reaching a local peak, but then begins to decrease for $\bar{\lambda}_1$=0.04. This decreasing trend continues for higher values of $\bar{\lambda}_1$=0.1, 0.15, and 0.2 showing progressively lower entropy generation. The curves for these higher elasticity values exhibit a noticeable downward trend, which can be attributed to the influence of elasticity in reducing irreversibility in the system. As elasticity increases, the fluid transitions from a Newtonian to a viscoelastic behavior, where internal friction and shear-induced entropy generation are minimized. Additionally, higher elasticity enhances the ability of the fluid to store and recover energy rather than dissipating it irreversibly, leading to reduced entropy production. This effect stabilizes the system by optimizing energy transport, minimizing both thermal and shear-induced entropy. Finally, the lowest entropy is observed at $\bar{\lambda}_1$=0.2, indicating that at sufficiently high elasticity, the fluid system experiences the most efficient energy transport with minimal dissipation.

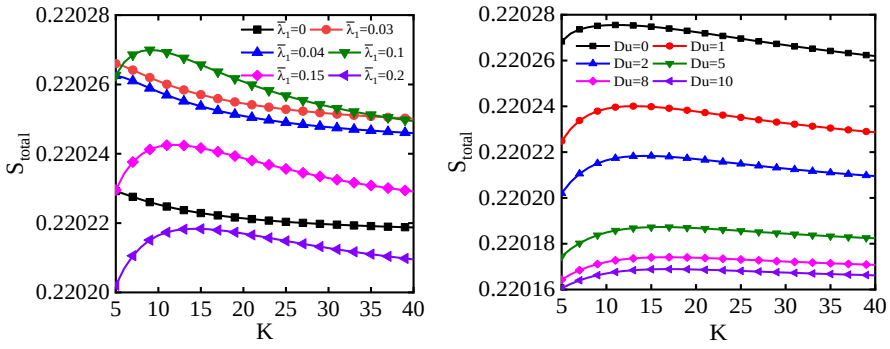

(a) $\bar{\lambda}_1$=0.2 (b) Du=2

Fig. 7.13 Global entropy generation distribution across a channel of Oldroyd-B fluid as a function of K for different values of Du, $\bar{\lambda}_1$, respectively at K = 10, Ha = 2, Ω = 1.5, λ = 5, τ = π/2, Nr = 2, and J_h = 5.

7.3.3. Sensitivity analysis of key parameters on EKEC efficiency and entropy generation

The convergence of sensitivity indices illustrates how the model output responds to variations in both first-order and total effect input parameters. This analysis helps improve model accuracy and reduce uncertainty [371,372]. The provided sensitivity analysis, presented in Fig. 7.14 directly addresses the influence of three key non-dimensional parameters such as: zeta potential ($\bar{\xi}$), Hartmann number (Ha), and relaxation time ($\bar{\lambda}_1$) on two critical performance metrics: EKEC efficiency (η_c) and entropy generation (S_{total}). These bar plots display both the first-order Sobol indices and total effect indices, thereby offering insight into both the individual (direct) and interaction-based (total) contributions of each parameter.

Fig. 7.14a shows the sensitivity indices for η_c, the first-order effect of $\bar{\xi}$ is relatively low (~0.2), indicating that its isolated influence on efficiency is limited. However, the corresponding total-effect index is significantly higher (~0.78), suggesting that $\bar{\xi}$ plays a major role through interactions with other parameters, likely influencing the structure and strength of the electric double layer (EDL) and thus modulating streaming potential and flow nonlinearly. The Hartmann number (Ha) exhibits a moderate contribution in both first order and total effect indices (~0.5), indicating that magnetic effects (through the Lorentz force) directly affect η_c while also engaging in moderate interaction effects. The relaxation time ($\bar{\lambda}_1$), characterizing fluid viscoelasticity, shows a small first order impact (~0.1), but a large total-effect index (~0.85), highlighting that viscoelastic effects predominantly influence the EKEC efficiency via synergistic interactions with electric and magnetic forces.

Fig. 7.14b corresponds to entropy generation (S_{total}), the sensitivity patterns shift. The zeta potential ($\bar{\xi}$) now exhibits a higher direct impact (first order index ~0.35) and even stronger interaction contributions (total effect ~0.65), underscoring its central role in governing electrokinetic forces that affect thermal gradients and entropy production. Ha has an extremely small first order contribution but a very large total effect index (~0.95), indicating that magnetic field strength, while not independently dominant, significantly amplifies entropy generation when combined with other parameters likely due to enhanced Joule heating and damping effects. ($\bar{\lambda}_1$) shows moderate sensitivity in both indices (~0.45–0.55), confirming that viscoelasticity directly and indirectly modulates thermal irreversibility and fluid damping behavior. This sensitivity analysis reveals that while Ha directly affects entropy more than efficiency, $\bar{\xi}$ and $\bar{\lambda}_1$are critical for both metrics mainly through nonlinear coupling. These results provide strong justification for emphasizing these parameters in physical interpretation and optimization, and directly enhance the clarity and rigor of the study's conclusions.

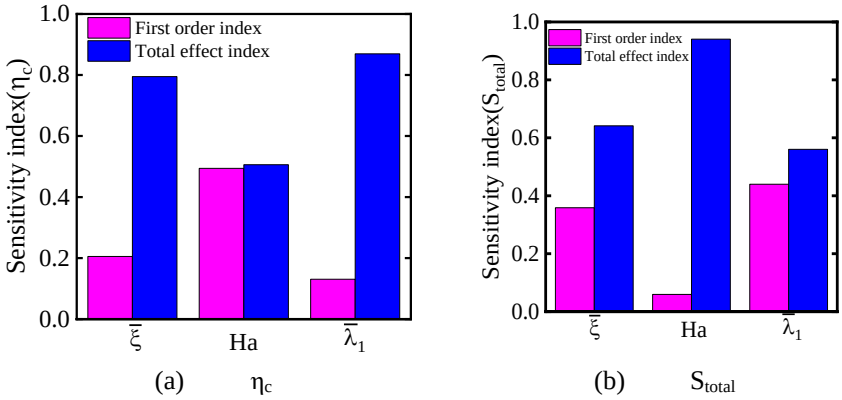

Fig. 7.14 First order and total effect Sobol sensitivity indices for the parameters influencing (a) EKEC efficiency and (b) total entropy generation at K = 10, Ω= 0, λ = 5, τ = π/2, Nr = 2, Du = 2, λ_r = 0.05, and J_h = 5.

7.4. Concluding remarks

This study reveals critical insights into the complex rheology of Oldroyd-B fluids and their role in enhancing the performance of portable microfluidic devices in power generation, heat transfer, and energy dissipation. This study explores the intricate interplay of time-periodic flow, electro-magnetohydrodynamics, and electroviscous effects within a microchannel system. The nonlinear Poisson-Boltzmann equation, formulated without the Debye-Hückel approximation, governs the zeta potential and is integrated into the momentum equation alongside velocity slip, electromagnetic fields, and Stern layer currents. Key design parameters are analyzed to assess the flow field, volume flow rate, EKEC efficiency, concentration profile, mass transport rate, temperature profile, Nusselt number, and entropy production. The key findings highlight the intricate rheological and heat transfer characteristics of viscoelastic fluids as summarized below:

(i) The analysis conducted in this study also evaluates the flow characteristics of Maxwell and Newtonian fluids by selecting the appropriate viscoelastic parameter.

(ii) When Stern layer effects are neglected, the maximum electrokinetic energy conversion (EKEC) efficiency experiences a significant increase at high zeta potential ($\bar{\xi}$=4). Specifically, with a Dukhin number (Du=2), the EKEC efficiency improves by 59.8% compared to the scenario where Du=0.

(iii) Resonant behavior, influenced by the Re_ω, impacts the mass transfer rate and species separation. When Re_ω exceeds a critical value (Re_ω~0.2), the flow shifts from a viscous-dominated regime to an inertia-dominated regime. In this state, the effect of the Ha undergoes a notable transformation, resulting in charge separation. The concentration increased by 64.35% in the presence of a magnetic field (Ha = 2) compared to the absence of a magnetic field (Ha = 0) at the peak for Oldroyd-B fluid in the microchannel.

Chapter 8. Ion transport phenomena in electrokinetic desalination systems with ion concentration polarization in nanochannel arrays

8.1. Objectives of the chapter

This study investigates desalination of salt water for parallelizing nanochannels within a rectangular geometry and analyses the influence of gravity on the desalination process, comparing it with a hyperbolic geometry. The global demand for freshwater has spurred interest in alternative water supply solutions, such as desalination. Traditional desalination methods often face challenges such as high energy consumption and environmental impacts. Existing literature highlights desalination technologies, including ion concentration polarization (ICP)-based methods. Previous studies show that ICP can remove charged species and reduce fouling compared to conventional membranes. However, single-channel ICP devices have limited throughput. To address this, nanochannel arrays can be used for parallelization, and gravitational effects should also be considered. The present study implements a Multiphysics framework combining the Poisson-Nernst-Planck and Navier-Stokes equations to predict the electric field, concentration distribution, velocity profile, energy consumption rate, and salt removal ratio. The results also demonstrate that near the outlet region (≈93.4 nm), the rectangular nanochannel improves the SRR by 24.55% compared to the hyperbolic configuration under an applied voltage of 30 V_0 and a zeta potential of -0.05 V. This framework also integrates a techno-economic analysis to evaluate the levelized cost of water (LCOW) alongside the energy consumption. The LCOW compares the two nanochannel geometries. At the highest applied voltage of 50 V_0, the hyperbolic channel stabilizes at around \$0.7864/m^3, which is significantly lower than the rectangular channel \$0.9844/m^3.

8.2. Physical models and numerical methods

8.2.1. Physical setup

This study investigates the desalination process under steady-state conditions. The working fluid is a dilute sodium chloride (NaCl) solution, which behaves as a Newtonian fluid and flows in a laminar regime. A two-dimensional model is applied, assuming that all properties and variables remain constant along the third direction. For computations in this dimension, a unit length is used, which does not influence key outcomes such as flow velocity or salt removal efficiency. In real systems, this approach implies that the third dimension is considerably larger than the other two. Figs. 8.1a and 8.1b offer a detailed visual representation of our system, portraying a 2D model featuring a rectangular and convergent-divergent nanochannels. This channel incorporates a strategically positioned membrane barrier,

which is constructed with an array of nanochannels. The membrane serves as a selective filter, allowing precise control over the passage of substances. When saline water enters through the inlet, it embarks on a transformative journey as it traverses the intricate network of nanochannels. This journey is crucial, as the fluid undergoes filtration, facilitated by the nanochannel arrays. Architecturally, the framework is divided into three components: the primary inflow channel zone, a nanochannel-based ion-selective membrane, and the primary outflow channel zone. The main channel dimensions, including its same length L and the outlet widths of the rectangular and hyperbolic channels, h_r=40nm and h_r=80nm, play an important role in the system behavior. The nanochannels in the array, including their width ha, spacing hs, and length *l*, are carefully designed to be uniform across all geometries. The system includes n=10 nanoscale array, each with a width ha=2, and spacing hs=2 nm, and vertical span l= 25 nm. Adjacent to these, the main flow of hyperbolic nanochannel has a central width h_r= 40 nm and a vertical span L= 93.444 nm, optimized for functional efficiency (Fig. 8.1a and Fig. 8.1b). The ion-selective barrier is made of an ideal cation-permeable material and carries a uniform negative surface charge ($-\sigma_s$) to amplify filtration efficacy. A saline reservoir (sodium chloride, concentration c_0) interfaces with the inflow channel's upper boundary to sustain controlled fluid ingress. Key operational variables encompass inlet-applied voltage (V_E) and hydraulic pressure (p), while the outflow boundary is maintained at ambient pressure. The synergy of electrokinetic and hydraulic forces governs phenomena such as field-induced flow (EOF) and pressure-mediated transport (PDF).

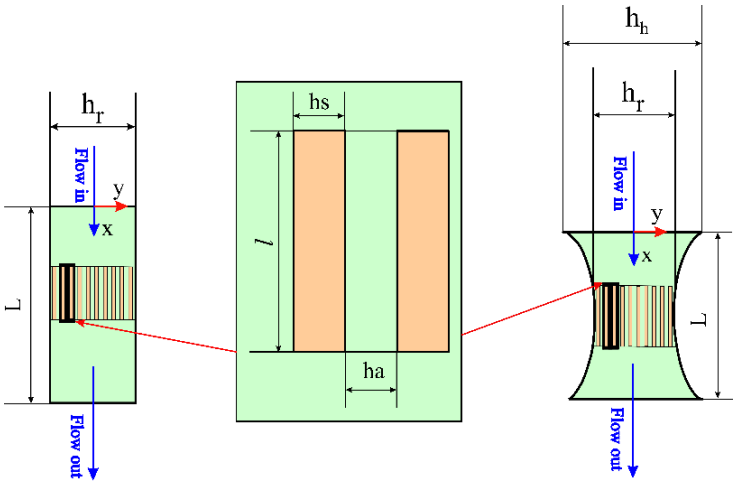

(a) Rectangular nanochannel (b) Hyperbolic nanochannel

Fig. 8.1 Schematic diagram of the nanochannel array model used in the desalination system.

8.2.2. Governing equations

The coupled dynamics of a non-compressible medium, ionic species migration, and electrostatic field evolution are resolved through a Multiphysics framework integrating momentum conservation principles, electro-diffusive flux formulations, and charge-potential coupling. The Navier-Stokes equations govern viscous momentum transfer, the Nernst-Planck relations describe ion transport under electrochemical gradients, and the Poisson equation correlates charge density to electrostatic potential. Collectively, these equations characterize the interplay between hydrodynamic, ionic, and electric phenomena.
The transport of ions follows the law of mass conservation, expressed by the Nernst-Planck equations are expressed as [23,342],

$$\nabla \cdot \mathbf{J}_{\pm} = 0 \tag{8.1}$$

$$\mathbf{J}_{\pm} = -\left(D_{\pm} \nabla c_{\pm} + \frac{D_{\pm} F}{RT} c_{\pm} \nabla \psi \right) + c_{\pm} \mathbf{U} \tag{8.2}$$

Here, J_+, J_-, D_+, D_-, c_+, and c_- are the flux density, diffusion coefficient and the concentration of Na^+ and Cl^- respectively. T is the temperature.
The coupled interaction between the electric potential and charge density of ion concentrations is represented by the Poisson are governed by [373],

$$\nabla \cdot \left(\varepsilon \nabla \psi \right) = -\rho_e \tag{8.3}$$

$$\rho_e = F\left(c_+ - c_- \right) \tag{8.4}$$

where the dielectric constant the solution $\varepsilon=\varepsilon_0\varepsilon_r$, where ε_0 is vacuum permittivity and ε_r is relative permittivity. R, and F are the universal gas constant and the Faraday's number, respectively.
The present analysis considers a steady, fully developed incompressible fluid flow model along with gravity force and generalizes the continuity and Cauchy momentum equations for this flow as [342],

$$\nabla \cdot \mathbf{U} = 0 \tag{8.5}$$

$$\rho\left(\mathbf{U} \cdot \nabla \right)\mathbf{U} = -\nabla p + \nabla \cdot \boldsymbol{\sigma} + \rho_e \mathbf{E} + \rho g \tag{8.6}$$

Here, $\mathbf{U} \equiv (u, v, 0)$ is the velocity of the fluid, p is the pressure, $\boldsymbol{\sigma}$ is the shear stress tensor, $\mathbf{E}=-\nabla\psi$ is the electric field (ψ is the electric potential), ρ_e is space charge density, ρ and μ are the density and dynamic viscosity of the fluid, respectively.

8.2.3. Electroosmotic slip velocity

In the case of a thin electric double layer, the model substitutes the explicit electrical double layer (EDL) description with the Helmholtz-Smoluchowski formulation, wherein the electroosmotic body force is accounted for through a slip velocity

boundary condition that links the electroosmotic velocity to the tangential component of the applied electric field [91].

$$u_{HS}=-\frac{\varepsilon\xi}{\mu}\nabla_s\psi \tag{8.7}$$

Here, u_{HS} represents the electroosmotic slip velocity , ξ is the wall zeta potential, $\nabla_s\psi$ indicates the tangential gradient of the electric potential along the channel surface.

8.2.4. Boundary conditions

To complete the coupled governing equations, the following boundary conditions are applied, At the inlet boundary conditions, (i) hydrostatic gauge pressure is maintained at p_0, (ii) both ion concentrations and particle densities are set to match those in the inlet reservoir as, $c_+=c_-=c_0$, (iii) electrostatic potential is assigned V_E [342].

$$p=p_0;\ c_+=c_-=c_0;\ \psi=V_E \tag{8.8}$$

The fluid velocity adheres to a Navier slip condition at the interiors nanochannel array. The concentration of Na^+, and Cl^-; at the membrane surface is $c_+=c_m$; and the flux of Cl^- is zero ($J_-\cdot\mathbf{n}=0$); The surface charge density is represented by, $\psi_{nanowall}=-\sigma_{surf}$ [91,374],

$$\mathbf{U}=a\frac{\partial \boldsymbol{U}}{\partial \boldsymbol{n}};\ c_+=c_m;\ J_-\cdot\mathbf{n}=0;\ \psi_{nanowall}=-\sigma_{surf} \tag{8.9}$$

At outlet boundary, (i) a zero-gauge pressure, (ii) convective outflow condition is imposed as $\mathbf{n}\cdot\nabla c=0$ (iii) electrostatic potential is grounded. Here, **n** is the outward normal vector, which is defined as the unit vector perpendicular to the boundary and directed outward from the fluid domain.

$$p=0;\ \mathbf{n}\cdot\nabla c=0;\ \psi=0 \tag{8.10}$$

The electroosmotic slip-on non-electrode walls is governed by the Helmholtz-Smoluchowski formulation (See Eq. 8.7).

8.2.5. Numerical method

The coupled system defined by Eqs. (8.1) -(8.6) and boundary conditions (8.7) -(8.10) is numerically resolved using COMSOL Multiphysics v6.2. Leveraging the system's symmetrical geometry (Figs.8.1a, and 8.1b), the computational domain is simplified by modelling a reduced domain representing one-half of the full configuration. A symmetry boundary condition is imposed along the computational boundary corresponding to the physical centreline of the system. To simulate laminar flow, electrostatic potential, and ionic species transport, built-in modules for laminar flow, electrostatic fields, and dilute species transport are implemented.

The coupled governing Eqs. (8.1-8.10) are iteratively solved with the MUMPS direct solver combined with Newton-Raphson iterations, ensuring robust convergence and numerical accuracy for the interdependent physics. This methodology balanced computational efficiency with precise resolution of the Multiphysics interactions.

3. Parameter estimation

In this study, electroosmotic slip at the channel walls is characterized by the zeta potential. Both the zeta potential and the surface charge density can be effectively regulated through coupled saltwater desalination processes. For the numerical simulations conducted in this work, the representative physical parameters corresponding to ion-selective polarization within the nanochannel array are summarized in Table 10, unless explicitly specified in the respective figures. The zeta potential is assigned a range of $0 \leq \xi \leq -0.2$ [V] [91].

Table 10
Key parameters for the present simulation model [23,342,353]

Parameters	Value	Unit
Boltzmann constant (k_B)	1.380649×10^{-23}	$m^2kg\ s^{-2}\ K^{-1}$
density of water (ρ)	1000	kgm^{-3}
dynamic viscosity (μ)	10^{-3}	Pa-s
Faraday constant (F)	96485	$Cmol^{-1}$
vacuum permittivity constant (ε_0)	8.854×10^{-12}	Fm^{-1}
relative permittivity constant (ε_r)	78	-
surface charge density (σ_{surf})	-4.5	mCm^{-2}
diffusivity of cation (D^+)	1.33×10^{-9}	m^2s^{-1}
diffusivity of anion (D^-)	2.03×10^{-9}	m^2s^{-1}
bulk concentration of c_0	10	$molm^{-3}$
gauge pressure (p_0)	10	Pa

8.3. Results and discussion

The behavior of the proposed desalination system employing an ion-selective membrane is analysed using a baseline configuration with representative parameter values. The electrolyte solution used in the present channel model is sodium chloride (NaCl). Based on this reference case, the underlying mechanisms are identified, followed by an assessment of how the applied voltage (V_E) and the zeta potential (ξ) influence the system's performance. This study compares two computational models that have the same vertical height of L = 93.444 nm. One model uses a rectangular nanochannel with a horizontal length of h_r = 40 nm, and the other uses a hyperbolic nanochannel with h_h = 80 nm. Both models include a set of 10 nanoscale conduits; each designed with structural dimensions of hs = ha = 2 nm. These dimensions induce convergence of electrostatic charge layers (EDLs) within the conduits. The analysis explores ionic flux across conductive and saturation phases by applying external potentials from 0 to $50V_0$ thermal voltage units ($V_0 = k_BT_a/(z_ve)$=25.85mV), achieving

steady-state conditions. Before beginning the present analysis, a grid independence test was carried out to identify a suitable mesh resolution. The computational model uses triangular elements, with finer meshes applied near important regions such as the membrane interface, channel walls, inlet, and outlet. Very fine elements are placed close to the membrane surfaces to capture sharp changes in field variables. The results of the average velocity grid independence test, shown in Table 11, confirm that the mesh with 69786 elements provides accurate and reliable results.

Table 11
The average velocity in the axial direction at the middle section of the hyperbolic channel using various mesh elements.

No. of Mesh elements	Average velocity along the axial position (u_{av})
24023	0.061697
60724	0.062056
69786	0.062112
158462	0.062334

The removal rate refers to the percentage of salt ions that are effectively prevented from passing through the array. The applied voltage across the channel significantly influences this salt removal ratio (SRR) is defined as [353],

$$SRR = 1 - \frac{c_{out}}{c_0} \tag{8.11}$$

where, C_{out} is the outlet concentration of Cl^- for rectangular and hyperbolic channels are defined as [23],

$$c_{out} = \begin{cases} \int_0^{h_r} J_{x^-}(L,y)\,dy \Big/ \int_0^{h_r} u(L,y)\,dy & \text{Rectangular channel} \\ \int_0^{h_h} J_{x^-}(L,y)\,dy \Big/ \int_0^{h_h} u(L,y)\,dy & \text{Hyperbolic channel} \end{cases} \tag{8.12}$$

Here, J_{x^-} is the x component of Cl^- flux **J**.. Here average velocity for rectangular and hyperbolic channels at outlet are defined as,

$$u_{av} = \begin{cases} \int_0^{h_r} \mathrm{u(L,y)dy} \Big/ h_r & \text{Rectangular channel} \\ \int_0^{h_h} \mathrm{u(L,y)dy} \Big/ h_h & \text{Hyperbolic channel} \end{cases} \tag{8.13}$$

(i) Concentration profile

Figure 8.2 presents the steady-state axial Na^+ concentration profiles at the midplane for rectangular and hyperbolic nanochannel arrays under different surface-potential strengths and applied voltages. In the rectangular configuration at V=30V (Fig. 8.2a), the Na^+ concentration exhibits a spatially dependent, non-monotonic response as the surface potential becomes more negative from ζ=-0.01 to -0.2. Near the inlet region on the left side, increasing |ζ| strengthens the electric double layer and enhances cation perm-selectivity, deepening the upstream depletion zone and causing the Na^+ concentration to progressively decrease. Within the nanochannel array in the central region, perm-selectivity and surface conduction reach a saturation state, resulting in minimal changes in the concentration profiles for moderate |ζ|. However, toward the downstream end on the right side, higher surface potentials (|ζ|≥0.05) promote strong EDL counterion accumulation and enhanced surface conduction, which drive additional Na^+ ions toward the outlet; consequently, the concentration increases again, producing a clear decrease-plateau-increase pattern along the channel. In Fig. 8.2(b), where the surface potential is fixed at ζ=-0.05, raising the applied voltage increases the electromigration strength, expands the depletion region, and yields consistently lower Na^+ concentrations, reflecting enhanced ion-removal capability. Comparatively, the hyperbolic nanochannel in Fig. 8.2(c) shows smoother concentration gradients and weaker depletion as |ζ| increases, because the curved geometry redistributes the electric field and mitigates polarization inside the channel. As a result, the outlet concentration remains higher than in the rectangular geometry for the same surface-charge conditions. Finally, Fig. 8.2(d) demonstrates that although increasing voltage in the hyperbolic channel still reduces Na^+ concentration, the extent of depletion remains relatively mild due to geometric field spreading, which stabilizes ion transport and prevents the formation of strong depletion fronts. Overall, the results highlight how surface potential, applied voltage, and channel geometry interact to control the strength and spatial structure of ion-depletion zones in nanochannel arrays.

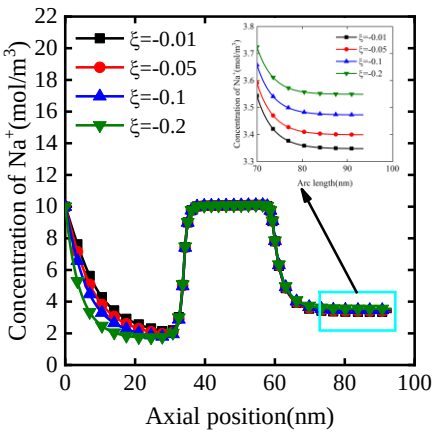

(a) Rectangular channel at $V_E=30V_0$

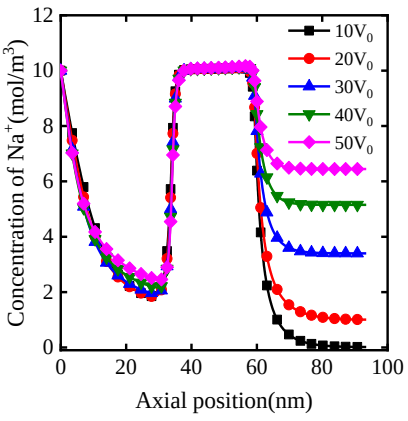

(b) Rectangular channel at ξ=-0.05

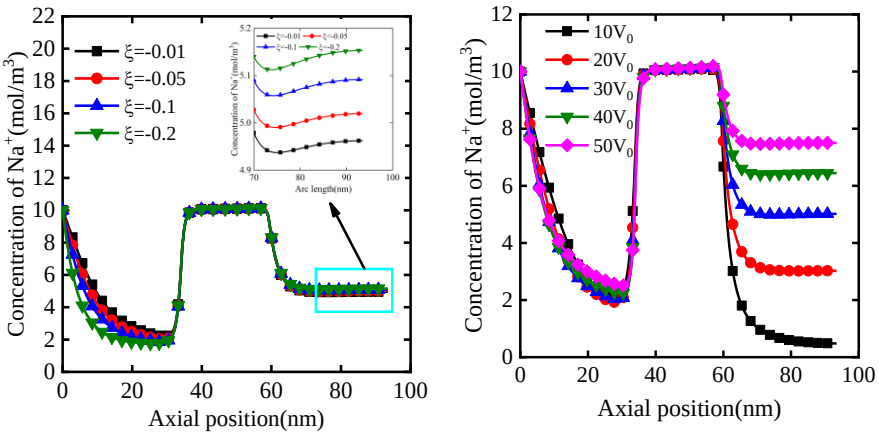

(c) Hyperbolic channel at $V_E=30V_0$ (d) Hyperbolic channel at $\xi=-0.05$

Fig. 8.2 Ionic species distributions along the axial x direction at the midplane for two configurations under surface charge constraints $\psi_{nanowall} = -\sigma_{surf}$ for Cationic (Na^+) concentration profile (a, b) Rectangular (c, d) Hyperbolic nanochannels.

Figure 8.3 presents the axial chloride-ion concentration profiles for rectangular and hyperbolic nanochannel arrays and highlights the strong influence of channel geometry and voltage on anion transport. In Fig. 8.3(a) and Fig. 8.3(c), the effect of ζ potential on the vertical Cl^- concentration profile shows a clear contrast between the region above the nanochannel array and the region inside/after the array, due to the presence of strong negative surface charge density within the nanochannels. For ζ ranging from -0.01 to -0.2, the top portion of the channel (before entering the array) exhibits relatively higher Cl^- concentration, because the local electric field is weak and the negatively charged walls have not yet imposed strong electrostatic exclusion; as |ζ| increases, anions accumulate slightly near the upper region due to field-driven vertical migration. However, once the flow enters the nanochannel array where negative surface charge is explicitly applied, the physics reverses. Inside the array, strong surface charge produces intense anion repulsion, suppressing Cl^- transport and forcing the concentration to drop to its minimum, regardless of ζ magnitude. After exiting the array (lower portion), the trend becomes opposite of the top region: higher |ζ| now leads to lower Cl^- concentration because the ions have just passed through a strongly repulsive constriction that amplifies depletion. Thus, the concentration is high at the top for all ζ values but becomes progressively lower after the array as |ζ| increases, reflecting the dominating influence of the array's negative surface charge and the transition from weak pre-array transport to strong intra-array exclusion. In Fig. 8.3(b) and Fig. 8.3(d), where voltage varies from $10V_0$-$50V_0$, the concentration before the nanochannel (top side) decreases with increasing voltage because stronger drift pulls anions rapidly toward the entrance, thinning the upstream boundary layer. After the nanochannel (bottom side), however, the trend reverses: higher voltages produce higher outlet concentrations, as strong

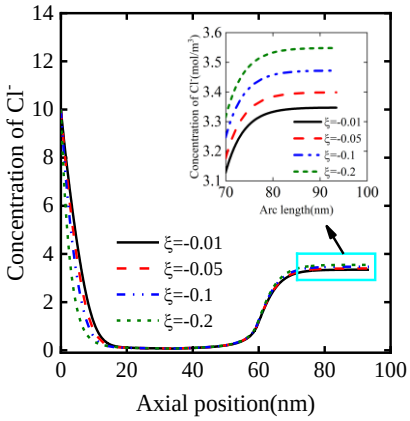

(a) Rectangular channel at $V_E=30V_0$

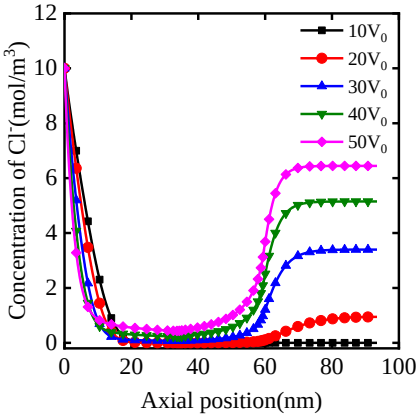

(b) Rectangular channel at ξ=-0.05

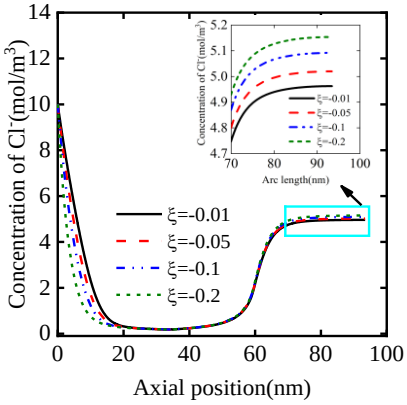

(c) Hyperbolic channel at $V_E=30V_0$

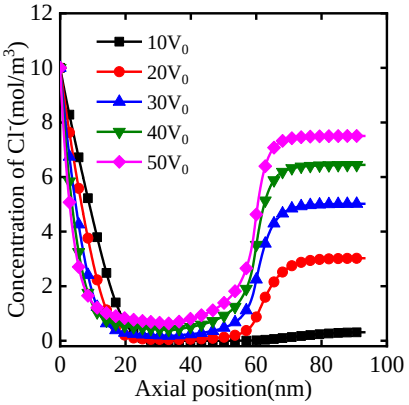

(d) Hyperbolic channel at ξ=-0.05

Fig. 8.3 Ionic species distributions the axial x direction at the midplane of hyperbolic nanochannel for different zeta potential for two configurations under surface charge constraints $\psi_{nanowall} = -\sigma_{surf}$ for anionic (Cl^-) concentration profile (a, b) Rectangular, (c, d) Hyperbolic nanochannels.

downstream electromigration accelerates ion transport once the ions exit the constriction. Comparing the two geometries, the rectangular nanochannel consistently yields a much lower outlet Cl^- concentration than the hyperbolic one. This occurs because the sharp, uniform constriction in the rectangular channel produces stronger field focusing and higher ionic resistance, sustaining deeper anion depletion than the smooth, gradually varying hyperbolic shape. At $10V_0$, the rectangular outlet concentration is nearly zero, while the hyperbolic outlet remains finite due to reduced field localization and weaker confinement. At an applied voltage of 30 V_0, the rectangular channel achieves approximately a 47.63% reduction in outlet Cl^- concentration compared with the hyperbolic channel, indicating that its sharper

geometry enhances anion exclusion and improves the desalination efficiency of the rectangular design.

The variation of Na^+ concentration across the midplane of a single nanochannel array for rectangular and hyperbolic geometries is presented in Fig. 8.4. In both cases, the profiles display a characteristic U-shaped pattern, with Na^+ concentration reaching its maximum near the channel walls and decreasing toward the centre. This behaviour arises from the negatively charged nanochannel surfaces, which attract cations and create an EDL where Na^+ accumulates adjacent to the walls. As the distance from the wall increases, the electrostatic influence decays, causing the Na^+ concentration to fall toward a minimum at the channel centre. Despite this common trend, the rectangular channel shows a slightly higher centreline Na^+ concentration compared to the hyperbolic channel. This difference occurs because the uniform cross-section of the rectangular geometry produces a more evenly distributed electric field across the width, allowing a greater portion of Na^+ ions to diffuse or migrate toward the centre. In contrast, the hyperbolic geometry with its gradually varying width induces stronger field localization near the throat region, which confines more ions near the walls and results in a lower Na^+ concentration at the centre.

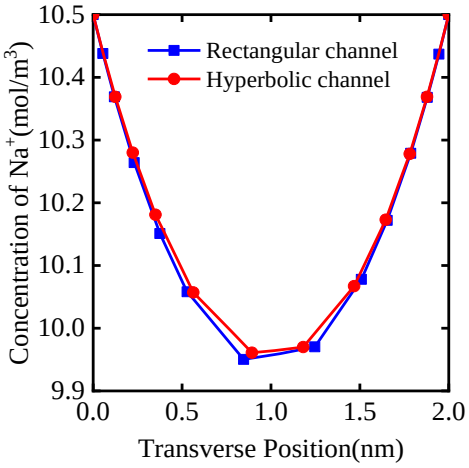

Fig. 8.4 Comparison of cationic concentration distribution at the midplane at the transverse direction for one nano-channel array with surface charge boundary condition $\psi_{nanowall} = -\sigma_{surf}$ at $\xi = -0.05$, $V_E = 30V_0$.

The observed dependencies of the average cross-sectional velocity on zeta potential and applied voltage in Fig. 8.5 are governed by the transition from electroosmosis to electroconvection, with channel geometry playing a critical role in modulating this instability. In the rectangular nanochannel (Fig. 8.5a), the non-monotonic velocity trend with voltage is a classic signature of this transition. At $10V_0$, the system operates in the ohmic or early limiting regime. The electric field is sufficient to generate a steady electroosmotic slip flow along the walls, but it is not strong enough to form a significant extended space charge layer (SCL) that would trigger electroconvection.

This results in a coherent, relatively high net flow. As the voltage increases to $20V_0$, the system enters a stable limiting current regime. A thick ion depletion zone and extended SCL develop, which dramatically increases local resistance. While this SCL sets the stage for instability, the voltage may be at a critical threshold where the electroosmotic flow is suppressed, but the electro-convective vortices are not yet energetic enough to contribute significantly to the net axial flow. This results in a pronounced dip in average velocity. At higher voltages ($40V_0$ and $50V_0$), the system enters the over-limiting current regime. The strong electric field acting on the SCL triggers vigorous electro-convective vortices. These vortices act as an internal pump, enhancing ion transport and, crucially, contributing to a net pumping effect that increases the average velocity once again. The order $10V_0 > 50V_0 > 40V_0 > 20V_0$ reflects this progression from stable electroosmosis, through a convective-onset minimum, to fully developed electroconvection.

In contrast, the hyperbolic nanochannel (Fig. 8.5b) exhibits a more monotonic and damped response due to its geometry. The smoothly varying cross-section prevents the sharp localization of the electric field and space charge that occurs at the entrance of a rectangular channel. This "smears out" the ion depletion, suppressing the formation of an intense, localized SCL. Consequently, the transition to electroconvection is more gradual and less violent. The velocity does not exhibit a sharp minimum because the electroosmotic component is never fully suppressed, and the developing electro-convective instability is milder. Therefore, as the voltage increases from $20V_0$ to $50V_0$, the average velocity rises steadily. The stronger driving force consistently overcomes the dissipative losses, leading to the more intuitive ordering where higher voltage results in higher average flow, driven by a combination of sustained electroosmosis and stabilized electro-convective mixing.

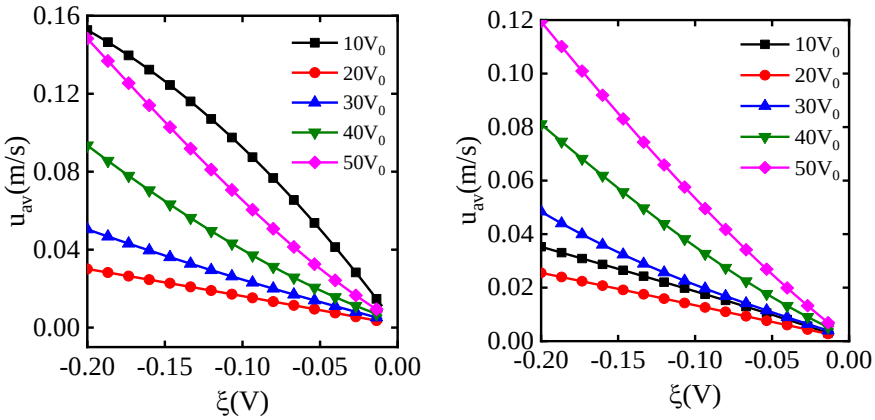

(a) Rectangular nanochannel (b) Hyperbolic nanochannel

Fig. 8.5 Dependencies of average velocity along the vertical length of the channel for different values of applied voltages of u as function of zeta potentials in (a) rectangular and (b) hyperbolic nanochannels.

(ii) Salt removal ratio profile

Figure 8.6 compares the evolution of the Salt removal ratio (SRR) along the arc length for rectangular and hyperbolic nanochannels at a fixed zeta potential (ξ = -0.05 V) under increasing applied voltage, revealing a fundamental trade-off between the intensity and stability of ion depletion governed by electro-convective phenomena. The axial SRR profile is characterized by distinct transport regions: in the initial portion (0-40 nm), the SRR exhibits a gradual rise as the applied electric field initiates concentration polarization, establishing an early ion depletion zone. This leads into the central region (40-60 nm), which encompasses the perm-selective interface of the nanochannel array, where overlapping electric double layers enforce strong ion selectivity and the SRR reaches its maximum. Beyond this peak, the SRR decreases sharply, not due to the electric field strength itself, but as a consequence of electro-convective instability, where the intense local field and extended space charge layer induce vortices that recirculate ions back into the depletion zone, thereby reducing local salt removal efficiency.

The behavior of the two geometries diverges significantly in response to increasing voltage. In the rectangular nanochannel (Fig. 8.6a), the uniform cross-section facilitates formation of a strong, coherent depletion layer at low to moderate voltages ($10V_0$ to $30V_0$), yielding high SRR values. However, at higher voltages ($40V_0$, $50V_0$), the system enters the over-limiting current regime where intense, localized electric fields trigger powerful electro-convective vortices. These vortices enhance ionic current but compromise depletion zone purity by recirculating ions from enriched regions, causing pronounced downstream SRR decay.

In contrast, for the rectangular channel, the SRR near the outlet region (≈93.4 nm) decreases by approximately 46.16% as the applied voltage increases from 30 V_0 to 50 V_0, although the variation remains relatively modest. Conversely, the hyperbolic nanochannel (Fig. 8.6b) exhibits more stable performance through its gradually expanding geometry, which disperses the electric field and prevents sharp space charge localization. While achieving slightly lower peak SRR, the hyperbolic geometry suppresses large-scale vortex formation, resulting in less severe downstream decay and maintaining more stable SRR profiles along the entire channel length at high voltages. The hyperbolic channel shows a noticeable drop in SRR at the outlet, decreasing by about 49.91% as the applied voltage rises from 30 V_0 to 50 V_0. This decline suggests that higher electric fields tend to weaken the stability of the depletion zone. This demonstrates the critical role of geometry in balancing peak ion removal efficiency with operational stability under strong electric fields.

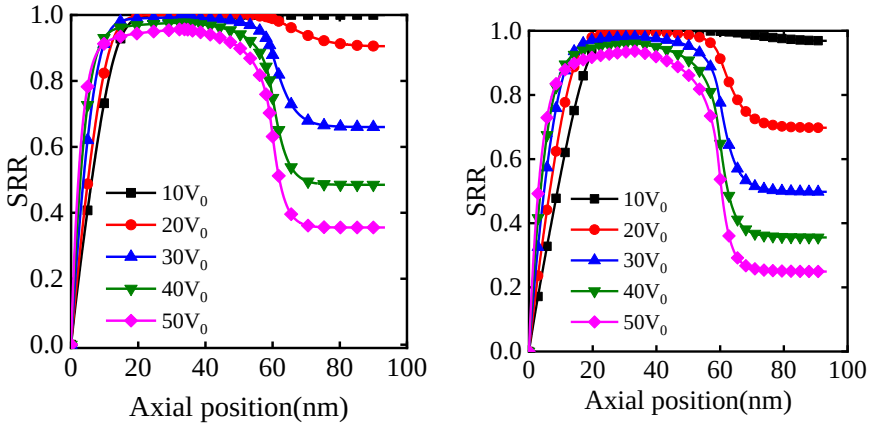

(a) Rectangular nanochannel (b) Hyperbolic nanochannel

Fig. 8.6 Comparison of salt removal ratio (SRR) across the channel with electroosmotic slip for different applied voltages along the arc length at ξ=-0.05(V) in (a) hyperbolic and (b) rectangular nanochannels.

(iii) Energy consumption rate distribution

Therefore, it is critical to analyse the energy distribution in our system to understand the key drivers of energy consumption in this novel desalination architecture, which is defined as follows:

$$\kappa = \iint_S F\left(\mathbf{J}_+ - \mathbf{J}_-\right)\cdot \mathbf{E} dxdy \tag{8.14}$$

$\kappa_y = \int_0^{ha} \kappa dy$ refers to the integrated energy consumption rate over a cross section in horizontal direction for single nanochannel array [23].

The variation of the energy consumption rate (κ_y) with surface potential (ξ) for rectangular and hyperbolic nanochannel for single arrays under different applied voltages is illustrated in Fig. 8.7. In both geometries, κ_y increases consistently with the applied voltage, reflecting the higher electrokinetic work required to sustain ion transport as the driving electric field strengthens. For all cases, κ_y decreases gradually with increasing ξ (from more negative toward neutral values), indicating that weaker wall potentials reduce the electroosmotic driving force and associated viscous dissipation. At low voltages ($10V_0$-$20V_0$), the energy consumption remains nearly constant, signifying ohmic conduction, where ionic migration is linearly proportional to the applied field and electro-convective effects are negligible. As the voltage increases ($30V_0$-$50V_0$), κ_y rises sharply, marking the transition to the over-limiting

regime, dominated by the formation of extended space-charge layers and electro-convective vortices, which enhance momentum exchange and Joule heating, as mentioned in Fig.8.7a. Comparing the two configurations, the hyperbolic nanochannel exhibits significantly higher κ_y values than the rectangular channel at identical conditions. This can be attributed to its curved geometry, which concentrates the local electric field near the constricted regions, intensifying charge transport and viscous energy loss. In contrast, Fig. 8.7(b) shows that the rectangular nanochannel maintains lower κ_y values, indicating a more uniform electric field distribution and reduced electro-convective energy dissipation. Quantitatively, at an applied voltage of 30 V_0 and a zeta potential of -0.05 V, the rectangular nanochannel exhibits approximately 95.43 % lower energy consumption than the hyperbolic configuration under identical operating conditions. This substantial reduction highlights the superior electrokinetic efficiency of the rectangular geometry, which maintains a more uniform electric field and lower viscous dissipation. Overall, Fig. 8.7 demonstrates that while the hyperbolic nanochannel enhances electrokinetic mixing and ion mobility through intensified local electric fields, it does so at the expense of increased energy consumption, whereas the rectangular configuration achieves more efficient ion transport with significantly reduced energetic losses under equivalent applied voltages.

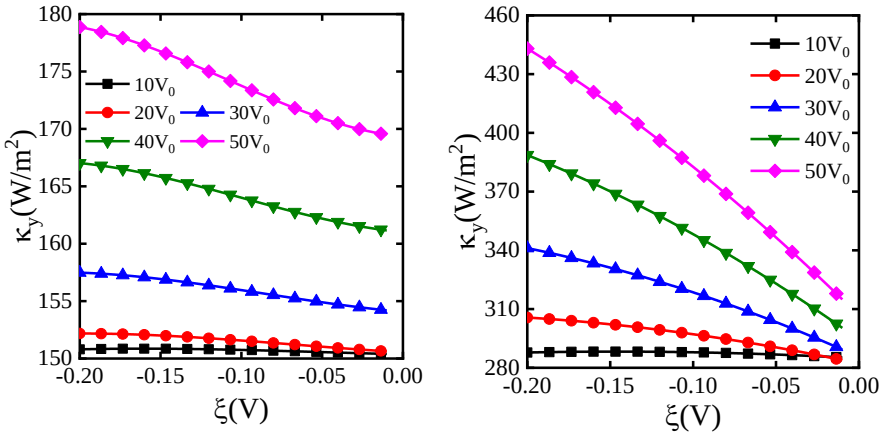

(a) Rectangular nanochannel (b) Hyperbolic nanochannel

Fig. 8.7 Distribution of energy consumption rate (κ_y) in the horizontal direction for a single nanochannel array as a function of applied voltages.

(iv) Levelized cost of water (LCOW) calculation

To conduct an economic assessment of various desalination system designs, the levelized cost of water (LCOW) serves as the primary metric for comparison. A key consideration is that energy consumption alone is an insufficient performance indicator, as it can be driven arbitrarily low by employing excessively slow flow rates.

This approach, however, leads to a prohibitive capital expense for the equipment per unit of water produced, which is economically impractical. Consequently, the total cost must include both operational and capital expenditures. Operational expenses were derived from electrical and hydraulic pumping energy requirements. The initial capital outlay, heavily influenced by the required membrane area in ICP systems, was estimated from the total system footprint. The following calculations determine these cost components, with the final LCOW presented as the sum of operational and capital costs in USD per cubic meter of processed feedwater [23,353].

Total Cost = Capital Cost + Operating Cost (Electricity + Pumping)

The specific cost of electricity is calculated as:

Electricity Cost = (Energy Price) × (Specific Energy Consumption)

For illustration, using an energy price of \$0.10 per kW-h, the electrical cost component for the rectangular nanochannel (with a specific energy consumption of 8.1797 kW-h/m^3) is approximately \$0.82 per cubic meter, while for the hyperbolic nanochannel (6.26 kW-h/m^3), it is approximately \$0.63 per cubic meter under standard parameters (n=10, V_E=30 V_o, p_0=10 Pa, ξ=-0.05).

In membrane-based desalination systems, the capital expenditure encompasses not only the cost of the membranes themselves but also the expenses associated with infrastructure development, equipment acquisition, system maintenance, pretreatment materials, labour, and other auxiliary requirements. Since accurately accounting for all these additional factors is complex and highly dependent on the specific plant design and location, it is customary to approximate the total investment primarily from the membrane cost. It is further assumed that the initial investment for system installation is financed through borrowing at a market interest rate (r) of 10% and is then distributed over the 20-year service lifetime (T_L) of the ICP unit to obtain the annualized capital cost.

A fundamental aspect of the economic analysis involves determining the capital expenditure, which is evaluated using an amortization framework to distribute the initial investment over the project's operational lifetime. The general form of this calculation is represented as [23,353]:

$$\text{Capital cost}=\left(\frac{A_m K_Q}{Q T_L}\right)\left[\frac{(1+r)^{T_L}-1}{r T_L}\right] \tag{8.14}$$

Here, K_Q refers to the projected cost per unit area, A_m is the total membrane area, Q is the flow rate of desalinated water.

Given the two-dimensional nature of the model, the channel depth *w* becomes essential for accurate costing. Using the expressions for membrane area $A=2h_h w$, $2h_r w$ and desalinated water feed flow rate $Q=2h_r w u_{av}$, $2h_h w u_{av}$. Eq. (8.14) reduces to a more compact form:

$$\text{Capital cost} = \left(\frac{K_Q}{u_{av}T_L}\right)\left[\frac{(1+r)^{T_L}-1}{rT_L}\right] \tag{8.15}$$

Using representative values with an average velocity of u_{av}=0.01316 m/s under the conditions n=10, ξ=-0.05, V_E=30V_0, and p_0=10 Pa, the capital cost was estimated at approximately 0.0002588 \$/m³ [23]. This value is remarkably low when compared to other conventional membrane stack ICP systems. This value is remarkably low compared to other electro-membrane processes like electrodialysis (ED), highlighting a key advantage of this design: its drastically reduced requirement for ion-exchange membrane material per unit of treated water, which is typically a major cost component in such systems.
However, given the architectural differences between this microporous system and conventional ED, a more conservative and detailed costing approach is warranted. Therefore, we separate the total capital cost into two distinct components:

Total Capital Cost = Membrane Cost + Auxiliary System Cost

The membrane-specific cost is formulated as [23]:

$$\text{Membrane cost} = \left(\frac{K_m}{u_{av}T_L}\right)\left(\frac{(1+r)^{T_L}-1}{rT_L}\right) \tag{8.16}$$

Substituting K_m=150 \$/m^2 along with standard assumptions for lifetime and interest rate yields a negligible membrane cost of about 0.000052\$/m^3.
The second component, termed the Auxiliary system cost, includes infrastructure, equipment, maintenance, labour, and pretreatment chemicals. Since these elements are challenging to derive from theoretical models but are expected to align with conventional electro-membrane installations, a separate area-based cost factor $K_{Auxiliary}$ is introduced. Thus, the auxiliary cost is expressed as [23]:

$$\text{Auxiliary cost} = \left(\frac{K_{Auxiliary}}{u_{av}T_L}\right)\left(\frac{(1+r)^{T_L}-1}{rT_L}\right) \tag{8.17}$$

For this analysis, $K_{Auxiliary}$ is set to 100000 \$/m^2, reflecting a scaled and conservative estimate that accounts for the system's reduced physical scale and unique operational features The auxiliary contribution from auxiliary components (equipment, maintenance, labour) amounts to 0.0345 \$/m^3.

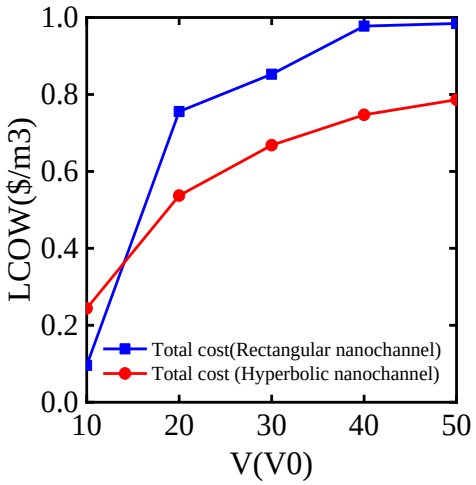

Fig. 8.8 Variation of LCOW with applied voltage for different geometries, with total cost calculated as the sum of electrical and capital expenses (USD per m³ of diluate).

The variation in the levelized cost of water (LCOW) with applied voltage for the rectangular and hyperbolic nanochannel geometries is shown in Fig. 8.8. The total cost is calculated as the sum of electrical energy consumption and capital expenses, expressed in USD per m³ of diluate. The hyperbolic channel demonstrates a consistently lower LCOW across the voltage range. At 10 V_0, the hyperbolic geometry begins at approximately \$0.10/m³, compared to the rectangular channel, which starts at a higher \$0.25/m³. This cost advantage for the hyperbolic channel persists as voltage increases. At 20 V_0, the hyperbolic channel's LCOW rises moderately to about \$0.50/m³, while the rectangular channel experiences a steeper increase to roughly \$0.75/m³.

This trend continues at higher voltages. At 30 V_0, the hyperbolic channel reaches about \$0.668/m³, whereas the rectangular channel climbs to approximately \$0.852/m³. Finally, at the highest applied voltage of 50 V_0, the hyperbolic channel's cost stabilizes around \$0.7864/m³, significantly lower than the rectangular channel, which reaches approximately \$0.9844/m³.

Overall, the estimated energy consumption for the rectangular and hyperbolic configurations is approximately 9.69 kWh/m³ and 7.65 kWh/m³, respectively. The corresponding total treatment costs are \$0.7864/m³ and \$0.9844/m³, demonstrating a competitive performance that justifies continued research and development. Under an applied voltage of 50 V_0, the rectangular nanochannel yields an LCOW that is 20.11% greater than that of the hyperbolic design. However, the LCOW increases with applied voltage for both geometries because of the rising electrical power demand. The hyperbolic nanochannel maintains a lower and more stable LCOW across all voltages, indicating better economic performance. In contrast, although the rectangular nanochannel exhibits a higher SRR than the hyperbolic design, its LCOW remains higher due to greater energy consumption. This

contrast highlights that the rectangular geometry yields higher salt removal but at a higher energy cost, whereas the hyperbolic geometry offers a more cost-efficient operation.

8.4. Conclusion

This study offers valuable insights into the complex behavior of saltwater desalination and its influence on the performance of portable microfluidic devices for power generation and salt removal. It examines how electroosmotic velocity slip, zeta potential, and applied voltage interact within a nanochannel system. The nonlinear Poisson equation, combined with the Nernst-Planck equations, is integrated into the Navier-Stokes equations along with Navier slip conditions and overlapping electric double layer effects. The study evaluates key design parameters to analyze the flow field, concentration distribution, salt removal ratio (SRR), and energy consumption rate.

(i) Ion transport characteristics: Within the nanochannel array in the central region, perm-selectivity and surface conduction reach a saturation state, resulting in minimal changes in the concentration profiles for moderate $|\zeta|$. However, toward the downstream end on the right side, higher surface potentials ($|\zeta| \geq 0.05$) promote strong EDL counterion accumulation and enhanced surface conduction, which drive additional Na^+ ions toward the outlet; consequently, the concentration increases again, producing a clear decrease-plateau-increase pattern along the channel.

(ii) Anion suppression efficiency: Applying 30 V_0, the rectangular channel lowers the Cl^- concentration at the outlet by nearly 48% relative to the hyperbolic channel, demonstrating that the sharper geometry effectively restricts anion passage and boosts desalination performance.

(ii) Geometric influence on electric field distribution: This behavior arises from the varying width of the hyperbolic channel, which smooths the axial electric field and reduces lateral electrostatic confinement on anions. As a result, Cl^- ions accumulate more along the centerline in a single hyperbolic channel array, whereas the rectangular channel, with its uniform width and stronger wall effects, more effectively suppresses centerline Cl^- concentration.

(iii) Salt removal performance: Near the outlet region (approximately 93.4 nm), the rectangular nanochannel attains a 24.55% higher salt removal ratio than the hyperbolic configuration under an applied voltage of 30 V_0 and a zeta potential of -0.05 V, reflecting a modest yet distinct enhancement in depletion-layer stability.

(iv) Energy consumption and cost analysis: The analysis reveals that the hyperbolic and rectangular nanochannel configurations consume approximately 7.65 kWh/m³ and 9.69 kWh/m³ of energy, respectively. Their associated treatment costs are estimated at \$0.9844/m³ and \$0.7864/m³, indicating that both designs offer cost-effective operation within practical desalination limits. At an applied voltage of 50 V_0, the levelized cost of water (LCOW) for the rectangular nanochannel is about 20.11% higher than that of the hyperbolic counterpart, underscoring the trade-off between enhanced ion removal and higher energy dema

Chapter 9. Integrated multi-objective optimization, MCDM, and ML analysis of couple-Stress Casson, Maxwell, and Oldroyd-B Fluids

9.1. Multi-objective optimization

Optimizing microchannel heat transfer requires evaluating thermal performance and irreversibility across diverse designs and operating conditions. Traditional single-objective optimization struggles due to conflicting metrics. As flow dynamics become more complex and operating conditions vary, optimization becomes time-consuming [375]. Multi-objective techniques offer Pareto optimal sets, representing ideal trade-offs, with the Pareto front guiding the selection of the best microchannel configuration [376].

The NSGA-II optimization process typically unfolds in four key steps [145]:
Step 1: The population is initialized within the defined problem bounds and constraints.
Step 2: Three core operations: selection, crossover, and mutation, are performed with specified probabilities. The offspring generated are then sorted according to non-dominated sorting criteria.
Step 3: For each non-dominated front, the crowding distance of each individual is calculated. A new parent population is formed by selecting individuals based on their crowding distance and non-dominated rank.
Step 4: This process continues iteratively, generating new parent populations until the algorithm satisfies the predefined stopping criteria.

The natural hunting behavior of grey wolves inspires the grey wolf optimizer (GWO) [377]. The hunting process comprises three distinct stages: the initial searching phase, the encircling phase, and the attack to capture the prey. The hierarchical dominance of wolves within the troop is depicted from top to bottom. In the hierarchy, the alpha wolves serve as leaders and primary decision-makers throughout the hunting process. However, as the hierarchy descends within the troop, wolves' decision-making authority and dominance diminish, with beta, gamma, and omega wolves assuming progressively subordinate roles. The determined absolute distance is a gap between the current best solution (represented by the wolf's current position) and the final position (either the prey's location or the optimal solution). The NSGWO algorithm is created by enhancing the grey wolf optimizer with a crowding distance criterion, an archive, and a method for selecting wolves' positions (based on their ranking) that aligns with the Pareto optimal dominance nature [144]. The optimization of the problem is to be compared by employing a multi-objective optimization using NSGA-II [378].

NSGWO archive size and the number of generations chosen are 200 and 100, respectively. For rigorous comparison, NSGWOA-generated predictions of electroviscous heat transfer and entropy production are cross-verified with NSGA-II

simulations, employing a population of 200 agents over 100 generational cycles. In this investigation, the selection of 200 generations stems from the observation that no substantial difference (with no variation up to two decimal points) is noticed with an increase in generations beyond 100. Opting for excessively high generations might not be computationally efficient, leading to increased computational costs.

(i) Chapter 5 introduces a multi-objective optimization framework for analyzing couple-stress Casson fluid flow using the Non-Dominated Sorting Genetic Algorithm II (NSGA-II). The study focuses on maximizing electrokinetic energy conversion (EKEC) efficiency and minimizing entropy generation (system irreversibility) through systematic variation of three key decision variables: the couple stress parameter, Casson parameter, and ionic Peclet number. This approach enabled the systematic identification of Pareto-optimal operating points, balancing thermofluidic performance and energy efficiency under electrokinetic conditions.

Maximize $\eta_c=f_1(\alpha, \beta, \gamma)$

Minimize $S_{total}= f_2(\alpha, \beta, \gamma)$

Subjected to: $0\leq\alpha\leq10$, $1\leq\beta\leq6$, and $1\leq\gamma\leq6$

(ii) Chapter 6 extends the optimization framework to investigate electroviscous heat transfer and entropy generation in transient Maxwell fluid flow within a microchannel under the influence of streaming potential. The study combines multi-criteria decision-making (MCDM) with machine learning (ML) to rigorously evaluate Pareto-optimal solutions. Two algorithms: Non-Dominated Sorting Gray Wolf Optimization Algorithm (NSGWOA) and Non-Dominated Sorting Genetic Algorithm II (NSGA-II) are employed, with five critical parameters (relaxation time, Hall current, ion slip, nanofluid volume fraction, and Hartmann number) varied to optimize thermofluidic-electromagnetic performance. Results from NSGWOA and NSGA-II are statistically compared to evaluate their effectiveness in balancing competing objectives, demonstrating NSGWOA's superiority in resolving complex trade-offs.

Maximize $\eta_h=f_1(\bar{\lambda}_1, \alpha_e, \alpha_s, \phi, Ha)$

Minimize $S_{total}=f_2(\bar{\lambda}_1, \alpha_e, \alpha_s, \phi, Ha)$

Subjected to: $0\leq\bar{\lambda}_1\leq1$, $0\leq\alpha_e\leq1$, $0\leq\alpha_s\leq3$, $0\leq\phi\leq0.05$, and $0\leq Ha\leq5$

(iii) Chapter 7 expands the optimization framework to address electroviscous Nusselt number enhancement and entropy generation minimization in time-periodic Oldroyd-B fluid flow within a microchannel subject to streaming potential conditions. Four decision variables: Hartmann number, electrokinetic width, zeta potential, and Dukhin number are identified as pivotal drivers of the Pareto-optimal front. The study incorporates TOPSIS to prioritize Pareto-optimal solutions and

employs the NSGWOA alongside NSGA-II for comparative analysis. The Pareto-optimal datasets for electroviscous Nusselt number and total entropy generation serve dual roles as inputs and outputs for two ML models: ANN, and ANFIS, enabling predictive modeling and multi-objective optimization.

Maximize Nu=f_1(Ha, K, $\bar{\xi}$, Du)

Minimize S_{total}=f_2(Ha, K, $\bar{\xi}$, Du)

Subjected to: $0 \le Ha \le 2$, $5 \le K \le 40$, $0 \le \bar{\xi} \le 10$, and $0 \le Du \le 10$

9.2. Multi-criteria decision making (MCDM)

An MCDM approach determines the optimal solution based on technical, economic, and sustainability criteria. We specifically choose the TOPSIS method to select the best solution. The TOPSIS algorithm transforms multiple responses into a single performance response. For the Pareto-optimal solutions in this study, each solution is characterized by two attributes:
(i) The rate of electroviscous heat transfer (η_h) and global entropy production (S_{total}) for the Maxwell fluid are evaluated in ***Chapter 6***.
(ii) Investigation of electroviscous Nusselt number (Nu) and total entropy generation (S_{total}) for Oldroyd-B fluid are analysed in ***Chapter 7***.

Two equal weights are employed to assess the relative significance of the decision-making process. TOPSIS ranks candidates based on proximity to a favorable reference point (closest) and remoteness from an adverse reference point (farthest). It involves choosing a relatively optimal scheme from available alternatives, each with multiple attributes [379].
Step 1: Construct the matrix for assessment involving *m* alternatives and *n* samples. We recorded the value measured for the i^{th} indicator in the j^{th} sample as x_{ij}, forming the matrix as $(x_{ij})_{m\times n}$.

$$\left(x_{ij}\right)_{m\times n} = \begin{bmatrix} x_{11} & x_{12} & \cdot & \cdot & x_{1n} \\ x_{21} & x_{22} & \cdot & \cdot & x_{2n} \\ \cdot & \cdot & \cdot & \cdot & \cdot \\ \cdot & \cdot & \cdot & \cdot & \cdot \\ x_{m1} & x_{m1} & \cdot & \cdot & x_{mn} \end{bmatrix} \tag{9.1}$$

Normalized the matrix is as,

$$\left(r_{ij}\right)_{m\times n} = \frac{x_{ij}}{\sqrt{\sum_{i=1}^{m} x_{ij}^2}},\ i \in \{1,2,3,....,m\},\ j \in \{1,2,3,....,n\} \tag{9.2}$$

Step 2: The computation of the matrix with weighted and normalized decisions is as follows,

$$V_{ij} = \left(w_j r_{ij}\right)_{m\times n} \ , \ i \in \{1,2,3,....,m\} \tag{9.3}$$

Determine the weights w_j such that $\sum_{j=1}^{n} w_j = 1$. Obtain the weighted normalized matrix by multiplying each element of the r_{ij} column by its corresponding weight w_j.

Step 3: The ideal best $\left(A_j^+\right)$ and ideal worst $\left(A_j^-\right)$ are to be evaluated.

Step 4: Determine the ideal positive (best) and ideal negative (worst) solutions for each response, respectively as,

$$A^+ = \left\{\left\langle \max\left(V_{ij}\middle| i=1,2,3....,m\right)\middle| \ j \in J_+ \right\rangle, \left\langle \min\left(V_{ij}\middle| i=1,2,3....,m\right)\middle| \ j \in J_- \right\rangle\right\}$$
$$\equiv \left\{V_{wj}\middle| \ j=1,2,3,...n\right\} \tag{9.4}$$

$$A^- = \left\{\left\langle \min\left(V_{ij}\middle| i=1,2,3....,m\right)\middle| \ j \in J_+ \right\rangle, \left\langle \max\left(V_{ij}\middle| i=1,2,3....,m\right)\middle| \ j \in J_- \right\rangle\right\}$$
$$\equiv \left\{V_{bj}\middle| \ j=1,2,3,...n\right\} \tag{9.5}$$

Step 5: Calculate the difference between each response from the ideal best and ideal worst solutions for target alternative *i*, respectively as,

$$d_{ib} = \sqrt{\sum_{j=1}^{n}\left(V_{ij} - V_{bj}\right)^2} \ , \ d_{iw} = \sqrt{\sum_{j=1}^{n}\left(V_{ij} - V_{wj}\right)^2} \tag{9.6}$$

Step 6: Ultimately, the assessment of proximity to the ideal solution is determined by,

$$C_{iw}=d_{iw}/(d_{iw}+d_{ib}),\ 0\leq C_{iw}\leq 1 \tag{9.7}$$

The alternatives are then ranked in descending order based on the value of C_{iw}, and the combination that holds the top rank is identified.

9.3. Results and discussion

9.3.1. Optimization results EKEC efficiency and total entropy generation of couple stress Casson fluids

Finally, the NSGA-II algorithm is employed to generate the Pareto front for the flow of couple-stress Casson fluid within a microchannel as depicted in Fig. 9.3. In this multi optimization process, three key decision variables α, β, and γ have been carefully considered and analysed. In this analysis fixed values of K=10, $\bar{\xi}_1$=1, $\bar{\xi}_2$=0.5, Ω=10, Ha=0.1, $\bar{a}_1$=0.05, $\bar{a}_1'$=0.01,J_h=10, Br=0.01, $Br = 0.01$, $\bar{d}_1$=0.05, and $\bar{d}_1'$=0.01 are taken. The Pareto optimal front exhibits a convex shape, indicating that both objective functions are also convex in nature. This shape also implies that for each fixed value of one objective, there exists an optimal value for the other objective function.

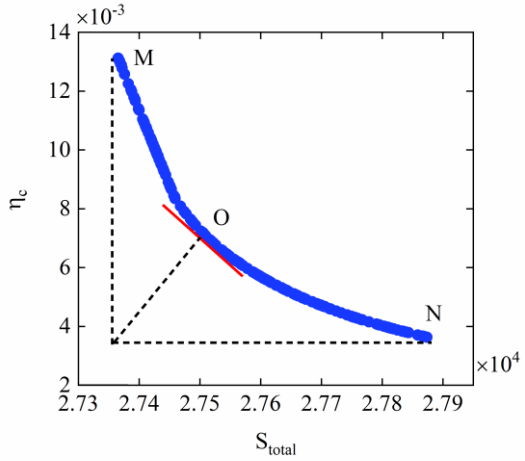

Fig. 9.1 Pareto front distribution for electrokinetic energy conversion efficiency and total entropy generation.

Point M is the best choice when overall electrokinetic energy conversion efficiency becomes a single objective function. On the other hand, point N should be carefully considered when the total entropy generation of the entire microchannel flow is taken into account as a single objective function. The ideal point is located at the intersection of the highest EKEC efficiency and the lowest total entropy generation lines, as shown in Fig 9.3. Consequently, the point O (closest to the ideal point) is the best solution. The multi-objective optimization reveals that at the optimal point, the total entropy reaches 2749×10^4 while the electrokinetic energy conversion efficiency achieves 0.568×10^{-3}.

9.3.2. Optimization results electroviscous heat transfer rate and total entropy generation of Maxwell fluids

Finally, the rate of electroviscous heat transfer and entropy production optimization for a Maxwell fluid within parallel plate microchannels is carried out using a two-stage process. The employed optimization algorithms include NSGWOA and NSGA-II, as illustrated in Fig. 9.4. In this optimization process, five pivotal decision variables, relaxation time, Hall current, ion slip, nanoparticle volume fraction, and Hartmann number have been carefully considered and analysed, while other parameters are kept constant. The comparison of results between NSGWOA and NSGA-II are then presented. Notably, the archived size in NSGWOA is configured to match the population size in NSGA-II. However, a subtle difference is observed due to the inherent stochastic nature of both techniques, relying on the random generation of numbers in each iteration.

The graphical representation of the final solution's Pareto front achieved through NSGWOA is illustrated in Fig. 9.5. This convex-shaped Pareto optimal front indicates the inherent convexity of both objective functions. This shape further implies that for every fixed value of one objective, an optimal value exists for the other objective function. Point M becomes optimal when the sole aim is the overall heat transfer efficiency. Conversely, Point N is strategically chosen when a primary objective is the global entropy generation of the entire microchannel flow. Consequently, a multi-criteria decision-making method is required to identify the most appropriate solution based on defined objectives. The final optimal outcome is selected using the TOPSIS technique [378]. Although Point I is designated as the theoretical optimum, it resides outside the Pareto frontier. Importantly, all solutions along the Pareto frontier are mutually non-inferior, meaning no single solution outperforms another across all objectives. For both NSGWOA and NSGA-II, TOPSIS prioritizes Point O as the preferred candidate due to its proximity to the theoretical ideal (Point I). The optimized decision variables obtained of the objective function electroviscous heat transfer rate and global entropy production are mentioned at Points M, N, and O. The details of the design variables and the optimum points are compared in Table 12, where both optimization techniques correctly predict the results. A comparative analysis between the base cases, i.e., η_h=0.43117 ,and S_{total}=0.64085 (K=20, ϕ=2%, $\bar{a}$=0.01, $\bar{\lambda}_1$=0.5, α_e=0.5, α_s=1.5, Da=0.1, Du=5, Br=0.01 ,J_h=10, $\bar{d}$=0.04, and τ=0.01) and the optimal point (O) reveals a notable enhancement in overall electroviscous heat transfer rate by 128% and a substantial reduction in overall irreversibility by 82.5%.

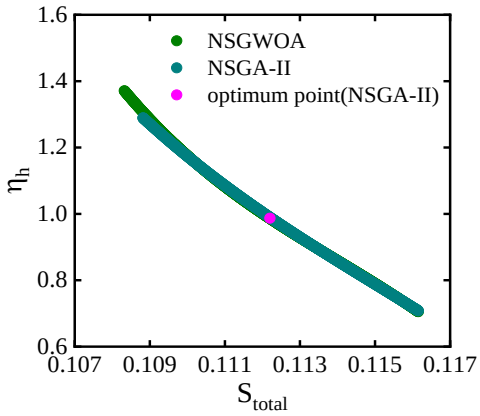

Fig. 9.2 Comparing the Pareto front outcomes of NSGWOA and NSGA-II.

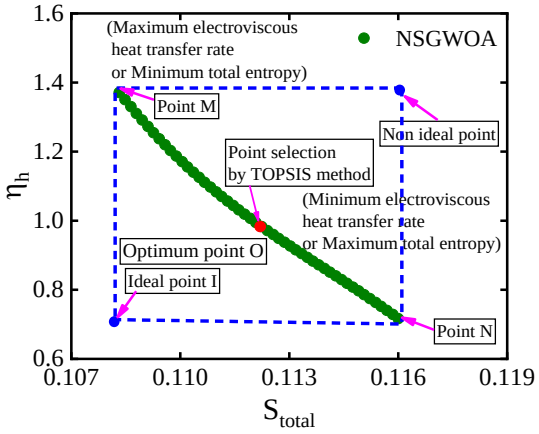

Fig. 9.3 Optimal solution points on the Pareto front distribution using NSGWOA for electroviscous heat transfer rate and total entropy generation.

Table 12
Optimal solutions on the global Pareto front characterized by design variables and objective functions at M, N, and O.

Parameters	NSGWOA (M)	NSGA-II (M)	NSGWOA (N)	NSGA-II (N)	NSGWOA (O)	NSGA-II (O)
$\bar{\lambda}_1$	0.1324	0.1929	0.1324	0.1324	0.3903	0.3346
α_e	1	0.9999	1	1	1	1
α_s	3	2.9999	3	3	3	3
ϕ	0	5.7×10^{-8}	0	0	0	6.25×10^{-9}
Ha	2.9269	1.7692	2.9269	2.9269	2.4189	1.6645
η_h	1.4121	1.2935	0.7138	0.7138	0.9831	0.9868
S_{total}	0.1083	0.1088	0.1161	0.1161	0.1122	0.1122

9.3.3. Optimization results electroviscous heat transfer rate and total entropy generation of Oldroyd-B fluids

Finally, a two-stage optimization process is employed to optimize electroviscous heat transfer and entropy generation for the periodic time of Oldroyd-B fluid flowing through parallel plate microchannels. This study leverages two advanced algorithms, NSGWOA and NSGA-II, as illustrated in Fig. 9.4. The optimization focuses on four critical decision variables: Hartmann number, electrokinetic width, zeta potential, and Dukhin number while keeping other parameters constant. A detailed comparison of the results obtained from NSGWOA and NSGA-II is presented. Notably, the archive size in NSGWOA is configured to match the population size in NSGA-II. However, minor variations are observed due to the inherent stochastic nature of both algorithms, which rely on random number generation during each iteration. Under the same settings, a 200-member population, and 100 generations, NSGWOA demonstrates stronger performance than NSGA-II. It yields a Pareto front that is not only better distributed but also shows improved convergence characteristics. The 90th generation typically observes convergence in NSGWOA, whereas NSGA-II continues progressing with only marginal improvements beyond this point. Moreover, the decision variables derived from NSGWOA are more stable and exhibit less variability across the Pareto set, reflecting consistent optimization behavior. These aspects collectively highlight NSGWOA's enhanced efficiency and robustness in solving the multi-objective electroviscous optimization problem.

Fig. 9.5 illustrates the Pareto front of the multi-objective optimization highlighting the trade-off between Nusselt number Nu and total entropy generation S_{total}. While higher Nu are desirable, they result in increased thermal irreversibility (S_{total}) which is unfavourable. Every solution located on the Pareto frontier corresponds to a uniquely optimized configuration defined by specific structural variables (Ha, K, $\bar{\xi}$, and Du) where no alternative solution outperforms it across all

objectives. From the optimization data point M maximizes *Nu* and point N minimizes S_{total}. Using the TOPSIS method [378] NSGWOA Point O is identified as the optimal choice being closest to the ideal point (depicted in Fig. 9.5). The structural parameters corresponding to the final optimal solutions and the selected optimal points identified using the TOPSIS method are summarized in Table 13. When compared to the base conditions, the structure identified by the TOPSIS method shows an 6.286 % increase in Nu, and a 6.872% reduction in S_{total}. System architects utilize the multi-objective optimality set to identify non-dominated solutions for integrated microanalysis systems, customizing functional outcomes in accordance with end-use specifications.

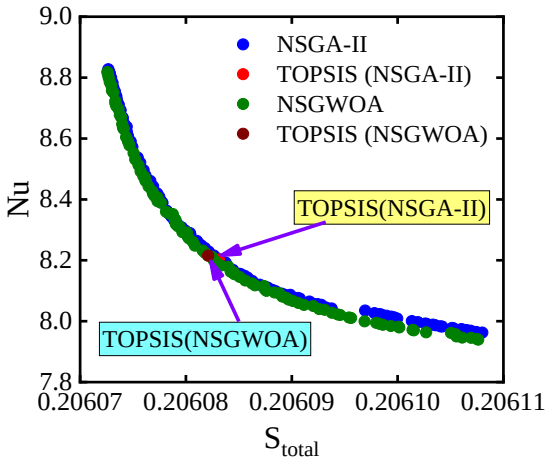

Fig. 9.4 Comparison of Pareto Fronts and Optimal Solutions Between NSGWOA and NSGA-II.

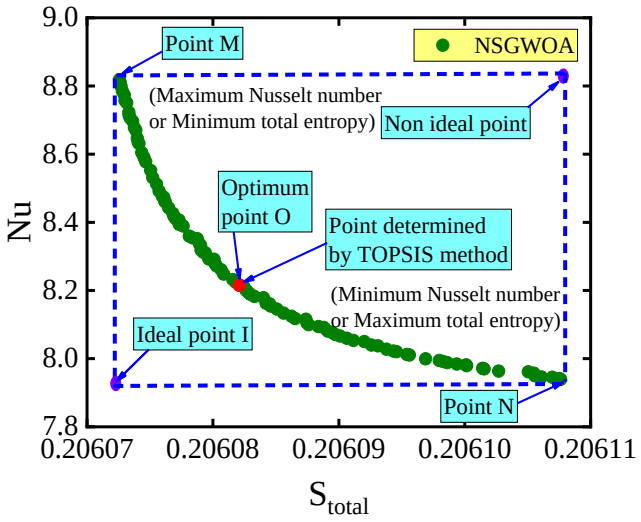

Fig. 9.5 Displays the Pareto front's optimal solution points for electroviscous heat transfer rate and total entropy generation derived using NSGWOA.

Table 13
Optimal solutions on the global Pareto front characterized by design variables and objective functions at M, N, and O.

Parameters	NSGWOA (M)	NSGA-II (M)	NSGWOA (N)	NSGA-II (N)	NSGWOA (O)	NSGA-II (O)
Ha	0.01301	0.01	2	2	1.0419	1.091
K	5.04286	5	5	21.426	5	5
$\bar{\xi}$	0.01849	0.73088	0.01	0.1165	0.0693	1.7806
Du	9.1479	5.99677	10	9.9151	7.7624	10
Nu	8.81832	8.82736	7.9392	7.9625	8.2154	8.2024
S_{total}	0.20607	0.20607	0.2061	0.2061	0.2060	0.2060

The distribution of optimal points for four decision variables: Ha, K, $\bar{\xi}$, and Du their influence on Nusselt number (Nu), and total entropy generation (S_{total}) are studied in Fig. 9.6. The interplay between Ha and K on Nu and S_{total} is depicted in Figs. 9.6a and 9.6b. The maximum Nu is achieved at approximately Ha≈0.01 and K≈5, resulting from the combined effects of optimal EDL thickness and surface charge potential. However, at lower Ha values, excessive thickening of the EDL, such as at K = 5 reduces the streaming potential. This reduction occurs because an overly thick EDL limits effective ion displacement near the channel walls, thereby diminishing its contribution to the streaming potential.
Similarly, the minimum entropy generation is observed under conditions where viscous losses are minimized and electric-fluid coupling is optimized, thereby reducing thermodynamic irreversibility. This leads to improved flow stability, suppressing chaotic mixing and localized turbulence, which further lowers entropy

generation. Moreover, intensified electrokinetic coupling ensures efficient energy transfer without excessive heat generation, thereby maintaining a well-balanced system with minimal thermodynamic losses.

Figs. 9.6c and 9.6d show the influence of zeta potential ($\bar{\xi}$) and Dukhin number (Du) on Nu and S_{total}. Optimal values of $\bar{\xi}$=0.01849 and Du≈9.1479 enhance surface conduction, thereby intensifying energy transport along the solid-liquid interface and promoting convective heat transfer, reaching a Nu of approximately 8.81832. Simultaneously, the minimum total entropy generation (S_{total}≈0.206072) observed under the same conditions reveals an ideal thermodynamic balance, where the improved heat transfer effectively offsets dissipative losses.

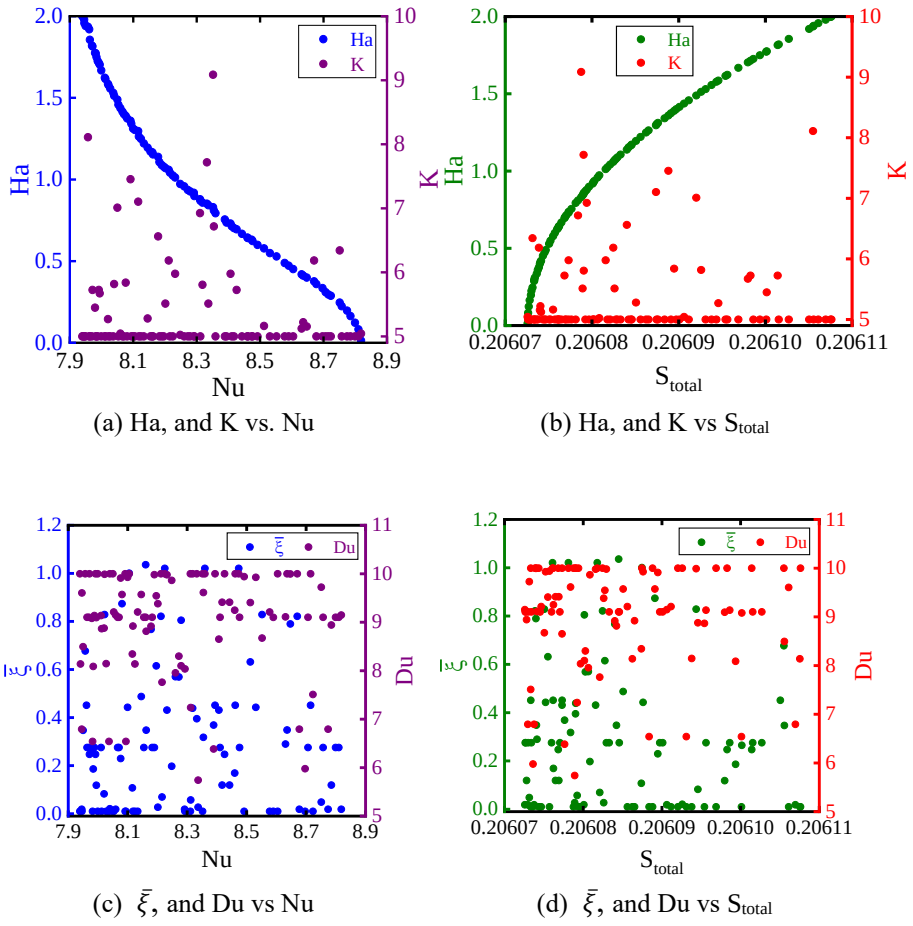

(a) Ha, and K vs. Nu

(b) Ha, and K vs S_{total}

(c) $\bar{\xi}$, and Du vs Nu

(d) $\bar{\xi}$, and Du vs S_{total}

Fig. 9.6 Optimal points for decision variables on the pareto front generated by NSGWOA for heat transfer and total entropy production (a) Ha, K, and (b) $\bar{\xi}$, Du.

9.4. Machine learning (ML) methods

Two ML methods (ANN and ANFIS) are applied to streaming potential flow for Maxwell fluid, which is analyzed in the present paper. The main focus is on two normalized objectives for heat transfer analysis: the electroviscous heat transfer rate and thermal irreversibility. Two design inputs are used, namely Hartmann number and nanofluid volume fraction. Accuracy benchmarks for neural and fuzzy-neural architectures are compared, with identical data splits: 70% allocated to training, 10% to validation, and 20% to testing phases.

9.4.1. Artificial neural network (ANN) method

Computational neural frameworks emulate biological neural networks through interconnected processing units organized hierarchically. These systems feature three functional stages: a primary layer for data intake, an intermediate layer for pattern abstraction, and a terminal layer for result synthesis. The number of neurons in an ANN's input and target layers is typically determined by the total number of features present in the input and target vectors, respectively [380]. The detailed construction and flowchart of the ANN are depicted in Fig. 9.1.

The output value of the ANN method is determined as follows [380]:

$$g_j = b_j + \sum_{i=1}^{m} w_{i,j} z_i \tag{9.8}$$

$$r_j = f\left(g_j\right) \tag{9.9}$$

Each neuron uses an activation function to process input value z_i with special weighted coefficients $w_{i,j}$ and produce an output value r_j. If a layer has m neurons, a specific neuron j in the next layer receives m input values. These inputs are weighted by their respective coefficients and combined with a bias term b_j. The activation function f then produces the output r_j from the neuron. Important statistical coefficients of the ANN method involve, i.e., mean absolute percentage error (MAPE), root mean squared error (RMSE), coefficients of determination (R^2) and (R), and the creation of a regression line is utilized to ensure the practicality of the fitted data-based model.

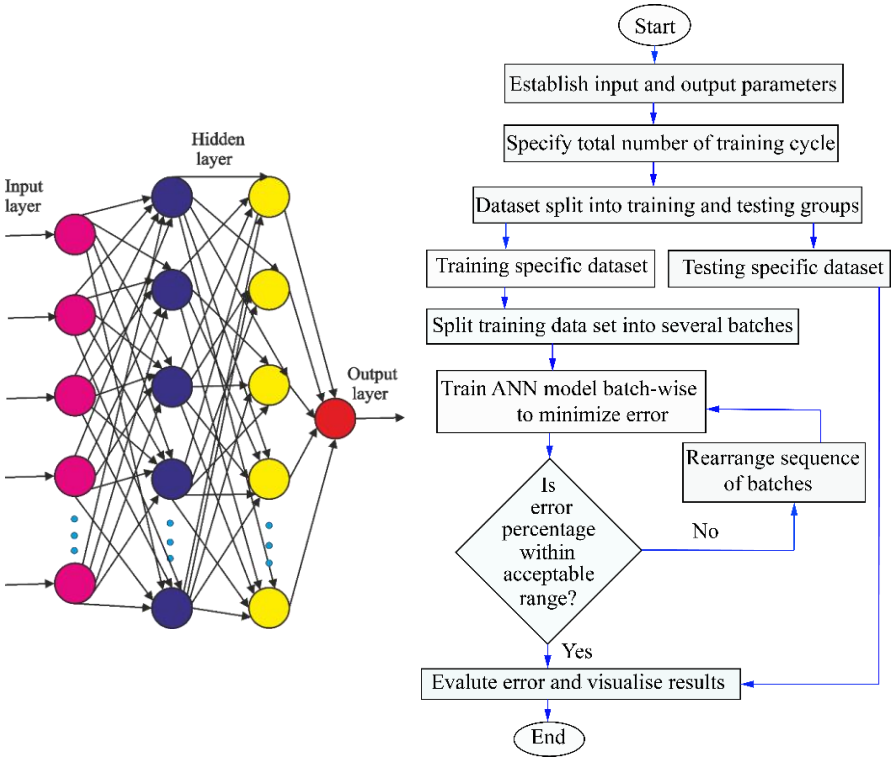

(a) (b)

Fig. 9.7 Schematic of ANN construction and flowchart: (a) Structural overview (b) Graphical summery of working principle.

9.4.2. Adaptive Network Based Fuzzy Inference System (ANFIS) method

The output of the ANN method is determined by processing input data through inter connected layers of neurons, where is neuron applied a weighted sum of inputs followed by an activation function to produce final output [365]. ANNs are very effective for modeling many real-world problems, but they also have some limitations. Hybrid neuro-fuzzy systems, capable of handling data with inherent uncertainties, frequently outperform conventional methods in scenarios requiring tolerance to imprecise inputs [367]. These systems are used in identification, control, and prediction [381]. The input-output relationship is intelligently processed through a learning procedure using ANN combined with a fuzzy system (ANFIS) to determine accurate solutions. ANFIS with its five operational processes, is a testament to its intelligent design. The first layer consists of input membership functions that perform the fuzzification process using the two inputs, g and z. The output from this layer represents the membership values of the inputs. Each node i is an adaptive node, with its functions, working principles, and associated equations detailed as follows:

In this case, there are four adaptive nodes: H_1, H_2, S_1, and S_2. Probabilistic rule-based relationships are defined below [382],

Rule 1: If z is H_1 and g is S_1, then

$$f_1=p_1g+q_1z+r_1 \tag{9.10}$$

Rule 2: If z is H_2 and g is S_2, then

$$f_2=p_2g+q_2z+r_2 \tag{9.11}$$

The consequent parameters are represented as p_i, q_i, and r_i, where i=1, 2. The first layer contains two inputs, labelled as g and z.

$$O_{1,i} = \mu_{A_i}(g),\ i=1,2 \tag{9.12}$$

$$O_{1,i} = \mu_{B_{i-2}}(z),\ i=3,4 \tag{9.13}$$

The second layer represents the rule layer, where the output reflects the fuzzy strength of each rule. Each node in this layer is a function of a multiplier, denoted by Π. The firing strength of each rule is determined by multiplying the input signals as given below.

$$O_{2,i} = w_i = \mu_{A_i}(g)\mu_{B_i}(z),\ i=1,2 \tag{9.14}$$

The normalized firing strength in the third layer is represented by the total weight function w_i. At this stage, the firing strength of the i^{th} rule is compared to the sum of all the rules in the model, denoted by M,

$$O_{3,i} = \bar{w}_i = \frac{w_i}{w_1+w_2},\ i=1,2 \tag{9.15}$$

The fourth-layer components are self-optimizing, with the parameter $\bar{w}_i f_i$ representing the output membership function. The outputs $f_i\ (i=1,2)$ are within the fuzzy region defined by the fuzzy rules, and it is expressed as,

$$f_i = \bar{w}_i(p_ig+q_iz+r_i) \tag{9.16}$$

For the final output of the ANFIS, all outputs from layer four are summed together. Layer five contains a single fixed node that performs a summation operation, as illustrated below,

$$O_{5,i} = \sum_i \bar{w}_i f_i \tag{9.17}$$

The R^2, RMSE, and MAPE are calculated for the ANN, and ANFIS methods as follows [367],

$$R^2 = 1 - \frac{\sum_{i=1}^{m} \left(z_i - \tilde{z}_i\right)^2}{\sum_{i=1}^{m} \left(z_i - \bar{z}_i\right)^2}; \quad 0 \le R^2 \le 1 \tag{9.18}$$

$$RMSE = \sqrt{\frac{1}{m} \sum_{i=1}^{m} \left(\tilde{z}_i - z_i\right)^2} \tag{9.19}$$

$$MAPE = \frac{1}{m} \sum_{i=1}^{m} \left| \frac{z_i - \tilde{z}_i}{z_i} \right| \times 100\% \tag{9.20}$$

Here, m, z_i , $\tilde{z}_i$, and $\bar{z}_i$ are the sample size, actual values, predicted values, and mean of the actual values, respectively. Well-trained ML models often have an R^2 above 0.9, indicating a strong match between the prediction and actual value. RMSE measures prediction error. A lower RMSE means predictions are closer to actual values. A good model has a low RMSE to improve accuracy. Fig. 9.2 shows calculation steps and flowchart for ANFIS.

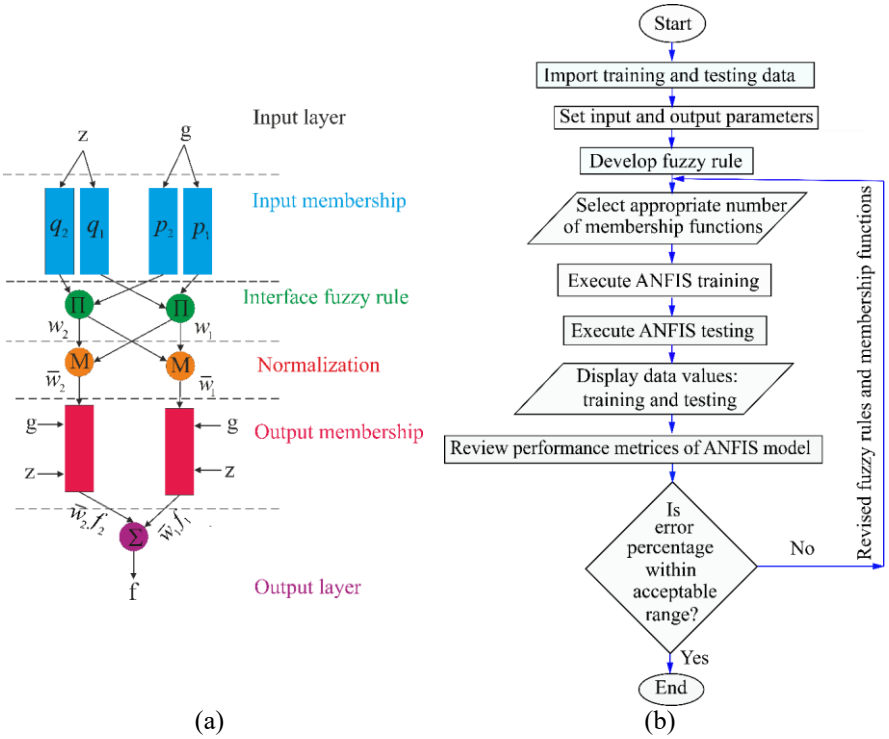

Fig. 9.8 Flowchart and graphical calculation steps for ANFIS: (a) Graphical summery of working principle (b) Flowchart for electroviscous heat transfer rate and total entropy generation.

9.4.3. Validation results for the regression analysis of ANN and ANFIS for Maxwell fluids

ANN and ANFIS methods are applied to predict the dimensionless electroviscous heat transfer rate. The predictions made by the ANN and ANFIS models in this study cover $0 \leq \phi \leq 0.05$ and $0 \leq Ha \leq 5$, respectively. Practically, particle concentration modifies thermophysical characteristics such as dielectric constant, mass density, viscous resistance, specific heat capacity, electrical conductance, and thermal diffusivity, governing hydrodynamic and thermal transport phenomena. The Hartmann number (Ha) serves as a dimensionless metric for magnetic field influence on flow regimes. Elevated Ha values correlate with intensified field interactions, a critical factor in MHD-driven processes such as liquid metal circulation and reactor cooling systems. Together, these parameters help to predict fluid behavior in systems influenced by magnetic fields. The actual value of η_h is 0.45653 while the predicted value is 0.44185 showcasing the precision of the forecast. The ANN and ANFIS models have two inputs (ϕ and Ha) and one output (η_h), as shown in Fig. 9.9. As

shown in Table 14, the ANN models achieve R values of 0.99921 during training and 0.99323 during testing. Additionally, the ANFIS models show a 0.034% and 0.63% improvement in R values for training and testing compared to the ANN models. Table 14 also reveals that the ANFIS method produces the lowest RMSE and MAPE values, with RMSE values of 3.7088×10^{-4} for training and 3.7683×10^{-4} for testing. Similarly, the corresponding MAPE values are 0.023298%, and 0.047201%, respectively.

In contrast, ANN and ANFIS models are employed to predict values of S_{total} for $0\leq\phi\leq0.05$ and $0\leq Ha\leq5$, respectively shown in Fig.9.10. The actual and predicted values for S_{total} are 0.45653 and 0.44185 respectively highlighting the accuracy of the prediction. Both methods show good accuracy, but the ANFIS model outperforms the ANN model. Each method uses ϕ and Ha as the input and total entropy generation as the output. Table 15 shows the accuracy of S_{total} predictions. The ANFIS model has R values 0.06% and 0.63% higher than the ANN model in training and testing, respectively. The R^2 value approaches 1, as shown in Tables 14 and 15. ANFIS also has the lowest RMSE and MAPE values. This means the error is much lower in ANFIS. The comparison shows that the models are reliable. ANFIS predicts normalized global entropy generation more accurately than ANN.

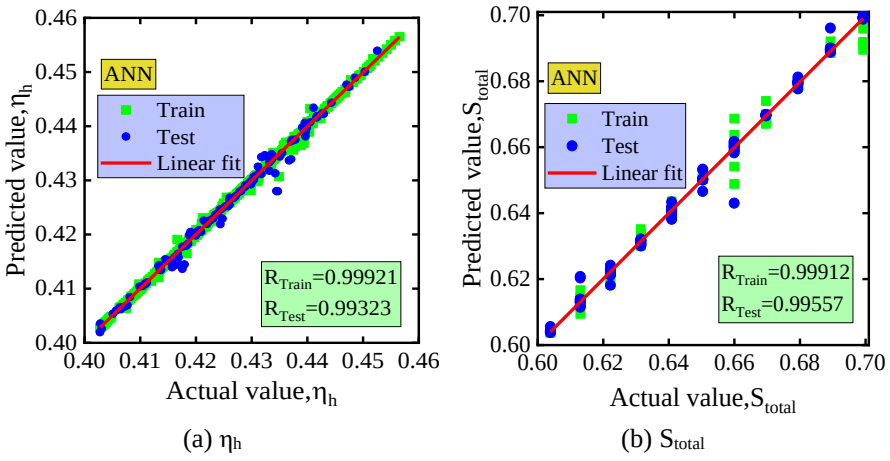

(a) η_h (b) S_{total}

Fig. 9.9 Regression plot of actual vs. predicted values for Maxwell fluids using the ANN method.

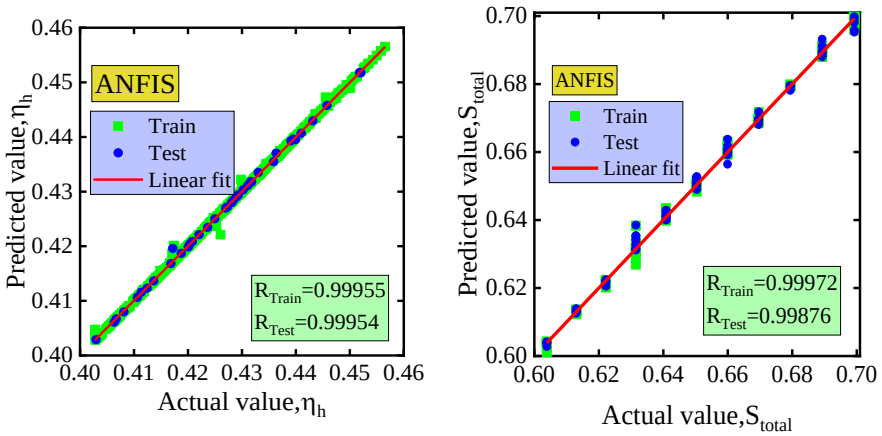

(a) η_h (b) S_{total}

Fig. 9.10 Regression plot of actual vs. predicted values for Maxwell fluids using the ANFIS method.

Table 14
Details of normalised electroviscous heat transfer rate prediction for Maxwell fluid.

Parameters	η_h	ANN		ANFIS	
		Train	Test	Train	Test
ϕ, Ha	RMSE	4.831×10^{-4}	13.804×10^{-4}	3.7088×10^{-4}	3.7683×10^{-4}
	MAPE	0.040645	0.18147	0.023298	0.047201
	R^2	0.99842	0.98651	0.99909	0.99905
	R	0.99921	0.99323	0.99955	0.99954

Table 15
Details of normalised total entropy generation prediction for Maxwell fluid.

Parameters	S_{total}	ANN		ANFIS	
		Train	Test	Train	Test
ϕ, Ha	RMSE	12.647×10^{-4}	27.175×10^{-4}	7.2395×10^{-4}	14.536×10^{-4}
	MAPE	0.0538	0.1821	0.03870	0.1331
	R^2	0.99824	0.99115	0.99943	0.99728
	R	0.9991	0.9955	0.9997	0.9987

The regression analyses in Figs. 9.11 and 9.12 highlight the predictive capabilities of ANN and ANFIS models for optimization data concerning η_h and S_{total} respectively. In Fig. 9.11, the regression plots illustrate a strong agreement between actual and predicted values for η_h, as reflected by high correlation coefficients for both models. As shown in Table 16, the ANN model achieves R values of 0.9988 for the training set and 0.9987 for the testing set, while the ANFIS model outperforms it with R values of 0.9998 for the training set and 0.9997 for the testing set, showcasing its ability to handle nonlinear relationships and uncertainties effectively.

Similarly, in Fig. 9.12, the regression analysis for S_{total} also reveals excellent predictive accuracy. The accuracy of the prediction is reflected in the actual value of S_{total} being 0.11615 and the predicted value being 0.11588. For the computational neural model, R scores of 0.9956 (training) and 0.9949 (testing) are observed, while the adaptive neuro-fuzzy system outperforms it with near-perfect R values of 0.9998 (training) and 0.9997 (testing), highlighting its superior adaptability to complex dataset. As illustrated in Tables 16 and 17, the R^2 value is nearly equal to 1, indicating a strong fit. Overall, both ANN and ANFIS models provide reliable predictions for η_h and S_{total}. However, ANFIS consistently outperforms ANN in terms of correlation coefficients, making it the preferred approach for optimization tasks requiring a higher precision. Finally, Tables 16 and 17 are constructed to know the optimum values of η_h and S_{total} determined using ANN and ANFIS from the Gray Wolf optimum data as input values.

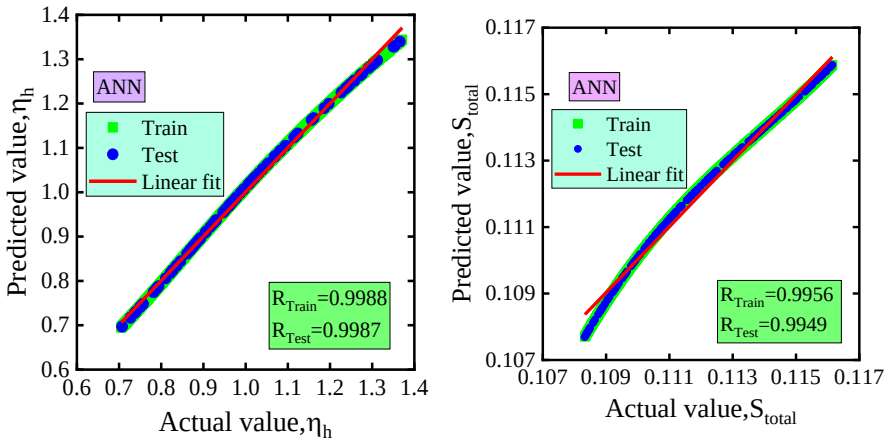

(a) η_h (b) S_{total}

Fig. 9.11 Regression plot of actual vs. predicted values from optimization data for Maxwell fluid using the ANN method

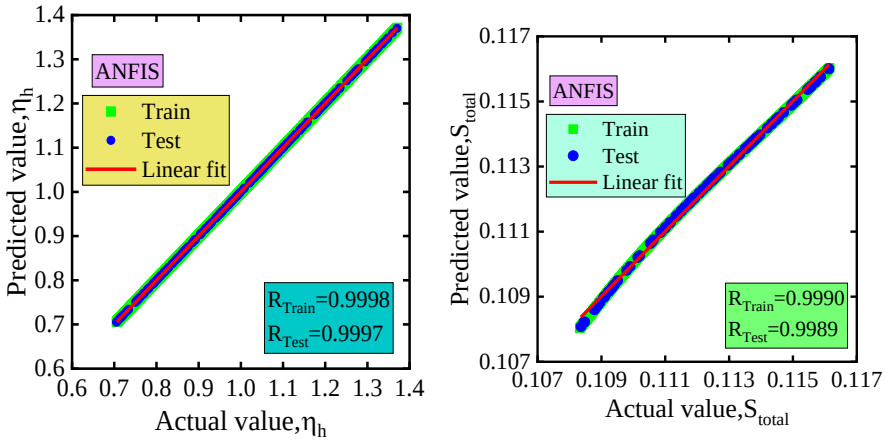

(a) η_h (b) S_{total}

Fig. 9.12 Regression plot of actual vs. predicted values from optimization data for Maxwell fluid using the ANFIS method

Table 16
Electroviscous heat transfer rate predicted by ANN and ANFIS using Gray Wolf optimization data for Maxwell fluid.

η_h	ANN		ANFIS	
	Train	Test	Train	Test
RMSE	0.91819×10^{-2}	0.91925×10^{-2}	0.040×10^{-3}	0.0409×10^{-3}
MAPE	0.7826	0.7999	0.0030	0.0031
R^2	0.9975	0.9973	0.9997	0.9996
R	0.9988	0.9987	0.9998	0.9997

Table 17
Total entropy production predicted by ANN and ANFIS using Gray Wolf optimization data Maxwell fluid.

S_{total}	ANN		ANFIS	
	Train	Test	Train	Test
RMSE	0.21×10^{-3}	0.2326×10^{-3}	1.0338×10^{-4}	1.0332×10^{-4}
MAPE	0.1605	0.1718	0.0793	0.0803
R^2	0.9912	0.9899	0.9980	0.9977
R	0.9956	0.9949	0.9990	0.9989

9.4.4. Validation results for the regression analysis of ANN and ANFIS for Oldroyd-B fluids

The performance evaluation metrics including MAPE, RMSE, R^2 and R used to assess the accuracy of different machine learning models are provided in Tables 16-15. The results indicate that both the ANN and ANFIS models produce highly accurate predictions. This investigation employs a dual-layer feedforward computational neural architecture, utilizing sigmoidal transforms in intermediary processing units and linear transforms in terminal nodes, to map correlations between design variables and target objectives, as depicted in Figs. 9.9-9.10. The optimization objectives Nu and S_{total} are used as both input variables and output results. As shown in Table 15 for Nu, ANN model achieves R values of 0.9556 for training and 0.9599 for testing. Furthermore, the ANFIS model provides a slight improvement of 2.747 % in training and 1.91 % testing over the ANN model in terms of the R value. As evidenced in Table 16, the adaptive neuro-fuzzy inference system (ANFIS) achieves minimal error metrics, with a training RMSE of 0.0432 and testing RMSE of 0.0506, alongside mean absolute percentage error (MAPE) scores of 0.0364 (training) and 0.0398 (testing). These outcomes underscore the framework's enhanced predictive accuracy, outperforming comparative methods in error minimization across both training and validation phases.

Table 16 summarizes the prediction accuracy of S_{total}. ANN model achieves R values of 0.9697 for training and 0.9658 for testing, while the ANFIS model achieves higher R values of 0.9839 for training and 0.9828 for testing respectively. The ANFIS model shows 50% and 133.33% lower RMSE value than the ANN model for training and testing respectively. Additionally, ANFIS exhibits the lowest MAPE value indicating a smaller error margin. This comparison highlights that while both models are reliable, ANFIS provides a more accurate prediction of normalized global entropy generation than the ANN.

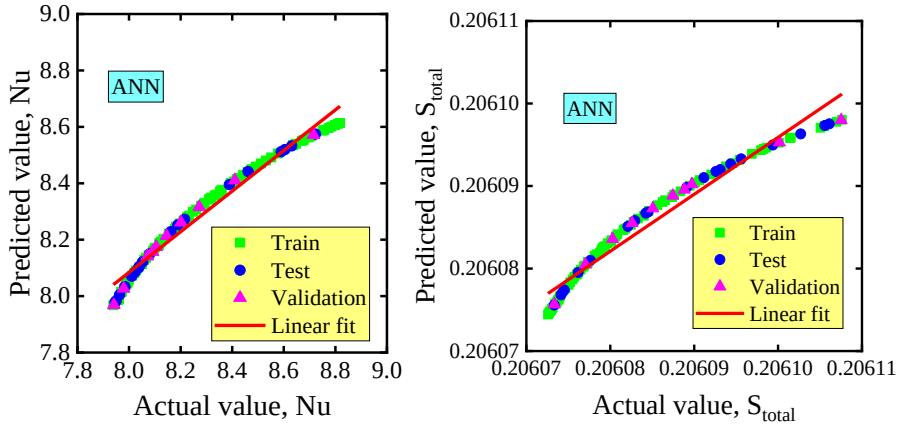

(a) Nu (b) S_{total}

Fig. 9.13 Regression Plot of Actual vs. Predicted Values Using the ANN Method.

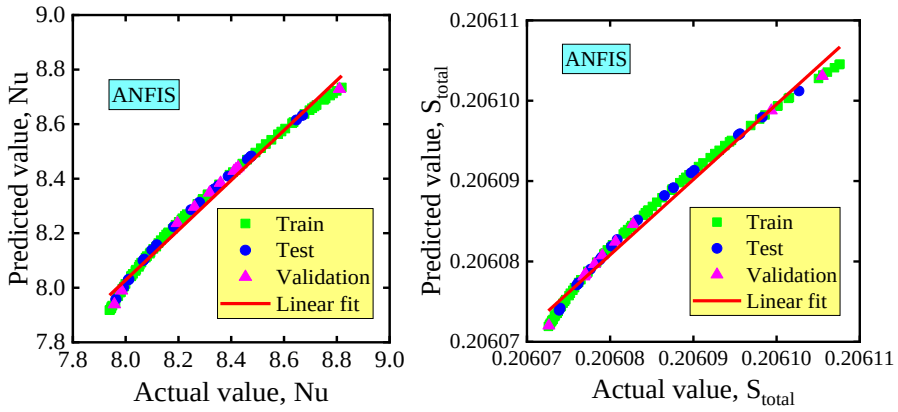

(a) Nu (b) S_{total}

Fig. 9.14 Regression Plot of Actual vs. Predicted Values Using the ANFIS Method.

Table 18
Details of Nusselt number prediction.

Nu	ANN		ANFIS	
	Train	Test	Train	Test
RMSE	0.0698	0.0697	0.0432	0.0506
MAPE	0.0591	0.0526	0.0364	0.0398
R^2	0.9131	0.9214	0.9655	0.9577
R	0.9556	0.9599	0.9826	0.9786

Table 19
Details of normalised total entropy production prediction.

S_{total}	ANN		ANFIS	
	Train	Test	Train	Test
RMSE	0.0006	0.0007	0.0004	0.0003
MAPE	0.0004	0.0006	0.0003	0.0003
R^2	0.9403	0.9327	0.9680	0.9660
R	0.9697	0.9658	0.9839	0.9828

9.5. Concluding remarks

This study brings together optimization methods and machine learning to examine three types of non-Newtonian fluids, namely couple stress Casson fluid,

Maxwell fluid, and Oldroyd B fluid under streaming potential conditions. The results give useful insight into the complex flow behavior of non-Newtonian fluids and show how they can improve the performance of portable microfluidic systems used for power generation, heat transfer, and energy control.

For the couple stress Casson fluid, the combined influence of the couple stress parameter, Casson constant, and ionic Peclet number leads to better electrokinetic energy conversion and lower thermal losses.

For the Maxwell fluid, multi objective optimization is carried out by adjusting relaxation time, Hall current, ion slip, nanoparticle volume fraction, and Hartmann number to achieve improved electroviscous heat transfer and reduced entropy production. These findings highlight the close link between fluid behavior and heat transport in viscoelastic systems.

In addition, the rheological behavior of Oldroyd B fluid is examined to evaluate its usefulness in microfluidic applications. A two objective optimization strategy is applied using Hartmann number, electrokinetic width, zeta potential, and Dukhin number as control parameters. This approach leads to better heat transfer performance and reduced entropy generation, confirming the potential of Oldroyd B fluids for more efficient microscale energy applications.

(i) According to the multi-objective optimization analysis, the best operating condition corresponds to a total entropy value of 2.75×10^{4} and an energy conversion efficiency of 7.24×10^{-3}. This work also brings together the analysis of couple stress, Casson, and Newtonian fluids into a single framework by carefully choosing the viscoplastic parameters. The optimal solutions cover a wide operating range, giving designers more freedom to handle practical design and manufacturing limits. By comparing the behavior of different fluids, it becomes easier to select the most suitable one for achieving better energy conversion with lower energy loss in microelectronic applications under the same working conditions.

(ii) Multi-objective optimization using NSGWOA and NSGA-II results in a 128% increase in electroviscous heat transfer rate and an 82.5% reduction in overall entropy generation, which demonstrates effective design strategies for microfluidic efficient energy harvesting.

(iii) Two-objective optimization of Oldroyd-B fluid using NSGWOA and NSGA-II achieves a 2.173% improvement in Nu and a 2.552% reduction in overall entropy generation. These results highlight effective design strategies for efficient energy harvesting in microfluidic systems.

(iv) The study compared artificial neural networks (ANN) and adaptive neuro-fuzzy inference systems (ANFIS) for data prediction. Results showed that ANFIS outperformed ANN in predicting Nusselt number and thermal irreversibility, demonstrating machine learning's effectiveness in modeling complex relationships and optimizing performance in intricate systems like Lab-on-a-Chip devices.

Chapter 10. Conclusions and direction for future studies

10.1. Conclusions

This thesis has comprehensively investigated the complex interactions of fluid dynamics, thermal/mass transfer, electrokinetic phenomena, and thermodynamic irreversibility in micro/nano scale systems using advanced mathematical modeling, optimization techniques, and machine learning algorithms. Each chapter addresses a unique facet of microfluidic transport phenomena with implications for improved energy conversion, thermal management, and system efficiency.

The initial phase examines scenarios lacking a perpendicular electric field. Here, flow velocity escalates gradually with low Hartmann numbers (Ha), while temperature rises until Ha=1, after which a decline occurs, signalling a behavioural inversion. Conversely, under perpendicular electric fields, temperature ascends with Ha at lower magnitudes. The investigation also probes rarefied flow dynamics and non-classical boundary constraints in rectangular microchannels, integrating secondary velocity slip and thermal discontinuity conditions. These higher-order formulations yield markedly distinct velocity and temperature profiles compared to traditional no-slip or first-order approximations. Specifically, secondary slip/jump conditions amplify velocity and thermal gradients relative to conventional models. Analysing heat transfer modulation via the Ha under electric fields, the Nusselt number (Nu) diminishes as Ha increases until a threshold, beyond which Nu rebounds. Additionally, Nu grows proportionally with K, though rarefaction and thermal discontinuities suppress Nu significantly. These findings underscore the sensitivity of microscale thermal management to electromagnetic and boundary condition effects.

The second investigation employs a combined analytical-numerical framework to analyse periodic electroosmosis-driven and pressure-activated flow of a viscoelastic Oldroyd-B fluid within a microscale conduit bounded by parallel plates. The imaginary part of the complex variables provides the fluid velocity and concentration governing equations to a set of nonlinear and nonhomogeneous types. At the peak point, the velocity amplitude for a higher elasticity $\bar{\lambda}_1$=0.18 increases by 18.45% compared to that for a lower elasticity ($\bar{\lambda}_1$=0.18). Similarly, for $\bar{\lambda}_1$=0.20, the velocity amplitude increment is 21.01%. The velocity profile for Maxwell fluid compared to the Oldroyd-B when other parameters were kept constant. The velocity and concentration amplitudes across the channel increase with higher zeta potential. Flow behavior is mainly controlled by viscous and elastic forces: elasticity enhances oscillations when viscosity is weak, while viscosity suppresses oscillations when elasticity is secondary. Near the channel center, velocity changes little and rises only slightly with increasing zeta potential. The peak speed has amplified approximately 142.75% for $\bar{\xi}$=4 with respect to $\bar{\xi}$=0.1. The volume flow rates under high zeta

potentials, viz. $\bar{\xi}$=2, 3 and 4, were boosted by 0.95%, 3.08%, and 9.32%, respectively, compared to that under the low zeta potential $\bar{\xi}$=0.1. Concentration profiles are mostly unaffected by slip, but time-modulated electric fields at $\tau = \pi/4$ greatly improve mixing and dispersion beyond the EDL. A resonant response linked to the angular Reynolds number influences mass transfer and species separation. Because of its combined elastic and viscous effects, the Oldroyd-B fluid shows higher mass transfer rates than the Maxwell fluid. This semi-analytical framework also captures Maxwell and Newtonian behavior by adjusting the viscoelastic parameter, allowing direct comparison across fluids and helping identify the most suitable fluid for maximizing mass transfer under the same design conditions.

The third investigation explores thermally developed, pressure-driven streaming potential dynamics of a viscoplastic Casson fluid with couple-stress properties under electromagnetic fields, incorporating slip-modulated zeta potentials. Analytical formulations quantify streaming potential, energy conversion efficiency, velocity/temperature profiles, heat transfer coefficients (Nu), and entropy generation under asymmetric zeta potential conditions influenced by slip. The study focuses on analysing the interplay of electromagnetic forces, non-Newtonian couple-stress effects, and yield stress characteristics on electrokinetic energy conversion, hydrodynamic behavior, and thermal transport. Validation against Newtonian fluid benchmarks confirms the model's accuracy in predicting electromagnetic-hydrodynamic (EMHD) impacts on flow velocity, temperature, and energy efficiency.

Comparative analysis reveals distinct enhancements in streaming potential, EKEC efficiency, velocity, and Nu for the couple-stress Casson fluid relative to Newtonian, Casson, and couple-stress fluid models. Energy conversion efficiency rises by 45.92% (couple-stress Casson), 47.10% (couple-stress), 42.81% (Casson), and 37.68% (Newtonian) under slip-dependent versus slip-independent zeta potentials. Velocity amplifies with elevated couple-stress (β), and Casson (γ) parameters, reflecting diminished non-Newtonian resistance. At β=2 and γ=2, velocity surges by 107.64% compared to β=1, γ=1. Joule heating amplifies temperature gradients, especially near the channel center, where jump boundary conditions raise mid-channel temperature by 2.95%. In viscoplastic fluids, the Nusselt number shows strong variation beyond critical Brinkman and Hartmann numbers. The combined effects of couple stress, Casson parameters, and ionic Peclet number maximize EKEC efficiency while minimizing heat-transfer irreversibility. Multi-objective optimization gives an optimal entropy of 2.749×10^{4} and an EKEC efficiency of 0.568×10^{-3}. A unified framework also captures Newtonian, Casson, and couple-stress behavior, and the Pareto set enables better design trade-offs, helping select the best fluid for high efficiency and low irreversibility in microelectronic systems.

This forth study investigates the rheology and heat transfer of viscoelastic fluids using the Poisson–Boltzmann and Debye-Hückel models to account for zeta potential, slip, porous effects, and Stern layer currents. A transient pressure-driven Maxwell fluid model with streaming potential and MHD effects was developed to evaluate flow, heat transfer, entropy, and EKEC efficiency. Results show that slip-dependent zeta potential increases streaming potential by 23.15% and boosts EKEC

efficiency by 809.91%. Maxwell fluids also outperform Newtonian fluids in flow rate and thermal performance due to strong elastic-viscous interactions. Multi-objective optimization of key parameters enhances η_h while minimizing S_{total}. Optimization strategies using NSGWOA and NSGA-II achieve a 128% increase in η_h and an 82.5% reduction in S_{total}, demonstrating robust frameworks for energy-efficient microfluidic design. Machine learning predictions further reveal that the ANFIS method outperforms ANN in accurately forecasting electroviscous η_h and S_{total}. These findings underscore the potential of machine learning to optimize thermal performance and decode the complexities of advanced microfluidic systems.

The fifth investigation reveals pivotal findings on the viscoelastic behavior of Oldroyd-B fluids and their role in advancing portable microfluidic systems for energy harvesting, thermal regulation, and power dissipation. This work dissects the dynamic interactions between time-modulated flow, electromagnetic-hydrodynamic forces, and field-induced viscous effects in microscale channels. A nonlinear Poisson-Boltzmann framework, formulated without simplified electrostatic assumptions, governs surface potential dynamics and couples with momentum equations incorporating velocity slip, electromagnetic stresses, and interfacial currents. Critical design variables: Ha, K, $\bar{\xi}$, and Du are optimized Nu, and S_{total}. Specifically, with a Dukhin number (Du=2), the EKEC efficiency falls by 95.38% compared to the scenario where Du=0. Resonant behavior, influenced by the Re_ω, impacts the mass transfer rate and species separation. When Re_ω exceeds a critical value (Re_ω~0.2), the flow shifts from a viscous-dominated regime to an inertia-dominated regime. At Ha = 2, the solute concentration increases by 64.35% in Oldroyd-B fluids compared to conditions at Ha = 0. In this state, the effect of the Ha undergoes a notable transformation, resulting in charge separation. Two-objective optimization using NSGWOA and NSGA-II achieves a 6.286% improvement in Nu and a 6.872% reduction in overall entropy generation. These results highlight effective design strategies for efficient energy harvesting in microfluidic systems. The study compared ANN, and ANFIS for data prediction. Results showed that ANFIS outperformed ANN in predicting Nusselt number and thermal irreversibility, demonstrating machine learning's effectiveness in modeling complex relationships and optimizing performance in intricate systems like energy harvesting devices.

The final part of this thesis assessed the combined effects of channel geometry and gravity on nanochannel desalination performance. The results demonstrate that geometric configuration plays a decisive role under identical operating conditions. At surface potential magnitudes above 0.05, enhanced electric double layer charge buildup strengthens surface-driven transport, producing a nonmonotonic axial concentration trend consisting of depletion, stabilization, and recovery near the outlet. At a downstream location of approximately 93.4 nm, the rectangular channel achieves a 24.55% higher salt removal than the hyperbolic design at 30 V_0 and a zeta potential of −0.05 V, reflecting improved depletion-layer resilience. Energy analysis shows that the hyperbolic and rectangular configurations consume about 7.65 kWh/m³ and 9.69 kWh/m³, with associated costs of \$0.9844/m³ and \$0.7864/m³, respectively. Although both remain economically viable, operation at 50 V_0 increases the levelized water cost of the rectangular channel by approximately 20.11% relative to the hyperbolic geometry, highlighting the trade-off

between enhanced ion separation and higher energy demand. These outcomes support the strategic use of gravity-assisted nanochannel designs for sustainable desalination applications.

This thesis provides a unified framework for understanding and optimizing microscale fluid behavior (electroosmotic and streaming potential) involving Newtonian, non-Newtonian rheology, electric and magnetic field effects, slip-flow conditions, and thermodynamic irreversibility. It also illustrates the immense potential of machine learning in capturing the nonlinearities of such systems. By integrating semi-analytical modeling, numerical optimization, and AI-based prediction, this work lays a foundation for next-generation energy-efficient microfluidic and nanofluidic systems used in biomedical, desalination, and energy harvesting applications.

10.2. Direction for future studies

Further research on streaming potential flows in microchannels is needed to formulate innovative approaches for evaluating fluid flow, heat transfer, and mass transfer characteristics across various electromagnetic devices.

(i) In analyzing the mixing process influenced by the interplay of diffusion, convection, and non-uniform wall temperatures, the non-Newtonian fluid behavior can be elucidated using a visco-elastic model. A modified Nernst-Planck-Poisson framework is integrated with the Navier-Stokes and energy equations with convection and wall temperature effects. This integration can quantify the interplay between fluid rheology, asymmetrical surface potential, and heat transfer.
(ii) A time-dependent, two-dimensional analysis of microchannel flow with a two-layer nanofluid configuration investigates the dynamics of rotating power-law fluids while incorporating slip and jump boundary conditions, all without relying on the Debye-Hückel approximation.
(iii) A theoretical framework evaluates oscillatory EMHD flow dynamics driven by streaming potentials and pressure gradients in microscale systems, incorporating Joule heating, frictional energy dissipation, and radiative thermal effects. The study focuses on maximizing thermal and molecular transport efficiency for viscoelastic Phan-Thien-Tanner (PTT) fluids within confined microgeometries
(iv) Thermal characteristics can be predicted by developing an analytical model for a time-dependent poly-electrolyte grafted nanochannel with ion partitioning and ion size effects of couple-stress Casson fluid.
(v) Future research will refine the analysis of Oldroyd-B fluid behavior by incorporating nanoparticle concentration, surface roughness, non-Newtonian effects, and streaming potential interaction.
(vi) There is no work available considering two-dimensional analysis for integration of magnetohydrodynamic effects, heat transfer maximization, entropy generation minimization, and mass transfer with the Nernst-Planck-Poisson framework and Navier-Stokes equations, which can enhance to improve practical predictions under time-periodic flow conditions.

(vii) The focus can be on experimental validation, real-world stability of nanofluids, and more accurate surface and boundary effects modeling, considering electromagnetic, hydrodynamic, and mass transfer interactions.
(viii) Advanced techniques such as molecular dynamics simulations can provide deeper insights into nanoparticle behavior at surfaces, interfaces, and under dynamic conditions.
(ix) The long-term stability of nanofluids can be investigated by considering factors like agglomeration, sedimentation, and interactions with surrounding media. At the same time, optimization techniques and hybrid models will be employed to improve the prediction accuracy for heat transfer, entropy generation, and mass transfer in practical applications.

References

[1] X. Li, L. Wei, R. Nie, Z. Wang, W. Huang, J. Liu, X. Zhang, Y. Chen, Integrating magnetic metal-organic frameworks-based sample preparation with microchannel resistance biosensor for rapid and quantitative detection of aflatoxin B1, J. Hazard. Mater. 438 (2022) 129425. https://doi.org/10.1016/j.jhazmat.2022.129425.

[2] Z. Wang, X. Yan, Q. Zhou, Q. Wang, D. Zhao, H. Wu, A Directly Moldable, Highly Compact, and Easy-for-Integration 3D Micromixer with Extraordinary Mixing Performance, Anal. Chem. 95 (2023) 8850–8858. https://doi.org/10.1021/acs.analchem.3c00335.

[3] A. Mora-Boza, A. Mulero-Russe, N. Di Caprio, J.A. Burdick, E. O'Neill, A. Singh, A.J. García, Facile photopatterning of perfusable microchannels in hydrogels for microphysiological systems, Nat. Protoc. 20 (2025) 272–292. https://doi.org/10.1038/s41596-024-01041-8.

[4] U.A. Gurkan, D.K. Wood, D. Carranza, L.H. Herbertson, S.L. Diamond, E. Du, S. Guha, J. Di Paola, P.C. Hines, I. Papautsky, S.S. Shevkoplyas, N.J. Sniadecki, V.K. Pamula, P. Sundd, A. Rizwan, P. Qasba, W.A. Lam, Next generation microfluidics: fulfilling the promise of lab-on-a-chip technologies, Lab Chip 24 (2024) 1867–1874. https://doi.org/10.1039/D3LC00796K.

[5] G.M. Whitesides, The origins and the future of microfluidics, Nature 442 (2006) 368–373. https://doi.org/10.1038/nature05058.

[6] Q. Shi, T. He, C. Lee, More than energy harvesting – Combining triboelectric nanogenerator and flexible electronics technology for enabling novel micro-/nano-systems, Nano Energy 57 (2019) 851–871. https://doi.org/10.1016/j.nanoen.2019.01.002.

[7] T. Handte, S. Bohm, B. Goj, L. Dittrich, E. Runge, S. Sinzinger, Compact MEMS-based sensor for refractive index monitoring of liquids, Sensors Actuators A Phys. 386 (2025) 116328. https://doi.org/10.1016/j.sna.2025.116328.

[8] M.T. Gokmen, F.E. Du Prez, Porous polymer particles—A comprehensive guide to synthesis, characterization, functionalization and applications, Prog. Polym. Sci. 37 (2012) 365–405. https://doi.org/10.1016/j.progpolymsci.2011.07.006.

[9] A. Tropmann, L. Tanguy, P. Koltay, R. Zengerle, L. Riegger, Completely Superhydrophobic PDMS Surfaces for Microfluidics, Langmuir 28 (2012) 8292–8295. https://doi.org/10.1021/la301283m.

[10] J.D. Tice, H. Song, A.D. Lyon, R.F. Ismagilov, Formation of Droplets and Mixing in Multiphase Microfluidics at Low Values of the Reynolds and the Capillary Numbers, Langmuir 19 (2003) 9127–9133. https://doi.org/10.1021/la030090w.

[11] K. Aran, A. Fok, L.A. Sasso, N. Kamdar, Y. Guan, Q. Sun, A. Ündar, J.D. Zahn, Microfiltration platform for continuous blood plasma protein extraction from whole blood during cardiac surgery, Lab Chip 11 (2011) 2858–2868. https://doi.org/10.1039/C1LC20080A.

[12] C. Wyatt Shields IV, C.D. Reyes, G.P. López, Microfluidic cell sorting: a review of the advances in the separation of cells from debulking to rare cell isolation, Lab Chip 15 (2015) 1230–1249. https://doi.org/10.1039/C4LC01246A.

[13] A. Sontheimer-Phelps, B.A. Hassell, D.E. Ingber, Modelling cancer in microfluidic human organs-on-chips, Nat. Rev. Cancer 19 (2019) 65–81. https://doi.org/10.1038/s41568-018-0104-6.

[14] E.W. Errill, Rheology of blood, Physiol. Rev. 49 (1969) 863–888. https://doi.org/10.1152/physrev.1969.49.4.863.

[15] L. Isa, R. Besseling, A.N. Morozov, W.C.K. Poon, Velocity Oscillations in Microfluidic Flows of Concentrated Colloidal Suspensions, Phys. Rev. Lett. 102 (2009) 58302. https://doi.org/10.1103/PhysRevLett.102.058302.

[16] M.R.G. Kopp, M. Linsenmeier, B. Hettich, S. Prantl, S. Stavrakis, J.-C. Leroux, P. Arosio, Microfluidic Shrinking Droplet Concentrator for Analyte Detection and Phase Separation of Protein Solutions, Anal. Chem. 92 (2020) 5803–5812. https://doi.org/10.1021/acs.analchem.9b05329.

[17] I. Bernacka-Wojcik, P. Lopes, A. Catarina Vaz, B. Veigas, P. Jerzy Wojcik, P. Simões, D. Barata, E. Fortunato, P. Viana Baptista, H. Águas, R. Martins, Bio-microfluidic platform for gold nanoprobe based DNA detection—application to Mycobacterium tuberculosis, Biosens. Bioelectron. 48 (2013) 87–93. https://doi.org/10.1016/j.bios.2013.03.079.

[18] C. Andreou, M.R. Hoonejani, M.R. Barmi, M. Moskovits, C.D. Meinhart, Rapid Detection of Drugs of Abuse in Saliva Using Surface Enhanced Raman Spectroscopy and Microfluidics, ACS Nano 7 (2013) 7157–7164. https://doi.org/10.1021/nn402563f.

[19] T.-H. Liu, S.-S. Cheng, H.-L. You, M.S. Lee, G.-B. Lee, Bacterial detection and identification from human synovial fluids on an integrated microfluidic system, Analyst 144 (2019) 1210–1222. https://doi.org/10.1039/C8AN01764F.

[20] K. Xiao, L. Jiang, M. Antonietti, Ion Transport in Nanofluidic Devices for Energy Harvesting, Joule 3 (2019) 2364–2380. https://doi.org/10.1016/j.joule.2019.09.005.

[21] K. Liu, T. Ding, X. Mo, Q. Chen, P. Yang, J. Li, W. Xie, Y. Zhou, J. Zhou, Flexible microfluidics nanogenerator based on the electrokinetic conversion, Nano Energy 30 (2016) 684–690. https://doi.org/10.1016/j.nanoen.2016.10.058.

[22] O.A. Ibrahim, M. Navarro-Segarra, P. Sadeghi, N. Sabaté, J.P. Esquivel, E. Kjeang, Microfluidics for Electrochemical Energy Conversion, Chem. Rev. 122 (2022) 7236–7266. https://doi.org/10.1021/acs.chemrev.1c00499.

[23] J. Tang, L. Gong, J. Jiang, Z. Li, J. Han, Numerical simulation of electrokinetic desalination using microporous permselective membranes, Desalination 477 (2020) 114262. https://doi.org/10.1016/j.desal.2019.114262.

[24] K. Saha, S. Sonkusale, A flexible and self-healable moisture-driven energy harvester based on 2D vanadium pentoxide nanosheets, J. Mater. Chem. C 13 (2025) 5617–5623. https://doi.org/10.1039/D4TC02876G.

[25] Z. Gao, X. Shang, J. Bai, Y. Yang, P. Li, Study on the uneven flow distribution and non-uniform heat transfer in microchannels, Appl. Therm. Eng. 230 (2023) 120824. https://doi.org/10.1016/j.applthermaleng.2023.120824.

[26] T. Halawa, A.S. Tanious, Investigation of the optimum design of magnetic field arrangement to enhance heat transfer performance of Fe3O4-water magnetic nanofluid, Int. J. Therm. Sci. 184 (2023) 108014. https://doi.org/10.1016/j.ijthermalsci.2022.108014.

[27] J. Gonzalez-Ayala, A. Calvo Hernández, J.M.M. Roco, From maximum power to a trade-off optimization of low-dissipation heat engines: Influence of control parameters and the role of entropy generation, Phys. Rev. E 95 (2017) 22131. https://doi.org/10.1103/PhysRevE.95.022131.

[28] P. Huang, M. Pan, Secondary heat transfer enhancement design of variable cross-section microchannels based on entransy analysis, Renew. Sustain. Energy Rev. 141 (2021) 110834. https://doi.org/10.1016/j.rser.2021.110834.

[29] G. Wang, K. Sheng, Y. Wang, G. Ding, D. Xie, Thermal hydraulic performance of tree-like microchannel heat sink with high branching level based on the improved Murray's law, Int. J. Heat Mass Transf. 231 (2024) 125875. https://doi.org/10.1016/j.ijheatmasstransfer.2024.125875.

[30] M. Bahiraei, N. Mazaheri, M.R. Daneshyar, A. Mwesigye, Two-phase simulation of irreversibilities for Ag–water nanofluid flow inside an elliptical pin-fin heat sink: Entropy generation and exergy considerations, Powder Technol. 409 (2022) 117723. https://doi.org/10.1016/j.powtec.2022.117723.

[31] W. Wu, S. Wang, W. Wu, K. Chen, S. Hong, Y. Lai, A critical review of battery thermal performance and liquid based battery thermal management, Energy Convers. Manag. 182 (2019) 262–281. https://doi.org/10.1016/j.enconman.2018.12.051.

[32] P. Biswal, T. Basak, Entropy generation vs energy efficiency for natural convection based energy flow in enclosures and various applications: A review, Renew. Sustain. Energy Rev. 80 (2017) 1412–1457. https://doi.org/10.1016/j.rser.2017.04.070.

[33] P.A.K. Lam, K.A. Prakash, Thermodynamic investigation and multi-objective optimization for jet impingement cooling system with Al2O3/water nanofluid, Energy Convers. Manag. 111 (2016) 38–56. https://doi.org/10.1016/j.enconman.2015.12.018.

[34] R.J. (Robert J. Hunter, L.R. White, D.Y.C. Chan, Foundations of colloid science, Clarendon Press,Oxford University Press, 1987.

[35] P.J. Heaney, C.T. Prewitt, G. V Gibbs, Silica: Physical Behavior, Geochemistry, and Materials Applications, De Gruyter, 2018.

[36] A. Revil, P.A. Pezard, P.W.J. Glover, Streaming potential in porous media: 1. Theory of the zeta potential, J. Geophys. Res. Solid Earth 104 (1999) 20021–20031. https://doi.org/10.1029/1999JB900089.

[37] R.F. F., Sur un Nouvel Effet de l'electricite Galvanique, Mem. Soc. Imp. Natur. Moscou 2 (1809) 327–337. https://cir.nii.ac.jp/crid/1571698600492350720.

[38] H. Helmholtz, Studien über electrische Grenzschichten, Ann. Phys. 243 (1879) 337–382. https://doi.org/10.1002/andp.18792430702.

[39] F. Jüttner, Handbuch der Elektrizität und des Magnetismus. Bearbeitet von F. Auerbach, Jena, K. Baedecker†, Jena, A. Becker, Heidelberg, E. Bräuer, Voigtsdorf, P. Cermak, Gießen, H. Diesselhorst, Braunschweig, A. Eichenwald, Moskau, G. Gehlhoff, Berlin, E. Gehrke, Ch, Zeitschrift Für Elektrochemie Und Angew. Phys. Chemie 30 (1924) 296A–297. https://doi.org/https://doi.org/10.1002/bbpc.192400076.

[40] M. Gouy, Sur la constitution de la charge électrique à la surface d'un électrolyte, J. Phys. Theor. Appl. 9 (1910) 457–468. https://doi.org/10.1051/jphystap:019100090045700.

[41] D.L. Chapman, LI. A contribution to the theory of electrocapillarity , London, Edinburgh, Dublin Philos. Mag. J. Sci. 25 (1913) 475–481. https://doi.org/10.1080/14786440408634187.

[42] O. Stern, ZUR THEORIE DER ELEKTROLYTISCHEN DOPPELSCHICHT, Zeitschrift Für Elektrochemie Und Angew. Phys. Chemie 30 (1924) 508–516. https://doi.org/10.1002/bbpc.192400182.

[43] R.J. Hunter, H.J.L. Wright, The dependence of electrokinetic potential on concentration of electrolyte, J. Colloid Interface Sci. 37 (1971) 564–580. https://doi.org/10.1016/0021-9797(71)90334-1.

[44] J. Wu, Understanding the Electric Double-Layer Structure, Capacitance, and Charging Dynamics, Chem. Rev. 122 (2022) 10821–10859. https://doi.org/10.1021/acs.chemrev.2c00097.

[45] H. Ban, B. Lin, Z. Song, Effect of electrical double layer on electric conductivity and pressure drop in a pressure-driven microchannel flow, Biomicrofluidics 4 (2010) 14104. https://doi.org/10.1063/1.3328091.

[46] B. Saha, S. Chowdhury, S. Sarkar, P.P. Gopmandal, Electroosmotic flow modulation and dispersion of uncharged solutes in soft nanochannel, Soft Matter 20 (2024) 6458–6489. https://doi.org/10.1039/D4SM00614C.

[47] C. Li, A. Hassan, M. Palmai, Y. Xie, P.T. Snee, B.A. Powell, L.C. Murdoch, C.J.G. Darnault, Experimental measurements and numerical simulations of the transport and retention of nanocrystal CdSe/ZnS quantum dots in saturated porous media: Effects of electrolytes, organic ligand, and natural organic matter, Sci. Total Environ. 897 (2023) 165387. https://doi.org/10.1016/j.scitotenv.2023.165387.

[48] L. Shi, L. Esfandiari, Emerging on-chip electrokinetic based technologies for purification of circulating cancer biomarkers towards liquid biopsy: A review, Electrophoresis 43 (2022) 288–308. https://doi.org/10.1002/elps.202100234.

[49] K.N. Vasista, S.K. Mehta, S. Pati, S. Sarkar, Electroosmotic flow of viscoelastic fluid through a microchannel with slip-dependent zeta potential, Phys. Fluids 33 (2021) 123110. https://doi.org/10.1063/5.0073367.

[50] P. Fadaei, H. Niazmand, M.A. Raoufi, Influence of finite size of ions on thermal transport of a simultaneous electrokinetic-pressure driven flow of power-law fluids in a slit microchannel, Colloids Surfaces A Physicochem. Eng. Asp. 634 (2022) 127857. https://doi.org/10.1016/j.colsurfa.2021.127857.

[51] R. Fernández-Mateo, V. Calero, H. Morgan, P. García-Sánchez, A. Ramos, Wall Repulsion of Charged Colloidal Particles during Electrophoresis in Microfluidic Channels, Phys. Rev. Lett. 128 (2022) 74501. https://doi.org/10.1103/PhysRevLett.128.074501.

[52] Z. Xie, Y. Jian, W. Tan, Streaming potential analysis and electrokinetic energy conversion efficiency of two immiscible fluids in a nanochannel, Sensors Actuators, B Chem. 273 (2018) 1257–1268. https://doi.org/10.1016/j.snb.2018.06.070.

[53] D. Jing, Y. Pan, Electroviscous effect and convective heat transfer of pressure-driven flow through microtubes with surface charge-dependent slip, Int. J. Heat Mass Transf. 101 (2016) 648–655. https://doi.org/10.1016/j.ijheatmasstransfer.2016.05.087.

[54] T. Wu, Z. Yang, R. Hu, Y.-F. Chen, H. Zhong, L. Yang, W. Jin, Film entrainment and microplastic particles retention during gas invasion in suspension-filled microchannels, Water Res. 194 (2021) 116919. https://doi.org/10.1016/j.watres.2021.116919.

[55] T. Morijiri, M. Yamada, T. Hikida, M. Seki, Microfluidic counterflow centrifugal elutriation system for sedimentation-based cell separation, Microfluid. Nanofluidics 14 (2013) 1049–1057. https://doi.org/10.1007/s10404-012-1113-5.

[56] A.O. El Moctar, N. Aubry, J. Batton, Electro-hydrodynamic micro-fluidic mixer, Lab Chip 3 (2003) 273–280. https://doi.org/10.1039/B306868B.

[57] J. Dhar, A. Bandopadhyay, S. Chakraborty, Electro-osmosis of electrorheological fluids, Phys. Rev. E 88 (2013) 53001. https://doi.org/10.1103/PhysRevE.88.053001.

[58] A.M. Bhaskaran, S. Agrawal, K. Sarkar, P. Dhar, Elasto-compliance of harmonically stimulated soft micro-gaps during electro-magneto-kinetic flows, Soft Matter 20 (2024) 5969–5982. https://doi.org/10.1039/D4SM00431K.

[59] Y. Li, Y. Ren, W. Liu, X. Chen, Y. Tao, H. Jiang, On controlling the flow behavior driven by induction electrohydrodynamics in microfluidic channels, Electrophoresis 38 (2017) 983–995. https://doi.org/https://doi.org/10.1002/elps.201600500.

[60] T. Ghonge, J. Chakraborty, R. Dey, S. Chakraborty, Electrohydrodynamics within the electrical double layer in the presence of finite temperature gradients, Phys. Rev. E 88 (2013) 53020. https://doi.org/10.1103/PhysRevE.88.053020.

[61] A. Richter, A. Plettner, K.A. Hofmann, H. Sandmaier, A micromachined electrohydrodynamic (EHD) pump, Sensors Actuators A Phys. 29 (1991) 159–168. https://doi.org/https://doi.org/10.1016/0924-4247(91)87118-M.

[62] T. Siva, S. Jangili, B. Kumbhakar, P.K. Mondal, Unsteady electromagnetohydrodynamic flow of couple stress fluid through a microchannel: A theoretical analysis, Eur. J. Mech.-B/Fluids 95 (2022) 83–93. https://doi.org/10.1016/j.euromechflu.2022.04.007.

[63] P. Majumdar, D. Dasgupta, Electromagnetohydrodynamic (EMHD) flow through porous media—Multiscale approach, J. Appl. Phys. 134 (2023) 224702. https://doi.org/10.1063/5.0174534.

[64] J. Zheng, Y. Jian, Transient rotating magnetohydrodynamic electroosmotic flow using time-fractional Caputo–Fabrizio derivative, Phys. Fluids 37 (2025) 22021. https://doi.org/10.1063/5.0254733.

[65] S. Hina, MHD peristaltic transport of Eyring–Powell fluid with heat/mass transfer, wall properties and slip conditions, J. Magn. Magn. Mater. 404 (2016) 148–158. https://doi.org/10.1016/j.jmmm.2015.11.059.

[66] Y. Liu, Y. Jian, C. Yang, Electrochemomechanical energy conversion efficiency in curved rectangular nanochannels, Energy 198 (2020) 117401. https://doi.org/10.1016/j.energy.2020.117401.

[67] S. Saha, B. Kundu, Multi-objective optimization of electrokinetic energy conversion efficiency and entropy generation for streaming potential driven electromagnetohydrodynamic flow of couple stress Casson fluid in microchannels with slip-dependent zeta potentials, Energy 284 (2023) 129288. https://doi.org/10.1016/j.energy.2023.129288.

[68] A. Hernández, A. Mora, J.C. Arcos, O. Bautista, Joule heating and Soret effects on an electro-osmotic viscoelastic fluid flow considering the generalized Phan-Thien–Tanner model, Phys. Fluids 35 (2023) 42010. https://doi.org/10.1063/5.0146034.

[69] M.O. Oni, B.K. Jha, A.O. Ajibade, Interplay of dual streaming potentials on electroosmotic mixed convection flow in a vertical microannulus with Joule heating effect, Int. Commun. Heat Mass Transf. 131 (2022) 105839. https://doi.org/10.1016/j.icheatmasstransfer.2021.105839.

[70] A. Hernández, A. Mora, M.B. Arce-Vazquez, J. de la Cruz-Alejo, M. Salazar-Pereyra, Non-isothermal electroosmotic flow of a viscoelastic fluid through a porous medium in a microchannel, Phys. Fluids 36 (2024) 82007. https://doi.org/10.1063/5.0223776.

[71] R. Chein, Y.C. Yang, Y. Lin, Estimation of Joule heating effect on temperature and pressure distribution in electrokinetic-driven microchannel flows, Electrophoresis 27 (2006) 640–649. https://doi.org/10.1002/elps.200500314.

[72] A.K. Singh, J. Kumar, Electrical characteristics, stability, electromigration, Joule heating, and reliability aspect of focused ion beam fabricated gold and copper nanobar interconnects on SiO2 and glass substrates, J. Vac. Sci. Technol. B 38 (2020) 62805. https://doi.org/10.1116/6.0000514.

[73] X. Wang, Y. Liu, H. Cheng, X. Ouyang, Surface Wettability for Skin-Interfaced Sensors and Devices, Adv. Funct. Mater. 32 (2022) 2200260. https://doi.org/10.1002/adfm.202200260.

[74] B. Zhang, B. Seong, J. Lee, V. Nguyen, D. Cho, D. Byun, One-Step Sub-micrometer-Scale Electrohydrodynamic Inkjet Three-Dimensional Printing Technique with Spontaneous Nanoscale Joule Heating, ACS Appl. Mater. Interfaces 9 (2017) 29965–29972. https://doi.org/10.1021/acsami.7b08375.

[75] X. Xuan, D. Li, Analytical study of Joule heating effects on electrokinetic transportation in capillary electrophoresis, J. Chromatogr. A 1064 (2005) 227–237. https://doi.org/10.1016/j.chroma.2004.12.033.

[76] X. Xuan, B. Xu, D. Sinton, D. Li, Electroosmotic flow with Joule heating effects, Lab Chip 4 (2004) 230–236. https://doi.org/10.1039/B315036D.

[77] K.J. Gowtham, B.J. Gireesha, C.G. Pavithra, Investigation of Third-Grade fluid flow in an inclined Microchannel: Utilizing the Hermite wavelet technique for second law analysis, Chem. Eng. Sci. 300 (2024) 120646. https://doi.org/10.1016/j.ces.2024.120646.

[78] G.L. Morini, Viscous heating in liquid flows in micro-channels, Int. J. Heat Mass Transf. 48 (2005) 3637–3647. https://doi.org/10.1016/j.ijheatmasstransfer.2005.01.011.

[79] S. Morteza Mousavi, B. Ehteshami, A. Ali Rabienataj Darzi, Two-and-three-dimensional analysis of Joule and viscous heating effects on MHD nanofluid forced convection in microchannels, Therm. Sci. Eng. Prog. 25 (2021) 100983. https://doi.org/10.1016/j.tsep.2021.100983.

[80] B.H. Salman, H.A. Mohammed, K.M. Munisamy, A.S. Kherbeet, Characteristics of heat transfer and fluid flow in microtube and microchannel using conventional fluids and nanofluids: A review, Renew. Sustain. Energy Rev. 28 (2013) 848–880. https://doi.org/10.1016/j.rser.2013.08.012.

[81] S. Mukherjee, P. Biswal, S. Chakraborty, S. DasGupta, Effects of viscous dissipation during forced convection of power-law fluids in microchannels, Int. Commun. Heat Mass Transf. 89 (2017) 83–90. https://doi.org/10.1016/j.icheatmasstransfer.2017.09.018.

[82] G.M. Chen, C.P. Tso, Effects of viscous dissipation on forced convective heat transfer in a channel embedded in a power-law fluid saturated porous medium, Int. Commun. Heat Mass Transf. 38 (2011) 57–62. https://doi.org/10.1016/j.icheatmasstransfer.2010.10.004.

[83] J. Prakash, D. Tripathi, A. Kumar Tiwari, A. Kumar Pandey, Melting heat transfer and irreversibility analysis in Darcy-Forchheimer flow of Casson fluid modulated by EMHD over cone and wedge surfaces, Therm. Sci. Eng. Prog. 52 (2024) 102680. https://doi.org/10.1016/j.tsep.2024.102680.

[84] S. Bilal, Asadullah, Predictive framework to evaluate ternary nanocomposite over surface subjected to novel physical perspective, Sci. Rep. 15 (2025) 8414. https://doi.org/10.1038/s41598-025-92839-3.

[85] S.R. Mishra, S. Panda, R. Baithalu, N.A. Shah, Peristaltic transport of mixed convective two-phase nanofluid with Ohmic heating used in drug delivery systems: Adomian decomposition method, Phys. Fluids 37 (2025) 22020. https://doi.org/10.1063/5.0254852.

[86] M. Dallakehnejad, S.A. Mirbozorgi, H. Niazmand, A numerical investigation of magnetic mixing in electroosmotic flows, J. Electrostat. 100 (2019) 103354. https://doi.org/10.1016/j.elstat.2019.103354.

[87] C. Bai, W. Zhou, S. Yu, T. Zheng, C. Wang, A surface acoustic wave-assisted micromixer with active temperature control, Sensors Actuators A Phys. 346 (2022) 113833. https://doi.org/10.1016/j.sna.2022.113833.

[88] M. Wu, Y. Gao, A. Ghaznavi, W. Zhao, J. Xu, AC electroosmosis micromixing on a lab-on-a-foil electric microfluidic device, Sensors Actuators B Chem. 359 (2022) 131611. https://doi.org/10.1016/j.snb.2022.131611.

[89] F.-J. Granados-Ortiz, M. Garcia-Cardosa, J. Ortega-Casanova, Effect of wall modifications in a vortex shedding-based mechanical micromixer for heat/mass exchange, Eur. J. Mech. - B/Fluids 92 (2022) 174–190. https://doi.org/10.1016/j.euromechflu.2021.12.004.

[90] Y. Wu, B. Hu, X. Ma, H. Zhang, W. Li, Y. Wang, S. Wang, Generation of droplets with adjustable chemical concentrations based on fixed potential induced-charge electro-osmosis, Lab Chip 22 (2022) 403–412. https://doi.org/10.1039/D1LC00983D.

[91] S. Saha, B. Kundu, Electroosmotic pressure-driven oscillatory flow and mass transport of Oldroyd-B fluid under high zeta potential and slippage conditions in microchannels, Colloids Surfaces A Physicochem. Eng. Asp. 647 (2022) 129070. https://doi.org/10.1016/j.colsurfa.2022.129070.

[92] Z. Li, B. Zhang, D. Dang, X. Yang, W. Yang, W. Liang, A review of microfluidic-based mixing methods, Sensors Actuators A Phys. 344 (2022) 113757. https://doi.org/10.1016/j.sna.2022.113757.

[93] G. R, V. Thangarasu, A. Vinayakaselvi M, A. Ramanathan, A critical review of recent advancements in continuous flow reactors and prominent integrated microreactors for biodiesel production, Renew. Sustain. Energy Rev. 154 (2022) 111869. https://doi.org/10.1016/j.rser.2021.111869.

[94] M. Liu, N. Li, S. Cui, G. Li, F. Yang, Biochemical Reaction Acceleration by Electrokinetic Mixing in a Microfluidic Chip, J. Phys. Chem. Lett. 13 (2022) 5633–5637. https://doi.org/10.1021/acs.jpclett.2c01308.

[95] E. Nady, G. Nagy, R. Huszánk, Improvement in mixing efficiency of microfluidic passive mixers functionalized by microstructures created with proton beam lithography, Chem. Eng. Sci. 247 (2022) 117006. https://doi.org/10.1016/j.ces.2021.117006.

[96] S. Zhao, J. Huang, J. Lei, D. Huo, Q. Huang, J. Tan, Y. Li, C. Hou, F. Tian, A portable and automatic dual-readout detector integrated with 3D-printed microfluidic nanosensors for rapid carbamate pesticides detection, Sensors Actuators B Chem. 346 (2021) 130454. https://doi.org/10.1016/j.snb.2021.130454.

[97] Y. Cheng, Y. Jiang, W. Wang, Numerical simulation for electro-osmotic mixing under three types of periodic potentials in a T-shaped micro-mixer, Chem. Eng. Process. - Process Intensif. 127 (2018) 93–102. https://doi.org/10.1016/j.cep.2018.03.017.

[98] I. Shah, S.W. Kim, K. Kim, Y.H. Doh, K.H. Choi, Experimental and numerical analysis of Y-shaped split and recombination micro-mixer with different mixing units, Chem. Eng. J. 358 (2019) 691–706. https://doi.org/10.1016/j.cej.2018.09.045.

[99] H. Hwang, B.-J. Jung, J. Park, Y. Jeong, Y. Choi, J.Y. Kang, W. Lee, Integrated Parylene-Based Thin-Film Microfluidic Device for Time-Resolved Cryo-Electron Microscopy, Adv. Funct. Mater. 35 (2025) 2418224. https://doi.org/10.1002/adfm.202418224.

[100] B. Mondal, S.K. Mehta, S. Pati, P.K. Patowari, Numerical analysis of electroosmotic mixing in a heterogeneous charged micromixer with obstacles, Chem. Eng. Process. - Process Intensif. 168 (2021) 108585. https://doi.org/10.1016/j.cep.2021.108585.

[101] A. Banerjee, A.K. Nayak, Influence of varying zeta potential on non-Newtonian flow mixing in a wavy patterned microchannel, J. Nonnewton. Fluid Mech. 269 (2019) 17–27. https://doi.org/10.1016/j.jnnfm.2019.05.007.

[102] R.B. Channon, R.F. Menger, W. Wang, D.B. Carrão, S. Vallabhuneni, A.K. Kota, C.S. Henry, Design and application of a self-pumping microfluidic staggered herringbone mixer, Microfluid. Nanofluidics 25 (2021) 31. https://doi.org/10.1007/s10404-021-02426-x.

[103] S. Rashidi, H. Bafekr, M.S. Valipour, J.A. Esfahani, A review on the application, simulation, and experiment of the electrokinetic mixers, Chem. Eng. Process. - Process Intensif. 126 (2018) 108–122. https://doi.org/10.1016/j.cep.2018.02.021.

[104] A. Qamareen, M.A. Ansari, S.S. Alam, Mixing enhancement using the aiding and opposing flow effects in curved micro channel, Chem. Eng. Process. - Process Intensif. 176 (2022) 108945. https://doi.org/10.1016/j.cep.2022.108945.

[105] S. Yuan, B. Jiang, T. Peng, M. Zhou, D. Drummer, Investigation of efficient mixing enhancement in planar micromixers with short mixing length, Chem. Eng. Process. - Process Intensif. 171 (2022) 108747. https://doi.org/10.1016/j.cep.2021.108747.

[106] S.K. Mehta, S. Pati, Enhanced Electroosmotic Mixing in a Wavy Micromixer Using Surface Charge Heterogeneity, Ind. Eng. Chem. Res. 61 (2022) 2904–2914. https://doi.org/10.1021/acs.iecr.1c04318.

[107] W. Su, Q. Li, Y. Zhang, L. Wu, Temperature jump and Knudsen layer in rarefied molecular gas, Phys. Fluids 34 (2022) 32010. https://doi.org/10.1063/5.0086076.

[108] C.-O. Ng, R. Sun, Pressure loss in channel flow resulting from a sudden change in boundary condition from no-slip to partial-slip, Phys. Fluids 29 (2017) 103603. https://doi.org/10.1063/1.4986268.

[109] S. Granick, Y. Zhu, H. Lee, Slippery questions about complex fluids flowing past solids, Nat. Mater. 2 (2003) 221–227. https://doi.org/10.1038/nmat854.

[110] J.-J. Shu, J. Bin Melvin Teo, W. Kong Chan, Fluid Velocity Slip and Temperature Jump at a Solid Surface, Appl. Mech. Rev. 69 (2017) 020801. https://doi.org/10.1115/1.4036191.

[111] J.-W. Dong, C.-Y. Huang, Integrating multiple physical properties of microchannel gas flow to extend the Navier–Stokes equations over a wide Knudsen number range, Phys. Fluids 33 (2021) 92006. https://doi.org/10.1063/5.0064756.

[112] J. Maurer, P. Tabeling, P. Joseph, H. Willaime, Second-order slip laws in microchannels for helium and nitrogen, Phys. Fluids 15 (2003) 2613–2621. https://doi.org/10.1063/1.1599355.

[113] B. Kumar, S. Jangili, Investigation of heat transfer and electrokinetic energy conversion efficiency on electromagnetohydrodynamic flow of couple stress fluid through a circular microchannel, Int. Commun. Heat Mass Transf. 155 (2024) 107381. https://doi.org/10.1016/j.icheatmasstransfer.2024.107381.

[114] P.A. Thompson, S.M. Troian, A general boundary condition for liquid flow at solid surfaces, Nature 389 (1997) 360–362. https://doi.org/10.1038/38686.

[115] J. Sanchez-Reyes, L.A. Archer, Interfacial Slip Violations in Polymer Solutions: Role of Microscale Surface Roughness, Langmuir 19 (2003) 3304–3312. https://doi.org/10.1021/la0265326.

[116] C. Neto, D.R. Evans, E. Bonaccurso, H.-J. Butt, V.S.J. Craig, Boundary slip in Newtonian liquids: a review of experimental studies, Reports Prog. Phys. 68 (2005) 2859. https://doi.org/10.1088/0034-4885/68/12/R05.

[117] G.Y. Dynnikova, General expression of aerodynamic force under different boundary conditions (slip, partial slip, no-slip), Phys. Fluids 33 (2021) 63104. https://doi.org/10.1063/5.0055304.

[118] S. Yu, T.A. Ameel, Slip-flow heat transfer in rectangular microchannels, Int. J. Heat Mass Transf. 44 (2001) 4225–4234. https://doi.org/10.1016/S0017-9310(01)00075-8.

[119] N.T.P. (Lê T.P.N. Le, Q.L. (Đặng L.Q. Dang, D.-N. (Nguyễn Đ.N. Nguyen, A. (Đặng V.Á. Van Dang, Effect of near-wall distance on velocity slip and temperature jump conditions in hypersonic rarefied gas flows, Phys. Fluids 36 (2024) 56102. https://doi.org/10.1063/5.0204025.

[120] R.G. Deissler, An analysis of second-order slip flow and temperature-jump boundary conditions for rarefied gases, Int. J. Heat Mass Transf. 7 (1964) 681–694. https://doi.org/10.1016/0017-9310(64)90161-9.

[121] Karniadakis GEM , Author, Beskok A , Author, Gad-el-Hak M , Reviewer, Micro Flows: Fundamentals and Simulation, Appl. Mech. Rev. 55 (2002) B76–B76. https://doi.org/10.1115/1.1483361.

[122] M. Gad-el-Hak, The Fluid Mechanics of Microdevices—The Freeman Scholar Lecture, J. Fluids Eng. 121 (1999) 5–33. https://doi.org/10.1115/1.2822013.

[123] K.M. Bataineh, M.A. Al-Nimr, 2D Navier–Stokes Simulations of Microscale Viscous Pump With Slip Flow, J. Fluids Eng. 131 (2009). https://doi.org/10.1115/1.3112390.

[124] B. Kundu, S. Saha, Review and Analysis of Electro-Magnetohydrodynamic Flow and Heat Transport in Microchannels, Energies 15 (2022) 7017. https://doi.org/10.3390/en15197017.

[125] T. Kumbalpuri, S. Sarkar, Thermally developing combined electroosmotic and pressure-driven flow of Phan–Thien–Tanner fluids in a microchannel, Phys. Fluids 35 (2023) 82015. https://doi.org/10.1063/5.0166296.

[126] H. Keramati, A. Sadeghi, M.H. Saidi, S. Chakraborty, Analytical solutions for thermo-fluidic transport in electroosmotic flow through rough microtubes, Int. J. Heat Mass Transf. 92 (2016) 244–251. https://doi.org/10.1016/j.ijheatmasstransfer.2015.08.089.

[127] A. Sadeghi, M.H. Saidi, Viscous dissipation effects on thermal transport characteristics of combined pressure and electroosmotically driven flow in microchannels, Int. J. Heat Mass Transf. 53 (2010) 3782–3791. https://doi.org/10.1016/j.ijheatmasstransfer.2010.04.028.

[128] J. Escandón, E. Jiménez, C. Hernández, O. Bautista, F. Méndez, Transient electroosmotic flow of Maxwell fluids in a slit microchannel with asymmetric zeta potentials, Eur. J. Mech. - B/Fluids 53 (2015) 180–189. https://doi.org/10.1016/j.euromechflu.2015.05.001.

[129] R. Chakraborty, R. Dey, S. Chakraborty, Thermal characteristics of electromagnetohydrodynamic flows in narrow channels with viscous dissipation and Joule heating under constant wall heat flux, Int. J. Heat Mass Transf. 67 (2013) 1151–1162. https://doi.org/10.1016/j.ijheatmasstransfer.2013.08.099.

[130] C. Yang, Y. Jian, Z. Xie, F. Li, Heat transfer characteristics of magnetohydrodynamic electroosmotic flow in a rectangular microchannel, Eur. J. Mech. - B/Fluids 74 (2019) 180–190. https://doi.org/10.1016/j.euromechflu.2018.11.015.

[131] Q. Liu, Y. Jian, L. Yang, Time periodic electroosmotic flow of the generalized Maxwell fluids between two micro-parallel plates, J. Nonnewton. Fluid Mech. 166 (2011) 478–486. https://doi.org/10.1016/j.jnnfm.2011.02.003.

[132] X. Wang, H. Xu, H. Qi, Transient magnetohydrodynamic flow and heat transfer of fractional Oldroyd-B fluids in a microchannel with slip boundary condition, Phys. Fluids 32 (2020) 103104. https://doi.org/10.1063/5.0025195.

[133] S. Sarkar, Streaming-potential-mediated pressure-driven transport of Phan-Thien-Tanner fluids in a microchannel, Phys. Rev. E 101 (2020) 1–23. https://doi.org/10.1103/PhysRevE.101.053104.

[134] M. Padma Devi, S. Srinivas, K. Vajravelu, Entropy generation in two-immiscible MHD flow of pulsating Casson fluid in a vertical porous space with Slip effects, J. Therm. Anal. Calorim. 149 (2024) 7449–7468. https://doi.org/10.1007/s10973-024-13337-8.

[135] Z. Xie, Y. Jian, Electrokinetic energy conversion of nanofluids in MHD-based microtube, Energy 212 (2020) 118711. https://doi.org/10.1016/j.energy.2020.118711.

[136] N.K. Ranjit, G.C. Shit, Entropy generation on electromagnetohydrodynamic flow through a porous asymmetric micro-channel, Eur. J. Mech. - B/Fluids 77 (2019) 135–147. https://doi.org/10.1016/j.euromechflu.2019.05.002.

[137] M.H. Abolbashari, N. Freidoonimehr, F. Nazari, M.M. Rashidi, Analytical modeling of entropy generation for Casson nano-fluid flow induced by a stretching surface, Adv. Powder Technol. 26 (2015) 542–552. https://doi.org/10.1016/j.apt.2015.01.003.

[138] C.Y. Soong, P.W. Hwang, J.C. Wang, Analysis of pressure-driven electrokinetic flows in hydrophobic microchannels with slip-dependent zeta potential, Microfluid. Nanofluidics 9 (2010) 211–223. https://doi.org/10.1007/s10404-009-0536-0.

[139] Z. Ding, Y. Jian, Electrokinetic oscillatory flow and energy conversion of viscoelastic fluids in microchannels: A linear analysis, J. Fluid Mech. 919 (2021) 1–31. https://doi.org/10.1017/jfm.2021.380.

[140] S. Saha, B. Kundu, Highest electro-viscous energy and lowest irreversibility analysis for Maxwell fluid in transient microchannel flow, Appl. Therm. Eng. 267 (2025) 125764. https://doi.org/10.1016/j.applthermaleng.2025.125764.

[141] J. Jiang, J. Tang, B. Al-Anzi, J. Han, Z. Li, On the validity of ion selective membrane simplification in concentration polarization, AIP Adv. 11 (2021) 35116. https://doi.org/10.1063/5.0037961.

[142] G. Sun, Y. Gou, R. Sun, L. Xing, S. Li, L. Gong, B. Al-Anzi, Z. Li, Locational enrichment of low-abundance analytes through force-environment-modulation microsystem with ion concentration polarization, Sep. Purif. Technol. 341 (2024) 126814. https://doi.org/10.1016/j.seppur.2024.126814.

[143] P. Duan, Z. Yu, K. Gao, L. Meng, Y. Han, F. Ye, Solving the multi-objective path planning problem for mobile robot using an improved NSGA-II algorithm, Swarm Evol. Comput. 87 (2024) 101576. https://doi.org/10.1016/j.swevo.2024.101576.

[144] P. Jangir, N. Jangir, A new Non-Dominated Sorting Grey Wolf Optimizer (NS-GWO) algorithm: Development and application to solve engineering designs and economic constrained emission dispatch problem with integration of wind power, Eng. Appl. Artif. Intell. 72 (2018) 449–467. https://doi.org/10.1016/j.engappai.2018.04.018.

[145] G. Wang, G. Ding, R. Liu, D. Xie, Y. Wu, X. Miao, Multi-objective optimization of a bidirectional-ribbed microchannel based on CFD and NSGA-II genetic algorithm, Int. J. Therm. Sci. 181 (2022) 107731. https://doi.org/10.1016/j.ijthermalsci.2022.107731.

[146] Z. Jiang, J. Chen, S. Xie, X. Li, H. Liu, L. Wang, C. Hong, G. Li, H. Li, K. Chen, Establishment of CFD-ANN-NSGA-II model for stirred reactor design, Chem. Eng. Sci. 311 (2025) 121614. https://doi.org/10.1016/j.ces.2025.121614.

[147] M. Goharimanesh, E. Abbasi Jannatabadi, M. Dehghani, S.M. Javadpour, Geometric and thermo hydrodynamic investigation of a 3D converging-diverging channel by Taguchi and ANFIS methods, Int. Commun. Heat Mass Transf. 138 (2022) 106285. https://doi.org/10.1016/j.icheatmasstransfer.2022.106285.

[148] K. Wu, Z. Dou, S. Deng, D. Wu, B. Zhang, H. Yang, R. Li, C. Lei, Y. Zhang, Q. Fu, G. Yu, Mechanochemistry-mediated colloidal liquid metals for electronic device cooling at kilowatt levels, Nat. Nanotechnol. 20 (2025) 104–111. https://doi.org/10.1038/s41565-024-01793-0.

[149] D. Deng, L. Zeng, W. Sun, A review on flow boiling enhancement and fabrication of enhanced microchannels of microchannel heat sinks, Int. J. Heat Mass Transf. 175 (2021) 121332. https://doi.org/10.1016/j.ijheatmasstransfer.2021.121332.

[150] D. Zhang, L. Fu, J. Guan, C. Shen, S. Tang, Investigation on the heat transfer and energy-saving performance of microchannel with cavities and extended surface, Int. J. Heat Mass Transf. 189 (2022) 122712. https://doi.org/10.1016/j.ijheatmasstransfer.2022.122712.

[151] Y.-B. Wang, H.-X. Liu, C.-X. Wang, K.-C. Yan, S.-Y. Wang, B.-X. Zhang, Z. Bo, Y.-R. Yang, X.-D. Wang, Effect of electrode arrangement on heat transfer enhancement by electrohydrodynamic conduction pumps in a rectangular channel, Appl. Therm. Eng. 259 (2025) 124884. https://doi.org/10.1016/j.applthermaleng.2024.124884.

[152] D. Das, N. Poddar, R. R. Kairi, Modulating solute transport in magnetohydrodynamic pulsatile electroosmotic micro-channel flow: Role of symmetric and asymmetric wall zeta potentials, Phys. Fluids 36 (2024) 92030. https://doi.org/10.1063/5.0223624.

[153] N.S. Bera, P. Dhar, Oscillatory electro-magneto-kinetics of confined-Stokes-second-problem micro-flows, Phys. Fluids 35 (2023) 122008. https://doi.org/10.1063/5.0174668.

[154] X. Qin, X. Wei, L. Li, H. Wang, Z. Jiang, D. Sun, Acoustic valves in microfluidic channels for droplet manipulation, Lab Chip 21 (2021) 3165–3173. https://doi.org/10.1039/D1LC00261A.

[155] S. Sarkar, S. Ganguly, P. Dutta, Thermally developing combined magnetohydrodynamic and electrokinetic transport in narrow confinements with interfacial slip, Int. J. Heat Mass Transf. 100 (2016) 451–463. https://doi.org/10.1016/j.ijheatmasstransfer.2016.04.101.

[156] G. Tang, D. Yan, C. Yang, H. Gong, C. Chai, Y. Lam, Joule heating and its effects on electrokinetic transport of solutes in rectangular microchannels, Sensors Actuators A Phys. 139 (2007) 221–232. https://doi.org/10.1016/j.sna.2007.06.002.

[157] J. Pan, X. Wang, C. Chiang, Y. Ma, J. Cheng, P. Bertani, W. Lu, L.J. Lee, Joule heating and electroosmotic flow in cellular micro/nano electroporation, Lab Chip 24 (2024) 819–831. https://doi.org/10.1039/D3LC00568B.

[158] S. Sánchez, G. Ascanio, F. Méndez, O. Bautista, Theoretical analysis of non-linear Joule heating effects on an electroosmotic flow with patterned surface charges, Phys. Fluids 30 (2018) 112002. https://doi.org/10.1063/1.5051175.

[159] H.S. Gaikwad, A. Roy, P.K. Mondal, N. Chimres, S. Wongwises, Irreversibility analysis in a slip aided electroosmotic flow through an asymmetrically heated microchannel: The effects of joule heating and the conjugate heat transfer, Anal. Chim. Acta 1045 (2019) 85–97. https://doi.org/10.1016/j.aca.2018.08.058.

[160] B. Kumar, S. Jangili, Time-periodic electroosmotic flow of non-Newtonian fluid through a polyelectrolyte-grafted circular microchannel, Phys. Fluids 37 (2025) 32043. https://doi.org/10.1063/5.0260942.

[161] A. López, G. Ibáñez, J. Pantoja, J. Moreira, O. Lastres, Entropy generation analysis of MHD nanofluid flow in a porous vertical microchannel with nonlinear thermal radiation, slip flow and convective-radiative boundary conditions, Int. J. Heat Mass Transf. 107 (2017) 982–994. https://doi.org/10.1016/j.ijheatmasstransfer.2016.10.126.

[162] S. Li, H. Zhang, J. Cheng, X. Li, W. Cai, Z. Li, F. Li, A state-of-the-art overview on the developing trend of heat transfer enhancement by single-phase flow at micro scale, Int. J. Heat Mass Transf. 143 (2019) 118476. https://doi.org/10.1016/j.ijheatmasstransfer.2019.118476.

[163] S. Colin, L. Pierre, R. Caen, Validation of a Second-Order Slip Flow Model in Rectangular Microchannels, Heat Transf. Eng. 25 (2004) 23–30. https://doi.org/10.1080/01457630490280047.

[164] Cé.A. Colin StÉphane, High-order boundary conditions for gaseous flows in rectangular microducts, Microscale Thermophys. Eng. 5 (2001) 41–54. https://doi.org/10.1080/108939501300005367.

[165] X. Huo, G. Yossifon, Tunable Electrorheological Fluid Microfluidic Rectifier: Irreversibility of Viscous Flow Due to Spatial Asymmetry Induced Memory Effects, Phys. Rev. Lett. 123 (2019) 194502. https://doi.org/10.1103/PhysRevLett.123.194502.

[166] J. Zhu, L.-H. Cai, All-aqueous printing of viscoelastic droplets in yield-stress fluids, Acta Biomater. 165 (2023) 60–71. https://doi.org/10.1016/j.actbio.2022.09.031.

[167] M. Brust, C. Schaefer, R. Doerr, L. Pan, M. Garcia, P.E. Arratia, C. Wagner, Rheology of Human Blood Plasma: Viscoelastic Versus Newtonian Behavior, Phys. Rev. Lett. 110 (2013) 78305. https://doi.org/10.1103/PhysRevLett.110.078305.

[168] E. Narimissa, M.H. Wagner, Review on tube model based constitutive equations for polydisperse linear and long-chain branched polymer melts, J. Rheol. (N. Y. N. Y). 63 (2019) 361–375. https://doi.org/10.1122/1.5064642.

[169] E.S.G. Shaqfeh, On the rheology of particle suspensions in viscoelastic fluids, AIChE J. 65 (2019) e16575. https://doi.org/10.1002/aic.16575.

[170] M. Viefhues, J. Regtmeier, D. Anselmetti, Fast and continuous-flow separation of DNA-complexes and topological DNA variants in microfluidic chip format, Analyst 138 (2013) 186–196. https://doi.org/10.1039/C2AN36056J.

[171] C. Richard, A. Renaudin, V. Aimez, P.G. Charette, An integrated hybrid interference and absorption filter for fluorescence detection in lab-on-a-chip devices, Lab Chip 9 (2009) 1371–1376. https://doi.org/10.1039/B819080A.

[172] N. Vasu, S. De, Electroosmotic flow of power-law fluids at high zeta potentials, Colloids Surfaces A Physicochem. Eng. Asp. 368 (2010) 44–52. https://doi.org/10.1016/j.colsurfa.2010.07.014.

[173] A. Haque, A.K. Nayak, B. Weigand, A. Banerjee, Time-Dependent Electroosmotic Flow with Variable Slips along Microchannel, Ind. Eng. Chem. Res. 59 (2020) 942–955. https://doi.org/10.1021/acs.iecr.9b05618.

[174] S. Nadeem, S. Ijaz, Theoretical analysis of metallic nanoparticles on blood flow through stenosed artery with permeable walls, Phys. Lett. A 379 (2015) 542–554. https://doi.org/10.1016/j.physleta.2014.12.013.

[175] T. Thumma, S.R. Mishra, M.A. Abbas, M.M. Bhatti, S.I. Abdelsalam, Three-dimensional nanofluid stirring with non-uniform heat source/sink through an elongated sheet, Appl. Math. Comput. 421 (2022) 126927. https://doi.org/10.1016/j.amc.2022.126927.

[176] S. Farooq, M.I. Khan, T. Hayat, M. Waqas, A. Alsaedi, Theoretical investigation of peristalsis transport in flow of hyperbolic tangent fluid with slip effects and chemical reaction, J. Mol. Liq. 285 (2019) 314–322. https://doi.org/10.1016/j.molliq.2019.04.051.

[177] J.P. Heller, M.S. Kuntamukkula, Critical review of the foam rheology literature, Ind. Eng. Chem. Res. 26 (1987) 318–325. https://doi.org/10.1021/ie00062a023.

[178] R. Khare, J.J. de Pablo, A. Yethiraj, Rheology of Confined Polymer Melts, Macromolecules 29 (1996) 7910–7918. https://doi.org/10.1021/ma960083x.

[179] J. Li, X. Si, B. Li, L. Cao, P. Zhang, The effects of depletion layer for electro-osmotic flow of fractional second-grade viscoelastic fluid in a micro-rectangle channel, Appl. Math. Comput. 385 (2020) 125409. https://doi.org/10.1016/j.amc.2020.125409.

[180] N.A. Shah, Y. Mahsud, M. Aziz, I. Tlili, Analytical solutions for unsteady electrohydrodynamics flows of Maxwell fluids in microchannels with circular cross section, Phys. Fluids 32 (2020) 13107. https://doi.org/10.1063/1.5128688.

[181] M. Xu, Y. Jian, Unsteady rotating electroosmotic flow with time-fractional Caputo-Fabrizio derivative, Appl. Math. Lett. 100 (2020) 106015. https://doi.org/10.1016/j.aml.2019.106015.

[182] C. Feng, X. Si, L. Cao, B. Zhu, The slip flow of generalized Maxwell fluids with time-distributed characteristics in a rotating microchannel, Appl. Math. Lett. 120 (2021) 107260. https://doi.org/10.1016/j.aml.2021.107260.

[183] E.A. Ramos, C. Treviño, J.J. Lizardi, F. Méndez, Non-isothermal effects in the slippage condition and absolute viscosity for an electroosmotic flow, Eur. J. Mech. - B/Fluids 93 (2022) 29–41. https://doi.org/10.1016/j.euromechflu.2022.01.001.

[184] A. Matías, S. Sánchez, F. Méndez, O. Bautista, Influence of slip wall effect on a non-isothermal electro-osmotic flow of a viscoelastic fluid, Int. J. Therm. Sci. 98 (2015) 352–363. https://doi.org/10.1016/j.ijthermalsci.2015.07.026.

[185] X. Wang, Y. Jiang, Y. Qiao, H. Xu, H. Qi, Numerical study of electroosmotic slip flow of fractional Oldroyd-B fluids at high zeta potentials, Electrophoresis 41 (2020) 769–777. https://doi.org/10.1002/elps.201900370.

[186] P. Liang, S. Wang, M. Zhao, Numerical study of rotating electroosmotic flow of Oldroyd-B fluid in a microchannel with slip boundary condition, Chinese J. Phys. 65 (2020) 459–471. https://doi.org/10.1016/j.cjph.2020.02.025.

[187] H. Ding, X. Zhong, B. Liu, L. Shi, T. Zhou, Y. Zhu, Mixing mechanism of a straight channel micromixer based on light-actuated oscillating electroosmosis in low-frequency sinusoidal AC electric field, Microfluid. Nanofluidics 25 (2021) 26. https://doi.org/10.1007/s10404-021-02430-1.

[188] S. Deng, T. Xiao, S. Wu, Two-layer combined electroosmotic and pressure-driven flow of power-law fluids in a circular microcapillary, Colloids Surfaces A Physicochem. Eng. Asp. 610 (2021) 125727. https://doi.org/10.1016/j.colsurfa.2020.125727.

[189] C.-Y. Lee, G.-B. Lee, L.-M. Fu, K.-H. Lee, R.-J. Yang, Electrokinetically driven active micro-mixers utilizing zeta potential variation induced by field effect, J. Micromechanics Microengineering 14 (2004) 1390–1398. https://doi.org/10.1088/0960-1317/14/10/014.

[190] G. Rojas, J. Arcos, M. Peralta, F. Méndez, O. Bautista, Pulsatile electroosmotic flow in a microcapillary with the slip boundary condition, Colloids Surfaces A Physicochem. Eng. Asp. 513 (2017) 57–65. https://doi.org/10.1016/j.colsurfa.2016.10.064.

[191] Q. Liu, Y. Jian, L. Yang, Alternating current electroosmotic flow of the Jeffreys fluids through a slit microchannel, Phys. Fluids 23 (2011) 102001. https://doi.org/10.1063/1.3640082.

[192] M. Peralta, O. Bautista, F. Méndez, E. Bautista, Pulsatile electroosmotic flow of a Maxwell fluid in a parallel flat plate microchannel with asymmetric zeta potentials, Appl. Math. Mech. 39 (2018) 667–684. https://doi.org/10.1007/s10483-018-2328-6.

[193] M. Peralta, J. Arcos, F. Méndez, O. Bautista, Mass transfer through a concentric-annulus microchannel driven by an oscillatory electroosmotic flow of a Maxwell fluid, J. Nonnewton. Fluid Mech. 279 (2020) 104281. https://doi.org/10.1016/j.jnnfm.2020.104281.

[194] Z. Wu, N.-T. Nguyen, Convective–diffusive transport in parallel lamination micromixers, Microfluid. Nanofluidics 1 (2005) 208–217. https://doi.org/10.1007/s10404-004-0011-x.

[195] S. Arulanandam, D. Li, Liquid transport in rectangular microchannels by electroosmotic pumping, Colloids Surfaces A Physicochem. Eng. Asp. 161 (2000) 89–102. https://doi.org/10.1016/S0927-7757(99)00328-3.

[196] Y. Hattori, T. Shimada, T. Yasui, N. Kaji, Y. Baba, Micro- and Nanopillar Chips for Continuous Separation of Extracellular Vesicles, Anal. Chem. 91 (2019) 6514–6521. https://doi.org/10.1021/acs.analchem.8b05538.

[197] P. Gascoyne, J. Satayavivad, M. Ruchirawat, Microfluidic approaches to malaria detection, Acta Trop. 89 (2004) 357–369. https://doi.org/10.1016/j.actatropica.2003.11.009.

[198] A.M. Thomas, R. Narayanan, Physics of oscillatory flow and its effect on the mass transfer and separation of species, Phys. Fluids 13 (2001) 859–866. https://doi.org/10.1063/1.1351549.

[199] H.-F. Huang, C.-L. Lai, Enhancement of mass transport and separation of species by oscillatory electroosmotic flows, Proc. R. Soc. A Math. Phys. Eng. Sci. 462 (2006) 2017–2038. https://doi.org/10.1098/rspa.2006.1668.

[200] H.-F. Li, J.-M. Lin, Applications of microfluidic systems in environmental analysis, Anal. Bioanal. Chem. 393 (2009) 555–567. https://doi.org/10.1007/s00216-008-2439-4.

[201] M. N. Kashid, A. Renken, L. Kiwi-Minsker, Influence of Flow Regime on Mass Transfer in Different Types of Microchannels, Ind. Eng. Chem. Res. 50 (2011) 6906–6914. https://doi.org/10.1021/ie102200j.

[202] S. Bera, S. Bhattacharyya, On mixed electroosmotic-pressure driven flow and mass transport in microchannels, Int. J. Eng. Sci. 62 (2013) 165–176. https://doi.org/10.1016/j.ijengsci.2012.09.006.

[203] G.I. Taylor, Dispersion of soluble matter in solvent flowing slowly through a tube, Proc. R. Soc. London. Ser. A. Math. Phys. Sci. 219 (1997) 186–203. https://doi.org/10.1098/rspa.1953.0139.

[204] R. Aris, G.I. Taylor, On the dispersion of a solute in a fluid flowing through a tube, Proc. R. Soc. London. Ser. A. Math. Phys. Sci. 235 (1997) 67–77. https://doi.org/10.1098/rspa.1956.0065.

[205] G. Ramon, Y. Agnon, C. Dosoretz, Solute dispersion in oscillating electro-osmotic flow with boundary mass exchange, Microfluid. Nanofluidics 10 (2011) 97–106. https://doi.org/10.1007/s10404-010-0650-z.

[206] J.C. Arcos, F. Méndez, E.G. Bautista, O. Bautista, Dispersion coefficient in an electro-osmotic flow of a viscoelastic fluid through a microchannel with a slowly varying wall zeta potential, J. Fluid Mech. 839 (2018) 348–386. https://doi:10.1017/jfm.2018.11.

[207] R. Baños, J. Arcos, O. Bautista, F. Méndez, Steric and Slippage Effects on Mass Transport by Using an Oscillatory Electroosmotic Flow of Power-Law Fluids, Micromachines 12 (2021) 539. https://doi.org/10.3390/mi12050539.

[208] R.D. Baños, J.C. Arcos, O. Bautista, F. Méndez, E.A. Merchán-Cruz, Mass transport by an oscillatory electroosmotic flow of power-law fluids in hydrophobic slit microchannels, J. Brazilian Soc. Mech. Sci. Eng. 43 (2021) 9. https://doi.org/10.1007/s40430-020-02746-z.

[209] P.C. Chatwin, On the longitudinal dispersion of passive contaminant in oscillatory flows in tubes, J. Fluid Mech. 71 (1975) 513–527. https://doi:10.1017/S0022112075002716.

[210] E.J. Watson, Diffusion in oscillatory pipe flow, J. Fluid Mech. 133 (1983) 233–244. https://doi:10.1017/S0022112083001883

[211] U.H. Kurzweg, M.J. Jaeger, Diffusional separation of gases by sinusoidal oscillations, Phys. Fluids 30 (1987) 1023–1025. https://doi.org/10.1063/1.866300.

[212] U.H. Kurzweg, Enhanced Diffusional Separation in Liquids by Sinusoidal Oscillations, Sep. Sci. Technol. 23 (1988) 105–117. https://doi.org/10.1080/01496398808057637.

[213] C. Teodoro, O. Bautista, F. Méndez, Mass transport and separation of species in an oscillating electro-osmotic flow caused by distinct periodic electric fields, Phys. Scr. 94 (2019) 115012. https://doi.org/10.1088/1402-4896/ab2a9a.

[214] I. Medina, M. Toledo, F. Méndez, O. Bautista, Pulsatile electroosmotic flow in a microchannel with asymmetric wall zeta potentials and its effect on mass transport enhancement and mixing, Chem. Eng. Sci. 184 (2018) 259–272. https://doi.org/10.1016/j.ces.2018.03.051.

[215] J. Muñoz, J. Arcos, O. Bautista, F. Méndez, Slippage effect on the dispersion coefficient of a passive solute in a pulsatile electro-osmotic flow in a microcapillary, Phys. Rev. Fluids 3 (2018) 84503. https://doi.org/10.1103/PhysRevFluids.3.084503.

[216] G. Mederos, J. Arcos, O. Bautista, F. Méndez, Hydrodynamics rheological impact of an oscillatory electroosmotic flow on a mass transfer process in a microcapillary with a reversible wall reaction, Phys. Fluids 32 (2020) 122003. https://doi.org/10.1063/5.0027818.

[217] V. Hoshyargar, M. Talebi, S.N. Ashrafizadeh, A. Sadeghi, Hydrodynamic dispersion by electroosmotic flow of viscoelastic fluids within a slit microchannel, Microfluid. Nanofluidics 22 (2017) 4. https://doi.org/10.1007/s10404-017-2021-5.

[218] M.S. Sotoudegan, O. Mohd, F.S. Ligler, G.M. Walker, Paper-based passive pumps to generate controllable whole blood flow through microfluidic devices, Lab Chip 19 (2019) 3787–3795. https://doi.org/10.1039/C9LC00822E

[219] N. Pamme, Magnetism and microfluidics, Lab Chip 6 (2006) 24–38. https://doi.org/10.1039/B513005K.

[220] G. Zhao, Y. Jian, F. Li, Streaming potential and heat transfer of nanofluids in microchannels in the presence of magnetic field, J. Magn. Magn. Mater. 407 (2016) 75–82. https://doi.org/10.1016/j.jmmm.2016.01.025.

[221] X. Gao, G. Zhao, N. Li, J. Zhang, Y. Jian, The electrokinetic energy conversion analysis of viscoelastic fluid under the periodic pressure in microtubes, Colloids Surfaces A Physicochem. Eng. Asp. 646 (2022) 128976. https://doi.org/10.1016/j.colsurfa.2022.128976.

[222] C.-O. Ng, Combined pressure-driven and electroosmotic flow of Casson fluid through a slit microchannel, J. Nonnewton. Fluid Mech. 198 (2013) 1–9. https://doi.org/10.1016/j.jnnfm.2013.03.003.

[223] N.K. Ranjit, G.C. Shit, D. Tripathi, Electrothermal analysis in two-layered couple stress fluid flow in an asymmetric microchannel via peristaltic pumping, J. Therm. Anal. Calorim. 144 (2021) 1325–1342. https://doi.org/10.1007/s10973-020-10380-z.

[224] V. Kumar, J. Mukherjee, S.K. Sinha, U. Ghosh, Combined electromechanically driven pulsating flow of nonlinear viscoelastic fluids in narrow confinements, J. R. Soc. Interface 19 (2022) 20210876. https://doi.org/10.1098/rsif.2021.0876.

[225] N. Casson, Flow Equation for Pigment-oil Suspensions of the Printing Ink-type, Rheol. Disperse Syst. (1959) 84–104. https://cir.nii.ac.jp/crid/1571980076287959296.

[226] C.-O. Ng, C. Qi, Electroosmotic flow of a viscoplastic material through a slit channel with walls of arbitrary zeta potential, Phys. Fluids 25 (2013) 103102. https://doi.org/10.1063/1.4825368.

[227] S. Saleem, S. Akhtar, S. Nadeem, A. Saleem, M. Ghalambaz, A. Issakhov, Mathematical study of Electroosmotically driven peristaltic flow of Casson fluid inside a tube having systematically contracting and relaxing sinusoidal heated walls, Chinese J. Phys. 71 (2021) 300–311. https://doi.org/10.1016/j.cjph.2021.02.015.

[228] N. Bag, S. Bhattacharyya, Electroosmotic flow of a non-Newtonian fluid in a microchannel with heterogeneous surface potential, J. Nonnewton. Fluid Mech. 259 (2018) 48–60. https://doi.org/10.1016/j.jnnfm.2018.05.005.

[229] C. Qi, C.-O. Ng, Rotating electroosmotic flow of viscoplastic material between two parallel plates, Colloids Surfaces A Physicochem. Eng. Asp. 513 (2017) 355–366. https://doi.org/10.1016/j.colsurfa.2016.10.066.

[230] V. Rajaram, B. Varadharaj, P. Jayavel, Impact of electroosmotic flow on a Casson fluid driven by chemical reaction and convective boundary conditions, Heat Transf. 50 (2021) 4993–5019. https://doi.org/10.1002/htj.22113.

[231] V.K. Stokes, Couple Stresses in Fluids BT - Theories of Fluids with Microstructure: An Introduction, in: V.K. Stokes (Ed.), Springer Berlin Heidelberg, Berlin, Heidelberg, 1984: pp. 34–80. https://doi.org/10.1007/978-3-642-82351-0_4.

[232] T. Siva, B. Kumbhakar, S. Jangili, P.K. Mondal, Unsteady electro-osmotic flow of couple stress fluid in a rotating microchannel: An analytical solution, Phys. Fluids 32 (2020) 102013. https://doi.org/10.1063/5.0023747.

[233] V. Sridhar, K. Ramesh, D. Tripathi, V. Vivekanand, Analysis of thermal radiation, Joule heating, and viscous dissipation effects on blood-gold couple stress nanofluid flow driven by electroosmosis, Heat Transf. 51 (2022) 4080–4101. https://doi.org/10.1002/htj.22490.

[234] Z. Ding, Y. Jian, L. Wang, L. Yang, Analytical investigation of electrokinetic effects of micropolar fluids in nanofluidic channels, Phys. Fluids 29 (2017) 82008. https://doi.org/10.1063/1.4999487.

[235] F.H.J. van der Heyden, D.J. Bonthuis, D. Stein, C. Meyer, C. Dekker, Electrokinetic Energy Conversion Efficiency in Nanofluidic Channels, Nano Lett. 6 (2006) 2232–2237. https://doi.org/10.1021/nl061524l.

[236] X. Chen, Y. Jian, Z. Xie, Electrokinetic flow of fluids with pressure-dependent viscosity in a nanotube, Phys. Fluids 33 (2021) 122002. https://doi.org/10.1063/5.0070938.

[237] X. Gao, G. Zhao, N. Li, Y. Zhang, Y. Jian, The electrokinetic energy conversion analysis of Newtonian fluids with pressure-dependent viscosity in rectangular nanotube, J. Mol. Liq. 371 (2023) 121022. https://doi.org/10.1016/j.molliq.2022.121022.

[238] X. Chen, Y.J. Jian, Streaming potential analysis on the hydrodynamic transport of pressure-driven flow through a rotational microchannel, Chinese J. Phys. 56 (2018) 1296–1307. https://doi.org/10.1016/j.cjph.2018.03.001.

[239] Y. Jian, F. Li, Y. Liu, L. Chang, Q. Liu, L. Yang, Electrokinetic energy conversion efficiency of viscoelastic fluids in a polyelectrolyte-grafted nanochannel, Colloids Surfaces B Biointerfaces 156 (2017) 405–413. https://doi.org/10.1016/j.colsurfb.2017.05.039.

[240] X. Chen, Y. Jian, Z. Xie, Slippery electrokinetic flow of viscoelastic fluids with pressure-dependent viscosity and relaxation time, Colloids Surfaces A Physicochem. Eng. Asp. 639 (2022) 128354. https://doi.org/10.1016/j.colsurfa.2022.128354.

[241] Z. Xie, Electrokinetic energy conversion of core-annular flow in a slippery nanotube, Colloids Surfaces A Physicochem. Eng. Asp. 642 (2022) 128723. https://doi.org/10.1016/j.colsurfa.2022.128723.

[242] S. Chanda, S. Sinha, S. Das, Streaming potential and electroviscous effects in soft nanochannels: towards designing more efficient nanofluidic electrochemomechanical energy converters, Soft Matter 10 (2014) 7558–7568. https://doi.org/10.1039/C4SM01490A.

[243] X. Chen, Y. Jian, Z. Xie, Z. Ding, Thermal transport of electromagnetohydrodynamic in a microtube with electrokinetic effect and interfacial slip, Colloids Surfaces A Physicochem. Eng. Asp. 540 (2018) 194–206. https://doi.org/10.1016/j.colsurfa.2017.12.061.

[244] G. Zhao, Y. Jian, F. Li, Streaming potential and heat transfer of nanofluids in parallel plate microchannels, Colloids Surfaces A Physicochem. Eng. Asp. 498 (2016) 239–247. https://doi.org/10.1016/j.colsurfa.2016.03.053.

[245] P. V Satya Narayana, N. Tarakaramu, G. Sarojamma, I.L. Animasaun, Numerical Simulation of Nonlinear Thermal Radiation on the 3D Flow of a Couple Stress Casson Nanofluid Due to a Stretching Sheet, J. Therm. Sci. Eng. Appl. 13 (2021) 021028. https://doi.org/10.1115/1.4049425.

[246] S. Najjaran, S. Rashidi, M.S. Valipour, An entropy production analysis for electroosmotic flow and convective heat transfer: a numerical investigation, J. Therm. Anal. Calorim. 145 (2021) 1877–1889. https://doi.org/10.1007/s10973-021-10691-9.

[247] A. Bejan, Entropy generation minimization: The new thermodynamics of finite-size devices and finite-time processes, J. Appl. Phys. 79 (1996) 1191–1218. https://doi.org/10.1063/1.362674.

[248] J. Escandón, O. Bautista, F. Méndez, Entropy generation in purely electroosmotic flows of non-Newtonian fluids in a microchannel, Energy 55 (2013) 486–496. https://doi.org/10.1016/j.energy.2013.04.030.

[249] Z.-Y. Xie, Y.-J. Jian, Entropy generation of two-layer magnetohydrodynamic electroosmotic flow through microparallel channels, Energy 139 (2017) 1080–1093. https://doi.org/10.1016/j.energy.2017.08.038.

[250] Z. Xie, Y. Jian, Entropy generation of magnetohydrodynamic electroosmotic flow in two-layer systems with a layer of non-conducting viscoelastic fluid, Int. J. Heat Mass Transf. 127 (2018) 600–615. https://doi.org/10.1016/j.ijheatmasstransfer.2018.07.065.

[251] G. Ibáñez, A. López, J. Pantoja, J. Moreira, J.A. Reyes, Optimum slip flow based on the minimization of entropy generation in parallel plate microchannels, Energy 50 (2013) 143–149. https://doi.org/10.1016/j.energy.2012.11.036.

[252] S. Zare Harofte, M. Soltani, S. Siavashy, K. Raahemifar, Recent Advances of Utilizing Artificial Intelligence in Lab on a Chip for Diagnosis and Treatment, Small 18 (2022) 1–29. https://doi.org/10.1002/smll.202203169.

[253] R. Riahi, A. Tamayol, S.A.M. Shaegh, A.M. Ghaemmaghami, M.R. Dokmeci, A. Khademshosseini, Microfluidics for advanced drug delivery systems, Curr. Opin. Chem. Eng. 7 (2015) 101–112. https://doi.org/10.1016/j.coche.2014.12.001.

[254] T. Hayat, S.B. Khan, M. Khan, The influence of Hall current on the rotating oscillating flows of an Oldroyd-B fluid in a porous medium, Nonlinear Dyn. 47 (2007) 353–362. https://doi.org/10.1007/s11071-006-9034-z.

[255] C. Sanchez, D. El Hajj Diab, V. Connord, P. Clerc, E. Meunier, B. Pipy, B. Payré, R.P. Tan, M. Gougeon, J. Carrey, V. Gigoux, D. Fourmy, Targeting a G-protein-coupled receptor overexpressed in endocrine tumors by magnetic nanoparticles to induce cell death, ACS Nano 8 (2014) 1350–1363. https://doi.org/10.1021/nn404954s.

[256] X. Li, S. Liu, P. Fan, C.F. Werner, K. Miyamoto, T. Yoshinobu, A bubble-assisted electroosmotic micropump for a delivery of a droplet in a microfluidic channel combined with a light-addressable potentiometric sensor, Sensors Actuators B Chem. 248 (2017) 993–997. https://doi.org/10.1016/j.snb.2017.02.165.

[257] S. Wang, Y. Xie, S. Niu, L. Lin, Z.L. Wang, Freestanding Triboelectric-Layer-Based Nanogenerators for Harvesting Energy from a Moving Object or Human Motion in Contact and Non-contact Modes, Adv. Mater. 26 (2014) 2818–2824. https://doi.org/10.1002/adma.201305303.

[258] L. Joly, C. Ybert, E. Trizac, L. Bocquet, Hydrodynamics within the Electric Double Layer on Slipping Surfaces, Phys. Rev. Lett. 93 (2004) 257805. https://doi.org/10.1103/PhysRevLett.93.257805.

[259] H. Chen, Z. Yu, S. Bai, H. Lu, D. Xu, C. Chen, D. Liu, Y. Zhu, Microfluidic models of physiological or pathological flow shear stress for cell biology, disease modeling and drug development, TrAC - Trends Anal. Chem. 117 (2019) 186–199. https://doi.org/10.1016/j.trac.2019.06.023.

[260] B. Gollapelli, A.K. Tatipamula, S. Dewanjee, R.S. Pathinti, J. Vallamkondu, Detection of bile acids using optical biosensors based on cholesteric liquid crystal droplets, J. Mater. Chem. C 9 (2021) 13991–14002. https://doi.org/10.1039/d1tc02801d.

[261] R.A. Mahdi, H.A. Mohammed, K.M. Munisamy, N.H. Saeid, Review of convection heat transfer and fluid flow in porous media with nanofluid, Renew. Sustain. Energy Rev. 41 (2015) 715–734. https://doi.org/10.1016/j.rser.2014.08.040.

[262] S. Gajbhiye, A. Warke, R. Katta, Heat transfer and fluid flow analysis of non-Newtonian fluid in a microchannel with electromagnetohydrodynamics and thermal radiation, Heat Transf. 51 (2022) 1601–1621. https://doi.org/10.1002/htj.22366.

[263] R.K. Lodhi, K. Ramesh, Comparative study on electroosmosis modulated flow of MHD viscoelastic fluid in the presence of modified Darcy's law, Chinese J. Phys. 68 (2020) 106–120. https://doi.org/10.1016/j.cjph.2020.09.005.

[264] J. Bae, M.S. Kim, T. Oh, B.L. Suh, T.G. Yun, S. Lee, K. Hur, Y. Gogotsi, C.M. Koo, I.D. Kim, Towards Watt-scale hydroelectric energy harvesting by Ti3C2TX-based transpiration-driven electrokinetic power generators, Energy Environ. Sci. 15 (2022) 123–135. https://doi.org/10.1039/d1ee00859e.

[265] N. Sezer, M. Koç, A comprehensive review on the state-of-the-art of piezoelectric energy harvesting, Nano Energy 80 (2021) 105567. https://doi.org/10.1016/j.nanoen.2020.105567.

[266] J. Zhang, K. Zhan, S. Wang, X. Hou, Soft interface design for electrokinetic energy conversion, Soft Matter 16 (2020) 2915–2927. https://doi.org/10.1039/c9sm02506e.

[267] W. Olthuis, B. Schippers, J. Eijkel, A. Van Den Berg, Energy from streaming current and potential, Sensors Actuators, B Chem. 111–112 (2005) 385–389. https://doi.org/10.1016/j.snb.2005.03.039.

[268] Y. Ren, D. Stein, Slip-enhanced electrokinetic energy conversion in nanofluidic channels, Nanotechnology 19 (2008) 195707. https://doi.org/10.1088/0957-4484/19/19/195707.

[269] C.L.A. Berli, Electrokinetic energy conversion in microchannels using polymer solutions, J. Colloid Interface Sci. 349 (2010) 446–448. https://doi.org/10.1016/j.jcis.2010.05.083.

[270] Y. Xie, D. Bos, L.J. De Vreede, H.L. De Boer, M.J. Van Der Meulen, M. Versluis, A.J. Sprenkels, A. Van Den Berg, J.C.T. Eijkel, High-efficiency ballistic electrostatic generator using microdroplets, Nat. Commun. 5 (2014) 1–5. https://doi.org/10.1038/ncomms4575.

[271] Y. Liu, Y. Jian, C. Yang, Steric-effect-induced enhancement of electrokinetic energy conversion efficiency in curved nanochannels with rectangular sections at high zeta potentials, Colloids Surfaces A Physicochem. Eng. Asp. 591 (2020) 124558. https://doi.org/10.1016/j.colsurfa.2020.124558.

[272] P. Soleymani, Y. Ma, E. Saffarifard, R. Mohebbi, M. Babaie, N. Karimi, S. Saedodin, Numerical investigation on turbulent flow, heat transfer, and entropy generation of water-based magnetic nanofluid flow in a tube with hemisphere porous under a uniform magnetic field, Int. Commun. Heat Mass Transf. 137 (2022) 106308. https://doi.org/10.1016/j.icheatmasstransfer.2022.106308.

[273] D. Dewanjee, B. Kundu, A review of applications of green nanofluids for performance improvement of solar collectors, Renew. Energy 240 (2025) 122182. https://doi.org/10.1016/j.renene.2024.122182.

[274] A.Y. Sayed, S.I. Ahmed, K.S. Mekheimer, M.S. Abdel-wahed, Electromagnetohydrodynamic effects with single-walled carbon nanotubes particles in a corrugated microchannel, Chaos, Solitons and Fractals 168 (2023) 113126. https://doi.org/10.1016/j.chaos.2023.113126.

[275] Y. Liu, J. Xing, Y. Jian, Heat transfer and entropy generation analysis of electroosmotic flows in curved rectangular nanochannels considering the influence of steric effects, Int. Commun. Heat Mass Transf. 139 (2022) 106501. https://doi.org/10.1016/j.icheatmasstransfer.2022.106501.

[276] T. Siva, S. Jangili, B. Kumbhakar, Entropy generation on EMHD transport of couple stress fluid with slip-dependent zeta potential under electrokinetic effects, Int. J. Therm. Sci. 191 (2023) 108339. https://doi.org/10.1016/j.ijthermalsci.2023.108339.

[277] S. Pabi, S.K. Mehta, S. Pati, Analysis of thermal transport and entropy generation characteristics for electroosmotic flow through a hydrophobic microchannel considering viscoelectric effect, Int. Commun. Heat Mass Transf. 127 (2021) 105519. https://doi.org/10.1016/j.icheatmasstransfer.2021.105519.

[278] Q. Zhao, H. Xu, L. Tao, Nanofluid flow and heat transfer in a microchannel with interfacial electrokinetic effects, Int. J. Heat Mass Transf. 124 (2018) 158–167. https://doi.org/10.1016/j.ijheatmasstransfer.2018.03.043.

[279] D.K. Tan, Y. Liu, Combined effects of streaming potential and wall slip on flow and heat transfer in microchannels, Int. Commun. Heat Mass Transf. 53 (2014) 39–42. https://doi.org/10.1016/j.icheatmasstransfer.2014.02.009.

[280] G. Zhao, Y. Jian, F. Li, Heat transfer of nanofluids in microtubes under the effects of streaming potential, Appl. Therm. Eng. 100 (2016) 1299–1307. https://doi.org/10.1016/j.applthermaleng.2016.02.101.

[281] B. Mallick, Thermofluidic characteristics of electrokinetic flow in a rotating microchannel in presence of ion slip and Hall currents, Int. Commun. Heat Mass Transf. 126 (2021) 105350. https://doi.org/10.1016/j.icheatmasstransfer.2021.105350.

[282] G. Zhao, Z. Wang, Y. Jian, Heat transfer of the MHD nanofluid in porous microtubes under the electrokinetic effects, Int. J. Heat Mass Transf. 130 (2019) 821–830. https://doi.org/10.1016/j.ijheatmasstransfer.2018.11.007.

[283] J. Wang, F. Li, Electroosmotic flow and heat transfer through a polyelectrolyte-grafted microchannel with modulated charged surfaces, Int. J. Heat Mass Transf. 216 (2023) 124545. https://doi.org/10.1016/j.ijheatmasstransfer.2023.124545.

[284] J. Zhang, G. Zhao, X. Gao, N. Li, Y. Jian, Streaming potential and electrokinetic energy conversion of nanofluids in a parallel plate microchannel under the time-periodic excitation, Chinese J. Phys. 75 (2022) 55–68. https://doi.org/10.1016/j.cjph.2021.10.029.

[285] Y. Jian, Transient MHD heat transfer and entropy generation in a microparallel channel combined with pressure and electroosmotic effects, Int. J. Heat t Transf. 89 (2015) 193–205. https://doi.org/10.1016/j.ijheatmasstransfer.2015.05.045.

[286] J.P. Escandón, D.A. Torres, C.G. Hernández, J.R. Gómez, R.O. Vargas, Transient Analysis of the Electro-Osmotic Flow of Multilayer Immiscible Maxwell Fluids in an Annular Microchannel, Colloids and Interfaces 6 (2022) 60. https://doi.org/10.3390/colloids6040060.

[287] S. Wang, M. Zhao, Analytical solution of the transient electro-osmotic flow of a generalized fractional Maxwell fluid in a straight pipe with a circular cross-section, Eur. J. Mech. - B/Fluids 54 (2015) 82–86. https://doi.org/10.1016/j.euromechflu.2015.06.016.

[288] S. Zeng, B. Li, X. Su, J. Qin, B. Lin, Microvalve-actuated precise control of individual droplets in microfluidic devices, Lab Chip 9 (2009) 1340–1343. https://doi.org/10.1039/B821803J.

[289] K.A. Heyries, M.G. Loughran, D. Hoffmann, A. Homsy, L.J. Blum, C.A. Marquette, Microfluidic biochip for chemiluminescent detection of allergen-specific antibodies, Biosens. Bioelectron. 23 (2008) 1812–1818. https://doi.org/10.1016/j.bios.2008.02.025.

[290] C. Zhou, H. Zhang, Z. Li, W. Wang, Chemistry pumps: a review of chemically powered micropumps, Lab Chip 16 (2016) 1797–1811. https://doi.org/10.1039/C6LC00032K.

[291] R. Pol, F. Céspedes, D. Gabriel, M. Baeza, Microfluidic lab-on-a-chip platforms for environmental monitoring, TrAC Trends Anal. Chem. 95 (2017) 62–68. https://doi.org/10.1016/j.trac.2017.08.001.

[292] M.A.P. Mahmud, S.R. Bazaz, S. Dabiri, A.A. Mehrizi, M. Asadnia, M.E. Warkiani, Z.L. Wang, Advances in MEMS and Microfluidics-Based Energy Harvesting Technologies, Adv. Mater. Technol. 7 (2022) 2101347. https://doi.org/10.1002/admt.202101347.

[293] N. Pamme, Continuous flow separations in microfluidic devices, Lab Chip 7 (2007) 1644–1659. https://doi.org/10.1039/B712784G.

[294] E.K. Sackmann, A.L. Fulton, D.J. Beebe, The present and future role of microfluidics in biomedical research, Nature 507 (2014) 181–189. https://doi.org/10.1038/nature13118.

[295] P. Goswami, S. De, P.P. Gopmandal, Streaming Potential and Associated Electrokinetic Effects through a Channel Filled with Electrolyte Solution Surrounded by a Layer of Immiscible and Dielectric Liquid, Langmuir 40 (2024) 11695–11712. https://doi.org/10.1021/acs.langmuir.4c01082.

[296] W. Guo, L. Cao, J. Xia, F.-Q. Nie, W. Ma, J. Xue, Y. Song, D. Zhu, Y. Wang, L. Jiang, Energy harvesting with single-ion-selective nanopores: a concentration-gradient-driven nanofluidic power source, Adv. Funct. Mater. 20 (2010) 1339-1344. https://doi.org/10.1002/adfm.200902312.

[297] Z. Xie, X. Chen, F. Tan, Electrokinetic flow and energy conversion induced by streaming potential in nanochannels with symmetric corrugated walls, Phys. Fluids 36 (2024) 92016. https://doi.org/10.1063/5.0226494.

[298] I. Klapper, C.J. Rupp, R. Cargo, B. Purvedorj, P. Stoodley, Viscoelastic fluid description of bacterial biofilm material properties, Biotechnol. Bioeng. 80 (2002) 289–296. https://doi.org/https://doi.org/10.1002/bit.10376.

[299] P. Suly, J. Sevcik, D.J. Dmonte, P. Urbanek, I. Kuritka, Inkjet Printability Assessment of Weakly Viscoelastic Fluid: A Semidilute Polyvinylpyrrolidone Solution Ink Case Study, Langmuir 37 (2021) 8557–8568. https://doi.org/10.1021/acs.langmuir.1c01010.

[300] Y. Matsuoka, Y. Nakayama, T. Kajiwara, Effects of viscoelasticity on shear-thickening in dilute suspensions in a viscoelastic fluid, Soft Matter 16 (2020) 728–737. https://doi.org/10.1039/C9SM01736D.

[301] L. Gong, J. Wu, L. Wang, K. Cao, Streaming potential and electroviscous effects in periodical pressure-driven microchannel flow, Phys. Fluids 20 (2008) 063603. https://doi.org/10.1063/1.2939391.

[302] M. Buren, Y. Jian, Y. Zhao, L. Chang, Electroviscous effect and electrokinetic energy conversion in time periodic pressure-driven flow through a parallel-plate nanochannel with surface charge-dependent slip, J. Phys. D Appl. Phys. 51 (2018) 205601. https://doi.org/10.1088/1361-6463/aabc73.

[303] Y. Liu, Y. Jian, Electroviscous effect on electromagnetohydrodynamic flows of Maxwell fluids in parallel plate microchannels, Appl. Math. Mech. 40 (2019) 1457–1470. https://doi.org/10.1007/s10483-019-2526-9.

[304] Q. Luo, A. He, S. Xu, M. Miao, T. Liu, B. Cao, K. Shan, B. Tang, X. Hu, L. Huang, H. Jiang, Utilization of low-grade heat for desalination and electricity generation through thermal osmosis energy conversion process, Chem. Eng. J. 452 (2023) 139560. https://doi.org/10.1016/j.cej.2022.139560.

[305] Z. Xie, Y. Jian, X. Chen, Electrokinetic energy conversion of high pressure-driven flow with pressure-viscosity effect at high zeta potential, Int. J. Eng. Sci. 184 (2023) 103819. https://doi.org/10.1016/j.ijengsci.2023.103819.

[306] C. Li, Z. Li, T. Rui, Z. Liu, X. Zhang, Thermally-driven electrokinetic power generation system utilizing microporous NiO wicks and nanoporous AAO membranes for low-grade heat harvesting, Chem. Eng. J. 496 (2024) 154276. https://doi.org/10.1016/j.cej.2024.154276.

[307] Z. Liu, Y. Feng, L. Wang, Q. Liu, G. Liu, Electrokinetic energy conversion in the nanochannel coupled with surface charge and slip effects, Int. J. Heat Mass Transf. 204 (2023) 123874. https://doi.org/10.1016/j.ijheatmasstransfer.2023.123874.

[308] D. Gillespie, High Energy Conversion Efficiency in Nanofluidic Channels, Nano Lett. 12 (2012) 1410–1416. https://doi.org/10.1021/nl204087f.

[309] R. Qiao, C. Fu, H. Forgham, I. Javed, X. Huang, J. Zhu, A.K. Whittaker, T.P. Davis, Magnetic iron oxide nanoparticles for brain imaging and drug delivery, Adv. Drug Deliv. Rev. 197 (2023) 114822. https://doi.org/10.1016/j.addr.2023.114822.

[310] M. Habibi Matin, Electroviscous effects on thermal transport of electrolytes in pressure driven flow through nanoslit, Int. J. Heat Mass Transf. 106 (2017) 473–481. https://doi.org/10.1016/j.ijheatmasstransfer.2016.08.100.

[311] K. Govindarajulu, A. Subramanyam Reddy, Magnetohydrodynamic pulsatile flow of third grade hybrid nanofluid in a porous channel with Ohmic heating and thermal radiation effects, Phys. Fluids 34 (2022) 13105. https://doi.org/10.1063/5.0074894.

[312] K. Guedri, A. Khan, T. Gul, S. Mukhtar, W. Alghamdi, M.F. Yassen, E. Tag Eldin, Thermally Dissipative Flow and Entropy Analysis for Electromagnetic Trihybrid Nanofluid Flow Past a Stretching Surface, ACS Omega 7 (2022) 33432–33442. https://doi.org/10.1021/acsomega.2c04047.

[313] M. Bahiraei, S. Heshmatian, Electronics cooling with nanofluids: A critical review, Energy Convers. Manag. 172 (2018) 438–456. https://doi.org/10.1016/j.enconman.2018.07.047.

[314] A. Bejan, Second-Law Analysis in Heat Transfer and Thermal Design, in: J.P. Hartnett, T.F.B.T.-A. in H.T. Irvine (Eds.), Elsevier, 1982: pp. 1–58. https://doi.org/10.1016/S0065-2717(08)70172-2.

[315] M. Mieczkowski, P. Furmański, P. Łapka, Optimization of a microchannel heat sink using entropy minimization and genetic aggregation algorithm, Appl. Therm. Eng. 191 (2021) 116840. https://doi.org/10.1016/j.applthermaleng.2021.116840.

[316] C. Feng, B. Li, X. Si, W. Wang, J. Zhu, The electro-osmotic flow and heat transfer of generalized Maxwell fluids with distributed-order time-fractional characteristics in microtubules under an alternating field, Phys. Fluids 33 (2021) 113105. https://doi.org/10.1063/5.0073752.

[317] X. Yang, M. Zhao, S. Wang, Y. Xiao, Electro-osmotic flow of Maxwell fluid induced by an alternating electric field in curved rectangular microchannels, Phys. Fluids 35 (2023) 53106. https://doi.org/10.1063/5.0149681.

[318] H. Li, Y. Jian, Dispersion for periodic electro-osmotic flow of Maxwell fluid through a microtube, Int. J. Heat Mass Transf. 115 (2017) 703–713. https://doi.org/10.1016/j.ijheatmasstransfer.2017.07.065.

[319] S. Ghosal, Z. Chen, Nonlinear Waves in Capillary Electrophoresis, Bull. Math. Biol. 72 (2010) 2047–2066. https://doi.org/10.1007/s11538-010-9527-2.

[320] D. Banerjee, S. Pati, P. Biswas, Analysis of electroviscous effect and heat transfer for flow of non-Newtonian fluids in a microchannel with surface charge-dependent slip at high zeta potentials, Phys. Fluids 34 (2022) 112016. https://doi.org/10.1063/5.0123964.

[321] S. Ahmed, H. Xu, Forced convection with unsteady pulsating flow of a hybrid nanofluid in a microchannel in the presence of EDL, magnetic and thermal radiation effects, Int. Commun. Heat Mass Transf. 120 (2021) 105042. https://doi.org/10.1016/j.icheatmasstransfer.2020.105042.

[322] F. Vazquez, M.A. Olivares-Robles, S. Medina, Size Effects on the Entropy Production in Oscillatory Flow between Parallel Plates, Entropy 13 (2011) 542–553. https://doi.org/10.3390/e13020542.

[323] V.G. Gude, Desalination and water reuse to address global water scarcity, Rev. Environ. Sci. Bio/Technology 16 (2017) 591–609. https://doi.org/10.1007/s11157-017-9449-7.

[324] M.M. Mekonnen, A.Y. Hoekstra, Four billion people facing severe water scarcity, Sci. Adv. 2 (2025) e1500323. https://doi.org/10.1126/sciadv.1500323.

[325] M.A. Shannon, P.W. Bohn, M. Elimelech, J.G. Georgiadis, B.J. Mariñas, A.M. Mayes, Science and technology for water purification in the coming decades, Nature 452 (2008) 301–310. https://doi.org/10.1038/nature06599.

[326] Water And Sanitation in Developing Countries: Including Health in the Equation, Environ. Sci. Technol. 41 (2007) 17–24. https://doi.org/10.1021/es072435t.

[327] B. Chen, M.Y. Han, K. Peng, S.L. Zhou, L. Shao, X.F. Wu, W.D. Wei, S.Y. Liu, Z. Li, J.S. Li, G.Q. Chen, Global land-water nexus: Agricultural land and freshwater use embodied in worldwide supply chains, Sci. Total Environ. 613–614 (2018) 931–943. https://doi.org/10.1016/j.scitotenv.2017.09.138.

[328] M.M. Hasan, K. Alam, Inequality in access to improved drinking water sources and childhood diarrhoea in low- and middle-income countries, Int. J. Hyg. Environ. Health 226 (2020) 113493. https://doi.org/10.1016/j.ijheh.2020.113493.

[329] W.H. Organization, Guidelines for drinking-water quality: incorporating the first and second addenda, World Health Organization, 2022.

[330] S.E. Tank, J.W. McClelland, R.G.M. Spencer, A.I. Shiklomanov, A. Suslova, F. Moatar, R.M.W. Amon, L.W. Cooper, G. Elias, V. V Gordeev, C. Guay, T.Y. Gurtovaya, L.S. Kosmenko, E.A. Mutter, B.J. Peterson, B. Peucker-Ehrenbrink, P.A. Raymond, P.F. Schuster, L. Scott, R. Staples, R.G. Striegl, M. Tretiakov, A. V Zhulidov, N. Zimov, S. Zimov, R.M. Holmes, Recent trends in the chemistry of major northern rivers signal widespread Arctic change, Nat. Geosci. 16 (2023) 789–796. https://doi.org/10.1038/s41561-023-01247-7.

[331] C.-C. Lai, C.-J. Chang, Y.-S. Huang, W.-C. Chang, F.-G. Tseng, Y.-L. Chueh, Desalination of saline water by nanochannel arrays through manipulation of electrical double layer, Nano Energy 12 (2015) 394–400. https://doi.org/10.1016/j.nanoen.2014.10.039.

[332] J. López, A. Culcasi, M. Fernández de Labastida, A. Tamburini, G. Micale, A. Cipollina, J.L. Cortina, Integration of nanofiltration, ion exchange, and electrodialysis with bipolar membranes for the valorisation of brines: From seawater desalination plants to on-site chemicals production facilities, J. Environ. Manage. 381 (2025) 125119. https://doi.org/10.1016/j.jenvman.2025.125119.

[333] M. Elimelech, W.A. Phillip, The Future of Seawater Desalination: Energy, Technology, and the Environment, Science 333 (2011) 712–717. https://doi.org/10.1126/science.1200488.

[334] C. Fritzmann, J. Löwenberg, T. Wintgens, T. Melin, State-of-the-art of reverse osmosis desalination, Desalination 216 (2007) 1–76. https://doi.org/10.1016/j.desal.2006.12.009.

[335] K.B. Gregory, R.D. Vidic, D.A. Dzombak, Water Management Challenges Associated with the Production of Shale Gas by Hydraulic Fracturing, Elements 7 (2011) 181–186. https://doi.org/10.2113/gselements.7.3.181.

[336] L.F. Greenlee, D.F. Lawler, B.D. Freeman, B. Marrot, P. Moulin, Reverse osmosis desalination: Water sources, technology, and today's challenges, Water Res. 43 (2009) 2317–2348. https://doi.org/10.1016/j.watres.2009.03.010.

[337] D.T. Nguyen, V.S. Pham, Ions transport in electromembrane desalination: A numerical modeling for the return flow ion-concentration-polarization desalination system, Chem. Eng. Res. Des. 184 (2022) 366–377. https://doi.org/10.1016/j.cherd.2022.06.013.

[338] S. Choi, B. Kim, J. Han, Integrated pretreatment and desalination by electrocoagulation (EC)–ion concentration polarization (ICP) hybrid, Lab Chip 17 (2017) 2076–2084. https://doi.org/10.1039/C7LC00258K.

[339] V. V Nikonenko, A. V Kovalenko, M.K. Urtenov, N.D. Pismenskaya, J. Han, P. Sistat, G. Pourcelly, Desalination at overlimiting currents: State-of-the-art and perspectives, Desalination 342 (2014) 85–106. https://doi.org/10.1016/j.desal.2014.01.008.

[340] J.-P. Hsu, H.-H. Wu, C.-Y. Lin, S. Tseng, Ion Current Rectification Behavior of Bioinspired Nanopores Having a pH-Tunable Zwitterionic Surface, Anal. Chem. 89 (2017) 3952–3958. https://doi.org/10.1021/acs.analchem.6b04325.

[341] R. Sun, Y. Gou, S. Jing, X. Liu, B. Al-Anzi, Y. Gu, Z. Li, Mechanistic insights into monovalent cation selectivity in modified ion selective membranes: A model-based and experimental study, J. Memb. Sci. 735 (2025) 124573. https://doi.org/10.1016/j.memsci.2025.124573.

[342] D.T. Nguyen, V.-S. Pham, Modeling non-linear ion transport phenomena in ion-selective membranes: Three simplified models, Sep. Purif. Technol. 333 (2024) 125929. https://doi.org/10.1016/j.seppur.2023.125929.

[343] B. Qiu, L. Gong, Z. Li, J. Han, Electrokinetic flow in the U-shaped micro-nanochannels, Theor. Appl. Mech. Lett. 9 (2019) 36–42. https://doi.org/10.1016/j.taml.2019.01.006.

[344] Y.-C. Wang, A.L. Stevens, J. Han, Million-fold Preconcentration of Proteins and Peptides by Nanofluidic Filter, Anal. Chem. 77 (2005) 4293–4299. https://doi.org/10.1021/ac050321z.

[345] M. Li, R.K. Anand, Recent advancements in ion concentration polarization, Analyst 141 (2016) 3496–3510. https://doi.org/10.1039/C6AN00194G.

[346] Z. Ahmed, Y. Bu, L. Yobas, Conductance Interplay in Ion Concentration Polarization across 1D Nanochannels: Microchannel Surface Shunt and Nanochannel Conductance, Anal. Chem. 92 (2020) 1252–1259. https://doi.org/10.1021/acs.analchem.9b04417.

[347] D. Manikandan, V.V.R. Nandigana, Overlimiting current near a nanochannel a new insight using molecular dynamics simulations, Sci. Rep. 11 (2021) 15216. https://doi.org/10.1038/s41598-021-94477-x.

[348] R. Kwak, V.S. Pham, B. Kim, L. Chen, J. Han, Enhanced Salt Removal by Unipolar Ion Conduction in Ion Concentration Polarization Desalination, Sci. Rep. 6 (2016) 25349. https://doi.org/10.1038/srep25349.

[349] R.B. Schoch, J. Han, P. Renaud, Transport phenomena in nanofluidics, Rev. Mod. Phys. 80 (2008) 839–883. https://doi.org/10.1103/RevModPhys.80.839.

[350] M. Amoretti, C. Amsler, G. Bonomi, A. Bouchta, P. Bowe, C. Carraro, C.L. Cesar, M. Charlton, M.J.T. Collier, M. Doser, V. Filippini, K.S. Fine, A. Fontana, M.C. Fujiwara, R. Funakoshi, P. Genova, J.S. Hangst, R.S. Hayano, M.H. Holzscheiter, L. V Jørgensen, V. Lagomarsino, R. Landua, D. Lindelöf, E.L. Rizzini, M. Macrì, N. Madsen, G. Manuzio, M. Marchesotti, P. Montagna, H. Pruys, C. Regenfus, P. Riedler, J. Rochet, A. Rotondi, G. Rouleau, G. Testera, A. Variola, T.L. Watson, D.P. van der Werf, Production and detection of cold antihydrogen atoms, Nature 419 (2002) 456–459. https://doi.org/10.1038/nature01096.

[351] S. Nam, I. Cho, J. Heo, G. Lim, M.Z. Bazant, D.J. Moon, G.Y. Sung, S.J. Kim, Experimental Verification of Overlimiting Current by Surface Conduction and Electro-Osmotic Flow in Microchannels, Phys. Rev. Lett. 114 (2015) 114501. https://doi.org/10.1103/PhysRevLett.114.114501.

[352] Y. Green, S. Park, G. Yossifon, Bridging the gap between an isolated nanochannel and a communicating multipore heterogeneous membrane, Phys. Rev. E 91 (2015) 11002. https://doi.org/10.1103/PhysRevE.91.011002.

[353] S. Choi, B. Kim, K.G. Nayar, J. Yoon, S. Al-Hammadi, J.H. Lienhard V, J. Han, B. Al-Anzi, Techno-economic analysis of ion concentration polarization desalination for high salinity desalination applications, Water Res. 155 (2019) 162–174. https://doi.org/10.1016/j.watres.2019.02.023.

[354] A. Rabiee, M. Ahmadian-Elmi, M.R. Hajmohammadi, M. Mohammadifar, Multi-objective optimization of rectangular microchannel heat sink based on entropy generation and hydro-thermal performance using NSGA-II algorithm, Int. Commun. Heat Mass Transf. 149 (2023) 107140. https://doi.org/10.1016/j.icheatmasstransfer.2023.107140.

[355] J. Cheng, H. Xu, Z. Tang, P. Zhou, Multi-objective optimization of manifold microchannel heat sink with corrugated bottom impacted by nanofluid jet, Int. J. Heat Mass Transf. 201 (2023) 123634. https://doi.org/10.1016/j.ijheatmasstransfer.2022.123634.

[356] K. Li, K. Bai, P. Jiao, H. Chen, H. He, L. Shao, Y. Sun, Z. Zheng, R. Li, N. Bin Chang, Developing unbiased estimation of atmospheric methane via machine learning and multiobjective programming based on TROPOMI and GOSAT data, Remote Sens. Environ. 304 (2024). https://doi.org/10.1016/j.rse.2024.114039.

[357] M.S.G. Nandagopal, E. Abraham, N. Selvaraju, Advanced neural network prediction and system identification of liquid-liquid flow patterns in circular microchannels with varying angle of confluence, Chem. Eng. J. 309 (2017) 850–865. https://doi.org/10.1016/j.cej.2016.10.106.

[358] A. Baghban, M. Kahani, M.A. Nazari, M.H. Ahmadi, W.-M. Yan, Sensitivity analysis and application of machine learning methods to predict the heat transfer performance of CNT/water nanofluid flows through coils, Int. J. Heat Mass Transf. 128 (2019) 825–835. https://doi.org/10.1016/j.ijheatmasstransfer.2018.09.041.

[359] A. Baghban, M. Bahadori, J. Rozyn, M. Lee, A. Abbas, A. Bahadori, A. Rahimali, Estimation of air dew point temperature using computational intelligence schemes, Appl. Therm. Eng. 93 (2016) 1043–1052. https://doi.org/10.1016/j.applthermaleng.2015.10.056.

[360] S.D. Farahani, M.K. Zare, A. Alizadeh, Enhancing PVT/air system performance with impinging jet and porous media: A computational approach with machine learning predictions, Appl. Energy 377 (2025) 124509. https://doi.org/10.1016/j.apenergy.2024.124509.

[361] C.A. Richter do Nascimento, V.C. Mariani, L. dos S. Coelho, Integrative numerical modeling and thermodynamic optimal design of counter-flow plate-fin heat exchanger applying neural networks, Int. J. Heat Mass Transf. 159 (2020) 120097. https://doi.org/10.1016/j.ijheatmasstransfer.2020.120097.

[362] A. Larrañaga, J. Martínez, J.L. Míguez, J. Porteiro, Robust optimization of heat-transfer-enhancing microtextured surfaces based on machine learning surrogate models, Int. Commun. Heat Mass Transf. 151 (2024) 107218. https://doi.org/10.1016/j.icheatmasstransfer.2023.107218.

[363] A. Baghban, F. Pourfayaz, M.H. Ahmadi, A. Kasaeian, S.M. Pourkiaei, G. Lorenzini, Connectionist intelligent model estimates of convective heat transfer coefficient of nanofluids in circular cross-sectional channels, J. Therm. Anal. Calorim. 132 (2018) 1213–1239. https://doi.org/10.1007/s10973-017-6886-z.

[364] S.A. Khan, U. Farooq, M. Imran, H. Liu, T. Muhammad, M. Alghamdi, Mathematical and artificial neural network modeling to predict the heat transfer of mixed convective electroosmotic nanofluid flow with Helmholtz-Smoluchowski velocity and multiple slip effects: An application of soft computing, Case Stud. Therm. Eng. 61 (2024) 104950. https://doi.org/10.1016/j.csite.2024.104950.

[365] M.S. Giri Nandagopal, N. Selvaraju, Prediction of Liquid–Liquid Flow Patterns in a Y-Junction Circular Microchannel Using Advanced Neural Network Techniques, Ind. Eng. Chem. Res. 55 (2016) 11346–11362. https://doi.org/10.1021/acs.iecr.6b02438.

[366] P. Naphon, S. Wiriyasart, T. Arisariyawong, Artificial neural network analysis the pulsating Nusselt number and friction factor of TiO2/water nanofluids in the spirally coiled tube with magnetic field, Int. J. Heat Mass Transf. 118 (2018) 1152–1159. https://doi.org/10.1016/j.ijheatmasstransfer.2017.11.091.

[367] P. Naphon, T. Arisariyawong, S. Wiriyasart, A. Srichat, ANFIS for analysis friction factor and Nusselt number of pulsating nanofluids flow in the fluted tube under magnetic field, Case Stud. Therm. Eng. 18 (2020) 100605. https://doi.org/10.1016/j.csite.2020.100605.

[368] K. Ramesh, D. Kumar, M. Devakar, Electrokinetically modulated flow of couple stress magneto-nanofluids in a microfluidic channel, Heat Transf. Res. 48 (2019) 379–397. https://doi.org/10.1002/htj.21389.

[369] F. Vázquez, M.Á. Olivares-Robles, S. Cuevas, Viscoelastic Effects on the Entropy Production in Oscillatory Flow between Parallel Plates with Convective Cooling, Entropy 11 (2009) 4–16. https://doi.org/10.3390/e11010004.

[370] R.J. Hunter, The significance of stagnant layer conduction in electrokinetics, Adv. Colloid Interface Sci. 100–102 (2003) 153–167. https://doi.org/10.1016/S0001-8686(02)00060-X.

[371] Z. Wang, M. Li, F. Ren, B. Ma, H. Yang, Y. Zhu, Sobol sensitivity analysis and multi-objective optimization of manifold microchannel heat sink considering entropy generation minimization, Int. J. Heat Mass Transf. 208 (2023) 124046. https://doi.org/10.1016/j.ijheatmasstransfer.2023.124046.

[372] S.D. Farahani, M. Hossieni, A. Alizadeh, Performance prediction of concentrated photovoltaics with mini-channel and elastic cylinders using ANFIS and sobol sensitivity analysis, Renew. Energy 256 (2026) 123889. https://doi.org/10.1016/j.renene.2025.123889.

[373] S. Liu, X. Zhang, Y. Yang, N. Hu, Ion Transport in Multi-Nanochannels Regulated by pH and Ion Concentration, Anal. Chem. 96 (2024) 5648–5657. https://doi.org/10.1021/acs.analchem.4c00406.

[374] V.-T. Dang, V.-S. Pham, Determination of Critical Dimensions of Microchannels to Ensure the Electrokinetic Biomolecule Preconcentration: Analytical and Numerical Studies, Langmuir 40 (2024) 6051–6064. https://doi.org/10.1021/acs.langmuir.4c00300.

[375] X. Li, J. Feng, Y. Tan, Z. Wang, G. Tian, L. Wang, Examination of convective heat transfer and entropy generation performance in twisted elliptical tubes using response surface method, Appl. Therm. Eng. 248 (2024) 123164. https://doi.org/10.1016/j.applthermaleng.2024.123164.

[376] L. Wang, X. Luo, J. Zhang, Y. Fan, Numerical study and multi-optimization of heat transfer performance in counter flow minichannel heat sink with slots on ribs using NSGA-II, Therm. Sci. Eng. Prog. 48 (2024) 102413. https://doi.org/10.1016/j.tsep.2024.102413.

[377] S. Mirjalili, S. Saremi, S.M. Mirjalili, L. dos S. Coelho, Multi-objective grey wolf optimizer: A novel algorithm for multi-criterion optimization, Expert Syst. Appl. 47 (2016) 106–119. https://doi.org/10.1016/j.eswa.2015.10.039.

[378] A. Bhowmick, B. Kundu, Extremum analysis based on exergy and economic principle for ejector-absorption cycles combined with regenerative organic-Rankine and gas-turbine cycles, Energy Convers. Manag. 253 (2022) 115174. https://doi.org/10.1016/j.enconman.2021.115174.

[379] Y. Ge, S. Wang, Z. Liu, W. Liu, Optimal shape design of a minichannel heat sink applying multi-objective optimization algorithm and three-dimensional numerical method, Appl. Therm. Eng. 148 (2019) 120–128. https://doi.org/10.1016/j.applthermaleng.2018.11.038.

[380] M.A. Jamil, W.M. Ashraf, N. Imtiaz, B. Bin Xu, S.M. Zubair, H. Yaqoob, M. Imran, M.W. Shahzad, Machine learning-based process design of a novel sustainable cooling system, Energy Convers. Manag. 319 (2024) 118941. https://doi.org/10.1016/j.enconman.2024.118941.

[381] A.A. Alnaqi, H. Moayedi, A. Shahsavar, T.K. Nguyen, Prediction of energetic performance of a building integrated photovoltaic/thermal system thorough artificial neural network and hybrid particle swarm optimization models, Energy Convers. Manag. 183 (2019) 137–148. https://doi.org/10.1016/j.enconman.2019.01.005.

[382] T. Wilberforce, A.G. Olabi, D. Monopoli, M. Dassisti, E.T. Sayed, M.A. Abdelkareem, Design optimization of proton exchange membrane fuel cell bipolar plate, Energy Convers. Manag. 277 (2023) 116586. https://doi.org/10.1016/j.enconman.2022.116586.

Signature of the Candidate: Sujit Saha

(Author's name)

Date: 31.12.2025

31-12-2025

Dr. Balaram Kundu
Professor
Dept. of Mechanical Engineering
Jadavpur University
Kolkata-700032